CONDUCTIVE M–PYRAZOLATE COORDINATION FRAMEWORKS BASED ON REDOX-ACTIVE AROMATIC DIIMIDES

Grant Matthew Brown

Doctor of Philosophy

University of York

Department of Chemistry

October 2023

ABSTRACT

The effectiveness of a solid-state material as a semiconducting entity within contemporary electronic frameworks fundamentally hinges on its molecular structure. Chapter 1 provides a foundational elucidation of charge transport within ordered solids, delineating the *through-space* and *through-bond* charge transport pathways within supramolecular assemblies. However, the deliberate manipulation of such charge transport routes to attain heightened conductivity levels poses a significant challenge. Therefore, strategies involving hydrogen bonding and metal coordination to orchestrate the assembly of supramolecular structures, with the aim of achieving pronounced π-orbital overlap within each corresponding charge transport pathway are introduced. Chapter 2 explores harnessing hydrogen bonding to autonomously assemble monomeric units in the solid state, surmounting the inherent repulsion between aromatic π-surfaces and culminating in the creation of organic material proficient in *through-space* charge transport through the convergence of discrete π-orbitals. Chapter 3, building upon the material obtained in Chapter 2, centres on the development of a coordination polymer possessing robust chemical and thermal characteristics. The objective is to propagate both *through-bond* and *through-space* charge transport pathways, thereby yielding highly conductive materials tailored for energy storage applications. In Chapter 4, an isoreticular strategy was implemented to scrutinise the manipulation of the topological framework of the material acquired in Chapter 3. To generate isostructural materials endowed with augmented charge transport pathways, Fe-salts containing anions of different sizes were used, leading to frameworks with identical topologies. In Chapter 5, the selection of an alternative inorganic linker to what was observed in Chapters 3 and 4 will be examined to discern the impact of distinctive coordination modes on charge transport pathways. While the methodologies for modulating the *through-space* and *through-bond* pathways are currently undergoing refinement, this Thesis endeavours to underscore the efficacy of deploying hydrogen bonding and isoreticular design strategies in shaping molecular assemblies towards achieving elevated levels of conductivity.

Dedicated to my Friends and Family

TABLE OF CONTENTS

Chapter 1 Introduction

Chapter 2 | Hydrogen-bond assisted tuning of conductive NDI assembles with high π-orbital overlap

Chapter 3 | An electroactive Fe–pyrazolate porous coordination polymer

Chapter 4 | Anion bridge variation of isostructural Fe(X)NDI-1 frameworks

Chapter 5 Formate-bridged coordination polymers with highly conductive *through-space* charge transport pathways

---

Chapter 6 Summary and Outlook

Chapter 7 | Appendix

AUTHOR'S DECLARATION

I declare that this thesis is a presentation of original work and I am the sole author. This work has not previously been presented for a degree or other qualification at this University or elsewhere. All sources are acknowledged as references.

Signed: G. Brown

Date: 02nd October 2023

ACKNOWLEDGEMENTS

Alyssa-Jennifer Avestro. I cannot begin to thank you enough for the outstanding job that you do. The atmosphere that you've created in your group is inspirational. No hierarchy. Calm. Welcoming. Fun. I hope that while I've been in the group, I've been able to propagate the type of environment that you've tried so hard to create. I have learnt so much more than I thought I would from you. Chemistry. Writing. Mentoring. I'm so grateful to you for your teachings and guidance, and no matter what environment I find myself in the future, I'll aim to make it similar to what I've experienced in your group.

Alison Parkin. Alison, from the TAP meetings that we've had throughout these four years, I'm really appreciative of the time, effort and care that you've put in. You've been a fantastic IPM, and I really like your straightforward and realistic way of speaking. Thank you!

The University of York. During my four years at York, my experience of the university has felt inclusive and happy. There hasn't been a time where I've felt left out or unsupported. I'd also like to give a big thank you to all the members of the table tennis club for the years of fun and games, and the University of York Student's Union for funding the table tennis club.

Funding bodies. I am very grateful to the EPSRC for funding my PhD studies for the past 3.5 years.

Marjaana Heiniö. Outside of University you were my strongest supporter. I am so grateful to have had you in my life for so many years. Thank you.

My family. Thank you so much for all the support throughout my thesis. I will be grateful to you for the rest of my life.

Original AJA group members. In no particular order, Pavan Yerramsetti, Ruhee Dawood, Fraser Arnold, Jamie Gould. I'm so thankful that I've had all of you throughout the majority of my PhD. I couldn't have hoped for a better bunch of people to spend 4 years with. Thank you for all the support, advice, and companionship. I will miss your constant presence in my life.

Friends of E214. From the members of the various research groups that have been in the E214 lab over the years (Spicer group, Wilkinson group, Bruce group, Cowling group) and the lab tech Iman Khazal. Thank you for making my lab experience so enjoyable. It wouldn't have been the same without you.

The ChemGrad office. Every time that I've asked a question, be it in person or *via* email, you've been there to provide patient and informative answer. I cannot thank you more for providing this service, not just to me, but to all graduate students.

Professor David Smith. Thank you for being my second supervisor and providing me with critical advice and feedback during the early years of my PhD.

LIST OF COLLABORATORS

Ruhee Dawood, Avestro Group, University of York. Carried out computational analysis for Chapter 2. Carried out the initial synthetic procedures in Chapter 2, which were later replicated by myself.

Fraser H. N. Arnold, Avestro Group, University of York. Carried out the initial synthetic procedures in Chapter 2, which were later replicated by myself. Grew single-crystals of two materials in Chapter 2 (**NDI-1**, **NDI-3**)

Dr Dmitry Yufit, Durham University. Single-crystal X-ray diffraction analysis of crystalline samples grown by Fraser Arnold.

Dr Stuart Cavill, SPET, University of York. For training and access to a Keithly sourcemeter.

Dr Adrian Whitwood, University of York. Single-crystal X-ray diffraction collection and solving for crystalline samples I had grown in Chapters 2 and 5. Also solved the data collected for **Fe(Cl)NDI-1** at Diamond Light Source (see below for more details) in Chapter 3.

Dr Jamie Gould, Avestro Group, University of York. Carried out the initial synthetic protocols for Chapter 3 and Chapter 4 (one material only, **Fe(OH)NDI-1**), which were later replicated by myself.

Dr Philip A. Hope, Avestro Group, Durham University. Collected high-resolution electron microscopy images in Chapters 3 and 4.

Dr James Quirk, SPET, University of York. Carried out computational analysis for Chapters 3 and 4.

Dr. Jeppe Christensen, Diamond Light Source, UK. Carried out single-crystal X-ray diffraction of **Fe(Cl)NDI-1** using Beamline I19.

Crystal Yu, Avestro Group, University of York. Carried out work to determine the optimal synthetic conditions to synthesise **FeCPNDI-1** in Chapter 5.

CHAPTER 1 |

INTRODUCTION

SYNOPSIS

In the realm of modern electronics, the molecular-level structural properties of a material play a pivotal role in enabling efficient charge transport. Understanding and controlling charge transport pathways, namely *through-space* and *through-bond* mechanisms, are crucial in developing high-performance semiconducting materials. In this study, we explore both coordination polymers (CPs) and purely organic materials to discern the optimal conditions for creating the next generation of semiconducting compounds. Within organic materials, hydrogen bonding interactions are identified as a key factor in generating supramolecular structures that surmount the repulsion between aromatic molecules. Overcoming repulsion leads to the formation of *through-space* charge transport pathways between overlapped π-orbitals, resulting in semiconducting materials that are highly solution-processable. Concerning CPs, *through-space* charge transport is modulated by the selection of metal centres and ligands that allow for close distances and spatially high π-orbital overlap between aromatic units. In other CP frameworks, *through-bond* charge transport is observed to be enhanced by choosing appropriate metal centres and linkers with good orbital overlap. In both cases, an isoreticular design strategy proves instrumental to obtained desirable charge transport. An isoreticular strategy involves using one topological framework net as a starting point to generate new frameworks with the same topological net, enabling the screening of various linkers or metal centres to identify components which relate to the most superior charge transport properties.

1.1 CHARGE TRANSPORT AND BAND THEORY IN ORDERED SOLID-STATE MATERIALS

The theory underpinning charge transport in solid-state materials constitutes the fundamental principle behind modern semiconductors, which rely on well-ordered conductive materials to drive current technologies.[1] The electrical conductivity of a solid material is a measure of how efficiently charge moves through its structure and is determined by a combination of two charge carriers, namely electrons and holes, along with their respective concentrations (see Equation 1).

$$\sigma = e(\mu_e n_e + \mu_h n_h) \tag{1}$$

σ = conductivity, e = elemental charge, μ_e = electron mobility, μ_h = hole mobility, n_e = electron concentration, n_h = hole concentration.

The concentrations of each type of charge carrier are contingent upon the electronic structure of a material, influenced by a spectrum of chemical factors, including crystallographic arrangement, bonded associations, defect densities, valence electron count, impurity presence, and structural irregularities.[2] In conventional materials, predominance of either electrons or holes as charge carriers typically characterises overall electrical conductivity.

Charge transport phenomena have been conceptualised through two prevailing models: hopping transport and band transport.[3] Hopping transport manifests with charge carriers localised at discrete locales within a material, requiring an activation energy barrier to be overcome, to enable transport between sites. Hopping transport finds theoretical substantiation in organic semiconductors and materials exhibiting pronounced structural disorder. In contrast, band transport is a consequence of robust interactions between charge carrier sites, resulting in the formation of a continuous energy band, as opposed to discreet molecular orbitals observed in hopping transport. Predominantly witnessed in crystalline inorganic or metallic materials, band transport engenders the delocalisation of charge carriers across the system. Materials that display hopping conductive pathways tend to exhibit diminished conductivity values, while those governed by band transport mechanisms typically display heightened conductivity. For example, pentacene was analysed as a thin film in a device by Ghosh and co-workers. Through injecting sufficient charge carriers into the pentacene layer, charge transport was converted from hopping to band transport, demonstrating higher charge mobilities after conversion.[4]

Moreover, the band and hopping mechanisms can be discerned through their reliance on applied temperature, which closely correlates with the charge carrier concentration. Materials operating under hopping transport exhibit a propensity for enhanced conductivity with increasing temperatures, a product of the improved availability of electrons or holes.[5–7] In materials employing band transport, conductivity can be either thermally activated or deactivated.[8] In metals, at the zenith of charge carrier concentrations, an inversely proportional relationship between conductivity and temperature emerges, stemming from escalating scattering effects as temperatures increase.[9,10]

In the categorisation of materials into conductive and non-conductive classes, the band model imparts three classifications: insulators, semiconductors, and conductors.[11] The band model's schematic representation (Figure 1.1) comprises the valence and conduction bands, that are separated by the band gap (E_g). In line with the Bohr model[12], elucidating the manifold energy levels that electrons may occupy within an atom, juxtaposed, interdependent atoms exhibit a fan-like dispersion of their discrete energy levels, culminating in a broad energy spectrum no longer attributed to a singular atom. At elevated energy levels, the valence electrons of one atom interact with the energy levels of neighbouring atoms, facilitating the detachment of valence electrons from an individual atom. In clusters of numerous atoms, a solitary valence electron eludes exclusive assignment, yielding continuous energy bands, specifically the valence band.

Insulators boast generous band gaps, with the valence band thoroughly populated by electrons, necessitating a substantial amount of energy to elevate an electron to the conduction band. Consequently, insulating materials demonstrate meagre conductivities, typically falling below 10^{-10} S cm^{-1}. Semiconductors feature narrower band gaps, wherein, under ambient conditions, valence band electrons can be seamlessly promoted to the conduction band. These promoted electrons function as charge carriers, leaving behind a vacancy in the valence band that is amenable to occupation by other electrons. Additionally, there subsists a temperature-dependent aspect tied to the charge carrier concentration of semiconductors, a characteristic contributory to material identification. Perfect conductors, devoid of an E_g, yield scenarios where either a charge carrier from the valence band ascends to the conduction band, or a saturated valence band intersects with an unoccupied conduction band. Invariably, conductivity values in conductors surpass those observed in semiconductors, frequently exceeding 102 S cm^{-1}.[13]

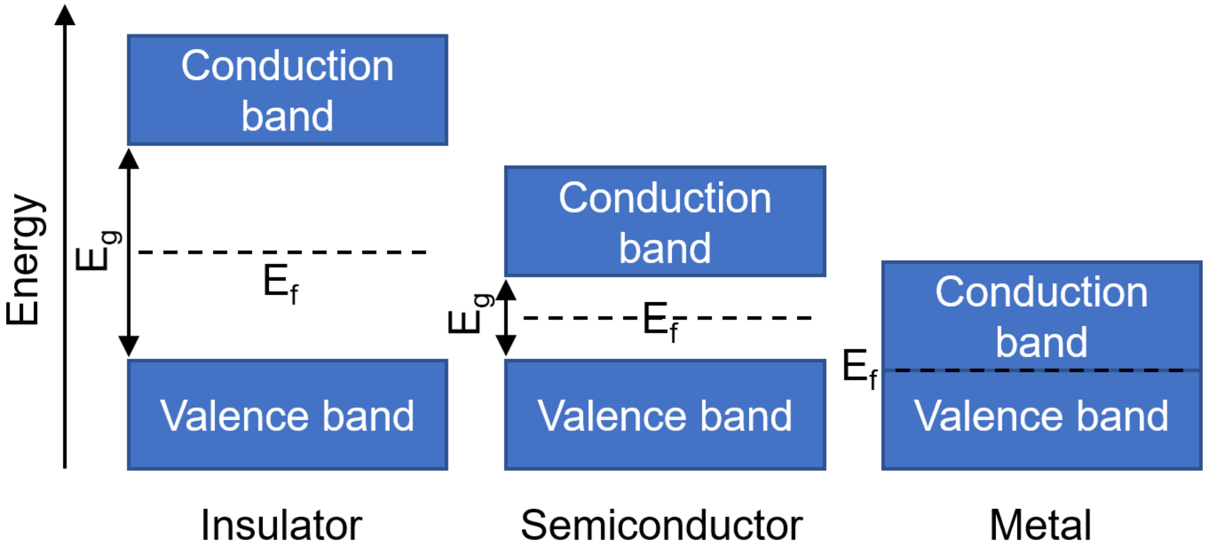

Figure 1.1. A simple representation of the electronic band structures of insulators, semiconductors and metals.

1.2 DETERMINING THE CONDUCTIVITY OF A MATERIAL

Interrogating a bulk material in an experimental setting is a crucial practice to assess its charge transport capabilities. The conductivity value indicates how effectively charge propagates through a system, which is indicative of its potential as a conductive material in electronic devices. Resistivity tests are conducted on prepared samples to generate an I–V curve (I = electrical current, V = voltage) following Ohm's law, typically resulting in a straight line.[14] However, in cases involving insulating samples, non-linear I–V curves may arise due to low current density[14] or poor contacts,[15] requiring a line to be fit onto the experimental I–V curve. To calculate a conductivity value, Equation 2 and 3 can be used in conjunction with Equation 4.

$$\mathrm{J} = \frac{\mathrm{I}}{\mathrm{A}} \tag{2}$$

$$\mathrm{E} = \frac{\mathrm{V}}{\mathrm{t}} \tag{3}$$

$$\sigma = \frac{\mathrm{J}}{\mathrm{E}} \tag{4}$$

σ = Electrical conductivity, J = current density, E = electric field strength, I = current, A = area of the pellet, t = thickness of pellet.

Samples can be prepared for resistivity analysis in one of three ways: as single crystals, thin films, or pressed powders, each method offering distinct advantages and disadvantages. Ideally, resistivity measurements on single crystals are preferred, as they eliminate contributions from grain boundaries, allowing for the probing of anisotropic charge transport. However, the preparation of single crystals that are large enough is a challenging task, often requiring significant time and effort. Additionally, constructing nano-scale devices for single crystal analysis can be a demanding process, requiring significant time and incurring additional costs.[16]

As an alternative, the preparation of polycrystalline materials in the form of thin films or pressed pellets is often a more practical choice in terms of time and effort. Pressed pellets, especially those compressed under high pressures, are the most readily available option due to the ease of preparation, manipulation, and analysis. Nevertheless, pressed pellets have two drawbacks when compared to single crystals. The random arrangement of crystallites in a pressed pellet renders the analysis of anisotropy impossible, which would otherwise be observable in a single crystal. Furthermore, grain boundaries, representing defective interfaces between two crystallites, disrupt charge transport that would be intrinsic in a single crystal, causing differences in grain sizes and pellet pressurisation to affect the resistivity measurement. Consequently, resistivity measurements on pressed pellets are limited to evaluating the least conductive charge transport direction, with the added complexity of grain boundaries leading to an overall underestimation of conductivity.[17]

In lieu of pressed pellets, polycrystalline films can be grown or deposited on insulating layers, albeit at the expense of additional effort in generation. For example, the molecular precursor method requires the appropriate solvent and appropriate heating/cooling method to be screening, in order to obtain a desired phase.[18] More advanced techniques such as magnetron sputtering or pulsed laser deposition require expensive equipment.[18] Despite the longer preparation times, polycrystalline films exhibit higher conductivity values due to a higher material density in comparison to pressed pellets. However, they are subject to the same drawbacks as pressed pellets, namely the presence of grain boundaries and the arrangement of crystalline structures.

Furthermore, when analysing resistivity, it is imperative to consider the impact of substances in the surrounding atmosphere (e.g., oxygen, water), the temperature of the material, and the influence of visible light on the sample. Each of these factors can either decrease or increase the measured conductivity depending on the identity of the material under analysis. Consequently, the ideal analysis would be conducted on single crystals in a vacuum, at a constant temperature, and in darkness. However, practical constraints and the additional time and effort required to produce single crystals render this approach unattainable in many situations.

In order to analyse prepared samples, two-probe setups are utilised for pressed pellets, while four-probe and van der Pauw methods are often employed for thin films and single crystals.[19,20] For meaningful values with a two-probe setup, the material must have a considerably higher resistance than the contacts and wires used. The four-probe method takes into account the resistance of the contacts and wires, allowing for the analysis of materials with resistances close to or higher than that of the contacts and wires.

While experimental methods need to account for bulk material properties, such as grain boundaries and anisotropy, an examination of the structural properties of a material at the molecular level is imperative to comprehend the transport of charge. In particular, understanding the pathway through which charge traverses a material is crucial to provide insights into enhancing charge transport.

1.3 CHARGE TRANSPORT PATHWAYS IN COORDINATION POLYMERS

There are two main charge transport pathways that will be commented on in this work which enable the movement of electrons or holes throughout an ordered solid, where charge transport can occur as the result of *through-bond* or *through-space*, *via* band transport or electron hopping mechanisms.[16,21] Understanding and controlling charge transport pathways in ordered solids is vital to obtaining materials with highly conductive properties, causing the study and control of such properties to be a high priority.[22] In this work, the majority of the discussion will focus on *through-space* and *through-bond* charge transport pathways within mixed metal-organic systems i.e., CPs.

CPs are a class of highly ordered crystalline solids that consist of metal nodes that connect to organic linkers. Depending upon the choice of metal node and organic linker, different dimensionality (0D, 1D, 2D, 3D) can be obtained that is often directly related to the preferred coordination geometry of the coordinating metal ion (Figure 1.2). Pores can result from the formed coordination network, resulting in materials called metal organic frameworks (MOFs). All other CPs without porosity are simply called "coordination polymers". For the purposes of this thesis, MOFs will be renamed "porous coordination polymers" (PCPs), and coordination polymers without porosity will be named "non-porous coordination polymers" (NP-CPs). PCPs have been developed more extensively than NP-CPs since their inception back in 1990.[23] The first generation of PCPs were insulating materials (e.g., the IRMOF series)[24], but new advancements made in the past 15 years include the addition of charge-transport pathways into CPs that has led to the development of conductive CPs. As a consequence of the porous nature of PCPs that allow access to internal structural elements of the framework, PCPs have been developed for use in a multitude of applications (e.g., energy storage,[21] electrocatalysis,[25] chemiresistors[26]).

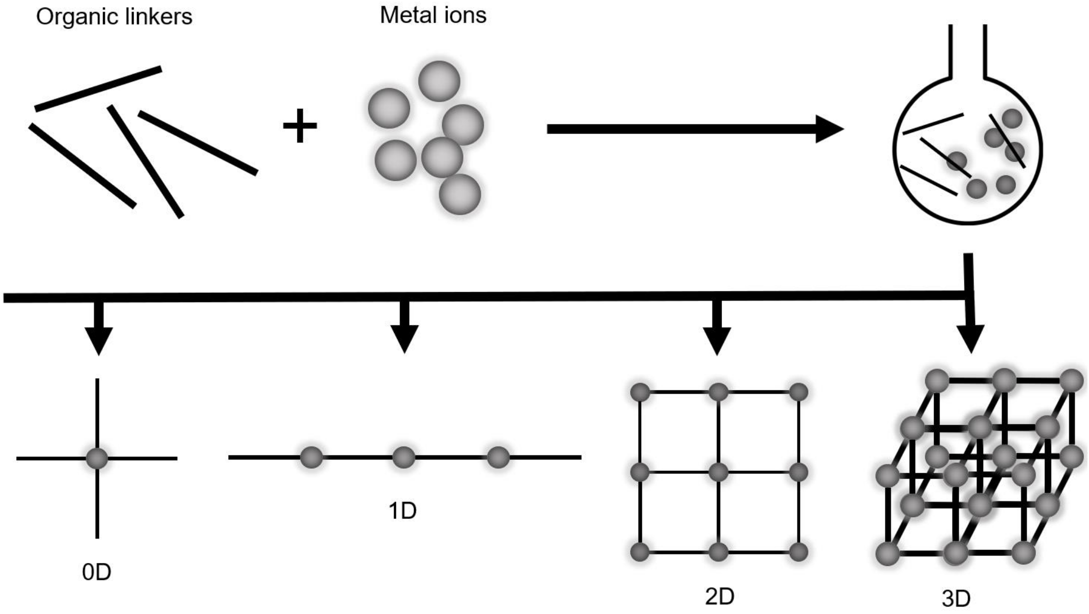

Figure 1.2. A simplified reaction scheme for the synthesis of CPs.

To access the *through-bond* pathway in CPs, metal nodes and organic linkers that have good orbital overlap need to be selected that form continuous chains allowing for electron delocalisation through a CP framework (Figure 1.3a). In recent years, a plethora of metal node/organic linker combinations (e.g., Fe/N, Fe/S, Cu/S) have been identified to overlap well and form conductive pathways, allowing researchers to synthesise CPs expressing *through-bond* characteristics by screening a wide range of appropriate reagents until a desired product with the appropriate levels of conductivity is achieved.

On the other hand, *through-space* charge transport originates from interactions between π-orbitals, that are located on aromatic molecules that are not chemically bonded together (Figure 1.3b). Most vital to electronically desirable semiconductor properties in *through-space* pathways are the propagation of long-range order, combined with packing motifs that display close π–π stacking distances and high π-orbital overlap between discreet aromatic molecules. In the context of PCPs, examples of π-orbital overlap have been developed using aromatic molecules such as 1,4,5,8-naphthalenetetracarboxylic acid diimide (NDI), perylene-3,4,9,10-tetracarboxylic acid diimide (PDI), 2,3,6,7,10,11-hexahydroxytriphenylene (HTTP), resulting in high conductivities. However, controlling π-interactions towards electronically desirable orientations that are desirable for *through-space* transport is challenging, requiring multiple factors to be considered, that will be covered in the following section.

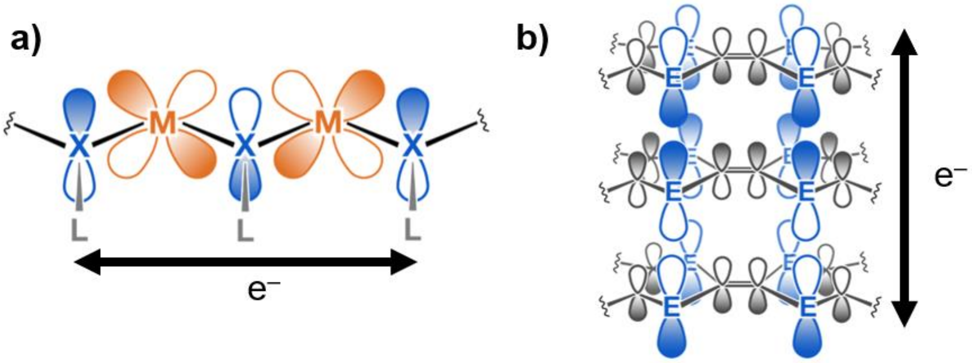

Figure 1.3. The (a) *through-bond* and (b) *through-space* charge transport pathways in coordination polymers. The figure is reproduced from the work of Xie et al.[16]

1.3.1 *THROUGH-SPACE* TRANSPORT: UNDERSTANDING π–π INTERACTIONS

Interactions between two individual arene units are the most numerous examples of π-interactions in supramolecular and organic chemistry, and upon assembly of π-surfaces, either as dimer or as a continuous array, can lead to a wide range of electronic, optical and stabilisation properties at the macroscopic level that are not expressed as a solitary monomer. As a result, π-stacking configurations between aromatic rings have garnered a large amount of interest for application in a wide array of areas (e.g., protein folding,[27] crystal engineering,[28] drug design,[29] semiconductors[30]). However, due to the quadrupole that is intrinsic to all aromatic molecules as well as other factors (van der Waals, solvent), π-stacking configurations are difficult to control towards an electronically desired orientation and instead self-assemble into electrostatically favourable arrangements. Hence, understanding and controlling π-interactions is vital to propagating *through-space* charge transport pathways enabling the future of advanced electronically active materials semiconducting.

The term "π–π stacking" suggests that aromatic molecules possess unique properties that pertain to stacking, however, π-cloud electron density has negligible influence on packing between aromatic molecules. Instead, interactions between aromatic molecules are influenced by three major factors: (i) electrostatic interactions (ii) hydrophobic affects (iii) and van der Waals interactions (London dispersion forces)[31,32], causing multiple sources to comment that "π–π stacking" is a misleading term.[33,34] Despite the controversy surrounding the term "π–π stacking", this text will continue to use the term "π–π stacking" in the context of interactions between aromatic molecules.

The combination of the three interaction parameters governs the packing arrangement that will be adopted by aromatic molecules, leading to a complicated analysis of the various strengths of each individual interaction. In addition, the geometry associated with a studied π–π interaction affects the relative strengths of interactions (i) and (iii), i.e., electrostatic interactions depend upon the charge distributed around the π-stacked aromatic molecules, and van der Waals forces are affected by the contact surface area. Further complicating the understanding of π–π interactions are the nature of aromatic quadrupolar dipoles, that differs from what is observed between smaller atomic constructs i.e., H_2O. In the case of water, oxygen possesses a greater electronegativity than that of hydrogen, which results in a partially negative charge on the oxygen atom, and partially positive charge on both hydrogen atoms. In the case of water, the partial separation of charges results in multiple dipole moments within the same molecule, of which a vector can be assigned to the overall direction of the charge (Figure 1.4a). On the other hand, the aromatic molecule benzene possesses individual dipoles between C–H atoms that are cancelled out due to the internal symmetry of the molecule, resulting in no overall dipole moment (Figure 1.4b). Despite not possessing an overall dipole moment, benzene has a quadrupole moment that results in a partial negative charge over areas where delocalised π-electrons are present, and partial positive charges around the periphery of benzene (Figure 1.4c).[27] As benzene possesses π-electrons above and below its aromatic faces, the same charges are present on both sides of the molecule. Therefore, benzene possesses two dipoles that are aligned from end-to-end, where one dipole originates from the centre of the molecule and points up, and the other originates from the same place and points down. The alignment of dipoles in an aromatic molecule that result in no net dipole is known as a quadrupole.

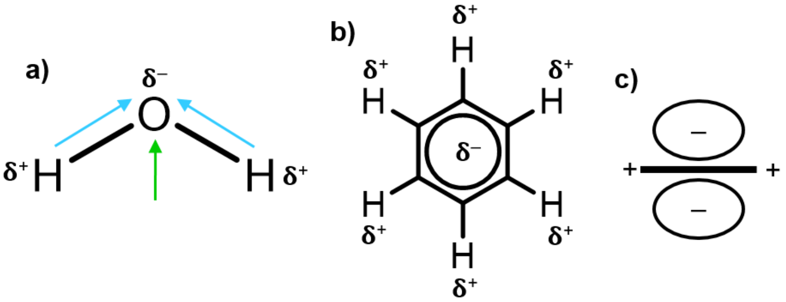

Figure 1.4. Simple representations of (a) water, showing two individual dipole moments (blue), and an overall dipole moment (green), (b) benzene showing partial charges, (c) a rotated benzene representation showing partial negative charges above its flat plane and partial positive charges around its periphery.

To explain π–π stacking, Hunter and Sanders presented the widely accepted model based on quadrupole moments.[35] Using benzene as a simplistic example, Hunter and Sanders explained that the partially positively charged σ-framework is sandwiched between two partially negatively charged π–electron clouds, and critically that these two systems should be considered separately. Hunter and Sanders also assigned, at the nucleus of each carbon atom in benzene's aromatic system a value of +1, and a value of –0.5 at a distance above each face of benzene. Once combined, the values add up to +6 for the for the carbon nuclei, while a contribution of –3 is observed for the π–electron clouds above the aromatic faces. Overall, the model predicts that π-clouds will repulse one-another, causing a close co-facial arrangement (Figure 1.5a) to be disfavoured, while attractive interactions between σ-frameworks and π-systems cause edge-to-face (Figure 1.5b) and parallel displaced (Figure 1.5c) orientations to be favoured. Theoretical work has provided support for the predicted packing arrangements of benzene molecules in Hunter and Sander's model (co-facial –1.48 kcal mol^{-1}, edge-to-face –2.46 kcal mol^{-1}, parallel displaced –2.48 kcal mol^{-1}), where a more negative integer corresponds to larger attractive interaction.[36] Further work to interrogate benzene dimers theoretically led near-identical results, demonstrating that edge-to-face and parallel displaced arrangements were near-isoenergetic, and that an eclipsed stacking arrangement is the least favoured.[37]

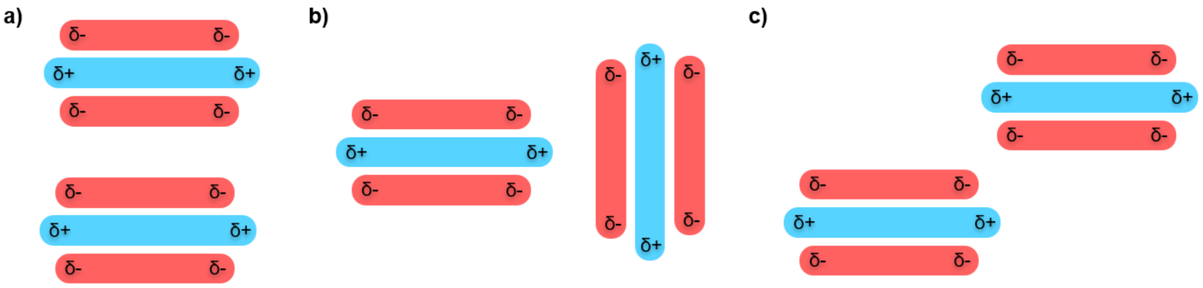

Figure 1.5. A basic representation of the three main aromatic π–π stacking motifs. a) co-facial, electrostatically unfavourable, b) edge-to-face or T-shaped, electrostatically favourable, c) parallel displaced or slip-stacked. This figure was adapted from the work done by Carter-Fenk and Herbert.[38]

The Hunter and Sanders model also predicts that benzene will form co-facial stacks with aromatic molecules that have reversed quadrupoles, due to attractive electrostatic interactions.[35] Therefore, with respect to benzene, hexafluorobenzene has strong electron-withdrawing fluorine atoms in place of hydrogen atoms, resulting in a reversed quadrupole that was theorised by Hunter and Sanders to form co-facial stacks with benzene. One recent article demonstrated supporting evidence for an attractive interaction between reversed quadrupoles when hexafluorobenezene and 1,3,5-trimethylbenzene were mixed, forming crystals that displayed alternating co-facial stacks, using atmospheric conditions that allowed for the crystals to be prepared by pre-university students.[39]

As a consequence of π–π interactions described in the Hunter and Sanders model that result in close co-facial π-orbital overlap between π-surfaces, charge transfer complexes can form between two systems. With respect to electron-rich aromatic molecules such as benzene, overlap of aromatic surfaces allows the transport of holes *via* low-lying highest occupied molecular orbitals (HOMOs) that exist above each flat plane. Conversely, π-overlapped electron-poor aromatic molecules act as electron transporters, allowing charge to delocalise between lowest unoccupied molecular orbitals (LUMOs).[33,40]

The Hunter and Sanders predictive model draws its wisdom for the determination of aromatic π–π stacking from the electrostatic interaction of quadrupoles, largely disregarding van der Waals interactions and hydrophobic effects, which has led to criticism of the model.[33] Researchers have suggested that the Hunter and Sanders model, rather than a set of rules, should be used as a loose guide, while still taking into account other major interaction (i.e., van der Waals interactions and hydrophobic effects) that can influence aromatic packing configurations.[33,38,41–45] The debate about the hunters and sanders model continues to this day, but will not be covered in this study.

In the context of conductive PCPs that are designed to propagate *through-space* charge transport pathways, the discussed fundamentals of π–π interactions make it clear that there are a multitude of factors that influence the packing of π-surfaces. Therefore, careful consideration should be given to picking aromatic linkers and metal centres that will lead to high overlap of π-surfaces to enable the most conductive *through-space* pathways that will benefit the semiconductor industry.

1.4 STRATEGIES TO CONTROL CHARGE TRANSPORT PATHWAYS

The design of PCPs involves the careful selection of metal centres and organic linkers to achieve the desired topology or functionality, forming a "net" that dictates the connectivity of the PCP.[46] The isoreticular design approach is strategically employed to modify the building blocks of a PCP while preserving the original net, aiming to obtain the most desirable properties.[47] Through this strategy, the porosity and structural rigidity of PCPs can be tailored while maintaining the original net for optimal properties.[48]

Isoreticular design was implemented early in the development of PCPs, exemplified by the classic case of isoreticular metal organic framework 1 (IRMOF-1[49], also known as MOF-5), which marked the beginning of a series of materials synthesised through isoreticular chemistry.[24] The initial PCP, IRMOF-1, featured Zn–O–C clusters linked by benzene connectors in a cubic net.[49] By substituting the dicarboxylic acid starting material, new linkers replaced the original benzene connectors, leading to adjustments in pore window size or creating larger pores, all while preserving the original cubic net structure (Figure 1.6).[24] As a result of the isoreticular approach, IRMOFs 1–16 were synthesised, among which four (IRMOF-9, 11, 13, 15) experienced interpenetration, losing their permanent porosity. In contrast, IRMOFs (1, 3, 8) have been extensively studied for their diverse properties.[46,50,51] Thus, isoreticular design has proven to be an effective strategy for tuning pore and pore window size, indicating that other aspects of CPs, such as *through-bond* and *through-space* charge transport, can also be influenced using this technique.

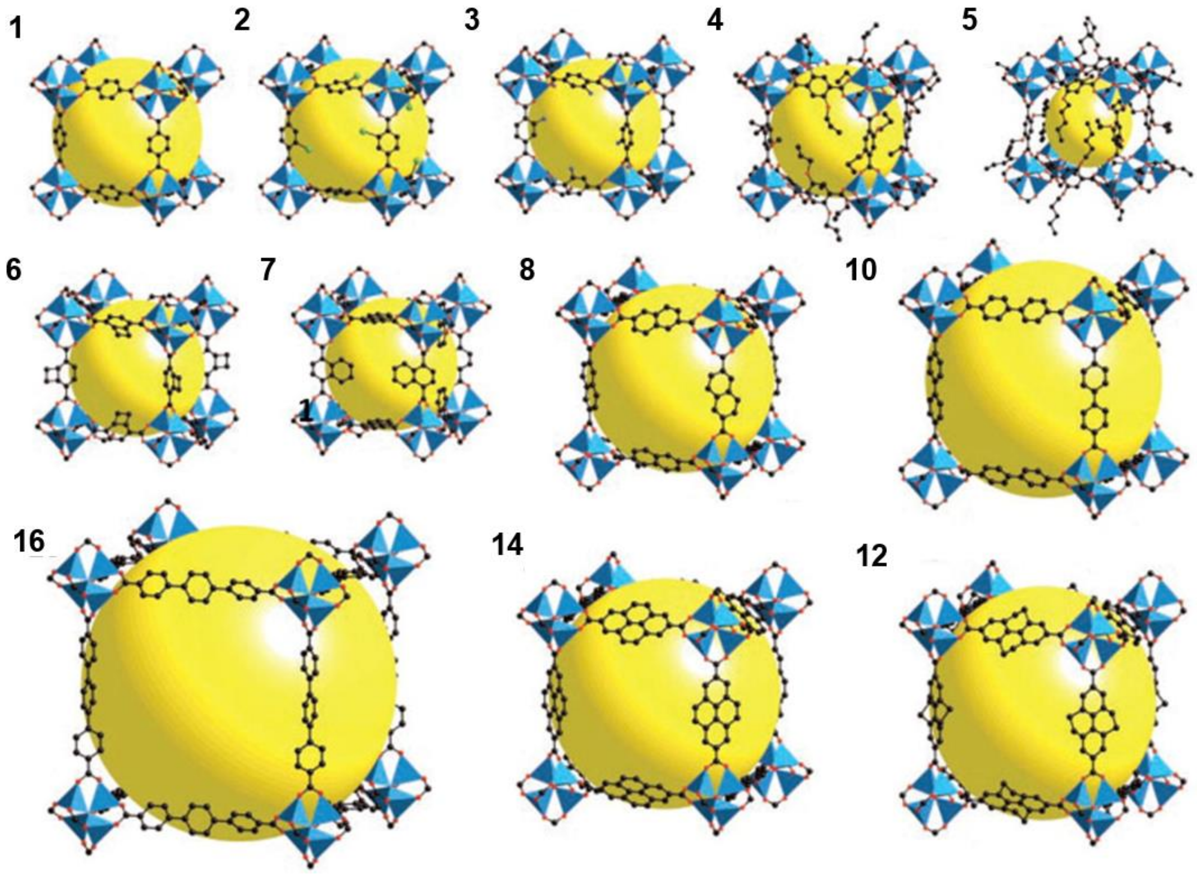

Figure 1.6. The non-interpenetrated IRMOFs. Each number represents the corresponding IRMOF, i.e., IRMOF-1, Reproduced from the work of Huang and co-workers.[25]

1.4.1 CONTROLLING *THROUGH-SPACE* CHARGE TRANSPORT IN COORDINATION POLYMERS

In the context of controlling aromatic surfaces to achieve high π-orbital overlap for potential semiconductor applications, an isoreticular strategy has been widely employed in the synthesis of *through-space* conductive CPs. One notable example of this approach was presented by Skorupskii et al.,[52] where they developed a series of 2D isostructural frameworks incorporating four different lanthanide metals (La, Nd, Ho, Yb) along with the ligand HTTP. The four frameworks shared a honeycomb-like structure (Figure 1.7b), where lanthanide metal centres coordinated to seven oxygen atoms on the HTTP linkers. The coordination geometry led to the high porosity of the framework and the emergence of a *through-space* charge transport pathways from π–π stacking between overlapping HTTP linkers (Figure 1.7a). The π–π distance between the HTTP linkers was influenced by the atomic radius of the incorporated lanthanide metal centre. The smallest π–π distances were observed in Yb (3.01 Å) and Ho (3.05 Å), affecting the electronic band structure of each PCP. The conductivity measurements of pressed pellets revealed similar conductivities of 0.09 S cm^{-1} and 0.05 S cm^{-1} for the

Yb and Ho PCPs, emphasising the importance of interchanging metal centres using an isoreticular design strategy to identify materials with enhanced *through-space* conductive properties.

A more recent study by Xue et al.[53] in 2023 focused on the development of a trio of interpenetrated PCPs employing an NDI linker. The isoreticular design strategy allowed for the synthesis of three PCPs, each featuring a distinct coordination geometry (Co^{2+} = Octahedral, Ni^{2+} = square planar, Zn^{2+} = tetrahedral) around the metal centre, while remaining isoreticular. The trio of PCPs exhibited self-interpenetration, resulting in long-range overlap between NDI π-surfaces, potentially facilitating *through-space* electron delocalisation (Figure 1.7c). Distances between the spatially stacked π-systems were modulated by each respective metal node (Co-pyNDI = 3.25 Å, Ni-pyNDI = 3.37 Å, ZnpyNDI = 3.5 Å), (Figure 1.7d). Conductivity measurements demonstrated that smaller π–π distances between NDI π-surfaces led to higher conductivity readings, suggesting that charge transport occurred *through-space* in this set of PCPs. Density of states (DOS) theoretical calculations further supported distance-conductivity relationship, showing that valence and conduction bands near the Fermi level were primarily localised to C, N, and O, attributed to the ligand. Additional studies revealed that, regardless of the self-interpenetration, pore sizes were modulated due to the coordination geometry around the metal centre (pore size = Ni > Zn > Co), enabling selective gas sensing. Moreover, the change in metal centre significantly influenced the arrangement of SBUs around each metal centre, resulting in modified π–π distances and pore sizes, underscoring the utility of the isoreticular design approach in tailoring PCPs with desired properties.

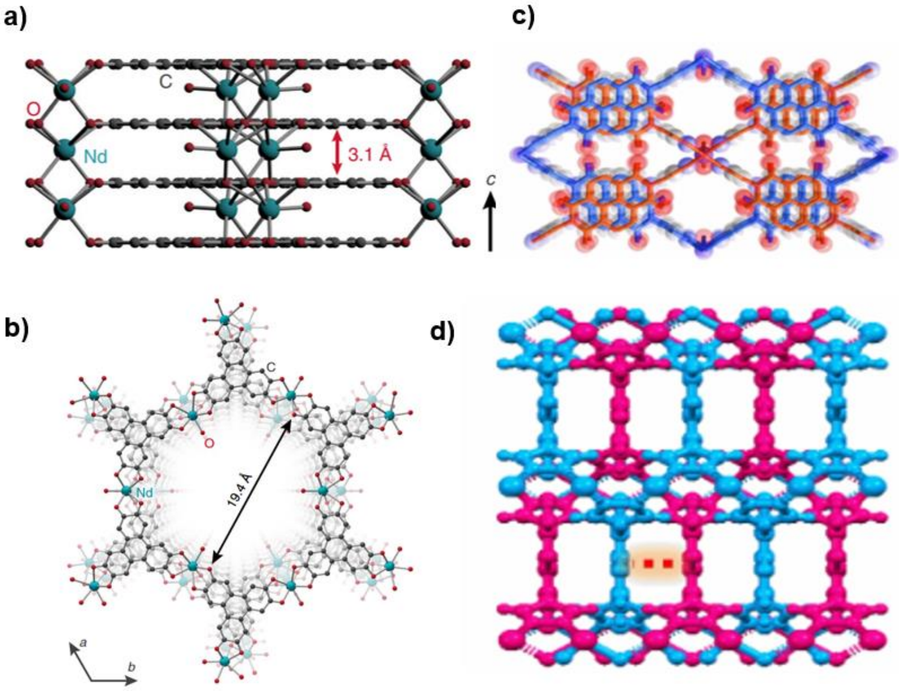

Figure 1.7. (a) Close π–π stacking between NDI linkers, (b) and the honeycomb structure in the Nd PCP developed by Skorupskii et al. Both images were copied from the work of Skorupskii et al.[52] (c) the interpenetrated framework, (d) and the π–π stacking between NDI ligands in the work of Xue et al. Both images were copied from the work of Xue et al.[53]

1.4.2 CONTROLLING *THROUGH-SPACE* CHARGE TRANSPORT IN ORGANIC MATERIALS

As an alternative to PCPs, organic aromatic materials with *through-space* charge transport pathways have gained prominence in modern electronics.[54,55] In contrast to their inorganic counterparts, these materials are lightweight, physically flexible, cost-effective, and can form solution-processable thin films with ease.[56–60] As a result, organic aromatic materials featuring *through-space* charge transport pathways mediated by π-orbital overlap have found applications in devices such as field effect transistors (FETs),[61,62] solar cells (SCs),[63,64] and light emitting diodes (LEDs).[65,66] To further advance organic electronics, design strategies must focus on arranging aromatic molecules in close proximity with high π-orbital overlap orientations, ultimately benefiting the semiconductor industry.[67,68]

One effective design strategy involves harnessing non-covalent interactions, particularly hydrogen bonds,[69] which are among the strongest non-covalent forces, with strengths reaching up to -15 kJ mol^{-1}.[70] A hydrogen bond acceptor (A) is typically an electronegative atom with access to excess electronic charge (e.g., a lone pair) and forms an attractive interaction with a hydrogen atom (X–H···A). Common hydrogen bond acceptors include O, N, and S, due to their availability of lone pairs, enabling researchers to design molecules with specific regions conducive to hydrogen bonding and desired frameworks. The hydrogen bond is highly directional and robust, playing a fundamental role in crystal engineering,[28] resulting in well-ordered hydrogen-bonded crystalline materials that exhibit desirable properties both as single crystals and in bulk.[29,71]

Utilising hydrogen bonds to guide aromatic molecular assemblies into a desired packing patterns has been demonstrated in self-assembly processes, from solution-state to solid-state, employing complementary sets of hydrogen bonds.[72,73] For instance, PDI aromatic surfaces were organised into a co-facial array through self-complementary hydrogen bonding between substituted trinitrobenzene molecules.[72] Thin films of these tape-like superstructures were generated from chloroform and integrated into an organic FET device, showcasing, for an FET device, a relatively low electron mobility of 1.0×10^{-4} cm^2 V^{-1} S^{-1} and remarkable solution-processability.[72] In another study,[73] two regioisomers self-assembled *via* hydrogen bonding between hexamer units to form an 0D ring-like nanostructure (Figure 1.8a) and a 1D rod-like nanostructure (Figure 1.8b), displaying distinct π–π overlap between naphthalene π-surfaces based on the formed nanostructure (Figure 1.8a). Conductivity measurements using flash photolysis time-resolved microwave techniques revealed that the 1D rod-like nanostructure with co-facial packing between naphthalene units exhibited a conductivity four times higher than that of the 0D ring-like nanostructure, underscoring the significance of both hydrogen bonding and regiochemistry in determining different packing structures. Unlike other organic strategies that aim to facilitate *through-space* charge transport via π-orbital overlap, such as polymers or COFs, supramolecular systems self-assembled with hydrogen bonds offer the advantage straight-forward solution-processability, enabling the production of thin films with greater ease and allowing for smooth incorporation of self-assembled materials into devices.

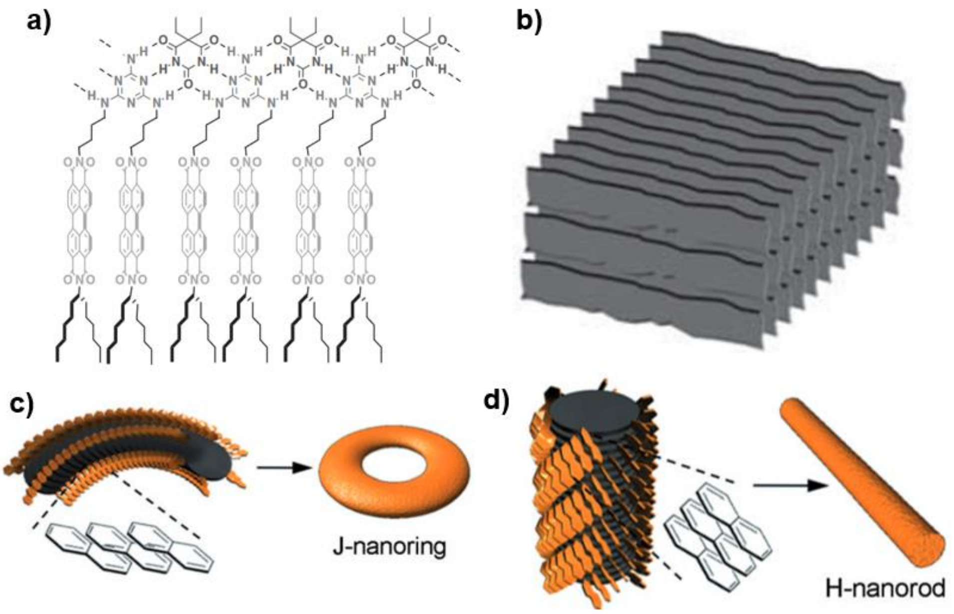

Figure 1.8. (a) Molecular packing of tape-like structure,[72] (b) and the lamellar superstructure of multiple tape-like structures, Both images were copied from the work of Seki et al.[72] (c) molecular models of the ring-like superstructure[73] (d) and rod-like superstructure. Both images were copied from the work of Yagai et al.[73]

1.4.3 CONTROLLING *THROUGH-BOND* CHARGE TRANSPORT IN COORDINATION POLYMERS

The *through-bond* charge transport pathway occurs between orbitals of chemically bonded atoms, leading to much closer interactions (typically 1–3 Å) compared to overlapped aromatic π-surfaces (3–4 Å). Resultingly, the formation of *through-bond* pathways is made less complicated than configuring arene units into electronically desirable configurations. However, in modern electronics, achieving desirable *through-bond* charge transport requires maximised orbital overlap and close matching between energy levels.[74] Such pathways have been established in materials such as organic polymers,[75,76] hydrogen-bonded frameworks,[77,78] and covalently bonded frameworks. [79,80] In this context of this work, only CPs expressing *through-bond* charge transport pathways will be covered.

In recent years, numerous metal centre/organic linker combinations (e.g., Fe–N,[81] Fe–S,[82] Mn–S[83]) have shown promise in providing strong orbital overlap, resulting in the formation of *through-bond* conductive pathways. For example, Pathak et al.[84] developed a 2D NP-CP with 6-mercaptonicotinate (6-mn) ligands coordinated to Cu metal centres (Figure 1.9a). The resulting $(\text{–Cu–S–})_n$ chain theoretically formed a *through-bond* pathway extending into 2D. Density of states (DOS) calculations confirmed the *through-bond* pathway, with the valence band model (VBM) consisting mostly of states related to the Cu atoms, along with some contributions from the S atoms. Experimental four-point single crystal measurements demonstrated an impressive conductivity of 11 S cm^{-1}, showcasing the remarkable charge transport capabilities of Cu–S bonds.

Through-bond charge transport pathways have also been identified between Fe–N bonds. Long et al.[85] generated a PCP named **Fe(tri)₂** that was characterised by coordination between Fe metal centres and 1,2,3-triazole linkers, forming a *through-bond* charge transport pathway (Figure 1.9b). **Fe(tri)₂** exhibited a two-point pressed pellet conductivity measurement of 7.7×10^{-5} S cm^{-1} which was a high value for a low-spin Fe^{2+} metal centre in conjunction with 1,2,3-triazole linkers.[17] Upon activation, a conductivity of 7×10^{-9} S cm^{-1} was observed, suggesting that oxidation of the Fe^{2+} metal centres by atmospheric air had occurred. Controlled oxidation with thianthrenium tetrafluoroborate revealed a Fe^{2+}/Fe^{3+} mixed valence framework that was identified by Mössbauer spectroscopy and displayed a conductivity of 0.3 S cm^{-1} which was eight orders of magnitude higher than that observed for the activated material. The work done by Long et al. underscores the potency of generating a Fe^{2+}/Fe^{3+} mixed valence framework in enhancing the conductivity of Fe–pyrazolate CPs.

Another instance of a Fe^{2+}/Fe^{3+} mixed valence framework was demonstrated by Dincà and co-workers,[86] who synthesised a PCP with Fe^{2+} metal centres bridged by 1,4-benzeneditetrazole (BDT) ligands **$Fe_2(BDT)_3$** (Figure 1.9c). Conductivity measurements immediately after synthesis and activation revealed a conductivity of 6×10^{-5} S cm^{-1}. After exposure to air for 30 days and subsequent Mössbauer spectroscopy analysis, it was found that low-spin Fe^{2+} metal centres had formed. As a result of the oxidation in air, an impressive single crystal conductivity of 1.2 S cm^{-1} was observed, further highlighting the appeal of forming Fe–pyrazolate CPs with Fe^{2+}/Fe^{3+} mixed valence metal centres.

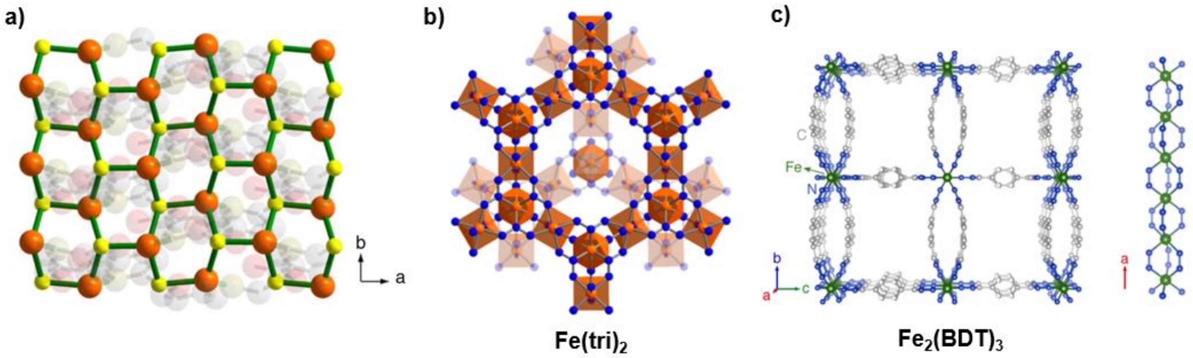

Figure 1.9. The frameworks of (a) the 2D NP-CP, copied from the work of Pathak et al.,[84] (b) Fe(tri)₂,copied from the work of Long et al.[85] (c) $Fe_2(BDT)_3$, copied from the work of Dincà and co-workers.[86]

Another comprehensive study conducted by Sun et al.[82] utilised an isoreticular chemistry design strategy to generate 20 PCPs, which were categorised into four structurally distinct families. Within each family, a variety of metal centres (i.e., Mg, Mn, Fe, Co, Cu, Zn, Cd, Ni) were examined to determine the metal centre that imparted the most superior *through-bond* semiconductor properties (i.e., conductivity, activation energy). Among the four distinct structural families, each containing different linkers, SBUs, and coordinated solvent molecules, Fe demonstrated the highest two-point pressed pellet conductivity measurements, surpassing other metal centres by five orders of magnitude, and displaying activation energies that were 0.12–0.54 eV smaller. Crucially, Fe^{2+} outperformed the other metal centres due to several factors: (i) it possesses the smallest ionisation energy, (ii) it is the most easily oxidisable, and (iii) it exhibits the highest propensity to lose a valence electron. Consequently, Fe is likely to form mixed valence Fe^{2+}/Fe^{3+} redox couples at room temperature, resulting in materials that possess higher charge densities and lead to significantly increased conductivity measurements. Therefore, by employing an isoreticular design strategy and screening multiple metal centres among the four distinct structural families, Sun et al determined that Fe was an attractive choice of metal centre for incorporation into future Fe–pyrazolate CPs.

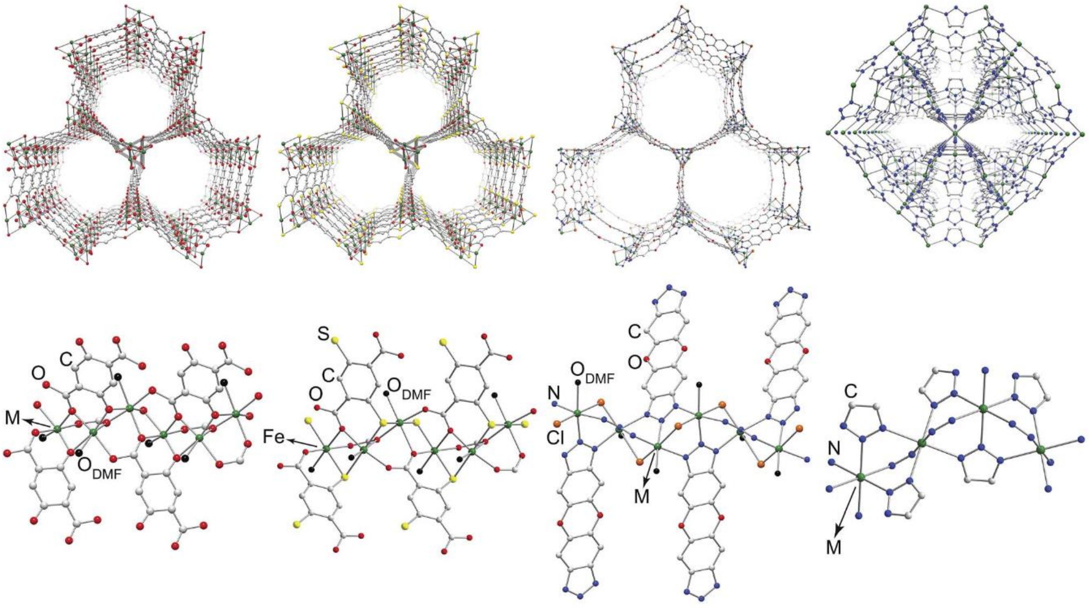

Figure 1.10. The four distinct structural families presented by Sun et al, which was copied from work carried out by Sun et al.[82]

1.4.4 AN ALTERNATIVE CHARGE TRANSPORT PATHWAY IN COORDINATION POLYMERS

In many cases, the *extended-conjugation* pathway builds upon the established *through-bond* pathway, utilising non-innocent ligands to aid in charge conduction, resulting in conductive CP materials that consistently exhibit some of the highest conductivity values reported to date (Figure 1.11a).[58,87] The incorporation of non-innocent ligands, such as -dithiols, -diamines, or ortho-diols, plays a dual role: (i) assisting in CP self-assembly, and (ii) contributing to charge delocalisation as mixed-valency linker species.[16] The use of non-innocent organic ligands is not exclusive to CPs and is a common motif in inorganic complexes, often leading to materials utilised as molecular conductors.[88,89] Furthermore, the majority of *extended-conjugation* CPs are 2D, allowing for charge transport to occur across 2D as opposed to only 1D. However, evidence suggests that in such *extended-conjugation* CPs charge transport can also occur through non-covalent *through-space* interactions between layers.[89,90]

One of the highest reported conductivities was observed in **$Ni_3(HITP)_2$**, which featured 2,3,6,7,10,11-hexaiminotriphenylene (HITP) linkers coordinated to Ni metal centres, resulting in a 2D layered honeycomb-like PCP (Figure 1.11b).[91] In another publication analyses of **$Ni_3(HITP)_2$** demonstrated a single crystal conductivity of 150 S cm^{-1}.[87] Initially, it was believed that charge transport occurred exclusively via the *extended-conjugation* pathway along the 2D coordinated metal-ligand sheets. However, later findings suggested that charge transport might also occur through the *through-space* pathway, *via* almost-eclipsed co-facial stacking between overlapping HITP linkers. Due to the high observed conductivity of **$Ni_3(HITP)_2$**, it has been investigated for its use as a supercapacitor, finding that as a transparent thin film it displayed superior capacitive performance rate capacity, and flexibility in comparison to other reported inorganic semiconductors.[92]

Another example of the *extended-conjugation* charge transport pathway was exhibited by **Cu-BHT** (BHT = benzenehexathiol), a NP-CP featuring π-d conjugation between Cu metal centres and BHT ligands (Figure 11.1c), allowing charge transport in 2D.[58] **Cu-BHT** was grown as a thin film directly onto a substrate, exhibiting a transparency of 82% and an exceptionally high conductivity of 2500 S cm^{-1}, owing to the ordered 20 nm layer and *extended-conjugation* pathway. When incorporated into a solar cell in place of indium tin oxide (ITO), **Cu-BHT** demonstrated comparable electrode performance and increased flexibility, highlighting that materials derived from more abundant resources could find use in modern electrode applications, paving the way for cost-effective, solution-processable materials.

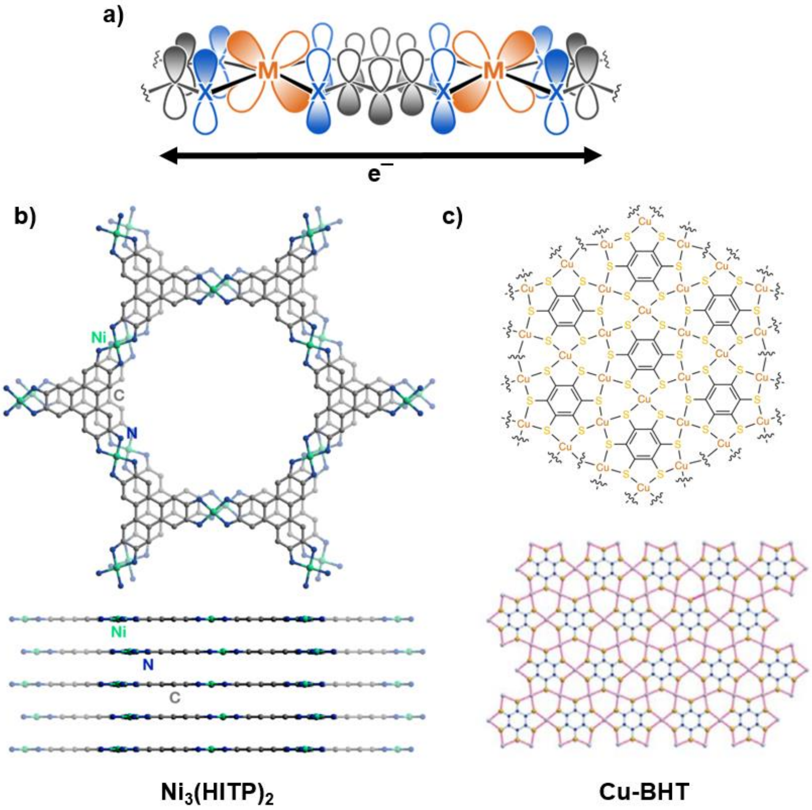

Figure 1.11. (a) The extended conjugation pathway, adapted from the work of Xie et al.[16] (b) The honey-comb like structure (top) and stacking (bottom) between 2D layers of **$Ni_3(HITP)_2$**, copied from the work of Sheberla et al.[91] and (c) the structure of **Cu-BHT,** copied from the work of Jin et al.[58]

1.5 CONCLUSIONS

In the realm of ordered solid-state materials, the study of charge transport has been a focal point, particularly within organic and mixed organic-inorganic semiconductors. One of the pivotal charge transport pathways, known as *through-space* charge transport, hinges on the close proximity and substantial orbital overlap between aromatic π-systems on adjacent arene units. However, regulating aromatic interactions involves nuanced factors that influence π–π interactions among these units.

A compelling strategy to induce proximity among organic molecular π-systems and enhance orbital overlap between arene units is through hydrogen bonding which has shown promise in driving aromatic systems towards orientations with heightened electronic desirability. Systems formed through hydrogen bonds are noteworthy for their solution processability and composition from common elements like C, N, and O, causing hydrogen bonding to be an appealing choice for contemporary electronic semiconducting materials. Conductive CPs that offer porosity and other functionalities (i.e., redox activity, highly ordered structures) also demonstrate *through-space* pathways between π-overlapped aromatic units within their structures. Notably, employing an isoreticular design strategy to modify an existing topological network has proven effective in achieving shorter π–π distances between aromatic units which enhances π-orbital overlap and results in desirable semiconducting properties.

Through-bond charge transport pathways, occurring due to orbital overlap and closely matched energy levels between repeating chemically bonded atoms, have been another avenue of exploration in CPs. Various combinations of metal centres and organic linkers, such as Fe–N, Fe–S, and Mn–S, have demonstrated efficient orbital overlap, leading to exceptional semiconductor properties. The application of an isoreticular design approach has yielded a plethora of frameworks, with Fe metal centres emerging as the preferred choice in conjunction with nitrogen-based linkers for creating highly conductive *through-bond* pathways. Particularly noteworthy are the remarkable semiconducting properties achieved by generating mixed valency Fe^{3+}/Fe^{2+} pairs within Fe–pyrazolate materials, solidifying their position as a promising choice for modern semiconducting materials.

Conductive CP materials have been observed to exhibit a coexistence of multiple charge transport modes, underscoring the persistent challenge in their deliberate design, optimisation, and seamless integration into forthcoming semiconductor technologies. Therefore, an ongoing and in-depth exploration of the interplay between synthesis, structure, and properties of CPs is a necessity. The primary focus of this Thesis is to delve into the diverse *through-bond* and *through-space* phenomena that underlie the conductivity of PCPs with analogous compositions, utilising redox-active NDI electron acceptors as ligands. The research presented here demonstrates that, through strategic employment of rational design, hydrogen bonding, and isoreticular design strategies, it is possible to create self-assembled materials that manifest multiple highly conductive charge transport pathways, constituting a significant stride forward in the development of modern semiconducting materials.

1.6 REFERENCES

(1) Brédas, J. L.; Calbert, J. P.; Filho, D. A. da S.; Cornil, J. Organic Semiconductors: A Theoretical Characterization of the Basic Parameters Governing Charge Transport. *Proc. Natl. Acad. Sci. U.S.A.* **2002**, *99*, 5804–5809. https://doi.org/10.1073/pnas.092143399.

(2) Coropceanu, V.; Cornil, J.; da Silva Filho, D. A.; Olivier, Y.; Silbey, R.; Brédas, J.-L. Charge Transport in Organic Semiconductors. *Chem. Rev.* **2007**, *107*, 926–952. https://doi.org/10.1021/cr050140x.

(3) Oberhofer, H.; Reuter, K.; Blumberger, J. Charge Transport in Molecular Materials: An Assessment of Computational Methods. *Chem. Rev.* **2017**, *117*, 10319–10357. https://doi.org/10.1021/acs.chemrev.7b00086.

(4) Rani, V.; Kumar, P.; Sharma, A.; Yadav, S.; Singh, B.; Ray, N.; Ghosh, S. Carrier Induced Hopping to Band Conduction in Pentacene. *Sci Rep* **2019**, *9* (1), 20193. https://doi.org/10.1038/s41598-019-56558-w.

(4) Han, M. Y.; Brant, J. C.; Kim, P. Electron Transport in Disordered Graphene Nanoribbons. *Phys. Rev. Lett.* **2010**, *104,* 056801. https://doi.org/10.1103/PhysRevLett.104.056801.

(5) Yu, Z.; Song, X. Variable Range Hopping and Electrical Conductivity along the DNA Double Helix. *Phys. Rev. Lett.* **2001**, *86*, 6018–6021. https://doi.org/10.1103/PhysRevLett.86.6018.

(7) Brütting, W. Introduction to the Physics of Organic Semiconductors. In *Physics of Organic Semiconductors*; John Wiley & Sons, Ltd, 2005; pp 1–14. https://doi.org/10.1002/3527606637.ch.

(7) Sakanoue, T.; Sirringhaus, H. Band-like Temperature Dependence of Mobility in a Solution-Processed Organic Semiconductor. *Nat. Mater.* **2010**, *9*, 736–740. https://doi.org/10.1038/nmat2825.

(9) Bleaney, B. I. *Electricity and Magnetism / B. I. Bleaney and B. Bleaney.*, 3rd ed.; University Press: Oxford, 1976.

(9) Matula, R. A. Electrical Resistivity of Copper, Gold, Palladium, and Silver. *J. Phys. Chem. Ref. Data*. **1979**, *8*, 1147–1298. https://doi.org/10.1063/1.555614.

(11) Altmann, S. L. *Band Theory of Solids: An Introduction from the Point of View of Symmetry / Simon L. Altmann.*; Oxford science publications; Clarendon Press ; Oxford University Press: Oxford [England] : New York, 1991.

(12) Bohr, N. On the Constitution of Atoms and Molecules, Part I. **1913**. https://doi.org/10.1080/14786441308634955.

(13) Pan, C.; Gaur, A. P. S.; Lynn, M.; Olson, M. P.; Ouyang, G.; Cui, J. Enhanced Electrical Conductivity in Graphene–Copper Multilayer Composite. *AIP Advances* **2022**, *12* (1), 015310. https://doi.org/10.1063/5.0073879.

(14) Saslow, W. M. Chapter 7 - Ohm's Law: Electric Current Is Driven by Emf, and Limited by Electrical Resistance. In *Electricity, Magnetism, and Light*; Saslow, W. M., Ed.; Academic Press: San Diego, 2002; pp 281–335. https://doi.org/10.1016/B978-012619455-5.50007-3.

(15) Nafari, A.; Angenete, J.; Svensson, K.; Sanz-Velasco, A.; Olin, H. Combining Scanning Probe Microscopy and Transmission Electron Microscopy. In *Scanning Probe Microscopy in Nanoscience and Nanotechnology 2*; Bhushan, B., Ed.; NanoScience and Technology; Springer: Berlin, Heidelberg, 2011; pp 59–99. https://doi.org/10.1007/978-3-642-10497-8_3.

(14) Xie, L. S.; Skorupskii, G.; Dincă, M. Electrically Conductive Metal–Organic Frameworks. *Chem. Rev.* **2020**, *120*, 8536–8580. https://doi.org/10.1021/acs.chemrev.9b00766.

(15) Sun, L.; Campbell, M. G.; Dincă, M. Electrically Conductive Porous Metal–Organic Frameworks. *Angew. Chem. Int. Ed.* **2016**, *55*, 3566–3579. https://doi.org/10.1002/anie.201506219.

(18) Hishimone, P. N.; Nagai, H.; Sato, M.; Hishimone, P. N.; Nagai, H.; Sato, M. Methods of Fabricating Thin Films for Energy Materials and Devices. In *Lithium-ion Batteries - Thin Film for Energy Materials and Devices*; IntechOpen, 2020. https://doi.org/10.5772/intechopen.85912.

(17) Chwang, R.; Smith, B. J.; Crowell, C. R. Contact Size Effects on the van Der Pauw Method for Resistivity and Hall Coefficient Measurement. *Solid State Electron.* **1974**, *17*, 1217–1227. https://doi.org/10.1016/0038-1101(74)90001-X.

(20) Singh, Y. Electrical Resistivity Measurements: A Review. *Int. J. Mod. Phys. Conf. Ser.* **2013**, *22*, 745–756. https://doi.org/10.1142/S2010194513010970.

(19) Calbo, J.; Golomb, M. J.; Walsh, A. Redox-Active Metal–Organic Frameworks for Energy Conversion and Storage. *J. Mater. Chem. A* **2019**, *7*, 16571–16597. https://doi.org/10.1039/C9TA04680A.

(20) Hoffmann, R. Interaction of Orbitals through Space and through Bonds. *Acc. Chem. Res.* **1971**, *4*, 1–9. https://doi.org/10.1021/ar50037a001.

(21) Hoskins, B. F.; Robson, R. Design and Construction of a New Class of Scaffolding-like Materials Comprising Infinite Polymeric Frameworks of 3D-Linked Molecular Rods. A

Reappraisal of the Zinc Cyanide and Cadmium Cyanide Structures and the Synthesis and Structure of the Diamond-Related Frameworks [N(CH3)4][CuIZnII(CN)4] and CuI[4,4',4'',4'''-Tetracyanotetraphenylmethane]BF4.xC6H5NO2. *J. Am. Chem. Soc.* **1990**, *112* 1546–1554. https://doi.org/10.1021/ja00160a038.

(22) Eddaoudi, M.; Kim, J.; Rosi, N.; Vodak, D.; Wachter, J.; O'Keeffe, M.; Yaghi, O. M. Systematic Design of Pore Size and Functionality in Isoreticular MOFs and Their Application in Methane Storage. *Science* **2002**, *295*, 469–472. https://doi.org/10.1126/science.1067208.

(23) Xu, W.; Thapa, K. B.; Ju, Q.; Fang, Z.; Huang, W. Heterogeneous Catalysts Based on Mesoporous Metal–Organic Frameworks. *Coord. Chem. Rev.* **2018**, *373*, 199–232. https://doi.org/10.1016/j.ccr.2017.10.014.

(24) Koo, W.-T.; Jang, J.-S.; Kim, I.-D. Metal-Organic Frameworks for Chemiresistive Sensors. *Chem* **2019**, *5*, 1938–1963. https://doi.org/10.1016/j.chempr.2019.04.013.

(25) Chipot, C.; Jaffe, R.; Maigret, B.; Pearlman, D. A.; Kollman, P. A. Benzene Dimer: A Good Model for Π−π Interactions in Proteins? A Comparison between the Benzene and the Toluene Dimers in the Gas Phase and in an Aqueous Solution. *J. Am. Chem. Soc.* **1996**, *118*, 11217–11224. https://doi.org/10.1021/ja961379l.

(26) Desiraju, G. R. Crystal Engineering: From Molecule to Crystal. *J. Am. Chem. Soc.* **2013**, *135*, 9952–9967. https://doi.org/10.1021/ja403264c.

(27) Datta, S.; Grant, D. J. W. Crystal Structures of Drugs: Advances in Determination, Prediction and Engineering. *Nat. Rev. Drug. Discov.* **2004**, *3*, 42–57. https://doi.org/10.1038/nrd1280.

(28) Beaujuge, P. M.; Fréchet, J. M. J. Molecular Design and Ordering Effects in π-Functional Materials for Transistor and Solar Cell Applications. *J. Am. Chem. Soc.* **2011**, *133*, 20009–20029. https://doi.org/10.1021/ja2073643.

(29) Hunter, C. A.; Lawson, K. R.; Perkins, J.; Urch, C. J. Aromatic Interactions. *J. Chem. Soc., Perkin Trans. 2* **2001**, *5*, 651–669. https://doi.org/10.1039/B008495F.

(30) Li, Q.; Li, Z. Molecular Packing: Another Key Point for the Performance of Organic and Polymeric Optoelectronic Materials. *Acc. Chem. Res.* **2020**, *53*, 962–973. https://doi.org/10.1021/acs.accounts.0c00060.

(31) Martinez, C. R.; Iverson, B. L. Rethinking the Term "Pi-Stacking." *Chem. Sci.* **2012**, *3*, 2191–2201. https://doi.org/10.1039/C2SC20045G.

(32) Grimme, S. Do Special Noncovalent π–π Stacking Interactions Really Exist? *Angew. Chem. Int. Ed.* **2008**, *47*, 3430–3434. https://doi.org/10.1002/anie.200705157.

(33) Hunter, C. A.; Sanders, J. K. M. The Nature of .Pi.-.Pi. Interactions. *J. Am. Chem. Soc.* **1990**, *112*, 5525–5534. https://doi.org/10.1021/ja00170a016.

(34) Tsuzuki, S.; Honda, K.; Uchimaru, T.; Mikami, M.; Tanabe, K. Origin of Attraction and Directionality of the π/π Interaction: Model Chemistry Calculations of Benzene Dimer Interaction. *J. Am. Chem. Soc.* **2002**, *124*, 104–112. https://doi.org/10.1021/ja0105212.

(35) Sinnokrot, M. O.; Sherrill, C. D. High-Accuracy Quantum Mechanical Studies of Π−π Interactions in Benzene Dimers. *J. Phys. Chem. A* **2006**, *110*, 10656–10668. https://doi.org/10.1021/jp0610416.

(38) Carter-Fenk, K.; M. Herbert, J. Electrostatics Does Not Dictate the Slip-Stacked Arrangement of Aromatic π–π Interactions. *Chem. Sci.* **2020**, *11*, 6758–6765. https://doi.org/10.1039/D0SC02667K.

(36) Timmer, B. J. J.; Mooibroek, T. J. Intermolecular π–π Stacking Interactions Made Visible. *J. Chem. Educ.* **2021**, *98*, 540–545. https://doi.org/10.1021/acs.jchemed.0c01252.

(37) Thakuria, R.; Nath, N. K.; Saha, B. K. The Nature and Applications of π–π Interactions: A Perspective. *Cryst. Growth Des.* **2019**, *19*, 523–528. https://doi.org/10.1021/acs.cgd.8b01630.

(39) Cubberley, M. S.; Iverson, B. L. 1H NMR Investigation of Solvent Effects in Aromatic Stacking Interactions. *J. Am. Chem. Soc.* **2001**, *123*, 7560–7563. https://doi.org/10.1021/ja015817m.

(40) Wheeler, S. E. Understanding Substituent Effects in Noncovalent Interactions Involving Aromatic Rings. *Acc. Chem. Res.* **2013**, *46*, 1029–1038. https://doi.org/10.1021/ar300109n.

(41) Mignon, P.; Loverix, S.; Geerlings, P. Interplay between π–π Interactions and the H-Bonding Ability of Aromatic Nitrogen Bases. *Chem. Phys. Lett.* **2005**, *401*, 40–46. https://doi.org/10.1016/j.cplett.2004.11.016.

(42) Banerjee, A.; Saha, A.; Saha, B. K. Understanding the Behavior of π–π Interactions in Crystal Structures in Light of Geometry Corrected Statistical Analysis: Similarities and Differences with the Theoretical Models. *Cryst. Growth Des.* **2019**, *19*, 2245–2252. https://doi.org/10.1021/acs.cgd.8b01857.

(43) Gung, B. W.; Emenike, B. U.; Lewis, M.; Kirschbaum, K. Quantification of CH···π Interactions: Implications on How Substituent Effects Influence Aromatic Interactions. *Chem. Eur. J.* **2010**, *16*, 12357–12362. https://doi.org/10.1002/chem.201001362.

(44) Britt, D.; Tranchemontagne, D.; Yaghi, O. M. Metal-Organic Frameworks with High Capacity and Selectivity for Harmful Gases. *Proc. Natl. Acad. Sci. U.S.A.* **2008**, *105*, 11623–11627. https://doi.org/10.1073/pnas.0804900105.

(45) Mai, Z.; Liu, D. Synthesis and Applications of Isoreticular Metal–Organic Frameworks IRMOFs-n (n = 1, 3, 6, 8). *Cryst. Growth Des.* **2019**, *19*, 7439–7462. https://doi.org/10.1021/acs.cgd.9b00879.

(48) Yaghi, O. M.; Kalmutzki, M. J.; Diercks, C. S. *Introduction to Reticular Chemistry: Metal-Organic Frameworks and Covalent Organic Frameworks*; John Wiley & Sons, 2019.

(47) Li, H.; Eddaoudi, M.; O’Keeffe, M.; Yaghi, O. M. Design and Synthesis of an Exceptionally Stable and Highly Porous Metal-Organic Framework. *Nature* **1999**, *402*, 276–279. https://doi.org/10.1038/46248.

(48) Ding, S.; Dong, Q.; Hu, J.; Xiao, W.; Liu, X.; Liao, L.; Zhang, N. Enhanced Selective Adsorption of CO2 on Nitrogen-Doped Porous Carbon Monoliths Derived from IRMOF-3. *Chem. Commun.* **2016**, *52*, 9757–9760. https://doi.org/10.1039/C6CC04416F.

(49) Rosi, N. L.; Eckert, J.; Eddaoudi, M.; Vodak, D. T.; Kim, J.; O’Keeffe, M.; Yaghi, O. M. Hydrogen Storage in Microporous Metal-Organic Frameworks. *Science* **2003**, *300*, 1127–1129. https://doi.org/10.1126/science.1083440.

(50) Skorupskii, G.; Trump, B. A.; Kasel, T. W.; Brown, C. M.; Hendon, C. H.; Dincă, M. Efficient and Tunable One-Dimensional Charge Transport in Layered Lanthanide Metal–Organic Frameworks. *Nat. Chem.* **2020**, *12*, 131–136. https://doi.org/10.1038/s41557-019-0372-0.

(51) Xue, Z.; Zheng, J.-J.; Nishiyama, Y.; Yao, M.-S.; Aoyama, Y.; Fan, Z.; Wang, P.; Kajiwara, T.; Kubota, Y.; Horike, S.; Otake, K.; Kitagawa, S. Fine Pore-Structure Engineering by Ligand Conformational Control of Naphthalene Diimide-Based Semiconducting Porous Coordination Polymers for Efficient Chemiresistive Gas Sensing. *Angew. Chem. Int. Ed.* **2023**, *62*, e202215234. https://doi.org/10.1002/anie.202215234.

(52) Facchetti, A. Semiconductors for Organic Transistors. *Mater. Today* **2007**, *10*, 28–37. https://doi.org/10.1016/S1369-7021(07)70017-2.

(53) Quinn, J. T. E.; Zhu, J.; Li, X.; Wang, J.; Li, Y. Recent Progress in the Development of N-Type Organic Semiconductors for Organic Field Effect Transistors. *J. Mater. Chem. C* **2017**, *5*, 8654–8681. https://doi.org/10.1039/C7TC01680H.

(54) Gao, X.; Hu, Y. Development of N-Type Organic Semiconductors for Thin Film Transistors: A Viewpoint of Molecular Design. *J. Mater. Chem. C* **2014**, *2*, 3099–3117. https://doi.org/10.1039/C3TC32046D.

(55) Jung, B. J.; Sun, J.; Lee, T.; Sarjeant, A.; Katz, H. E. Low-Temperature-Processible, Transparent, and Air-Operable n-Channel Fluorinated Phenylethylated Naphthalenetetracarboxylic Diimide Semiconductors Applied to Flexible Transistors. *Chem. Mater.* **2009**, *21*, 94–101. https://doi.org/10.1021/cm802281k.

(58) Jin, Z.; Yan, J.; Huang, X.; Xu, W.; Yang, S.; Zhu, D.; Wang, J. Solution-Processed Transparent Coordination Polymer Electrode for Photovoltaic Solar Cells. *Nano Energy* **2017**, *40*, 376–381. https://doi.org/10.1016/j.nanoen.2017.08.028.

(57) Zhan, X.; Facchetti, A.; Barlow, S.; Marks, T. J.; Ratner, M. A.; Wasielewski, M. R.; Marder, S. R. Rylene and Related Diimides for Organic Electronics. *Adv. Mater.* **2011**, *23*, 268–284. https://doi.org/10.1002/adma.201001402.

(58) Bronstein, H.; Nielsen, C. B.; Schroeder, B. C.; McCulloch, I. The Role of Chemical Design in the Performance of Organic Semiconductors. *Nat. Rev. Chem.* **2020**, *4*, 66–77. https://doi.org/10.1038/s41570-019-0152-9.

(59) Wang, C.; Dong, H.; Hu, W.; Liu, Y.; Zhu, D. Semiconducting π-Conjugated Systems in Field-Effect Transistors: A Material Odyssey of Organic Electronics. *Chem. Rev.* **2012**, *112*, 2208–2267. https://doi.org/10.1021/cr100380z.

(60) Li, L.; Tang, Q.; Li, H.; Yang, X.; Hu, W.; Song, Y.; Shuai, Z.; Xu, W.; Liu, Y.; Zhu, D. An Ultra Closely π-Stacked Organic Semiconductor for High Performance Field-Effect Transistors. *Adv. Mater.* **2007**, *19*, 2613–2617. https://doi.org/10.1002/adma.200700682.

(61) Günes, S.; Neugebauer, H.; Sariciftci, N. S. Conjugated Polymer-Based Organic Solar Cells. *Chem. Rev.* **2007**, *107*, 1324–1338. https://doi.org/10.1021/cr050149z.

(62) Zhang, J.; Bai, F.; Li, Y.; Hu, H.; Liu, B.; Zou, X.; Yu, H.; Huang, J.; Pan, D.; Ade, H.; Yan, H. Intramolecular π-Stacked Perylene-Diimide Acceptors for Non-Fullerene Organic Solar Cells. *J. Mater. Chem. A* **2019**, *7*, 8136–8143. https://doi.org/10.1039/C9TA00343F.

(63) Reineke, S.; Lindner, F.; Schwartz, G.; Seidler, N.; Walzer, K.; Lüssem, B.; Leo, K. White Organic Light-Emitting Diodes with Fluorescent Tube Efficiency. *Nature* **2009**, *459* , 234–238. https://doi.org/10.1038/nature08003.

(64) Uoyama, H.; Goushi, K.; Shizu, K.; Nomura, H.; Adachi, C. Highly Efficient Organic Light-Emitting Diodes from Delayed Fluorescence. *Nature* **2012**, *492*, 234–238. https://doi.org/10.1038/nature11687.

(65) Iwane, M.; Tada, T.; Osuga, T.; Murase, T.; Fujita, M.; Nishino, T.; Kiguchi, M.; Fujii, S. Controlling Stacking Order and Charge Transport in π-Stacks of Aromatic Molecules Based on Surface Assembly. *Chem. Commun.* **2018**, *54*, 12443–12446. https://doi.org/10.1039/C8CC06430J.

(66) Winkler, C.; Zojer, E. Strategies for Controlling Through-Space Charge Transport in Metal-Organic Frameworks via Structural Modifications. *Nanomaterials* **2020**, *10*, 2372. https://doi.org/10.3390/nano10122372.

(67) Steiner, T. The Hydrogen Bond in the Solid State. *Angew. Chem. Int. Ed.* **2002**, *41*, 48–76. https://doi.org/10.1002/1521-3773(20020104)41:1<48::AID-ANIE48>3.0.CO;2-U.

(68) Hobza, P. Calculations on Noncovalent Interactions and Databases of Benchmark Interaction Energies. *Acc. Chem. Res.* **2012**, *45*, 663–672. https://doi.org/10.1021/ar200255p.

(69) Bučar, D.-K. Engineering Molecular Crystals: Backbreaking, yet Gratifying. *Cryst. Growth Des.* **2017**, *17*, 2913–2918. https://doi.org/10.1021/acs.cgd.7b00210.

(70) Seki, T.; Karatsu, T.; Kitamura, A.; Yagai, S. Perylene Bisimide Organogels Formed by Melamine·cyanurate/Barbiturate Hydrogen-Bonded Tapes. *Polym. J.* **2012**, *44*, 600–606. https://doi.org/10.1038/pj.2012.22.

(71) Yagai, S.; Goto, Y.; Lin, X.; Karatsu, T.; Kitamura, A.; Kuzuhara, D.; Yamada, H.; Kikkawa, Y.; Saeki, A.; Seki, S. Self-Organization of Hydrogen-Bonding Naphthalene Chromophores into J-Type Nanorings and H-Type Nanorods: Impact of Regioisomerism. *Angew. Chem. Int. Ed.* **2012**, *51*, 6643–6647. https://doi.org/10.1002/anie.201201436.

(72) Troisi, A. Charge Transport in High Mobility Molecular Semiconductors: Classical Models and New Theories. *Chem. Soc. Rev.* **2011**, *40*, 2347. https://doi.org/10.1039/c0cs00198h.

(73) Li, G.; Shrotriya, V.; Huang, J.; Yao, Y.; Moriarty, T.; Emery, K.; Yang, Y. High-Efficiency Solution Processable Polymer Photovoltaic Cells by Self-Organization of Polymer Blends. *Nat. Mater.* **2005**, *4*, 864–868. https://doi.org/10.1038/nmat1500.

(74) Ohyama, A.; Hirata, N.; Oguma, N.; Ichikawa, M. Experimental Investigation of Naphthalene Based Organic Thin-Film Transistors by Combining a Polymer Dielectric and a Carrier Injection Layer. *J. Phys. D: Appl. Phys.* **2020**, *53*, 335102. https://doi.org/10.1088/1361-6463/ab8b04.

(75) Wang, B.; Lin, R.-B.; Zhang, Z.; Xiang, S.; Chen, B. Hydrogen-Bonded Organic Frameworks as a Tunable Platform for Functional Materials. *J. Am. Chem. Soc.* **2020**, *142*, 14399–14416. https://doi.org/10.1021/jacs.0c06473.

(76) Cai, S.; Shi, H.; Zhang, Z.; Wang, X.; Ma, H.; Gan, N.; Wu, Q.; Cheng, Z.; Ling, K.; Gu, M.; Ma, C.; Gu, L.; An, Z.; Huang, W. Hydrogen-Bonded Organic Aromatic Frameworks for Ultralong Phosphorescence by Intralayer π–π Interactions. *Angew. Chem. Int. Ed.* **2018**, *57*, 4005–4009. https://doi.org/10.1002/anie.201800697.

(77) Geng, K.; He, T.; Liu, R.; Dalapati, S.; Tan, K. T.; Li, Z.; Tao, S.; Gong, Y.; Jiang, Q.; Jiang, D. Covalent Organic Frameworks: Design, Synthesis, and Functions. *Chem. Rev.* **2020**, *120*, 8814–8933. https://doi.org/10.1021/acs.chemrev.9b00550.

(78) Wang, L.; Zeng, C.; Xu, H.; Yin, P.; Chen, D.; Deng, J.; Li, M.; Zheng, N.; Gu, C.; Ma, Y. A Highly Soluble, Crystalline Covalent Organic Framework Compatible with Device Implementation. *Chem. Sci.* **2019**, *10*, 1023–1028. https://doi.org/10.1039/C8SC04255A.

(79) Gándara, F.; Uribe-Romo, F. J.; Britt, D. K.; Furukawa, H.; Lei, L.; Cheng, R.; Duan, X.; O'Keeffe, M.; Yaghi, O. M. Porous, Conductive Metal-Triazolates and Their Structural Elucidation by the Charge-Flipping Method. *Chem. Eur. J.* **2012**, *18*, 10595–10601. https://doi.org/10.1002/chem.201103433.

(80) Sun, L.; Hendon, C. H.; Park, S. S.; Tulchinsky, Y.; Wan, R.; Wang, F.; Walsh, A.; Dincă, M. Is Iron Unique in Promoting Electrical Conductivity in MOFs? *Chem. Sci.* **2017**, *8*, 4450–4457. https://doi.org/10.1039/C7SC00647K.

(81) Sun, L.; Miyakai, T.; Seki, S.; Dincă, M. Mn2(2,5-Disulfhydrylbenzene-1,4-Dicarboxylate): A Microporous Metal–Organic Framework with Infinite (−Mn–S−)∞ Chains and High Intrinsic Charge Mobility. *J. Am. Chem. Soc.* **2013**, *135*, 8185–8188. https://doi.org/10.1021/ja4037516.

(82) Pathak, A.; Shen, J.-W.; Usman, M.; Wei, L.-F.; Mendiratta, S.; Chang, Y.-S.; Sainbileg, B.; Ngue, C.-M.; Chen, R.-S.; Hayashi, M.; Luo, T.-T.; Chen, F.-R.; Chen, K.-H.; Tseng, T.-W.; Chen, L.-C.; Lu, K.-L. Integration of a (–Cu–S–)n Plane in a Metal–Organic Framework Affords High Electrical Conductivity. *Nat. Commun.* **2019**, *10*, 1721. https://doi.org/10.1038/s41467-019-09682-0.

(83) Park, J. G.; Aubrey, M. L.; Oktawiec, J.; Chakarawet, K.; Darago, L. E.; Grandjean, F.; Long, G. J.; Long, J. R. Charge Delocalization and Bulk Electronic Conductivity in the Mixed-Valence Metal–Organic Framework Fe(1,2,3-Triazolate)$_2$(BF$_4$)$_x$. *J. Am. Chem. Soc.* **2018**, *140*, 8526–8534. https://doi.org/10.1021/jacs.8b03696.

(84) Xie, L. S.; Sun, L.; Wan, R.; Park, S. S.; DeGayner, J. A.; Hendon, C. H.; Dincă, M. Tunable Mixed-Valence Doping toward Record Electrical Conductivity in a Three-Dimensional Metal–Organic Framework. *J. Am. Chem. Soc.* **2018**, *140*, 7411–7414. https://doi.org/10.1021/jacs.8b03604.

(85) Day, R. W.; Bediako, D. K.; Rezaee, M.; Parent, L. R.; Skorupskii, G.; Arguilla, M. Q.; Hendon, C. H.; Stassen, I.; Gianneschi, N. C.; Kim, P.; Dincă, M. Single Crystals of Electrically Conductive Two-Dimensional Metal–Organic Frameworks: Structural and Electrical Transport Properties. *ACS Cent. Sci.* **2019**, *5*, 1959–1964. https://doi.org/10.1021/acscentsci.9b01006.

(86) Eisenberg, R.; Gray, H. B. Noninnocence in Metal Complexes: A Dithiolene Dawn. *Inorg. Chem.* **2011**, *50*, 9741–9751. https://doi.org/10.1021/ic2011748.

(87) Robertson, N.; Cronin, L. Metal Bis-1,2-Dithiolene Complexes in Conducting or Magnetic Crystalline Assemblies. *Coord. Chem. Rev.* **2002**, *227*, 93–127. https://doi.org/10.1016/S0010-8545(01)00457-X.

(88) Noro, S.; Chang, H.-C.; Takenobu, T.; Murayama, Y.; Kanbara, T.; Aoyama, T.; Sassa, T.; Wada, T.; Tanaka, D.; Kitagawa, S.; Iwasa, Y.; Akutagawa, T.; Nakamura, T. Metal−Organic Thin-Film Transistor (MOTFT) Based on a Bis(o-Diiminobenzosemiquinonate) Nickel(II) Complex. *J. Am. Chem. Soc.* **2005**, *127*, 10012–10013. https://doi.org/10.1021/ja052663s.

(89) Sheberla, D.; Sun, L.; Blood-Forsythe, M. A.; Er, S.; Wade, C. R.; Brozek, C. K.; Aspuru-Guzik, A.; Dincă, M. High Electrical Conductivity in Ni_3(2,3,6,7,10,11-Hexaiminotriphenylene)$_2$, a Semiconducting Metal–Organic Graphene Analogue. *J. Am. Chem. Soc.* **2014**, *136*, 8859–8862. https://doi.org/10.1021/ja502765n.

(90) Zhao, W.; Chen, T.; Wang, W.; Jin, B.; Peng, J.; Bi, S.; Jiang, M.; Liu, S.; Zhao, Q.; Huang, W. Conductive Ni3(HITP)2 MOFs Thin Films for Flexible Transparent Supercapacitors with High Rate Capability. *Sci. Bull.* **2020**, *65*, 1803–1811. https://doi.org/10.1016/j.scib.2020.06.027.

CHAPTER 2 |

HYDROGEN-BOND ASSISTED TUNING OF CONDUCTIVE NDI ASSEMBLIES WITH HIGH π-ORBITAL OVERLAP

SYNOPSIS

This chapter isaimed at probing the effect of a hydrogen bonding strategy in order to control aromatic interactions towards arrangements that are electronically desirable, with the ultimate goal of producing materials that have improved semiconductor properties. Specifically in this Chapter, the influence of groups that can self-complementary hydrogen bond (SCHB) will be used in conjunction with naphthalene diimide (NDI) molecules in order to arrange π-surfaces into electroactive orientations. To this end, four end-substituted NDI molecules will be synthesised and studied, featuring subtle differences (regiochemistry, steric) between pyrazole end-groups to determine conditions that are appropriate to propagate electroactive materials capable of transporting charge *via* π-orbitals. DFT calculations will be used to validate our experimental findings, probing the charge mobility properties and the geometrical considerations behind charge transport *via* π-orbital overlap. We will conclude that after achieving electronically superior configurations of π-surfaces that differ from conventionally orientated materials, multiple factors (i.e., distance, twist angle, orbital symmetries) should be considered when designing solid-state semiconducting materials.

AUTHOR CONTRIBUTIONS

The following people are gratefully acknowledged for their contribution to this Chapter. Ruhee Dawood and Fraser Arnold for establishing the initial synthetic procedures. Ruhee Dawood for performing the theoretical calculations with input from Joshua Brown. Dr Dmitry Yufit (University of Durham) and Dr Adrian Whitwood (University of York) for re-solving the single crystal structures. Dr Stuart Cavill for providing access to a Keithly source meter to enable conductivity measurements.

2.1 INTRODUCTION

Organic materials expressing electroactive properties have been subject to intense study over the last 15 years in light of their potential to replace more traditional conductive transition metal based materials.[1] In the development of electroactive organic materials, redox-active aromatic molecules have been used extensively for their conventional *through-bond* conjugated pathways that enable charge transport.[1] Aligning the π-surfaces of aromatic molecules towards orientations that enable good π-orbital overlap (i.e., close eclipsed arrangements) that result in *through-space* charge transport pathways has led to enhanced semiconductor properties.[2] One class of redox active aromatic molecules that have been used heavily as molecular building blocks towards the development of advanced semiconducting materials are known as rylene diimides (RDIs).[1,3] RDIs (e.g., naphthalene diimide[1] (NDI) and perylene diimide[4] (PDI)) feature high electron affinities along with excellent thermal, chemical and photochemical stabilities, preferring to adopt electrostatically desirable orientations that are less desirable for electroactive applications.[4] Designing and controlling aromatic assembly is a challenge that requires circumvention of the electrostatic repulsion barrier that originates from the quadrupole moment intrinsic to all aromatic molecules.[5] Therefore, without a controlling factor, aromatic molecules will self-assemble into thermodynamically desirable orientations (e.g., parallel displaced or edge-to-face), missing out on potential *through-space* charge transport pathway that could be a crucial contributor to enhancing semiconductor properties.

In an effort to control and direct π-assembly of RDI systems, several organic-based strategies (i.e., polymerisation, core-substitution, end-substitution) have been employed to obtain electronically desirable packing of π-surfaces. Core-substitution involves the addition of functional groups to the aromatic core of an RDI, imparting new functionality that has the potential to direct aromatic stacking towards more electronically desirable configurations. For example, Würthner et al.[6] carried out a range of fluorinations of PDI molecules at the bay positions and end groups, with the goal of influencing the LUMO level and influencing π–π stacking, resulting in an organic thin film transistor (OTFT) device with increased conductivity. From the range of PDI molecules presented by Würthner et al., most electronically desirable π–π stacking (50% overlap co-facial) was observed between PDI units that were unsubstituted at the bay positions and end-substituted with a perfluorinated butyl substituent (Figure 2.1a), resulting in charge carrier mobilities of 0.76 $cm^2\ V^{-1}\ s^{-1}$. PDI molecules that were bay substituted with F, Cl or Br led to less electronically desirable packing arrangements (edge-to-face), caused by a mixture of repulsive interactions between electronegative atoms (F, O) and a distorting of the aromatic system's planarity, resulting in lower device conductivities. Therefore, in the context of promoting electroactive aromatic packing, Würthner et al. found that only PDIs with end-substitutions led to packing arrangements with electronically desirable *through-space* charge transport. Another example of the effect of core-substitution on electronically desirable packing was presented by Zhang and co-workers, whom core-substituted PDI with tetramer acceptors that had central naphthalene units at either the α (Figure 2.1b, left) or β position (Figure 2.1b, right), incorporating them both into solar cells.[7] They found that the α tetramer formed close (3.6 Å) co-facial stacks with good orbital overlap between PDI surfaces, while the other displayed no significant π–π stacking between PDI units. The device that contained the co-facially stacked tetramer exhibited higher charge mobility, more efficient charge separation, and a higher fill factor, which all contributed to a superior organic solar cell. The two above studies demonstrate that core-substitution of RDIs does not always result in the most electronically desirable material, highlighting the importance careful choice of core-substituted substituents to influence π–π stacking towards obtaining semiconducting devices with improved semiconductor properties.

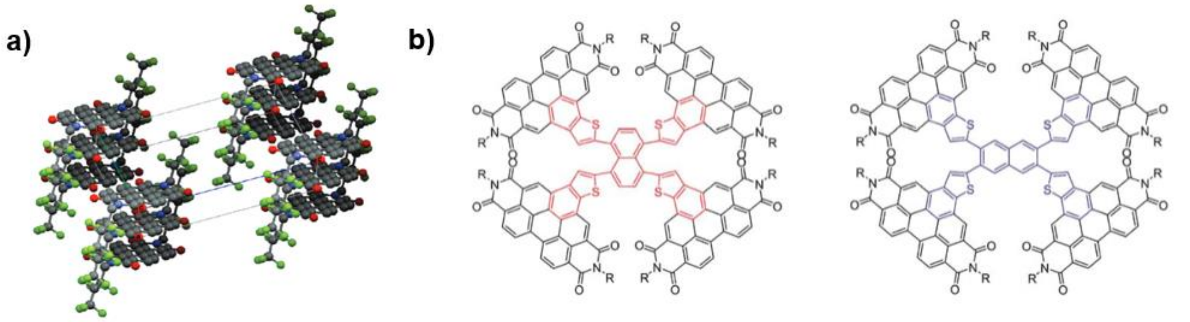

Figure 2.1. (a) 50% co-facial overlap between PDI units, with π–π distances of 3.3 Å, copied from the work of Würthner et al.[6] (b) Molecular structures of the core-substituted PDI molecules with central naphthalene units at the α (left) and β (right) positions, copied from the work of Zhang and co-workers.[7]

Polymerisation has also been used to knit π-systems together into electronically conjugated chains of RDIs, that have the potential to access *through-space* electronic pathways *via* π-orbital overlap. A study carried out by the Yang group[8] used NDI molecules that were end-substituted with alkyl groups and then polymerised at the core positions of the NDI, with either thiophene or bithiophene co-polymers (Figure 2.2a). Thin films of both polymers were generated using a range of different processing solvents (i.e., chloroform, acetonitrile, 1,4-dichlorobeneze, trichloroethylene) that formed different polymer packing configurations and film morphologies depending upon the solvent used. Conductivity tests of two NDI-thiophene or NDI-bithiophene films that were formed using chloroform possessed charge mobilities <one order of magnitude higher than polymer thin films processed using other solvents. The superior semiconductor properties were attributed to polymer molecular structure packing and film morphologies, in particular π–π stacking (3.80–3.90 Å), that was only identified in polymer thin films generated from chloroform. Therefore, the Yang group demonstrated that using the appropriate solvent is vital to obtain the most electroactive packing orientations between polymer units. Another more recent study that aimed to generate conductive n-type organic thin films for use in transistor devices

was carried out by Faccetti et al.[9] Polymers were generated using a π-extended thienopyridine-fused naphthalene amide (TPNA) species that were polymerised with either itself or two other aromatic moieties (i.e., thienyl or benzothiadiazole). The polymer formed with a benzothiadiazole connector (Figure 2.2b) was shown to exhibit a highly ordered crystalline structure, an increase in planarity of the aromatic units, and close π–π stacking distances (3.5–3.6 Å) between TPNA units. To investigate the conductive properties of TPNA-benzothiadiazole, thin films were incorporated into an organic thin film transistor device. TPNA-benzothiadiazole proved to have the most superior semiconducting properties (0.19 $cm^2\ V^{-1}\ s^{-1}$) in comparison to the alternatives, due to the increased crystallinity, π–π stacking, and planarity. The work done by Faccetti et al. highlights the screening of several different polymer connectors to achieve the most electroactive π–π stacking to result in superior *through-space* charge transport between aromatic units.

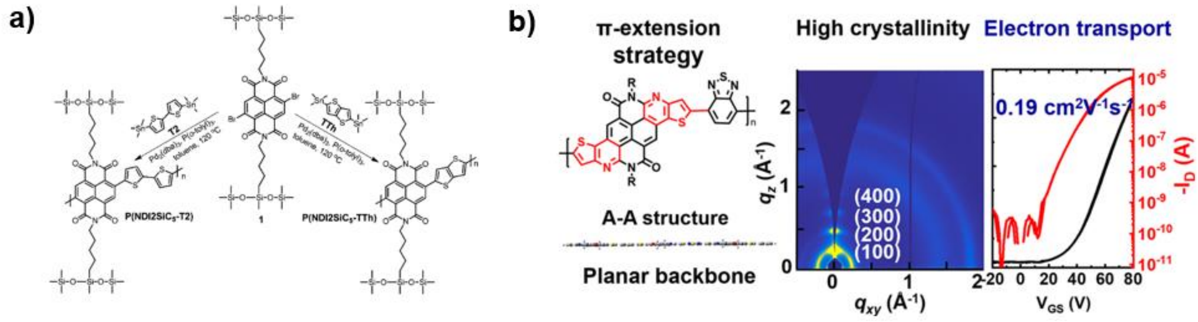

Figure 2.2. (a) The synthetic pathway to generate thiophene or bithiophene co-polymers, copied from the work of the Yang group.[8] (b) The structure of TPNA-benzothadiazole polymers (left) and supporting X-ray and conductivity data, copied from the work of Faccetti et al.[9]

Another strategy to manipulate aromatic interactions involves end-substitution that has been used to guide RDIs towards crystalline packing structures that are more electronically advantageous, by directing π-surfaces towards more desirable configurations. For instance, Welford and co-workers[10] synthesised end-substituted NDI molecules with alkyl groups of increasing lengths and branching (Figure 2.3a), followed by incorporation into thin film into transistor devices to assess their electroactive properties. X-ray diffraction showed that shortest alkyl chain lengths (C = 5) led to the closest π–π stacking between NDI π-surfaces and a conductivity of 0.18 $cm^2\ V^{-1}\ s^{-1}$, while the longest chain lengths (C = 12) resulted in longer π–π distances, but more uniform thin film morphology that resulted in a conductivity of 0.19 $cm^2\ V^{-1}\ s^{-1}$. In comparison, medium-chain alkyl chain length end-substituted NDIs resulted in lesser conductivity values, due to possessing neither the best π–π stacking or morphology characteristics. Ultimately, the work done by Welford and co-workers demonstrates the importance of screening several end-substituted units, and carrying out careful analysis of the end products to determine the origin of enhanced charge transport. In another recent study carried out by Komissarova et al.,[11] two end-substituted NDIs were studied to determine the effect of fluorination on crystal structure and charge mobility. The two end groups (benzene and *p*-fluorophenyl) were attached to NDIs, after which crystals were grown to analyse packing arrangements. Komisarova found that with respect to π-surface packing, the un-fluorinated species (Figure 2.3b) displayed a slip-stacked co-facial arrangement that was stabilised by attractive interactions between C•••H atoms, while the fluorinated species were edge-to-face stacked and influenced by attractive F•••H interactions, and repulsive F•••O interactions. Charge mobility values obtained from theoretical calculations showed that the fluorinated species had a higher charge mobility (0.048 cm^2 V^{-1} s^{-1}) in comparison to the un-fluorinated species (0.042 cm^2 V^{-1} s^{-1}). The enhanced charge mobility observed in the fluorinated species was attributed to a closer packing arrangement of charge carriers compared to the non-fluorinated species. Resultingly, the closer packing reduced the distance over which charge hopping occurred between aromatic units, underscoring the significance of fine-tuning aromatic stacking to facilitate closer proximity of charge carriers.

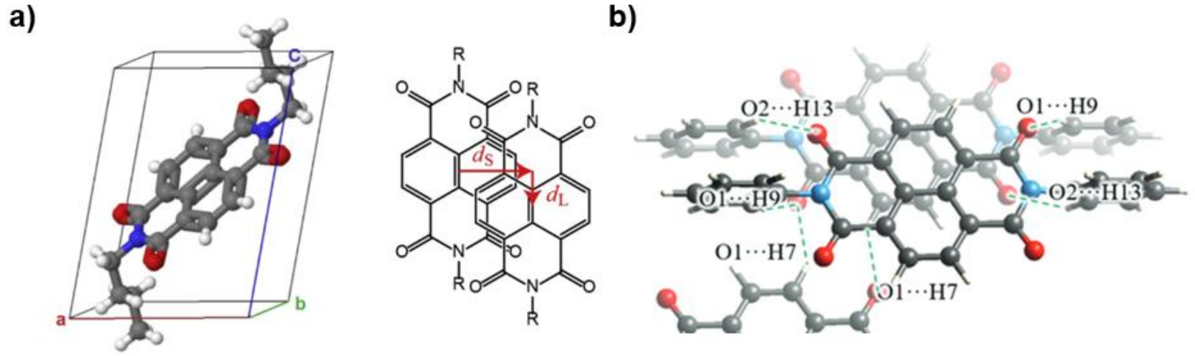

Figure 2.3. (a) The unit cell (left) and π–π overlap between NDI units with alkyl end groups (right), copied from the work of Welford and co-workers[10] (b) π–π overlap between non-core-fluorinated NDI molecules, copied from the work of Komisarova et al.[11]

A variety of semiconducting materials have been developed using polymerisation, core substitution and end-substitution in conjunction with RDI molecules, that have led to enhanced conductive properties *via* increased π-orbital overlap. Working with the above strategies has also led to other aspects (e.g. morphology, crystallinity, planarity) that have worked in combination with *through-space* conjugation to increase charge delocalisation through a system and lead to desirable semiconductor properties.

An alternative strategy to control the ordering of π-surfaces is hydrogen bonding, that provides a median (4–40 kJ mol^{-1})[12] and highly directional interaction, contributing heavily to molecular superstructures (e.g., proteins) observed in nature.[13] One example of using hydrogen bonding to control π–π interactions was presented by Molla and co-workers whom carried out four end-substitutions of NDI derivatives with alkyl chains on one end of the NDI molecule and carboxylic acid groups with methylene spaces (*n* = 1–4) on the other.[14] Each synthesised NDI underwent self-complementary hydrogen bonding (SCHBing) with an adjacent carboxylic acid group after aggregating from non-polar solvents (Figure 2.4a), resulting in superstructures that self-assembled to form slip-stacked π-surfaces (3.42 or 3.45 Å). The conductivity of the SCHB NDIs and a control that displayed no π-orbital overlap was tested, finding that the materials self-assembled with SCHB had conductivities between 1–7 x10^{-4} S cm^{-1}. The control compound displayed a conductivity of 10^{-9} S cm^{-1}, demonstrating that the cooperative SCHB between carboxylate groups for all NDIs resulted in greater π-orbital overlap and higher conductivity. In contrast to SCHB between carboxylic acid groups, Miljanić et al. deployed pyrazole groups that self-assembled into trimers, resulting in hexagonal frameworks that displayed π–π distances of 3.44–3.47 Å between parallel pyrazole and tetrafluorobenzene units (Figure 2.4b).[15] The electroactive properties of the hexagonal frameworks were not investigated, but the formation of such π-stacking demonstrate the potential for pyrazole units to be exploited for their SCHB properties towards achieving π-orbital overlap between aromatic surfaces. The use of SCHB to manipulate the packing of π-surfaces has shown to be a potent yet underemployed strategy, as evidenced by the scarcity of examples in the literature. Therefore, there exists a unique opportunity to develop novel materials incorporating SCHBing that could possess high π-orbital overlap and facilitate electroactive *through-bond* charge transport pathways between RDI units, using the wisdom gained from polymerisation, core-substitution, end-substitution strategies.

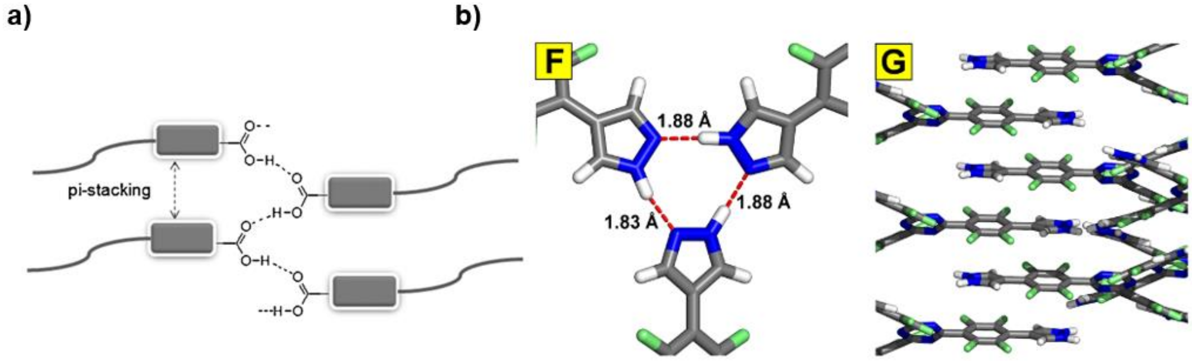

Figure 2.4. (a) The effect of SCHBing between carboxylate end groups after aggregation in non-polar solvents, copied from the work of Molla and co-workers.[14] (b) The trimer formed between pyrazole groups (left) and the π–π stacking between tetrafluorobenzene and pyrazole groups (right), copied from the work of Miljanić et al.[15]

Herein, we combine two strategies, i) end-substitution of NDI molecules ii) and SCHBing of pyrazoles to overcome the electrostatic repulsion barrier between π-surfaces and achieve electroactive materials. The first step will be to synthesise NDI molecules that have been end-substituted with pyrazoles that are different from one another by subtle regiochemical and steric changes. Regiochemical differences will probe the effect of directional SCHB between pyrazole end groups, and steric hinderance will investigate how additional bulk affects the propagation of SCHB networks to form. Ultimately, this chapter will uncover the most favoured packing arrangements between π-surfaces between a range of end-substituted NDI molecules using both experimental and theoretical data, allowing us to comment on the ideal conditions to produce electroactive π–π conjugated materials.

2.2 RESULTS AND DISCUSSION

2.2.1 SYNTHESIS OF *N*,*N*,-SUBSTITUTED NDI MOLECULES

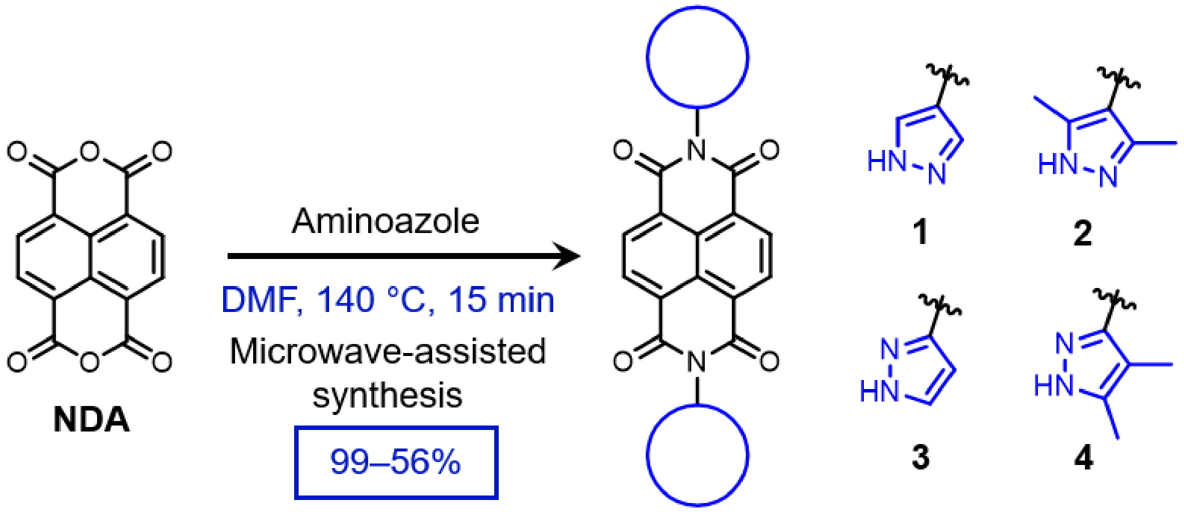

Figure 2.5. The general reaction parameters for the synthesis of NDIs **1**–**4**.

Among RDIs, the smallest homologue, NDI, displays typical RDI properties, possessing low-lying HOMOs and LUMOs that can promote n-type semiconductor properties.[16] In order to influence the aromatic interactions between π-surfaces with SCHB, end-substitution of NDI with four diverse pyrazole units that were separated by regiochemistry or additional steric appendages was envisaged. The first step to generating such end-substituted NDI units was to synthesise precursors **A1**[18] and **A2**[19] according to literature procedures (see methods section 2.4.2), while the remaining precursors were purchased and used without further treatment. Generally, to append NDI molecules with a wide variety of small molecule end groups, synthesis with a hot plate using naphthalene dianhydride (**NDA**) and the desired amino-appended end group results in symmetric end-substituted NDI molecules in high yields.[16] Typically, yields are between 70–90 %, and reaction times are between 12–48 h using solvent quantities between 100 – 500 mL. Microwave methodology was used to synthesise NDIs **1**–**4** thereby, (i) significantly reducing reaction times to 15 min, (ii) reducing solvent volumes to 4 mL, reducing the environmental impact of the synthesis in comparison to other studies. To synthesise NDIs **1**–**4** (Figure 2.5), **NDA** and the appropriate aminopyrazole were suspended in DMF, then subject to microwave irradiation for 15 minutes, (see methods, section 2.4.2) and confirmed to be analytically pure by ^{1}H and ^{13}C NMR (see the Appendix, section 7.1), and ESI-MS (see the Appendix, section 7.2). NDIs **1–4** were found to only solubilise in high boiling point organic solvents such as DMF and DMSO (1–2 mg mL^{-1}), suggesting that growth of single crystals from the solution-state would be challenging (see section 2.2.3 for details of crystal growth of NDIs **1–4)**.

2.2.2 SOLUTION-STATE OPTOELECTRONIC CHARACTERISATION

Solution-state UV-vis absorption analysis aimed to examine the ground-state transitions of NDIs **1–4** for any diversion from characteristic π–π* transitions, that appear as a band at ~380 nm.[17] A difference in the typical NDI ground-state transitions would indicate conjugation between the end groups and the NDI aromatic core was occurring in the solution-state. The absorption spectra of monomeric end-substituted NDIs displayed well-defined vibronic features at 340, 360 and 380 nm, that were characteristic of ground-state π–π* transitions (Figure 2.6).[17] Molar extinction coefficients for NDIs **1–4** were calculated with the Beer–Lambert law at 379 nm (see the Appendix, section 7.4 for details), demonstrating similar values for each molecule, suggesting that each material absorbs UV light at similar levels. To compliment UV-vis absorption data, emission spectra (Figure 2.7) were performed in DMF to detect the presence of any excited-state π-aggregates such as excimers.[18] Excitation of NDIs **1–4** at 330 nm in DMF displayed further characteristic evidence of monomerically dissolved NDI molecules at 410 and 430 nm,[19] allowing us to conclude that no π-aggregation in the form of an excimer occurs during emission experiments in the solution state.

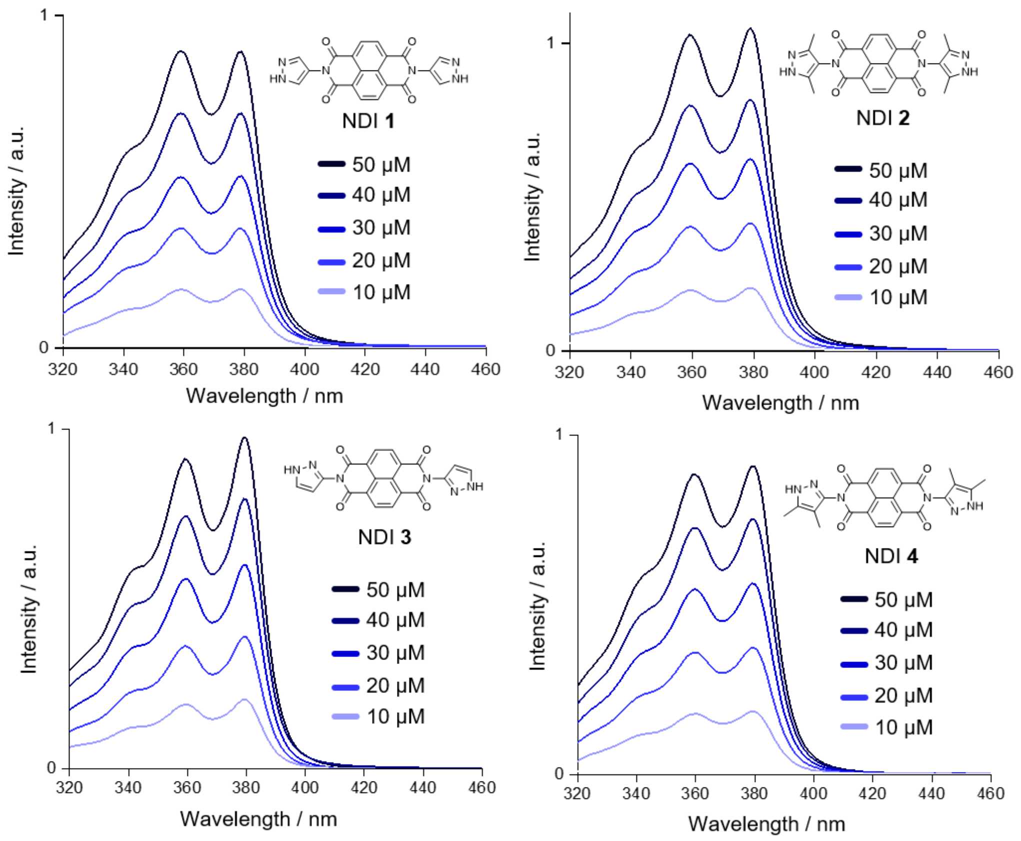

Figure 2.6. Concentration dependant UV-vis absorption data for NDIs **1**–**4** was carried out in DMF and demonstrated characteristic π–π* transitions at 340, 360 and 380 nm.

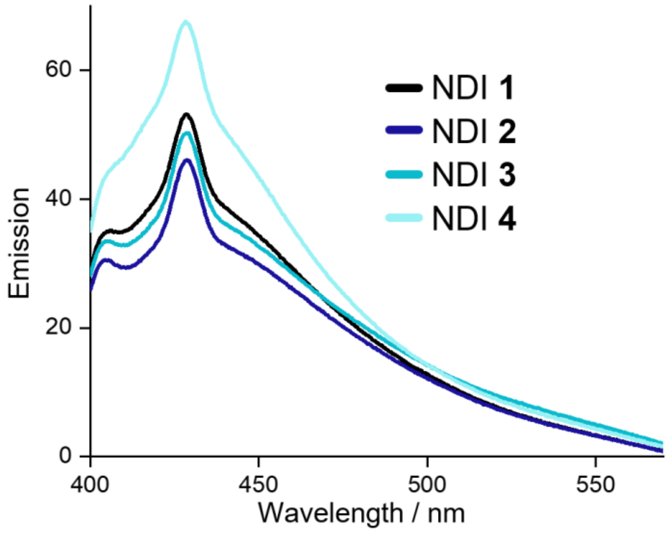

Figure 2.7. Emission data for NDIs **1**–**4**, carried out in DMF at concentrations of 5 uM. There is a very small peak at ~500 nm, indicating that there could be an excimer forming for each NDI molecule under these conditions. Further emission studies would need to be carried out in order to probe the small peak.

Cyclic voltammetry (CV) was carried out on the NDIs, revealing two reversible one electron-reductions for each molecule, that are characteristic of electron-accepting NDIs (Figure 2.8).[20,21] First-wave reductions of NDIs **1**–**4** are present between –1.00 to –1.01 V, occurring sooner than other aryl end-substituted NDIs.[17] Second-wave reductions also occur within a small window (–1.48 to –1.53 V) for NDIs **1**–**4**, with demethylated pyrazole end group NDIs (**2** and **4**) occurring at slightly more negative potentials.

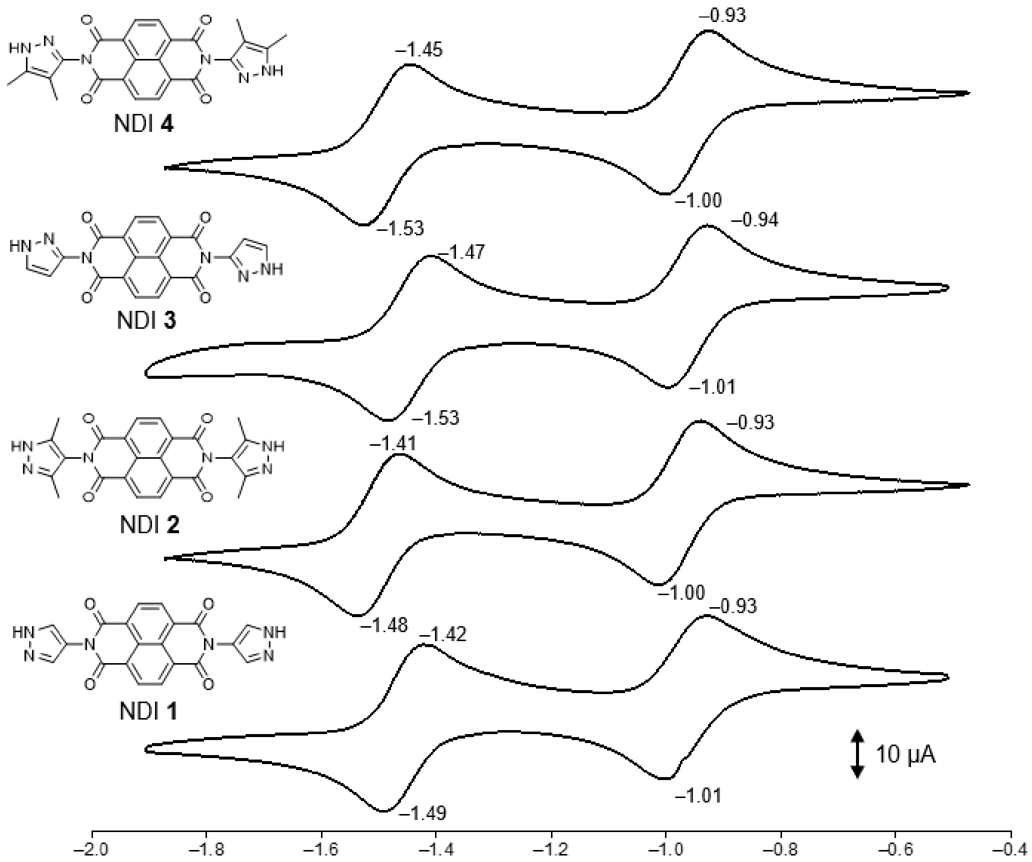

Figure 2.8. CV data for NDIs **1**–**4**. Experiments were recorded at 100 mV s^{-1} in dry, degassed DMF (1 mM), containing $TBAPF_6$ (0.1 M) as the supporting electrolyte. Voltammograms were referenced with respect to the Fc/Fc^+ redox couple (0.57 V vs Ag/AgCl) recorded under the same sample conditions.

optical band gap ($E_{bg.opt}$) of NDIs **1**–**4** were calculated using equation 1 in conjunction with UV-vis absorption data to determine if substitution with azole end groups had an effect on the frontier orbital energy levels. The energy of the electrochemical LUMO level (E_{LUMO}) was then determined by using the onset of the first reduction peak (E^{red}_{onset}) for NDIs **1**–**4**, which was obtained from CV data in conjunction with equation 2. Finally, the energy of the HOMO level (E_{HOMO}) was then calculated in equation 3. The band gap energies (Table 2.1) demonstrate that end-substitution of NDI with azoles groups had a negligible effect on either the HOMO or LUMO energy levels, in line with other studies.[11]

Table 2.1. Summary of frontier orbital properties of NDIs **1**–**4**.

NDI compound	λ_{onset} / nm	E^{red}_{onset} / V	E_{LUMO} / eV	E_{HOMO} / eV	$E_{bg.opt}$ / eV
1	393	–0.91	–3.89	–7.06	3.14
2	391	–0.91	–3.89	–7.00	3.11
3	392	–0.89	–3.92	–7.09	3.15
4	394	–0.89	–3.91	–7.08	3.13

$$FE_{bg,opt}(eV) = \frac{hc}{\lambda_{onset}} \times 6.242 \times 10^{18} \qquad (1)$$

$$E_{LUMO}(eV) = -\mathrm{e}\ \mathrm{x}\ (E_{onset.red} + 4.8) \qquad (2)$$

$$E_{HOMO}(eV) = E_{LUMO} - E_{bg,opt} \qquad (3)$$

To draw a comparison with experimentally obtained band gap data, DFT calculations (B3LYP/6-31G(*d*,*p*)-GD3BJ in DMF) were carried out to determine the frontier molecular orbital energy levels. The results verified that each NDI's respective LUMO orbital was similar in energy (between –3.34 eV and –3.36 eV, see Table 2.2) and were centered around the aromatic NDI core in a π* orbital (Table 2.2), agreeing with experimental LUMO energies calculated with CV data (Table 2.1). Furthermore, calculated HOMO orbital energy levels were also similar in energy (between –6.45 eV and –6.94 eV, see Table 2.2) and were centered more broadly across the molecule in the cases of sterically unhindered NDIs 1 and 3, and were centered on the end groups for NDIs 2 and 4 (Table 2.2).

Table 2.2. Summary of calculated frontier orbital energy levels.

	NDI **1**	NDI **2**	NDI **3**	NDI **4**
LUMO energy / eV	–3.34	–3.34	–3.36	–3.34
LUMO	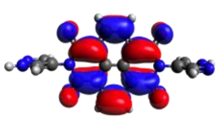	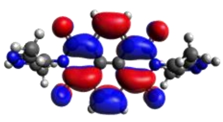	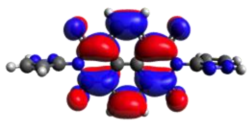	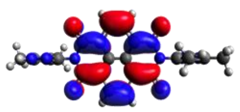
HOMO	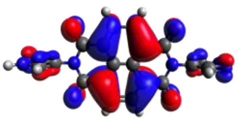		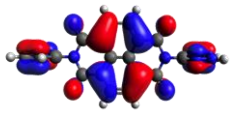	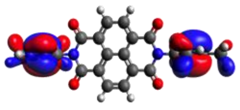
HOMO energy / eV	–6.94	–6.54	–6.94	–6.45

2.2.3 SOLID-STATE STUDIES

High-quality single crystals were grown *via* a range of techniques (slow evaporation, vapor diffusion, layering, thermal deprotection), then analysed *via* single crystal X-ray diffraction (SC-XRD) with the goal of elucidating the effect of different pyrazole end groups of NDIs **1**–**4** (i.e., regiochemistry, steric hinderance). Of the single crystals grown, multiple solvated structures were obtained, owing to the high affinity of pyrazole N–H to act as hydrogen bond donors, and carbonyl oxygen atoms to act as hydrogen bond acceptors in hydrogen bonding interactions with solvents. Resultingly, solvents formed H-bonds with pyrazole end groups (Figure 2.8), interrupting potential SCHB between pyrazole groups.

Despite potentially blocking SCHB interactions between pyrazole end groups, some of the solvated crystal structures served to direct π-surfaces towards more electronically desirable configurations (Figure 2.9a). For example, **1**·DMSO features strong H-bonds (1.75 Å and 1.84 Å) between pyrazole N–H and disordered DMSO oxygen atoms, interrupting any potential SCHB between pyrazole end groups (Figure 2.9a). However, bonding between solvent and end-group promoted partial overlap between NDI π-surfaces, resulting in π–π distances of 3.29 Å between the closest carbon and nearest NDI plane. The continuous 1D π-orbital overlap observed between NDI π-surfaces in **1**·DMSO has the potential to act as a charge-transport pathway. Despite the observance of overlap of π-surfaces in **1**·DMSO, the material was not investigated for its properties due the instability of solvates outside of crystallisation solutions.

Another solvated crystal, **4**·2DMSO, was identified to form strong H-bonds (1.95 Å) between sulfonyl oxygen atoms and pyrazole end groups, interrupting any potential SCHB interactions (Figure 2.9b). Aggregation of π-surfaces was disturbed by a combination of DMSO and sterically bulky methyl groups located above and below π-surfaces. Overall, no electronically desirable π-orbital overlap between π-surfaces was observed in **4**·2DMSO, leading to the conclusion that no significant semiconductor properties would be expressed from this single crystal material. Similar to **1**·DMSO, this material was no investigated further due to the instability of solvates outside of their crystallisation solutions.

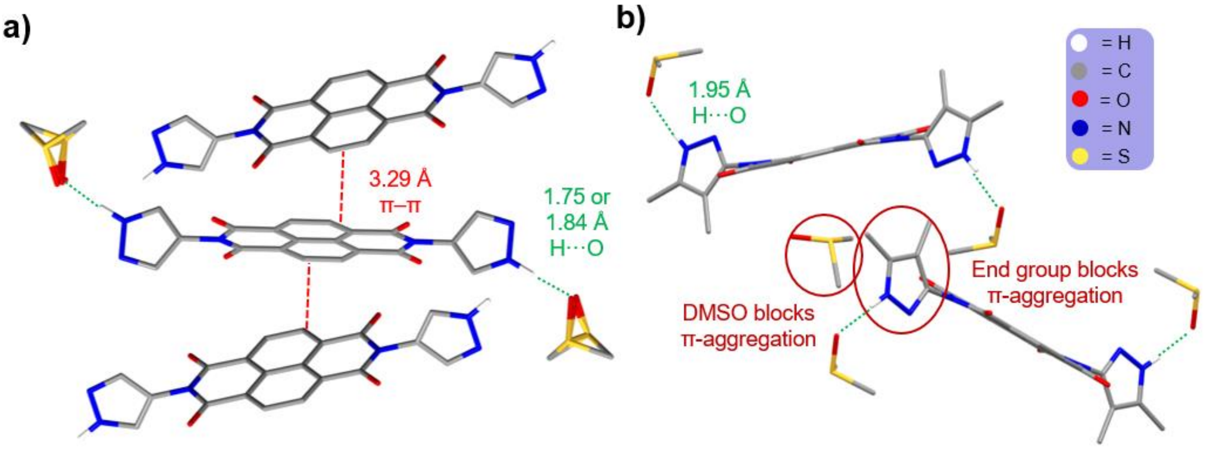

Figure 2.9. The solvated single crystals of (a) **1**·DMSO, featuring strong H-bonds and close distances between π-surfaces, (b) and **4**·2DMSO, featuring strong H-bonds between DMSO and end groups.

Solvent-free single crystals of **4** (Figure 2.10a) were obtained from slow diffusion of absolute ethanol into DMF-solubilised **4** molecules (full crystallographic information is available in the Appendix, section 7.5, Table 7.1). The superstructure of **4** reveals a thermodynamically favoured displaced arrangement of π-surfaces that are stabilised by SCHBs (H•••O = 2.02 Å) between NDI carbonyl oxygen groups and pyrazole N–H (Figure 2.10b), forming a continuous 1D chain of **4** molecules. As a result of the stabilising hydrogen bonding and interrupting effect provided by bulky dimethylated end groups that are positioned above the π-surface of each NDI, there are no π–π stacking interactions between NDI **4** π-surfaces (Figure 2.10c). Calculations carried out with Hirshfeld analysis demonstrate a lack of strong or median interactions over the π-surface of **4** (Figure 2.10d), and a C•••C interaction value of 0.6% that was attributed to interactions between end group methyl carbon atoms and NDI core carbon atoms (see Figure 2.14 and the Appendix, section 7.6, Figure 7.15 for details). The influence of sterically bulky methyl groups and the formation of strong H-bonds between NDI carbonyl oxygen groups and pyrazole N–H result cause any interactions between quadrupoles to be eliminated, despite the emergence of SCHBs between NDI carbonyl oxygen groups and pyrazole N–H. Ultimately, the absence of overlap between π-surfaces confirms that *through-space* charge transport would not be observed in **4**.

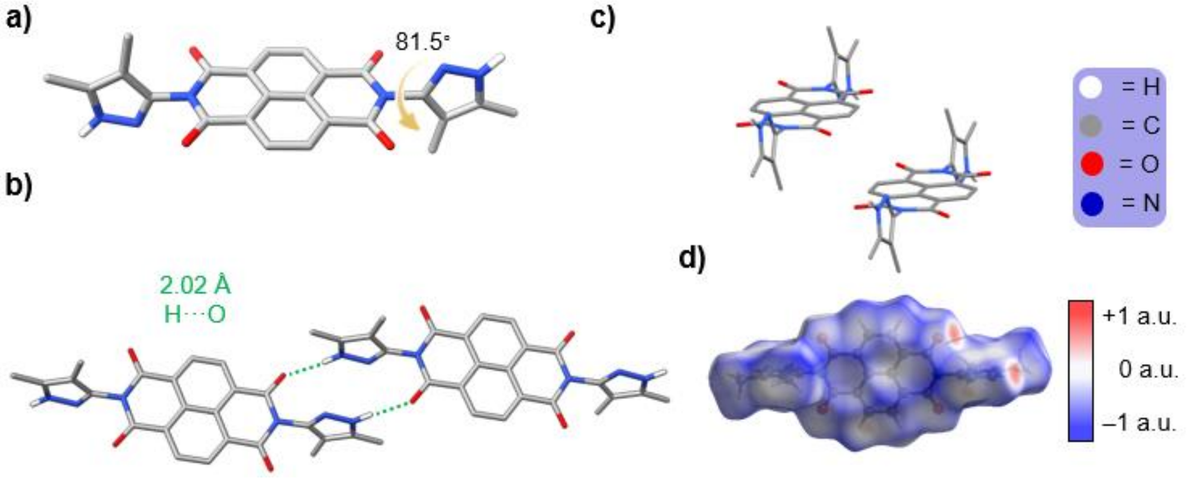

Figure 2.10. (a) The molecular structure of **4**, (b) Hydrogen bonding interactions between O and H (c) displaced overlap between NDI **4** molecules (d) Hirshfeld surface surrounding NDI **4** demonstrating no significant atom-atom interactions related to π–π stacking. Non-interacting hydrogen atoms removed for clarity.

In comparison to NDI **4**, the end groups of NDI **2** are regioisomers, and have methyl groups at the 3 and 5 positions that have the potential to provide a similar blocking effect towards interactions between π-surfaces (Figure 2.11a). To discover how the isomeric end group affected π-ordering, single crystal data of **2**, of which the crystals were previously grown *via* slow evaporation of DMF from **2** by Ke et al.,[22] were analysed (full crystallographic information is available in the Appendix, section 7.5, Table 7.1). The solvent-free structure of NDI **2** was supported by strong intermolecular SCHBs (H•••O = 1.80 Å) between pyrazole N–H and NDI carbonyl oxygen atoms (Figure 2.11b), causing end groups to be placed above adjacent π-surfaces in an edge-to-face arrangement (Figure 2.11c). Resultingly, the sterically hindered end groups occupied the majority of the space above both sides of the NDI π-surface, causing any interactions between neighbouring π-surfaces to be disfavoured. Hirshfeld analysis calculations demonstrated low to medium interaction strengths over the NDI π-surface of **2** (Figure 2.11d), and a C•••C interaction value of 2.9%, that were attributed to interactions between the end group and the π-surface (see Figure 2.14 and the Appendix, section 7.6, Figure 7.14 for details). Resultingly, the strong intermolecular bonding between pyrazole N–H and NDI carbonyl oxygen atoms led to end groups blocking any interactions between π-surfaces, despite SCHBs being observed between pyrazole N–H and NDI carbonyl oxygen atoms. As a result of the packing arrangement of **2** molecules, no overlap of π-surfaces is observed, causing any *through-space* charge transport pathways to be absent between NDI LUMO orbitals.

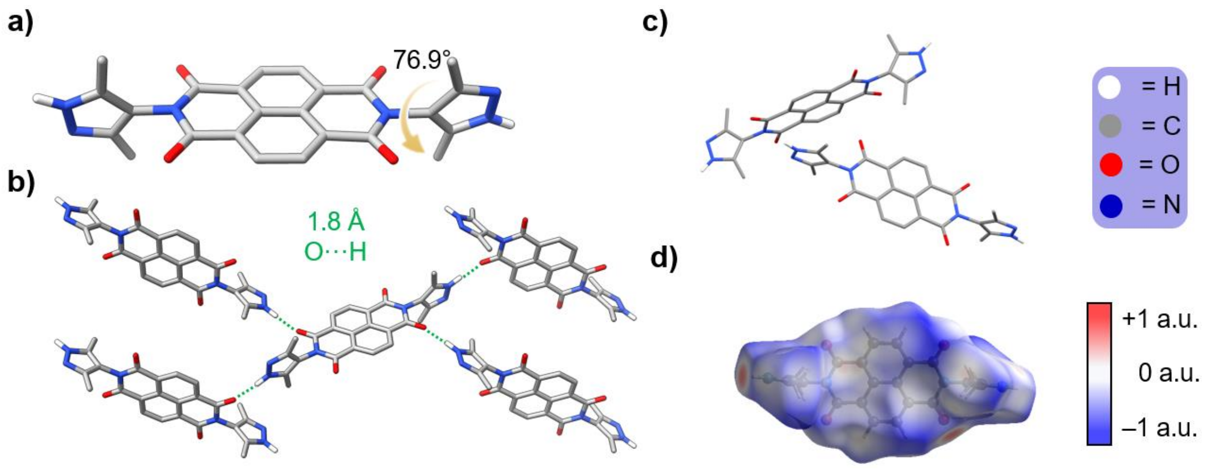

Figure 2.11. (a) The molecular structure of NDI **2** (b) hydrogen bonding between H•••O that stabilise the supramolecular structure (c) edge-to-face molecular packing between NDI **2** molecules (d) Hirshfeld surface surrounding NDI **2**, demonstrating no significant atom-atom interactions related to π–π stacking. Non-interacting hydrogen atoms removed for clarity.

The examination of the solvent-free single crystals of **2** and **4** have shown that the emergence of strong H-bonds between pyrazole N–H and NDI carbonyl oxygen atoms, in combination with sterically bulky methyl groups, led to packing arrangements that featured no interactions between aromatic surfaces. The different end-group regioisomers contributed to the blocking of π–π interactions most significantly, causing different packing arrangements to be adopted by each NDI molecule. Moreover, due to the lack of π-orbital overlap, both NDIs **2** and **4** are likely to not display any *through-space* electron delocalisation from overlapping π-orbitals, confirming that no enhancement of semiconductor properties will come from that source.

In comparison to the relative ease of crystallisation of both NDIs **2** and **4**, attempts to grow solvent-free single crystals of NDIs **1** was met with difficulties, owing to very low solubility (<1.5 mg mL^{-1}) in high boiling point organic solvents such as DMF and DMSO. Therefore, solubilising Boc groups were affixed to end group NH positions of NDI **1** (see synthetic details, section 2.4.2). Efforts to grow single crystals of NDI **1** by were met with success from thermal deprotection of Boc-**1** (1 mg mL^{-1}) by using a solvent mixture of DMF:EtOH (3:1) that was held at 80 °C for 48 h.

Molecule NDI **1** is distinguished from NDI **2** by the removal of sterically bulky methyl groups at the 3 and 5 positions on the pyrazole (Figure 2.12a), opening up the potential for SCHB between pyrazole groups. The solvent-free single crystal of NDI **1** (full crystallographic information is available in the Appendix, section 7.5, Table 7.1) is stabilised by strong SCHB (H•••N = 1.74 Å) between neighbouring pyrazole groups, that form a bifurcated pattern through the system (Figure 2.12b). The resulting framework of **1** displays continuous close co-facial (π–π = 3.24 Å) arrangement of π-surfaces due to the bifurcated SCHB, and when the π–π stack is viewed top-down, the low extent to which the π-systems are overlapped is revealed (Figure 2.12c). The close co-facial interactions were demonstrated on calculated Hirshfeld surfaces by the display of a white section above the NDI surface (Figure 2.12d, red oval) and were confirmed by a C•••C interaction value of 5%, that was attributed to NDI–NDI interactions (see Figure 2.14 and the Appendix, section 7.6, Figure 7.15 for details). Essentially, the removal of the sterically bulky groups has allowed for SCHB to occur between neighbouring pyrazoles, resulting in a small, but continuous alignment of π-surfaces. The array of partially overlapped NDI molecules is expected to delocalise electrons across the NDI π-orbitals, suggesting that *through-space* charge transport would be enhanced.

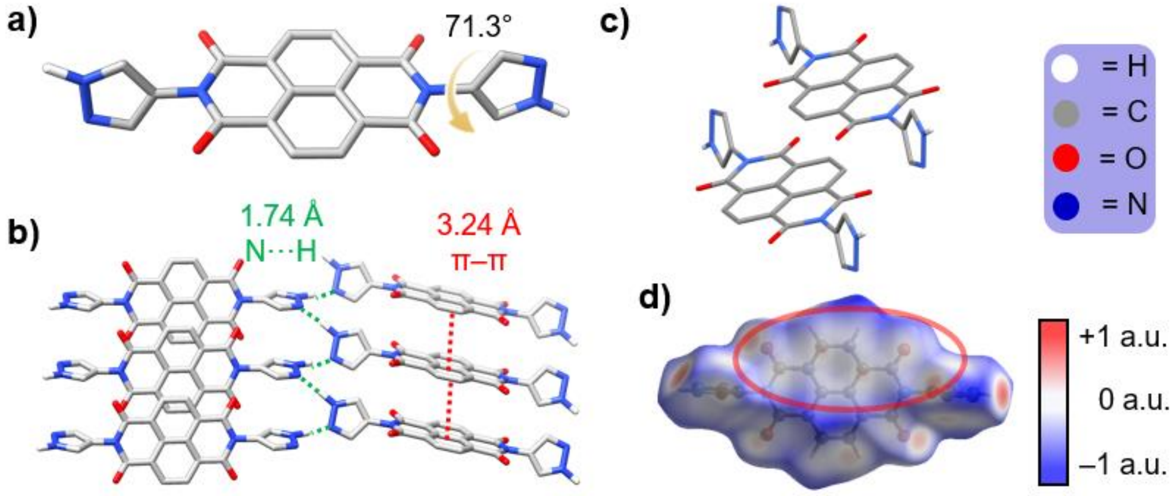

Figure 2.12. (a) The molecular structure of NDI **1**, (b) bifurcated SCHB between pyrazole end groups that enable co-facial π–π interactions, (c) co-facial packing of NDI **1** molecules, (d) the calculated Hirshfeld surface of NDI **1**, with circled area relating to π–π stacking. All non-interacting hydrogen atoms removed for clarity.

Similar to NDI **1**, NDI **3** also suffered from low solubility in high boiling point organic solvents (~1 mg mL^{-1}), requiring single crystals of NDI **3** to be obtained from a Boc-protected derivative (Boc-**3**, see synthetic details, section 2.4.2) that was dissolved (1 mg mL^{-1}) in a mixture of DMF and EtOH (3:1), and held at 80 °C for 48 h.

Regiochemically, the difference between NDI **1** and **3** were relatively small (i.e., from 4-pyrazole to 3-pyrazole, see Figure 2.13a), but considering the emergence of SCHB in sterically unhindered NDI **1**, we expected the resulting solvent-free framework of NDI **3** to form SCHBs. As expected, the single crystal structure of NDI **3** (full crystallographic information is available in the Appendix, section 7.5, Table 7.1) revealed SCHB (H•••N = 2.20 Å) with 50% disorder between neighbouring pyrazole group protons, due to the uncertainty of where the proton was located, causing a slight underestimation of the H-bond distance (Figure 2.13b). As a result of the SCHBs, π-surfaces were arranged into a co-facial array that were separated by distances of 3.47 Å, where the aromatic surfaces were related to one another by a S_2 symmetry operation. A top-down view of the π-stacked array demonstrated a high degree of

NDI–NDI overlap (Figure 2.13c), that is displayed on the calculated Hirshfeld surface as a near-solid white area over the π-surface (Figure 2.13d, red oval). Hirshfeld analysis also displayed a C•••C percentage interaction value of 16.8% that was attributed to the carbon-carbon interactions between aromatic NDI cores (see Figure 2.14 and the Appendix, section 7.6, Figure 7.14 for details) supporting that π-orbital mixing is occurring between stacked NDI units. As a consequence of the highly overlapped close co-facial interactions between NDI **3** aromatic cores, it was expected that electrons would delocalise through the array of overlapped π-orbitals, translating to superior semiconductor properties in comparison to the demethylated NDI species (NDIs **2** and **4**).

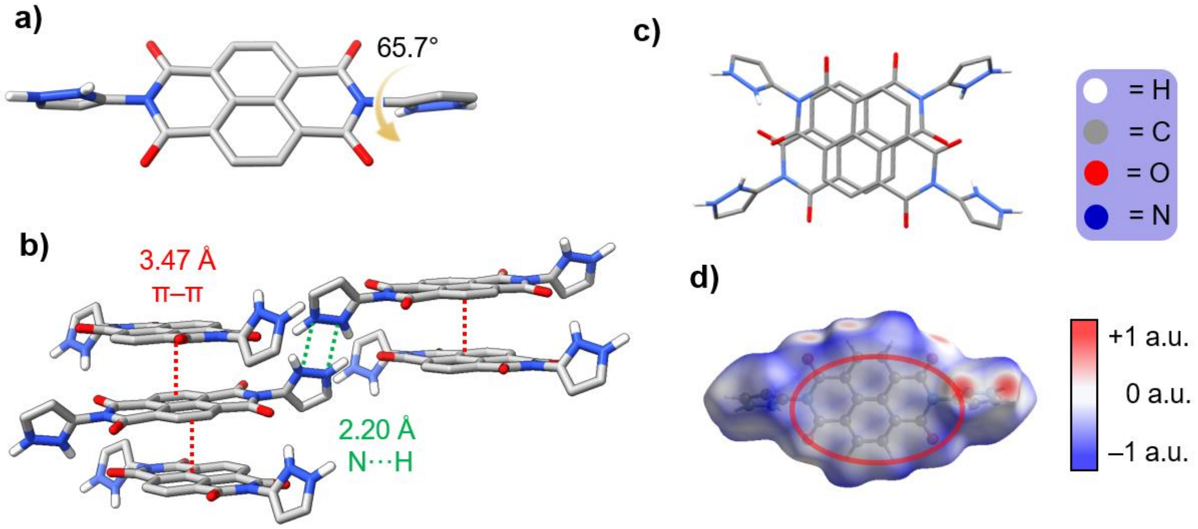

Figure 2.13. (a) The molecular structure of NDI **3**, (b) and intermolecular SCHB between pyrazole groups that support π–π stacking interactions, (c) and alternating color-coded co-facial stacks of NDI **3** molecules, (d) and the calculated Hirshfeld surface of NDI **3**, with circled area relating to π–π stacking. All non-interacting hydrogen atoms removed for clarity.

The four solvent-free supramolecular frameworks each displayed different packing of NDI π-surfaces that were a product of stabilising intermolecular H-bonding interactions, either between adjacent pyrazoles as SCHBs, or between NDI carbonyl oxygen atoms and pyrazole N–H atoms. Following these SC-XRD findings, analysis of the conductive properties of NDIs **1**–**4** is vital to understand how the diverse π-orbital overlap between the four materials affects semiconducting properties. Taking into account the absence of π-orbital overlap between NDI surfaces in NDIs **2** and **4**, low conductivity is expected. Conversely, increased conductivity values are expected from NDI **1** and **3**, owing to the NDI–NDI overlap and short π–π distances (**1** = 3.24 Å, **3** = 3.47 Å).

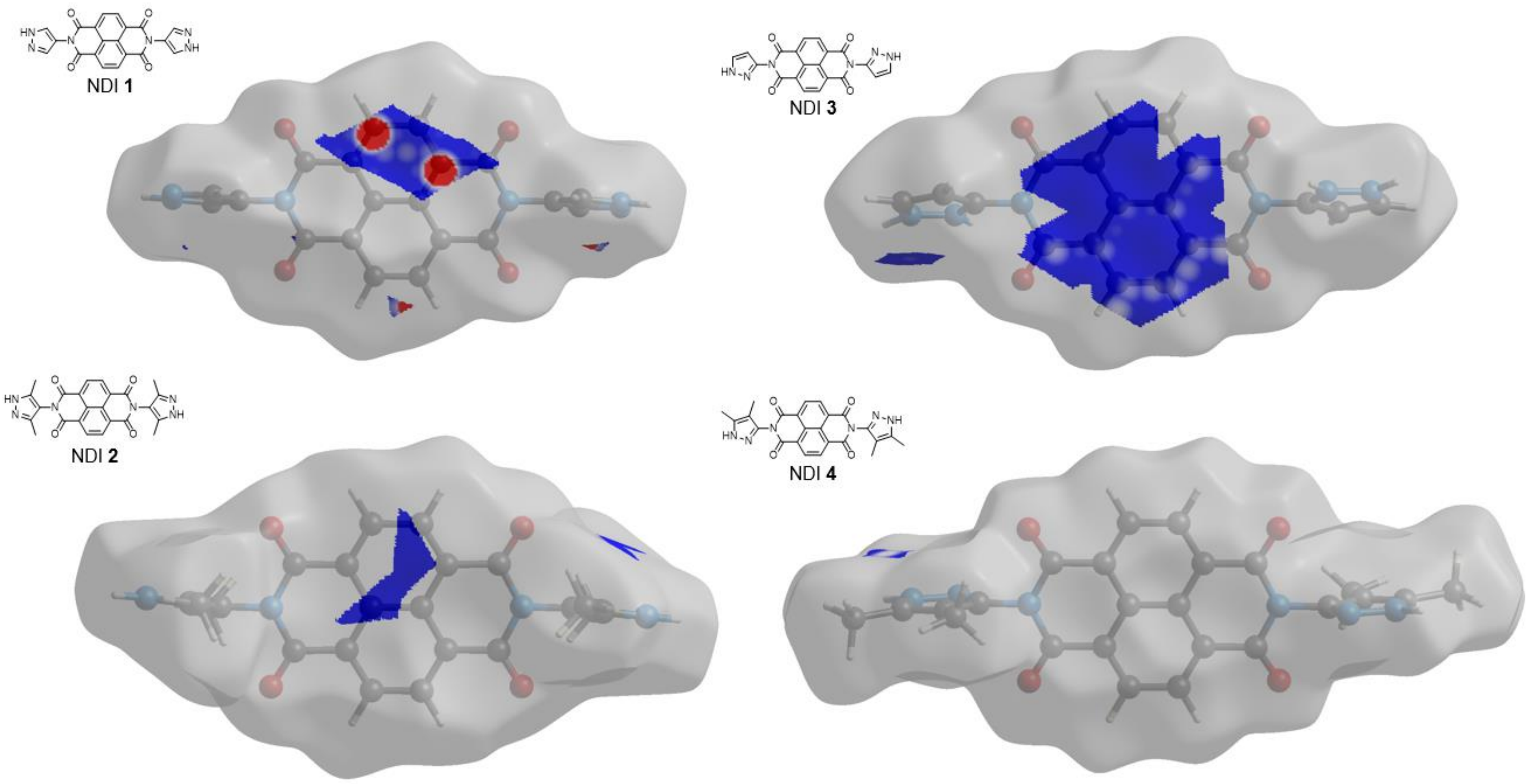

Figure 2.14. Hirshfeld surfaces of solvent-free single crystals of NDIs **1**–**4** that image only C•••C interactions on each surface.

2.2.4 CONDUCTIVITY ANALYSIS

A "home-built" custom designed two-point probe pellet press was developed in order to analyse the as-synthesised samples of NDIs **1**–**4** (a diagram is available in the Appendix, section 7.7, Figure 7.16) for which a sample preparation method and experimental method were developed (see the Appendix, section 7.1). Pictures of the experimental setup are also available in the Appendix, section 7.8, Figure 7.17.

The single crystals that had been grown for SC-XRD analysis were too small (~1 mm) for single crystal resistivity measurements, requiring the use of polycrystalline materials that displayed the same crystalline phase observed in the single crystal data. Powder X-ray diffraction (PXRD) data was collected for NDIs **1**–**4** NDIs and compared against simulated single crystal PXRD data, demonstrating matching between unit cells of corresponding data sets (Figure 2.15). Therefore, it was confirmed that as-synthesised NDIs **1**–**4** replicated the same ordering of π-surfaces as observed in the single crystal data, causing any testing of conductivity to effectively determine the effect of the diverse range of π-orbital overlap between the four NDIs. Furthermore, to confirm that each NDI retained the crystal phase observed in the single crystal data, PXRD patterns were taken at each stage of testing (i.e., post-grinding, post-pressing, post-voltage, see Figure 2.16). Crucially, a comparison between the tested patterns demonstrated that solvent-free single crystal structure phase purity of the NDI samples was maintained through the conductivity procedure.

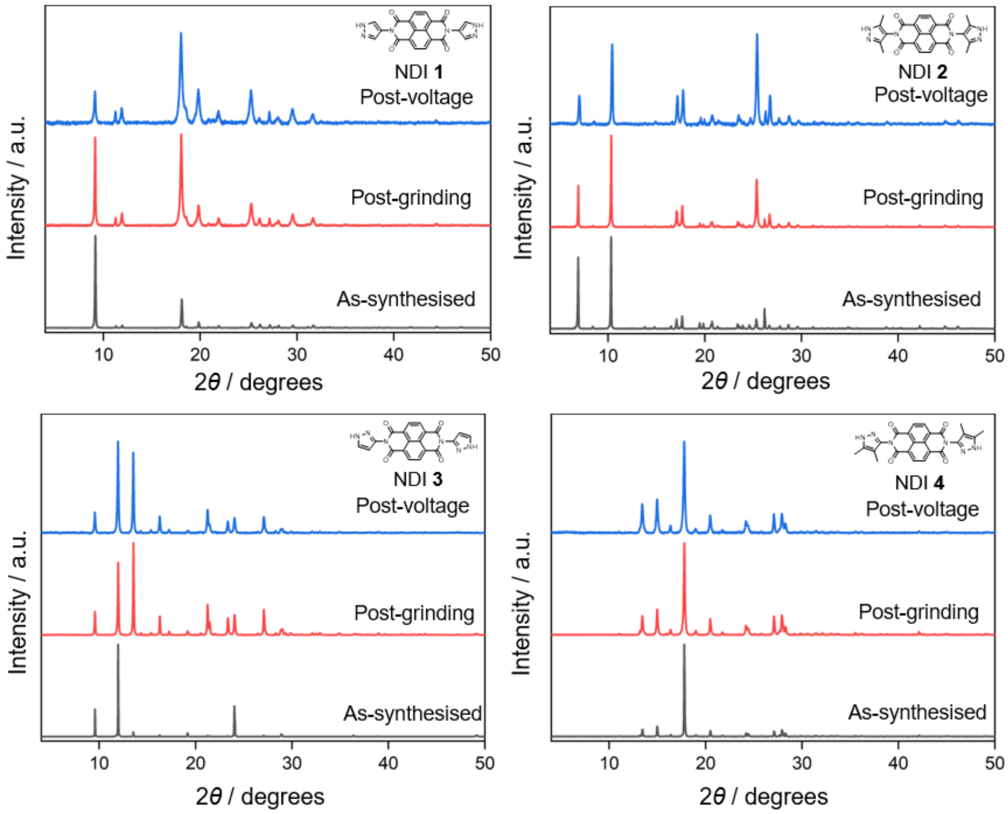

Figure 2.15. PXRD patterns for NDIs **1**–**4** that take place pre-grinding, post-grinding, and post-voltage. Each series of data demonstrates that the single crystalline phase is retained throughout the conductivity process.

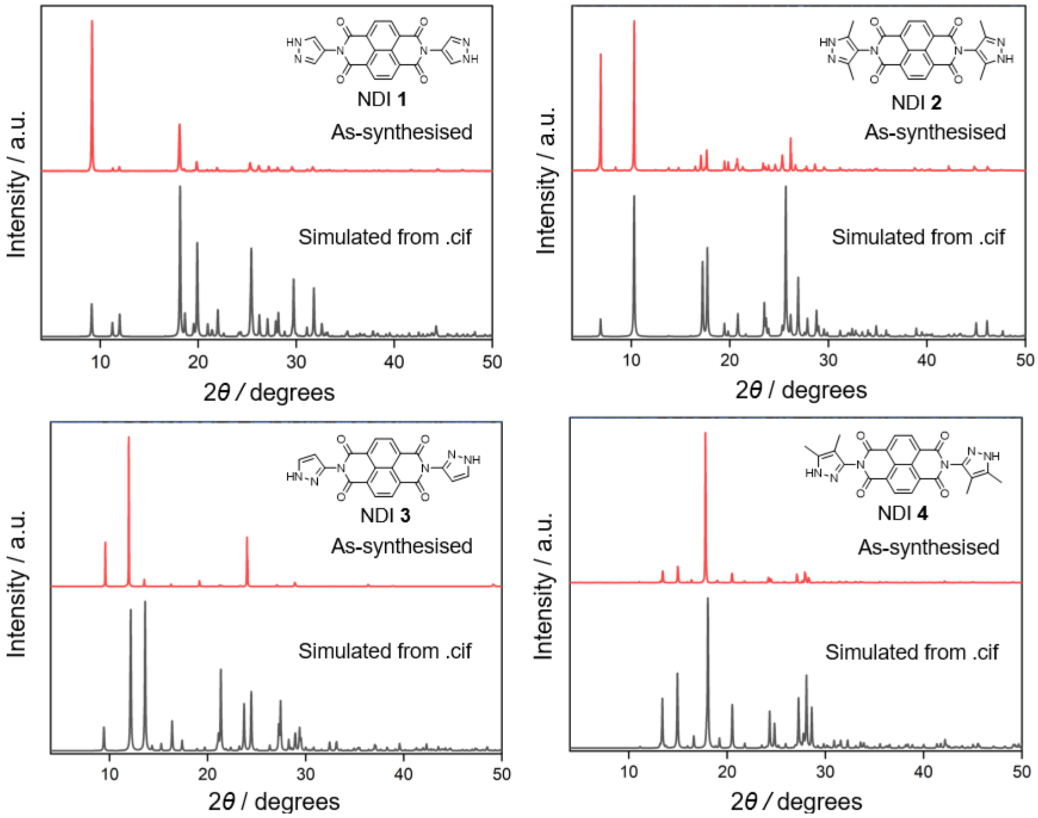

Figure 2.16. PXRD data showing a comparison between data simulated from single crystal information and patterns collected from as-synthesised NDIs.

Table 2.3. Conductivity analysis of NDIs **1**–**4**.

NDI compound	**1**	**2**	**3**	**4**
Conductivity / S cm^{-1}	2.63x10^{-11}	2.23x10^{-11}	2.67x10^{-8}	2.82x10^{-11}

The results of the conductivity tests are available in Table 2.3 and show that NDI **3** was found to have a conductivity three orders of magnitude higher (2.67x10^{-8} S cm^{-1}) than the remaining NDIs (raw I–V curves are available in the Appendix, section 7.9, Figure 7.18). The long-range ordering observed in the single crystal structure of NDI **3** translated to the propagation of a 1D array of π-stacked NDI units that experimentally demonstrated superior *through-space* charge-transporting properties in comparison to the remaining NDIs. Conversely, NDI **1** (2.63x10^{-11} S cm^{-1}) displayed lower conductivity readings in comparison to NDI **2**, defying conventional wisdom that suggests lower π–π distances yield higher conductivities. Instead, the data suggests that the higher degree of π-orbital overlap observed in NDI **2** significantly contributes to the overall conductivity measurement, highlighting the importance of both π–π stacking and π-orbital overlap to obtain desired semiconductor properties. NDIs **2** and **4** displayed conductivity measurements (2.23x10^{-11} S cm^{-1} and 2.82x10^{-11} S cm^{-1}) that were at the same level as NDI **1**, showing that the absence of π-orbital overlap between NDI π-surfaces results in lower electroactive properties. The fact that NDI **1** displays the same lower levels of conductivity as NDIs **2** and **4** that display no π-orbital overlap shows that the *through-space* charge transport pathway in NDI **1** is inactive while undergoing pellet press measurements.

2.2.5 DFT ANALYSIS

The experimental conductivity findings highlighted the importance of π-orbital overlap in the context of semiconductor devices, and that π–π distances should not be the only aspect that is considered when assessing the structures of potential aromatic semiconducting materials. To gain a further understanding how the solid-state packing aspects of NDIs **1**–**4** (i.e., distance, geometry, symmetry) led to the experimentally obtained conductivity values, DFT calculations were carried out (supported by CATNIP[23] to model and understand charge mobility between dimers, see the experimental details, section 2.4.1 for details of the DFT calculations). Using the single crystal data of NDIs **1**–**4**, charge transfer pathways were first determined between NDI molecules, and a charge transfer integral, J_i, was assigned for each directional pathway, using the dimer projection method (Figure 2.17).[24,25] The rate of charge transport in each direction k_i, was then calculated according to the Marcus equation (Equation 4) using the calculated values of J_i, and the reorganisation energy λ (Equation 5). Finally, the charge mobility of electron transport, μ, which is dependent upon the rate of charge transfer in all directions, k_i, and the centroid-centroid distance between dimers, r_i, was calculated using equation 6.

$$\mu = \frac{eD}{K_B T} = \frac{e}{6k_B T}\sum_i K_i r_i^2 p_i \qquad (4)$$

$$k_i = \frac{2\pi}{\hbar} J_i^2 \left(\frac{1}{4\pi\lambda k_B T}\right)^{\frac{1}{2}} e^{\left(-\frac{(\Delta E+\lambda)^2}{4\lambda k_B T}\right)} \qquad (5)$$

$$\lambda = (E_N^* - E_N) + (E_C^* - E_C) \qquad (6)$$

$$p_i = \frac{k_i}{\sum_i k_i} \qquad (7)$$

The results approximately match the trends observed for the experimental conductivity measurements (NDI **3** > **1** and **4** ≈ **2**; Table 2.4). Using the dimer projection method,[24,25] a significant charge transfer pathway (i.e., $k_i > 5\times10^{12}$ s^{-1} or $J_i > 20$ meV) was identified to exist across slip stacked NDI–NDI π-interaction in NDI **1** (Figure 2.13a, $J_1 = 108$ meV; $k_1 = 9.4\times10^{12}$ s^{-1}). Another charge transport pathway was observed between across the co-facial overlap in NDI **3** which results in the greatest charge transfer integral (Figure 2.13c, $J_2 = 182$ meV; $k_2 = 2.9\times10^{13}$ s^{-1}). Assemblies of NDI **4** highlight a pathway from a side-to-side π-interaction between NDI cores (Figure 2.13d, $J_1 = 45.2$ meV; $k_1 = 1.5\times10^{12}$ s^{-1}), however, no significant charge transfer pathways are observed in NDI **2** (Figure 2.17b). Despite the closer π–π distance in NDI **1**, the charge transfer calculations reveal that charge transfer pathway (J_1 in NDI **1**) does not contribute to the over-all charge mobility as much as charge transport pathways between the co-facial dimer in NDI **3** (J_2 in NDI **3**), resulting from poorer spatial overlap between orbitals in the LUMO of the dimer.

Table 2.4. Theoretical charge mobilities of NDIs **1**–**4**.

NDI compound	**1**	**2**	**3**	**4**
Charge mobility, μ / cm^2 V^{-1} s^{-1}	0.24	0.09	0.36	0.05

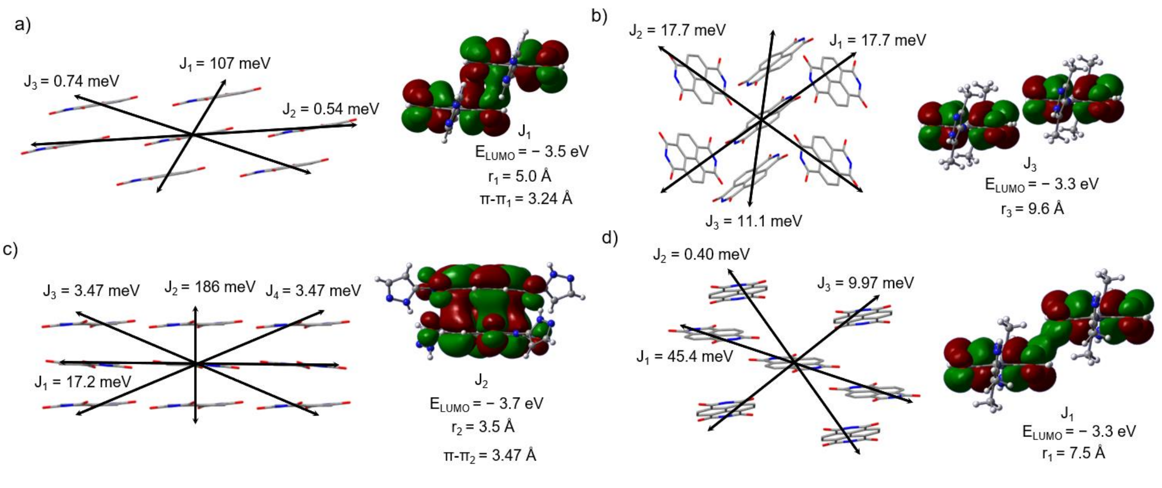

Figure 2.17. Charge transfer pathways and subsequent charge transfer integrals for NDIs, (a) **1;** (b) **2;** (c) **3;** (d) **4**. Pyrazole groups have hydrogen atoms omitted for clarity.

The charge mobility results are further highlighted in distance dependent calculations where the vertical distance (d_v) between the dimers in NDI **1** and **3** were altered and the resulting charge transfer integral calculated and plotted (Figure 2.18a). The results reveal that at any distance, NDI **3** can more freely transfer charge than NDI **1** due to the more efficient spatial overlap in the twisted and co-facial arrangement of NDIs in **3**. NDI **3** therefore displays the greatest theoretical charge mobility, larger than theoretical values that have previously been reported in the literature for some other NDI materials.[11,26] The distance dependent calculations suggest that the area/extent of LUMO π-orbital overlap is a significant factor in achieving high conductivity materials as it maximises the surface area of the most straightforward charge transfer pathway(s) in a material.

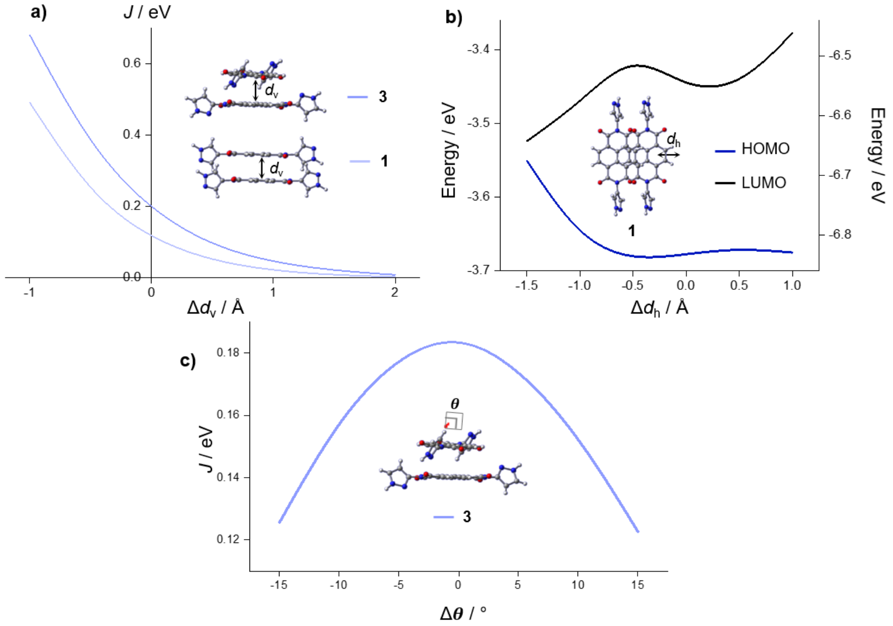

Figure 2.18. (a) The change in charge transfer integral upon variation of vertical π–π stacking distance in **1** and **3** (b) Dependence of J on the angle between co-facial dimer in **3** 0° refers to the angle defined in the solvent-free crystal structure between two monomers (c) variation of HOMO and LUMO energies of the resulting dimers as one molecule in the dimer is horizontally translated away from the crystal structure defined distance ($d_h = 0$) to alter the degree of slip-stacking.

Using the information provided by the distance dependent calculations, it was hypothesised that the twisted S_2 symmetry observed in NDI **3** appears to affect LUMO orbital lobe matching insinuating that π-overlap is maximised in comparison to the parallel arrangement of NDI surfaces in NDI **1**. To test these hypotheses, the horizontal distance, d_h observed in the single crystal data between NDI surfaces in the slip-stacked dimer in NDI **1** was used as a starting point, then moved closer together or further apart. The resulting energy of the HOMO and LUMO of the dimer was then plotted in Figure 2.18b to reveal that an energy increase is observed upon closer d_h, and a decrease on d_h that were further away, similar to what has been reported previously.[27] The results of the d_h variations hint at the criticality of quantum chemical symmetry alignments in enabling charge to flow in both NDIs **1** and **3**. The variable d_h result is further substantiated when the orientation of the arrangement of π-surfaces in NDI **3** is probed in more detail by altering the twist angle between two NDIs in the co-facial dimer the resulting charge transfer integral calculated and plotted (Figure 2.18c). At the crystal structure defined angle (which has been set to 0°), the charge transfer integral is at its maximum and steeply falls away as the angle is altered in either a clockwise or anticlockwise manner away from 0°. Evidently, the S_2 twisted orientation of NDIs maximises the electronic and quadrupolar interactions through efficient π-orbital overlap due to quantum mechanical orbital symmetry matching in the dimer and hence allows for a superior *through-space* charge transport in comparison to NDI **1**. Therefore, in line with the hypothesis, the twisted S_2 observed in NDI **3** proved to be the superior *through-space* charge transport pathway after the theoretical variable distance and twisting angle operations. Therefore, the theoretical data suggests that when designing electroactive materials that incorporate NDI, twisted S_2 symmetry that maximises π-orbital overlap and short distances between charge carriers will lead to the attractive *through-space* charge transport properties.

2.3 CONCLUSIONS

A family of four NDIs that were end-substituted with different pyrazole groups have allowed us to probe how various regiochemical and steric differences between end groups have influenced SCHB and any resulting interactions between NDI π-surfaces. Upon examining NDIs **2** and **4** in the solid-state, the bulky methyl-appended end groups disrupted SCHB, resulting in structures without any interactions between π-surfaces and any desirable semiconductor properties. However, in systems free of steric hinderance (NDIs **1** and **3**) SCHB was propagated, and the slight regiochemical differences between the two NDIs led to different SCHB and π–π packing arrangements. NDI **1** displayed a co-facial packing arrangement with close π–π distances, but a very small spatial overlap, resulting in conductivity values equalling to NDIs **2** and **4**. On the other hand, NDI **3** displayed a co-facial packing arrangement with close π–π distances, resulting in conductivity values that were three orders of magnitude higher than the other NDIs. Theoretical charge mobility calculations for NDIs **2**, **3** and **4** roughly agreed with the experimental conductivity results, showing that NDI **3** had the highest charge mobility, NDI **1** as second-best, and NDIs **2** and **4** as the lowest. Further DFT calculations revealed that varying the π–π distance between NDI **1** and **3** dimers resulted in a greater absolute charge transfer integral at all distances for NDI **3**, highlighting the importance of π-orbital overlap toward enabling charge transport. Twist angles were then examined theoretically for an NDI **3** dimer, confirming that the absolute charge transfer integral was highest at the crystal-structure defined angle, due to quantum symmetry matching, leading to efficient orbital overlap and charge transport. Overall, this work has shown that, through meticulous end group selection, SCHB can be exploited to influence the ordering of π-surfaces towards high π-orbital overlap and close π–π distances in the context of sterically unhindered species, resulting in more electroactive species. It has been uncovered that a parallel arrangement of π-surfaces does not necessarily lead to the most efficient π-orbital overlap, and instead that a twisted orientation of co-facial π-surfaces led to significantly higher semiconductor properties.

2.4 EXPERIMENTAL DETAILS

General details on materials and research methods as well as additional data for this Chapter can be found in the Appendix.

2.4.1 COMPUTATIONAL DETAILS

Density functional theory (DFT) calculations were prepared on GaussView 6.0 and submitted to the University of York Viking High performance Computing cluster and run on Gaussian 16 using Becke's three-parameter exchange functional with the gradient-corrected correlation formula of Lee, Yang and Parr (B3LYP)[28,29] paired with the split valence double-zeta 6-31G(d,p) basis set, PCM solvation model (DMF) and dispersion corrections (D3BJ)[30] unless stated otherwise. Electron transfer integrals J_{eff} were evaluated using a free open source software CATNIP.[23]

2.4.2 SYNTHETIC METHODS

GENERAL PROCEDURE FOR NDI SYNTHESIS

1,4,5,8-Napthalenetetracarboxylic dianhydride (1 equiv.) and amino-azole (2.1 equiv.) were added to a 35 mL oven-dried microwave vial containing anhydrous DMF (4 mL) and equipped with a stir bar. The reaction mixture was irradiated for 15 min at 140 °C under dynamic heating mode. The resulting solution was allowed to cool to rt and the solids were collected by vacuum filtration and washed with water (2 x 5 mL) and EtOH (2 x 5 mL).

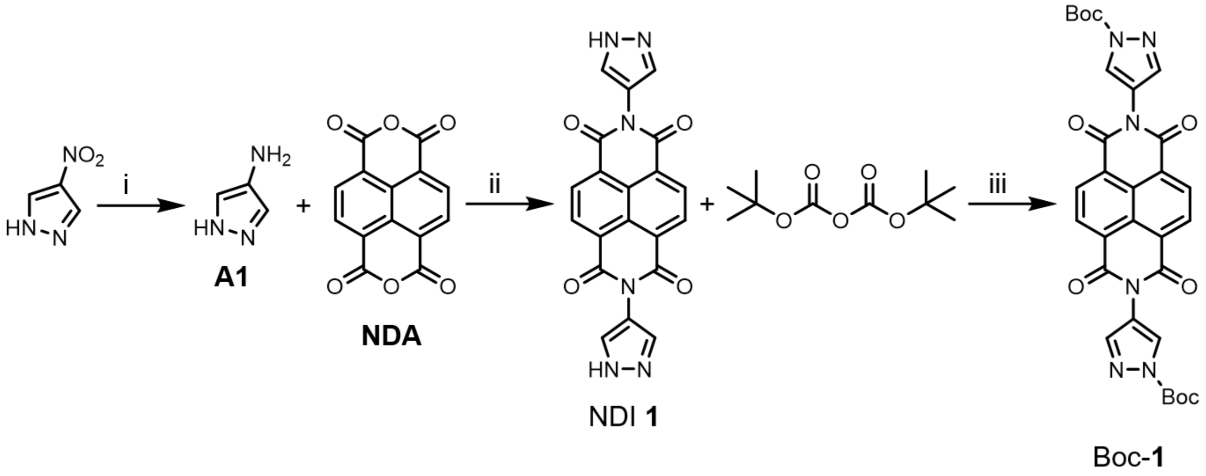

Figure 2.19. Synthesis of Boc-**1**. Reagents and conditions: (i) H_2 (balloon pressure), 10%% Pd/C, absolute EtOH, rt, 48 h, 99.9%; (ii) DMF µW: 140 °C, 15 min, 97%; (iii) Triethylamine, DMAP, DMF, rt, 48 h, 54%.

4-Aminopyrazole (A1). Pyrazole **A1** was prepared according to a modified literature procedure.[31] A flame-dried 250 mL round-bottomed flask equipped with a magnetic stirrer bar was charged with 10% Pd/C (1 g, 0.94 mmol, 0.01 equiv.) followed by absolute ethanol (150 mL) and 4-nitropyrazole (10 g, 88.4 mmol, 1 equiv.). The reaction mixture was degassed thoroughly by purging with nitrogen for 1 h before being evacuated and back-filled three time with H_2 gas *via* balloon. The reaction was allowed to stir at room temperature for 48 h, replacing the balloon as required to maintain a positive H_2 atmosphere. Upon full consumption of the starting material by TLC analysis (DCM/MeOH 90:10), the reaction mixture was filtered through a pad of Celite to remove insoluble materials which were further washed with absolute EtOH (50 mL). The filtrate was evaporated to dryness under reduced pressure to yield **A1** (7.34 g, 88.4 mmol, 99.9%) as a dark purple solid. Spectroscopic data were consistent with those previously published.

2,7-bis(1H-pyrazol-4-yl)-1,2,3,6,7,8-hexahydropyrene-1,3,6,8-tetrone (NDI 1). Applying the ***General Procedure*** for NDI synthesis described above, NDI **1** (385 mg, 0.97 mmol, 97%) was prepared from 1,4,5,8-napthalenetetracarboyxlic dianhydride (268 mg, 1 mmol, 1 equiv.) and **A1** (183 mg, 2.2 mmol, 2.2 equiv) as a gold powder. ^{1}**H NMR** (400 MHz, DMSO-d_6, 298 K): δ_H 13.11 (s, 2H^1), 8.72 (s, 4H^8), 7.96 (s, 2H^3), 7.65 (s, 2H^2). ^{13}**C NMR** (101 MHz, DMSO-d_6, 298 K) δ_C 162.67 (C^5), 130.96 (C^8), 126.75 (C^4), 126.89 (C^3), 115.35 (C^2). **HRMS** (ESI; $CHCl_3$, *ve*$^-$) calcd for $C_{20}H_9N_6O_4^-$: *m*/z = 397.0691 [*M*–H]$^-$; found 397.0677 [*M*–H]$^-$. **Elemental analysis:** Anal. calc for formula: $C_{20}H_{10}N_6O_4$ C, 60.31; H, 2.53; N, 21.10. Anal. found: C, 59.83; H, 2.6; N, 21.29 (–0.88 % C, +5.93 % H, –3.79 % N).

Boc-protected NDI (Boc-1). To a flame-dried 50 mL round bottomed flask containing DCM (5 mL) and equipped with a magnetic stir bar, **1** (100 mg, 0.25 mmol, 1 eq.), DMAP (5.6 mg, 0.05 mmol, 0.2

equiv.), EtN_3 (76 mg, 0.75 mmol, 3 equiv.) were added. The stirred reaction mixture was cooled to 0 °C, and di-tert-butyldicarbonate (121 mg, 0.55 mmol, 2.2 equiv.) was added dropwise. The reaction mixture was warmed to rt and left to stir for 48 h. The resulting crude material was concentrated *in vacuo*, and purified by column chromatography (eluent: DCM/MeOH gradient from 0 to 15 % MeOH), yielding Boc-**1** (81 mg, 0.14 mmol, 54 %) as a brown/yellow solid. No characterisation data available.

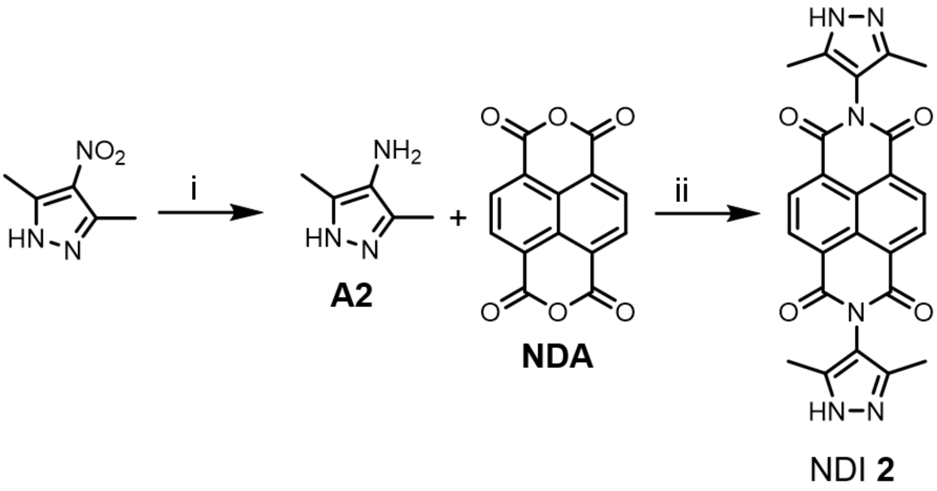

Figure 2.20. Synthesis of NDI **2**. Reagents and conditions: (i) H_2 (balloon pressure), 10%% Pd/C, absolute EtOH, rt, 48 h, 99%; (ii) DMF µW: 140 °C, 15 min, 97%.

4-Amino-3,5-dimethylpyrazole (A2). Pyrazole **A2** was prepared according to a modified literature[32] procedure. A flame-dried 100 mL round-bottomed flask equipped with a magnetic stirrer bar was charged with 10% Pd/C (0.5 g, 4.7 mmol, 0.47 equiv.) followed by absolute EtOH (35 mL) and then 4-nitro-3,5-dimethylpyrazole (1.41 g, 10 mmol, 1 equiv.) and a stir bar. The flask was evacuated, and the reaction mixture degassed by purging with nitrogen for 1 h. The flask was then purged, then back-filled with H_2 *via* balloon three times after which it was allowed to stir at room temperature for 48 h, inflating the balloon with H_2 when required and monitored by TLC (Eluent: DCM/MeOH 90:10). The reaction mixture was then filtered through a Celite pad and washed with absolute EtOH then dried under reduced pressure to yield **A2** (1.1 g, 9.9 mmol 99%) as an off-white solid. Spectroscopic data were consistent with those previously published.

2,7-bis(3,5-dimethyl-1H-pyrazol-4-yl)-1,2,3,6,7,8-hexahydropyrene-1,3,6,8-tetrone (NDI 2). Applying the ***General Procedure*** for NDI synthesis described above, NDI**2** (256 mg, 0.56 mmol, 56%) was prepared from 1,4,5,8-napthalenetetracarboyxlic dianhydride (268 mg, 1 mmol, 1 equiv.) and **A2** (183 mg, 2.2 mmol, 2.2 equiv) as a bright yellow powder. ^{1}**H NMR** (400 MHz, DMSO-d_6, 298 K): δ_H 12.51 (s, 2H^{1}), 8.74 (s, 4H^{9}), 2.06 (s, 6H^{4}), 1.96 (s, 6H^{3}). ^{13}**C NMR** (101 MHz, DMSO-d_6, 298 K) δ_C 162.34 (C^{5}), 136.20 (C^{7}), 130.86 (C^{8}), 126.78 (C^{6}), 112.03 (C^{2}), 11.42 (C^{5}), 9.04 (C^{4}). **HRMS** (ESI;

$CHCl_3$, ve^-) calcd for $C_{24}H_{17}N_6O_4^-$: m/z = 453.1317 [M–H]$^-$; found 453.1318 [M–H]$^-$. **Elemental analysis:** Anal. calc for formula: $C_{24}H_{17}N_6O_4$ C, 63.43; H, 3.99; N, 18.49. Anal. found: C, 63.3; H, 3.94; N, 18.27 (–0.20 % C, –1.50 % H, –1.14 % N)

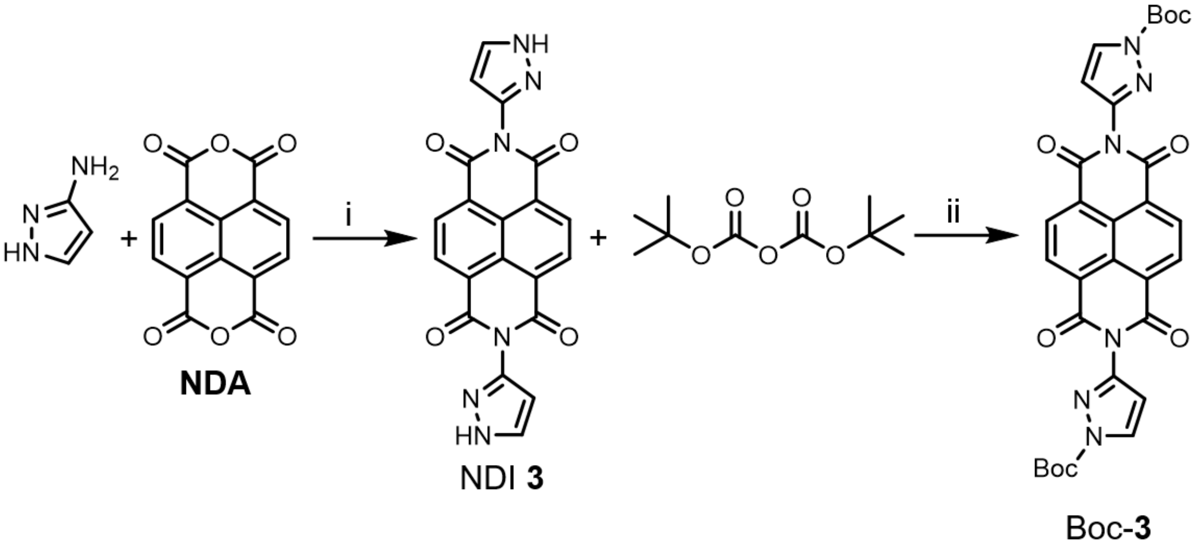

Figure 2.21. Synthesis of Boc-**3**. Reagents and conditions: (i) DMF μW: 140 °C, 15 min, 97%; (ii) Triethylamine, DMAP, DCM, rt, 48 h, 54%.

2,7-bis(1H-pyrazol-3-yl)-1,2,3,6,7,8-hexahydropyrene-1,3,6,8-tetrone (NDI 3). Applying the ***General Procedure*** for NDI synthesis described above, NDI **3** (397 mg, 0.99 mmol, 99%) was prepared from 1,4,5,8-naphthalene tetracarboxylic acid dianhydride (268 mg, 1 mmol, 1 equiv.) and 3-aminopyrazole (245 mg, 2.2 mmol, 2.2 equiv) as a yellow powder. ^{1}**H NMR** (400 MHz, DMSO-d_6, 298 K): δ_H 13.11 (s, 2H^1), 8.71 (s, 4H^8), 7.95 (s, 2H^2), 6.36 (s, 2H^3). ^{13}**C NMR** (101 MHz, DMSO-d_6, 298 K) δ_C 162.79 (C^5), 142.54 (C^7), 130.72 (C^8), 130.19 (C^6), 126.85 (C^4), 126.72 (C^2) 103.85 (C^3). **HRMS** (ESI; $CHCl_3$, ve+) calcd for $C_{20}H_{11}N_6O_4^+$: m/z = 399.0836 [M+H]$^+$; found 399.0836 [M+H]$^+$; calcd for $C_{20}H_{11}N_6O_4Na^+$: m/z = 421.0656 [M+Na]$^+$; found 421.0656 [M+Na]. **Elemental analysis:** Anal. calc for formula: $C_{20}H_{10}N_6O_4$: C, 60.31; H, 2.53; N, 21.1. Anal. found: C, 60.03; H, 2.52; N, 20.36 (–0.43 % C, –0.79 % H, –3.55 % N).

Boc-protected NDI (Boc-3). To a flame-dried 50 mL round bottomed flask containing DCM (5 mL) and equipped with a magnetic stir bar, **3** (100 mg, 0.25 mmol, 1 eq.), DMAP (5.6 mg, 0.05 mmol, 0.2 equiv.), EtN_3 (76 mg, 0.75 mmol, 3 equiv.) were added. The stirred reaction mixture was cooled to 0 °C, and di-tert-butyldicarbonate (121 mg, 0.55 mmol, 2.2 equiv.) was added dropwise. The reaction mixture was warmed to rt and left to stir for 48 h. The resulting crude material was concentrated *in* *vacuo*, and purified by column chromatography (eluent: DCM/MeOH gradient from 0 to 15 % MeOH), yielding Boc-**3** (81 mg, 0.14 mmol, 54 %) as a brown/yellow solid.

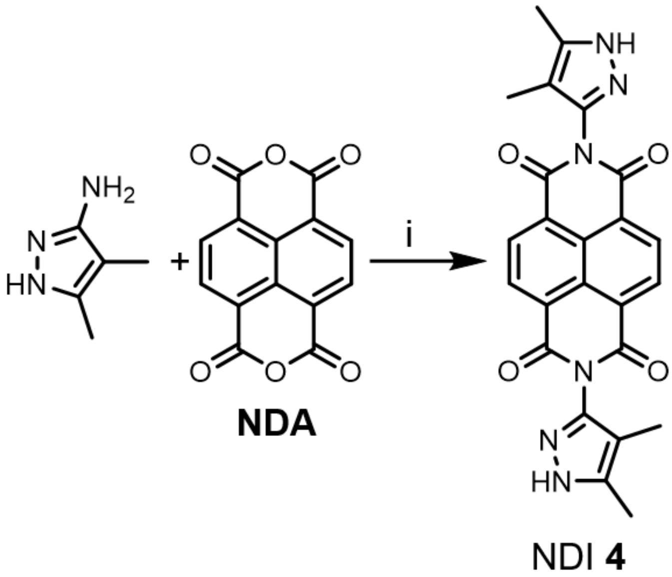

Figure 2.22. Synthesis of NDI **4**. Reagents and conditions: (i) DMF μW: 140 °C, 15 min, 97%.

2,7-bis(4,5-dimethyl-1H-pyrazol-3-yl)-1,2,3,6,7,8-hexahydropyrene-1,3,6,8-tetrone (NDI 4). Applying the ***General Procedure*** for NDI synthesis described above, NDI **4** (254 mg, 0.56 mmol, 56%) was prepared from 1,4,5,8-napthalene tetracarboyxlic acid dianhydride (268 mg, 1 mmol, 1 equiv.) and 4,5-dimethyl-1H-pyrazol-3-amine (245 mg, 2.2 mmol, 2.2 equiv) as a yellow powder. ^{1}**H NMR** (400 MHz, DMSO-*d*$_6$, 298 K): δ_H 12.63 (s, 2H, 2H^1), 8.74 (s, 4H^{10}), 2.25 (s, 6H^2), 1.78 (s, 6H^5). ^{13}**C NMR** (101 MHz, DMSO-*d*$_6$, 298 K) δ_C 162.54 (C^7), 141.73 (C^9), 136.94 (C^8), 130.90 (C^{10}), 127.03 (C^6), 126.64 (C^3), 109.03 (C^4), 108.93 (C^2), 9.55 (C^5), 6.44 (C^2). **HRMS** (ESI; CHCl$_3$, *ve*$^-$) calcd for $C_{24}H_{17}N_6O_4^-$: *m*/z = 453.1317 [*M*–H]$^-$; found 455.1310 [*M*–H]$^-$. **Elemental analysis:** Anal. calc for formula: $C_{24}H_{18}N_6O_4$: C, 63.43; H, 3.99; N, 18.49. Anal. found C, 63.13; H, 3.99; N, 18.2 (0.46 % C, –0.25 % H, –2.27 % N).

2.5 REFERENCES

(1) Zhan, X.; Facchetti, A.; Barlow, S.; Marks, T. J.; Ratner, M. A.; Wasielewski, M. R.; Marder, S. R. Rylene and Related Diimides for Organic Electronics. *Adv. Mater.* **2011**, *23*, 268–284. https://doi.org/10.1002/adma.201001402.

(2) Balakrishnan, K.; Datar, A.; Naddo, T.; Huang, J.; Oitker, R.; Yen, M.; Zhao, J.; Zang, L. Effect of Side-Chain Substituents on Self-Assembly of Perylene Diimide Molecules: Morphology Control. *J. Am. Chem. Soc.* **2006**, *128*, 7390–7398. https://doi.org/10.1021/ja061810z.

(3) Würthner, F.; Stolte, M. Naphthalene and Perylene Diimides for Organic Transistors. *Chem. Commun.* **2011**, *47*, 5109–5115. https://doi.org/10.1039/C1CC10321K.

(4) Yao, Z.-F.; Wang, J.-Y.; Pei, J. Control of π–π Stacking via Crystal Engineering in Organic Conjugated Small Molecule Crystals. *Cryst. Growth Des.* **2018**, *18*, 7–15. https://doi.org/10.1021/acs.cgd.7b01385.

(5) Vrbancich, J.; Ritchie, G. L. D. Quadrupole Moments of Benzene, Hexafluorobenzene and Other Non-Dipolar Aromatic Molecules. *J. Chem. Soc., Faraday Trans. 2* **1980**, *76*, 648–659. https://doi.org/10.1039/F29807600648.

(6) Schmidt, R.; Oh, J. H.; Sun, Y.-S.; Deppisch, M.; Krause, A.-M.; Radacki, K.; Braunschweig, H.; Könemann, M.; Erk, P.; Bao, Z.; Würthner, F. High-Performance Air-Stable n-Channel Organic Thin Film Transistors Based on Halogenated Perylene Bisimide Semiconductors. *J. Am. Chem. Soc.* **2009**, *131*, 6215–6228. https://doi.org/10.1021/ja901077a.

(7) Zhang, J.; Bai, F.; Li, Y.; Hu, H.; Liu, B.; Zou, X.; Yu, H.; Huang, J.; Pan, D.; Ade, H.; Yan, H. Intramolecular π-Stacked Perylene-Diimide Acceptors for Non-Fullerene Organic Solar Cells. *J. Mater. Chem. A* **2019**, *7*, 8136–8143. https://doi.org/10.1039/C9TA00343F.

(8) An, Y.; Long, D. X.; Kim, Y.; Noh, Y.-Y.; Yang, C. Improved Electron Transport Properties of N-Type Naphthalenediimide Polymers through Refined Molecular Ordering and Orientation Induced by Processing Solvents. *Phys. Chem. Chem. Phys.* **2016**, *18*, 12486–12493. https://doi.org/10.1039/C6CP01314G.

(9) Chen, J.; Zhuang, X.; Huang, W.; Su, M.; Feng, L.; Swick, S. M.; Wang, G.; Chen, Y.; Yu, J.; Guo, X.; Marks, T. J.; Facchetti, A. π-Extended Naphthalene Diimide Derivatives for n-Type Semiconducting Polymers. *Chem. Mater.* **2020**, *32*, 5317–5326. https://doi.org/10.1021/acs.chemmater.0c01397.

(10) Welford, A.; Maniam, S.; Gann, E.; Jiao, X.; Thomsen, L.; Langford, S. J.; McNeill, C. R. Influence of Alkyl Side-Chain Type and Length on the Thin Film Microstructure and OFET Performance of Naphthalene Diimide-Based Organic Semiconductors. *Org. Electron.* **2019**, *75*, 105378. https://doi.org/10.1016/j.orgel.2019.105378.

(11) Komissarova, E. A.; Dominskiy, D. I.; Zhulanov, V. E.; Abashev, G. G.; Siddiqui, A.; Singh, S. P.; Sosorev, A. Y.; Paraschuk, D. Y. Unraveling the Unusual Effect of Fluorination on Crystal Packing in an Organic Semiconductor. *Phys. Chem. Chem. Phys.* **2020**, *22*, 1665–1673. https://doi.org/10.1039/C9CP05455C.

(12) Gokel, G. W.; Barbour, L.; Atwood, J. L. *Comprehensive Supramolecular Chemistry II*; Elsevier Science & Technology Books, 2017.

(13) Johnson, E. R.; Keinan, S.; Mori-Sánchez, P.; Contreras-García, J.; Cohen, A. J.; Yang, W. Revealing Noncovalent Interactions. *J. Am. Chem. Soc.* **2010**, *132*, 6498–6506. https://doi.org/10.1021/ja100936w.

(14) Molla, M. R.; Gehrig, D.; Roy, L.; Kamm, V.; Paul, A.; Laquai, F.; Ghosh, S. Self-Assembly of Carboxylic Acid Appended Naphthalene Diimide Derivatives with Tunable Luminescent Color and Electrical Conductivity. *Chem. Eur. J.* **2014**, *20*, 760–771. https://doi.org/10.1002/chem.201303379.

(15) Hashim, M. I.; Le, H. T. M.; Chen, T.-H.; Chen, Y.-S.; Daugulis, O.; Hsu, C.-W.; Jacobson, A. J.; Kaveevivitchai, W.; Liang, X.; Makarenko, T.; Miljanić, O. Š.; Popovs, I.; Tran, H. V.; Wang, X.; Wu, C.-H.; Wu, J. I. Dissecting Porosity in Molecular Crystals: Influence of Geometry, Hydrogen Bonding, and [π···π] Stacking on the Solid-State Packing of Fluorinated Aromatics. *J. Am. Chem. Soc.* **2018**, *140*, 6014–6026. https://doi.org/10.1021/jacs.8b02869.

(16) Al Kobaisi, M.; Bhosale, S. V.; Latham, K.; Raynor, A. M.; Bhosale, S. V. Functional Naphthalene Diimides: Synthesis, Properties, and Applications. *Chem. Rev.* **2016**, *116*, 11685–11796. https://doi.org/10.1021/acs.chemrev.6b00160.

(17) Gawrys, P.; Djurado, D.; Rimarčík, J.; Kornet, A.; Boudinet, D.; Verilhac, J.-M.; Lukeš, V.; Wielgus, I.; Zagorska, M.; Pron, A. Effect of N-Substituents on Redox, Optical, and Electronic Properties of Naphthalene Bisimides Used for Field-Effect Transistors Fabrication. *J. Phys. Chem. B* **2010**, *114*, 1803–1809. https://doi.org/10.1021/jp908931w.

(18) Takenaka, S. Application of Naphthalene Diimide in Biotechnology. *Polym J* **2021**, *53*, 415–427. https://doi.org/10.1038/s41428-020-00434-2.

(19) Roy Chowdhury, S.; Nandi, S. K.; Mondal, S.; Kumar, S.; Haldar, D. White-Light-Emitting Supramolecular Polymer Gel Based on β-CD and NDI Host-Guest Inclusion Complex. *Polymers* **2021**, *13*, 2762. https://doi.org/10.3390/polym13162762.

(20) Reiner, B. R.; Foxman, B. M.; Wade, C. R. Electrochemical and Structural Investigation of the Interactions between Naphthalene Diimides and Metal Cations. *Dalton Trans.* **2017**, *46*, 9472–9480. https://doi.org/10.1039/C7DT02067H.

(21) Lee, S. K.; Zu, Y.; Herrmann, A.; Geerts, Y.; Müllen, K.; Bard, A. J. Electrochemistry, Spectroscopy and Electrogenerated Chemiluminescence of Perylene, Terrylene, and Quaterrylene Diimides in Aprotic Solution. *J. Am. Chem. Soc.* **1999**, *121*, 3513–3520. https://doi.org/10.1021/ja984188m.

(22) Ke, H.; Weng, L.-J.; Chen, S.-Y.; Chen, J.-Z.; Lin, M.-J. Naphthalene Diimide Cocrystals: A Facile Approach to Tune the Optical Properties. *Dyes. Pigm.* **2015**, *113*, 318–324. https://doi.org/10.1016/j.dyepig.2014.08.020.

(23) Brown, J. S. QC_Tools or CATNIP - ChArge TraNsfer Integral Package, 2023. https://github.com/JoshuaSBrown/QC_Tools (accessed 2023-09-25).

(24) Baumeier, B.; Kirkpatrick, J.; Andrienko, D. Density-Functional Based Determination of Intermolecular Charge Transfer Properties for Large-Scale Morphologies. *Phys. Chem. Chem. Phys.* **2010**, *12*, 11103–11113. https://doi.org/10.1039/C002337J.

(25) Valeev, E. F.; Coropceanu, V.; da Silva Filho, D. A.; Salman, S.; Brédas, J.-L. Effect of Electronic Polarization on Charge-Transport Parameters in Molecular Organic Semiconductors. *J. Am. Chem. Soc.* **2006**, *128*, 9882–9886. https://doi.org/10.1021/ja061827h.

(26) Gogoi, G.; Bhattacharya, L.; Sahoo, S. R.; Sahu, S.; Sarma, N. S.; Sharma, S. Enhancement of Air-Stability, π-Stacking Ability, and Charge Transport Properties of Fluoroalkyl Side Chain Engineered n-Type Naphthalene Tetracarboxylic Diimide Compounds. *RSC Adv.* **2021**, *11*, 57–70. https://doi.org/10.1039/D0RA08345C.

(27) Brédas, J. L.; Calbert, J. P.; Filho, D. A. da S.; Cornil, J. Organic Semiconductors: A Theoretical Characterization of the Basic Parameters Governing Charge Transport. *PNAS* **2002**, *99*, 5804–5809. https://doi.org/10.1073/pnas.092143399.

(35) Becke, A. D. Density-functional Thermochemistry. III. The Role of Exact Exchange. *J. Chem. Phys.* **1993**, *98*, 5648–5652. https://doi.org/10.1063/1.464913.

(36) Lee, C.; Yang, W.; Parr, R. G. Development of the Colle-Salvetti Correlation-Energy Formula into a Functional of the Electron Density. *Phys. Rev. B* **1988**, *37*, 785–789. https://doi.org/10.1103/PhysRevB.37.785.

(37) Grimme, S.; Antony, J.; Ehrlich, S.; Krieg, H. A Consistent and Accurate Ab Initio Parametrization of Density Functional Dispersion Correction (DFT-D) for the 94 Elements H-Pu. *J. Chem. Phys* **2010**, *132*, 154104. https://doi.org/10.1063/1.3382344.

(38) Maccallini, C.; Di Matteo, M.; Vullo, D.; Ammazzalorso, A.; Carradori, S.; De Filippis, B.; Fantacuzzi, M.; Giampietro, L.; Pandolfi, A.; Supuran, C. T.; Amoroso, R. Indazole, Pyrazole, and Oxazole Derivatives Targeting Nitric Oxide Synthases and Carbonic Anhydrases. *ChemMedChem* **2016**, *11*, 1695–1699. https://doi.org/10.1002/cmdc.201600204.

(32) Miller, A.; Schüler, P.; De, V. E. Chemical Substances Which Inhibit the Enzymatic Activity of Human Kallikrein-Related Peptidase 6 (Klk6). EP3305781 (A1), April 11, 2018. https://worldwide.espacenet.com/publicationDetails/biblio?FT=D&date=20180411&DB=&locale=en_EP&CC=EP&NR=3305781A1&KC=A1&ND=1 (accessed 2021-03-05).

CHAPTER 3 |

AN ELECTROACTIVE FE—PYRAZOLATE POROUS COORDINATION POLYMER

SYNOPSIS

This Chapter delineates the design of a novel porous coordination polymer (PCP) framework that displays notable thermal stability, chemical robustness, redox activity, and conductivity, rendering it a promising candidate for energy storage applications. Building upon the groundwork laid in Chapter 2, the structural motif of N,N'-bis(pyrazole)naphthalene diimide (NDI) **1** was strategically employed as a ligand to generate a Fe-pyrazolate 2D interpenetrated framework. The newly crafted framework was subsequently found to exhibit redox activity from NDI **1** linkers and possess small micropores resulting from self-interpenetration. Remarkably, conductivity measurements unveil a high level of electrical conductivity in comparison to similar frameworks, a phenomenon later elucidated by theoretical calculations, which reveal the existence of two charge transport pathways within the framework, *through-bond* and *through-space*. Moreover, the calculations suggest the potential formation of polarons, giving rise to a materials with mixed valency metal centres. The unanticipated emergence of a dual charge transport system, achieved through a deliberate design strategy, lays a solid foundation for the future development of similar semiconducting materials.

ACKNOWLEDGEMENTS

The following people are gratefully acknowledged for their contribution to this chapter. Dr Jamie A. Gould for establishing the initial synthetic procedures. Dr Philip A. Hope for collecting the high-resolution electron microscopy images. Dr. Jeppe Christensen of Diamond Light Source using Beamline I19 Diamond Light Source for collecting the data for **Fe(Cl)NDI-1** and Adrian Whitwood for solving the X-ray crystal structure of **Fe(Cl)NDI-1**. Dr James Quirk for carrying out the theoretical calculations relating to frontier molecular orbitals and polarons. Dr Stuart Cavill for providing access to a Keithly source meter to enable conductivity measurements.

3.1 INTRODUCTION

Coordination polymers (CPs) represent a distinctive class of highly ordered crystalline solids with some amorphous examples, comprising of metal nodes and organic or inorganic linkers that assemble into continuous supramolecular frameworks.[1–4] Concerning CPs, two subtypes are recognised in this thesis: (i) porous coordination polymers (PCPs), characterised by their frameworks containing accessible pores, and (ii) non-porous coordination polymers (NP-CPs), lacking such pores. Upon their inception, PCPs were regarded as insulating materials, yet their conductivity can be enhanced through the incorporation of charge transport pathways.[5] Such pathways, that discussed thoroughly in Chapter 1, can be classified as *through-bond*, *through-space*, or *extended conjugation*, facilitating the movement of electrons or holes throughout the CP framework *via* mechanisms such as band transport or electron hopping.[5,6] The combination of the ability of conductive PCPs to promote various chemical processes (e.g., separations, energy storage, catalysis) within their pores, along with their electroactive nature, has sparked significant interest in this field over the past decade.[5] Notably, conductive PCPs have been developed, yielding materials that have found utility as active components in semiconducting devices, including batteries,[7,8] supercapacitors,[9–11] and electrocatalysts.[12]

In the modern era, the global energy demand has reached unprecedented levels due to the burgeoning world population and the widespread adoption of energy-intensive technologies. The escalating energy demand, coupled with the adverse environmental impact of fossil fuel consumption, has necessitated the exploration and utilisation of alternative renewable energy sources such as wind and solar power.[13] However, the successful integration of such renewable energy technologies relies heavily on the advancement of efficient energy storage devices.[14] The development of robust energy storage systems assumes paramount importance to facilitate the storage of large quantities of electrical charge over extended periods. This imperative arises from the need to address global energy requirements effectively. Consequently, there is a pressing need to advance battery technology, which can provide energy storage devices possessing essential attributes, including high cycling rates, substantial charge capacity, and scalability.[15] Moreover, these energy storage solutions must be economically viable and affordable to ensure widespread accessibility.[16] By focusing on the aforementioned attributes, battery technology can play a pivotal role in enabling the efficient storage of renewable energy, thus mitigating the challenges posed by fluctuating energy availability and meeting the ever-increasing energy demands of the modern world.

With the advent of conductive PCPs, there is a foundation to develop them as functional materials towards energy storage and conversion applications due to their distinct qualities (i.e., intrinsic porosity, variable functionalisation, highly diverse ordered structures).[17] However, current PCPs developed as energy storage materials have suffered from pitfalls (i.e., high cost, low conductivity, low charge capacity, low stability), preventing use in practical applications.[18] New PCPs that for example comprise of sustainable low-cost metals and ligands, remain stable after multiple redox cycles, and have appropriately high conductivity could place PCPs at the forefront of battery technology. Therefore, PCPs that encompass the subsequent attributes: (i) chemical and thermal robustness, (ii) highly cyclable pore-accessible redox-active sites, (iii) and multiple conductive pathways would serve as excellent active materials in practical energy storage devices.

The use of pyrazole units as building blocks in conjunction with metal centres have led to a wide variety of PCPs that have displayed chemically and thermally robust properties. In order to act as active materials in an energy storage device, chemically and thermally resistive properties are vital to maintain optimal cycling. Demonstrating the robustness of the metal–pyrazolate bond in supramolecular structures, Long and co-workers[19] developed a range of PCPs that were synthesised by combining benzenetripyrazole (BTP) groups with a variety of metal centres (i.e., Ni, Cu, Zn, Co). The synthesised frameworks displayed open metal sites and porosities (930–1860 $m^2\ g^{-1}$) that in the cases of the **NiBTP** (Figure 3.1a) and **ZnBTP** (Figure 3.1b) frameworks, remained stable in air up to temperatures of 430 and 510 °C, respectively. Furthermore, both Ni and Zn frameworks remained stable in boiling aqueous solutions that were kept at a pH of 2 for 2–14 weeks, demonstrating the high chemical and thermal stability of pyrazolate bonds in this set of PCPs. In other work, a benzene dipyrazole (BDP) linker was used to form pyrazolate-based PCPs with Zn and Ni metal centres, **PFC-6** and **PFC-7**, respectively (Figure 3.1c).[20] Both PCPs displayed high porosity (**PFC-6** = 1537 $m^2\ g^{-1}$ and **PFC-7** = 2022 $m^2\ g^{-1}$), retaining their porosity and structure in aqueous media between pH 2–14 for 48 h. The PCPs were then trialled as drug carriers, finding that upon adsorption of the drug substance diclofenac (DCF), a slow release was observed over the course of three days in a pH = 7.4 buffer solution that mimicked the conditions inside a human body. The slow release of DCF was suggested to occur due an equilibrium of non-covalent interactions between drug molecules and solvent molecules to the pyrazolate backbones of **PFC-6** and **PFC-7**.

More recently, Ma et al.[21] formed a Zn-based PCP **$Zn_9O_2(OH)_2(L)_6$** that utilised salen ligands (Figure 3.2a) and pyrazolate clusters (Figure 3.2b), revealing a BET surface area of 934 $m^2\ g^{-1}$, despite being two-fold interpenetrated. To test the chemical stability of **$Zn_9O_2(OH)_2(L)_6$**, the material was suspended in aqueous solutions of HCl (pH 2), 2.5% ammonia, and 2 M NaOH over a period of 210 days, demonstrating no change in PXRD pattern. The outstanding acid-resistance of **$Zn_9O_2(OH)_2(L)_6$** prompted investigation of its catalytic activity by carrying out CO_2 cycloadditions of epoxides. At low catalyst loadings (0.5–1.5%), high yields (78–98%) of the corresponding catalytic products were observed, that outperformed other heterogeneous catalysts.

In other work, a PCP featuring triangular channels was developed by Herm et al.[22] by combining BDP linkers with Fe^{3+} metal centres, forming a pyrazolate framework that was named **Fe_2BDP_3** (Figure 2b). Two years later, Aubrey et al. demonstrated the excellent charge-transporting properties of Fe_2BDP_3 upon reducing the exposed metal centres with potassium ions to form a mixed-valency framework and boost the material's conductivity by five orders of magnitude in comparison to what was observed by Herm et al. originally (see Figure 3.2c, noting the green K ions).[23] The integration of pyrazolate bonds into PCPs has resulted in materials with high chemical and thermal stability in addition to improving conductive properties, suggesting that pyrazolate bonds can serve as promising structural motifs for achieving robust energy storage materials.

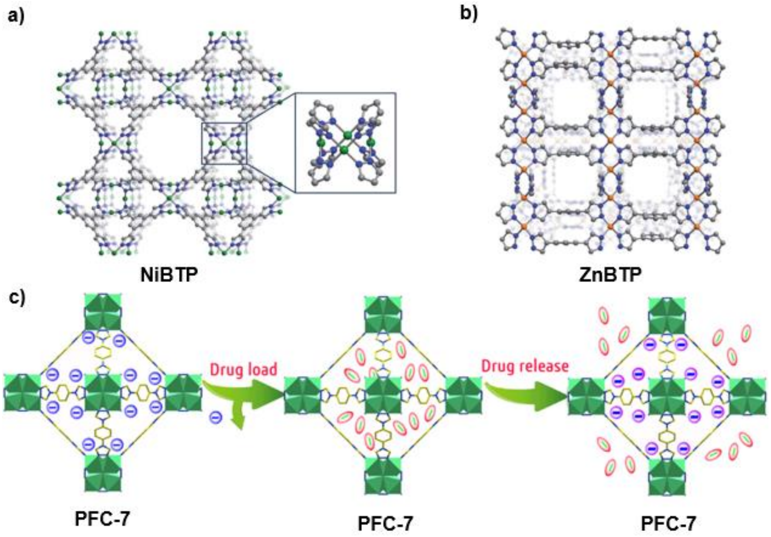

Figure 3.1. Structures of (a) **NiBTP**[19] and (b) **ZnBTP**, both copied from the work of Long and co-workers.[19] (c) action of drug loading and release from **PFC-7**, copied from the work of Liu et al.[20]

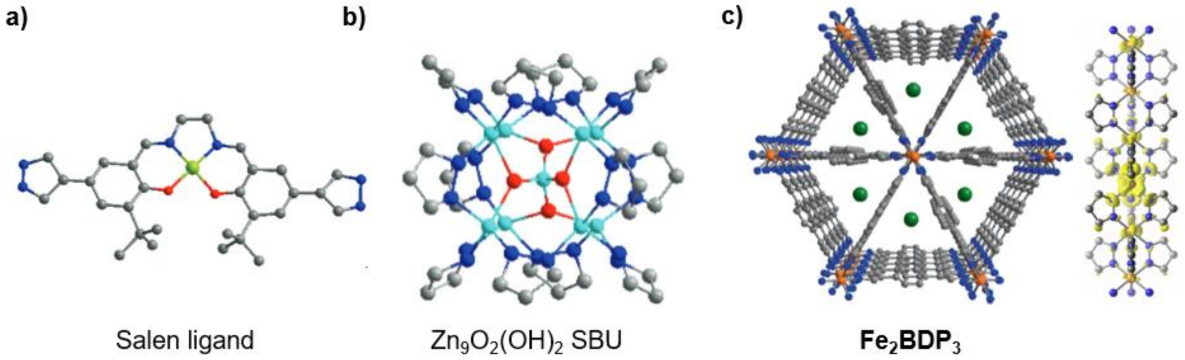

Figure 3.2. The (a) salen ligand and (b) $Zn_9O_2(OH)_2$ SBU of **$Zn_9O_2(OH)_2(L)_6$**, copied from the work of Ma et al.[21] (c) View down the triangular channels, supported by the 1D Fe–pyrazolate chains of **Fe_2BDP_3**, copied from the work of Herm et al.[22]

Outside of PCPs, the use of redox-active RDI units such as NDI in microporous purely organic molecular units has proven to be a highly successful strategy for the generation of excellent battery materials. In 2013, Stoddart and co-workers[23,24] developed a microporous NDI molecular triangle (**NDIΔ**) that was later used as an active material in an energy storage device by Chen et al.[24,25] in 2015. The **NDIΔ** structure consists of three NDI units interconnected through cyclohexane groups, facilitating the reversible reductive of six active sites on the triangular framework (Figure 3.3a). When incorporated into an energy storage device, **NDIΔ** exhibited a capacity of 71.1 mA h g^{-1} after cycling 300 times at 10 C, far exceeding the control compound (NDI end-substituted with cyclohexane), that experienced a substantial loss of capacity after 10 cycles. Another study by Wasielewski and co-workers[26] focused on developing electroactive covalent organic frameworks (COFs) for energy storage applications, drawing inspiration from G-quadruplexes found in guanine-rich DNA that arrange into 2D frameworks with tetragonal grids (Figure 3.3b). To achieve redox-active capabilities without disrupting the formation of the G-quadruplex motif, NDI and PDI units without substitution at the bay positions were selected for their lack of disruptive functional groups. Guanine moieties were then appended to the ends of the NDI and PDI units, creating hydrogen-bonded frameworks that mimicked G-quadruplex scaffolds, along with π-stacking interactions between NDI or PDI moieties. The frameworks were revealed to be redox active and, upon photoexcitation, exhibited the generation of long-lived charge carriers shared across multiple sites, prompting the exploration of energy storage properties in devices. Batteries were fabricated using the PDI species due to its superior structural stability compared to the NDI species, resulting in a capacity loss of less than 7% over 300 cycles, owing to the remarkable structural robustness of the material. In another study, Wang et al.[27] used NDI in conjunction with tris(4-aminophenyl) groups to form a 2D polyarylimide (PAI) material, that self-assembled onto the surface of carbon nano tubes (CNTs), see Figure 3.3c. As a result of the 2D-PAI material that was held in place by π-interactions, a high thermal (~500 °C) and chemical (aqueous acid, DMF, NMP, water over 24 h) resistance was observed, that allowed the intrinsic porosity of the CNT structure to be maintained throughout the stability tests. The 2D-PAI-CNT material was incorporated as active material in the cathode of a Li-ion battery, and upon cycling, an 82.9% active site capacity was observed. A further 8000 cycles were completed at 0.5 A g^{-1} without any degradation of the active site capacity, representing one of the highest stability polyimide materials to be incorporated into a rechargeable battery. The incorporation of NDI units into microporous organic materials has demonstrated exceptional redox properties and stability. Therefore, coordinating NDI units with metals to create PCPs could yield materials with analogous properties, making them promising candidates for integration into energy storage devices.

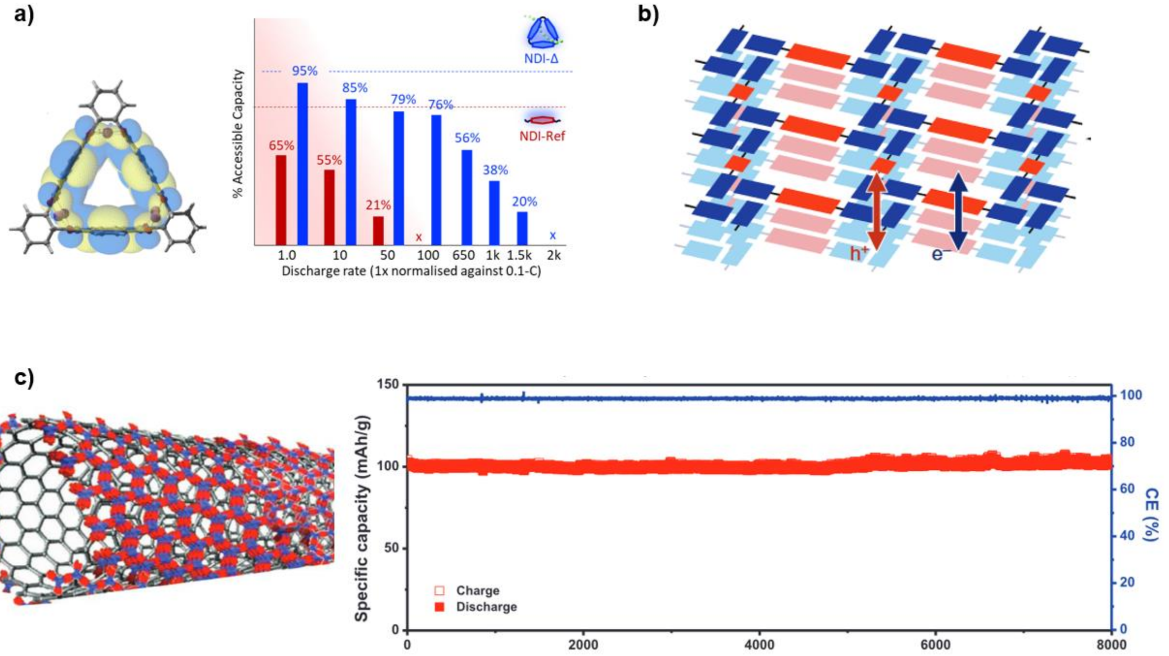

Figure 3.3. Displaying the (a) NDIΔ structure, copied from the work of Stoddart and co-workers[23,24] and discharge rate vs a NDI reference, copied from the work of Stoddart and co-workers and Chen et al.[24,25], (b) the layered superstructure of synthesised COFs with a g-quadruplex motif, copied from the work of Wasielewski and co-workers.[26], (c) the 2D PAI material and the retention of capacity after 8000 cycles, copied from the work of Wang and co-workers.[27]

The evidence supporting the advantageous characteristics of pyrazolate links in conferring thermal and chemical stability, combined with the suitability of NDI as a building block within redox-active porous materials, is compelling. Moreover, both pyrazolate links and NDIs have been demonstrated to enhance the overall conductivity of PCPs. Consequently, the integration of pyrazolate links and NDI units holds great promise for the development of conductive PCPs with inherent redox capabilities, offering a potential solution to address common cyclability issues in energy storage materials. By using a synergistic approach, a significant step forward towards advancing the field of energy storage holds considerable potential for realising high-performance and durable energy storage devices. Herein, the goal of this chapter is to synthesise a novel redox-active coordination framework, that displays thermal and chemical stability, while also displaying conductive properties at appropriate levels to be used in an energy storage device.

3.2 RESULTS AND DISCUSSION

3.2.1 SYNTHESIS OF Fe(Cl)NDI-1

Molecule NDI **1**, which was previously featured in Chapter 2, was explored for its potential to act as a redox-active ligand and form multidimensional coordination materials. In addition, NDI **1** is redox-active and can facilitate the formation of *through-space* conductive pathway that transports electrons through its low-lying LUMO orbitals. However, as discussed in Chapter 2, the control of aromatic interactions towards orientations that promote high charge transport is challenging and requires additional elements to overcome quadrupolar repulsion between π-surfaces. In order to control the aromatic interactions of NDI **1** π-surfaces in the context of a PCP, Fe was selected for its propensity to form π-overlapped 3D scaffolds that have displayed impressive *through-bond* and *through-space* conductivities in defect-rich and mixed valency frameworks.[23,28] By using Fe, the expectation was that enhanced charge-transport properties would emerge in comparison to PCPs generated with other 3d transition metals (e.g., Zn, Ni, Cu, Mn).[28] Furthermore, Fe is a plentiful resource in the earth's crust, is non-toxic and has a low market price, causing frameworks produced with Fe to be sustainable in comparison to other metals that demonstrate high toxicities (e.g., Co, Ni, Mn) or are expensive (e.g., Pd, Ir, Pt).[29,30]

With the aim of generating a conductive framework that had the potential to be used as active material in an energy storage device, a synergistic approach using a combination of Fe and NDI **1** was pursued. Previously commented on in the introduction, Herm et al.,[22] generated **Fe_2BDP** that was supported by a Fe–pyrazolate backbone and possessed triangular channels, closely resembling an agreeable coordination geometry for energy storage purposes, without redox active ligands. Therefore, the synthetic protocols were used by Herm et al.,[22] in which $Fe(acac)_3$ was reacted with BDP under dry inert solvothermal conditions were closely studied (Figure 3.4a). In an attempt to substitute BDP ligands for NDI **1** ligands, the synthetic protocols set by Herm et al.[22] were replicated (Figure 3.4b), using more readily available $Fe(Cl)_3$ in lieu of $Fe(acac)_3$. Post-reaction, the crude products were filtered and washed with DMSO, absolute EtOH and acetone to remove any reaction by-products and starting materials, yielding a mixture of red and black solids that were insoluble in all common solvents (i.e., MeOH, DMF, DMSO). The two materials were unable to be separated, causing microwave irradiation to be pursued as a greener alternative to conventional heating with a hotplate. The reaction was replicated using microwave heating, and the crude solids were washed with DMSO, absolute EtOH and acetone to yield a powdered red solid that was placed in a vacuum oven overnight at 200 °C to remove any residual solvent molecules (full synthetic details can be found in synthetic details, section 3.4.4, Figure 3.21). The powdered solid was then examined under a polarised microscope, showing that small transparent block-shaped crystals were visible, leading to the conclusion that a micro-crystalline material had been synthesised and was named **Fe(Cl)NDI-1**. Further interrogation of the micro-crystalline material was carried outby Philip A. Hope using a scanning electron microscope (SEM), visualising a homogenously sized distribution of crystallites (see the Appendix, section 7.15, Figures 7.33, 7.44 and 7.45). A sample of **Fe(Cl)NDI-1** synthesised by Dr Jamie Gould was sent off was sent to Diamond Light Source to be analysed by high intensity synchrotron X-ray radiation due to the small size of the crystallites (<0.1 mm).

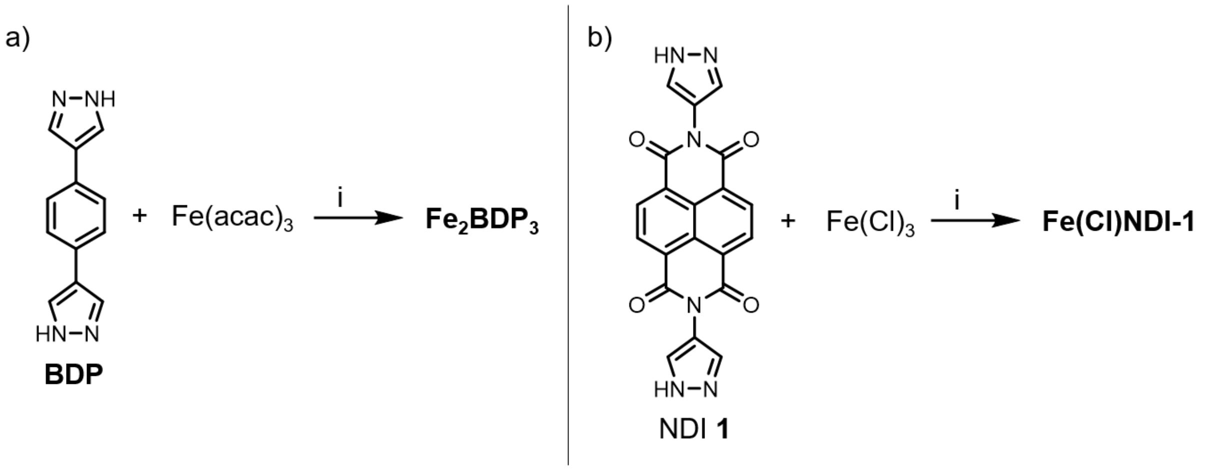

Figure 3.4. Synthesis of (a) **Fe_2BDP_3** Herm et al.[22] (b) **Fe(Cl)NDI-1** from this work. (i) DMF, μW: 200 °C, 15 min.

3.2.2 PRODUCT CONFIRMATION OF Fe(Cl)NDI-1

X-ray analysis reveal that **Fe(Cl)NDI-1** consisted of a 2D interpenetrated coordination network, with Fe^{3+} metal centres, NDI **1** linkers, and Cl bridging anions (see Figure 3.5 for details on the specific interactions, and Figure 3.6 for the interpenetrated framework). Specifically, the structure of **Fe(Cl)NDI-1** display octahedral coordination around the Fe metal centre comprising of four connections with pyrazole end group nitrogen atoms (Fe−N = 2.13 Å) and two connections with Cl atoms (Fe−Cl = 2.41 Å). Each Fe atom in the framework of **Fe(Cl)NDI-1** formally possessed an oxidation state of Fe^{3+}, donating one electron to Cl, and one electron to each coordinated nitrogen atom. The latter connections to each nitrogen act as negatively charged ligands, as a result of deprotonation during the synthetic process to form **Fe(Cl)NDI-1**. The pyrazolate chain (i.e., $(Fe{-}N{-}N{-})_\infty$ both acts as a supporting backbone to the structure of **Fe(Cl)NDI-1** and a potential *through-space* charge transport pathway. Conceivably, charge transport could occur *through-bond via* chemically bonded $(Fe{-}N{-}N{-})_\infty$ atoms similar to those observed in other Fe–pyrazolate materials.[31,32] However, between chemically bonded Fe atoms and NDI **1** linkers, charge transport was unlikely to occur *via* the *extended-conjugation* pathway due the negligible effect that N-substitution has on the electronic properties of NDIs **1**–**4**, as revealed by CV studies in Chapter 2. The self-interpenetrated network of **Fe(Cl)NDI-1** resulted in high spatial overlap between NDI π-surfaces and displayed close π–π distances (3.45 Å), justifying the use of the Fe metal centre to control π-interaction geometries in comparison to the slip-stacked arrangement of NDI **1** π-surfaces in Chapter 2. The uninterrupted arrangement of π-stacked NDI aromatic surfaces indicates the potential for a *through-space* pathway to emerge from the interpenetrated network of **Fe(Cl)NDI-1**. Due to a combination of the coordination bonds formed between pyrazole end groups and Fe, and the self-interpenetrated frameworks, the π-surfaces of NDI **1** were arranged into a configuration that has the potential to transport charge through the continuous π-overlapped array. However, upon gaining a potential *through-space* charge transport pathway, the interpenetrated nature of **Fe(Cl)NDI-1**, that has a guest accessible volume of 187.8 Å^3 (9.9%), potentially blocks the diffusion of counter anions capable of stabilising charges. If counter-anions are blocked from accessing redox sites, energy storage applications of **Fe(Cl)NDI-1** are likely to be limited. Following the acquisition of the crystal structure of **Fe(Cl)NDI-1**, materials that were obtained from microwave irradiation were analysed for their compositional purity before any further properties analysis could be carried out. Full crystallographic information can be found in the Appendix, section 7.14, Table 7.2.

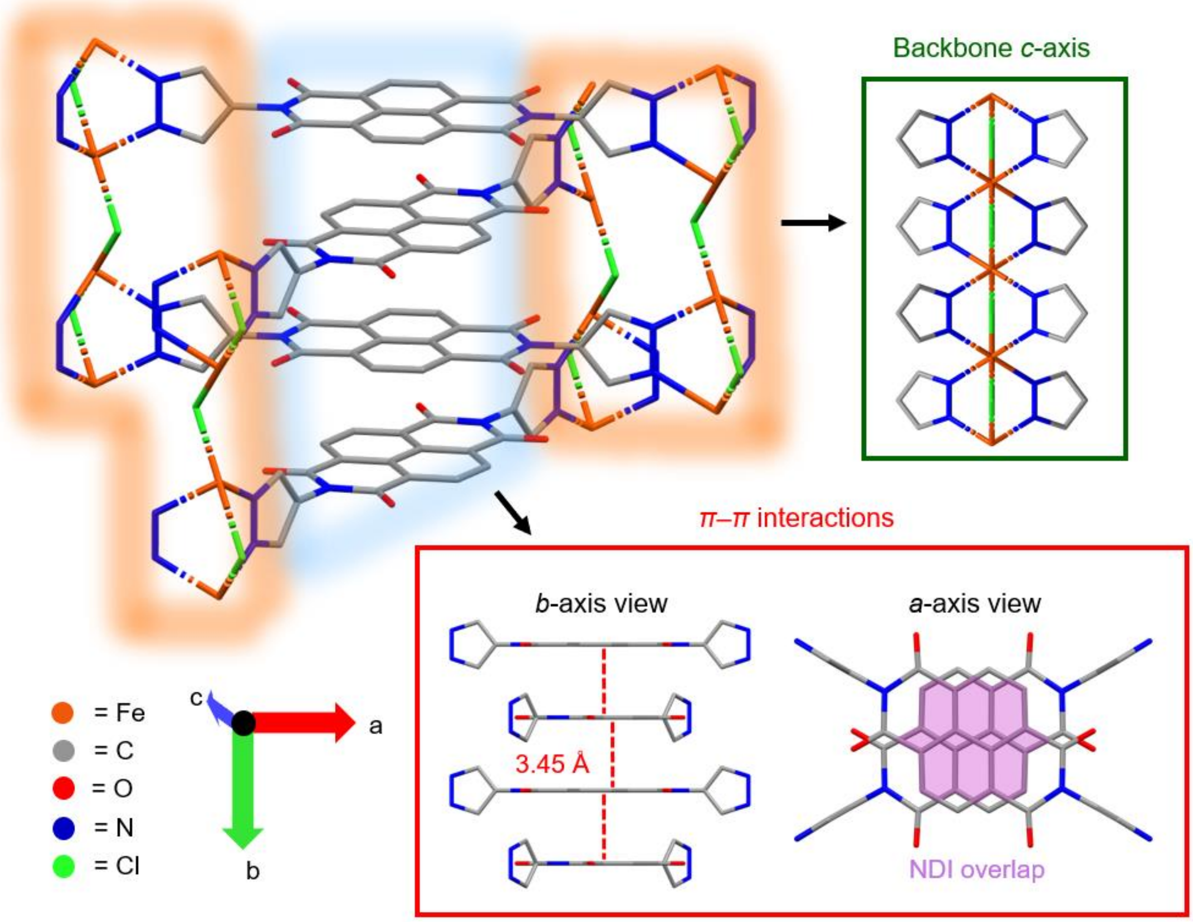

Figure 3.5. Single crystal packing of **Fe(Cl)NDI-1.**

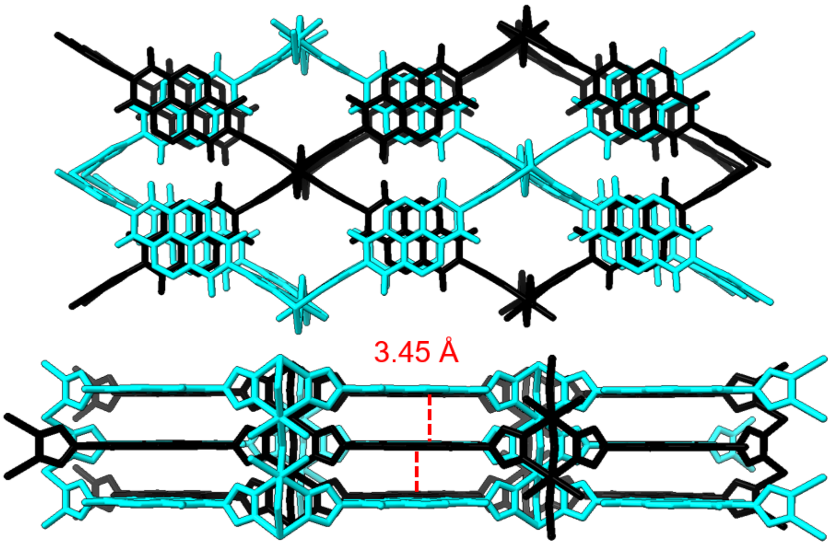

Figure 3.6. Interpenetrated superstructure of **Fe(Cl)NDI-1**, with highlighted (cyan, black) frameworks.

Taking into account the insoluble, paramagnetic and polymeric nature of **Fe(Cl)NDI-1**, physical characterisation methods i.e., elemental analysis (EA) and X-ray fluorescence (XRF), were pursued as an alternative to more commonly used characterisation techniques NMR and MS to confirm the purity of **Fe(Cl)NDI-1**. PXRD analysis was performed on as-synthesised **Fe(Cl)NDI-1** to enable a comparative assessment with a powder pattern simulated from single crystal data, aiming to identify any additional or absent peaks to determine the phase purity of the material (Figure 3.7). Peak-matching operations between the two sets of data determined no significant peaks were missing, and in addition, no peaks belonging to foreign crystalline material were present in the as-synthesised sample. However, PXRD provides no compositional information for **Fe(Cl)NDI-1**, causing the need for further characterisation studies to be carried out with EA and XRF.

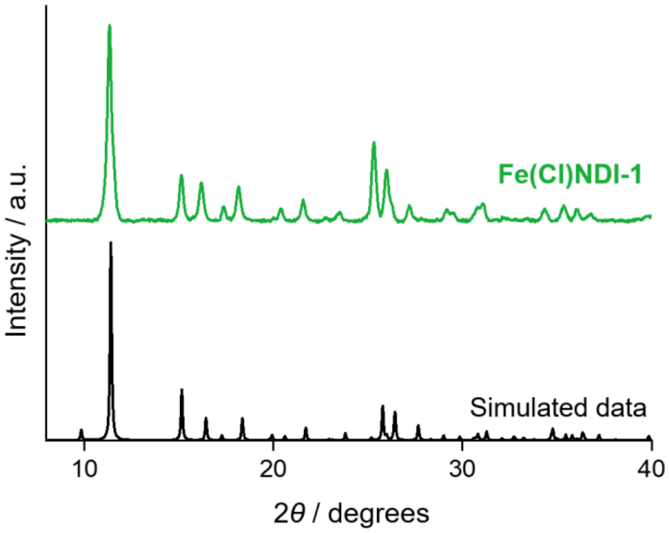

Figure 3.7. PXRD analysis of simulated and experimental data for **Fe(Cl)NDI-1**. Need to add peak matching table.

Characterisation using EA analysis gives an indication of the compositional purity of PCPs in conjunction with the molecular formular provided by SC-XRD data. However, solvent molecules or reaction by-products can become trapped within the pores of a PCPs, causing discrepancies between theoretical and experimental EA results. Therefore, PCP "activation" procedures (i.e., vacuum drying, solvent exchange, supercritical drying) are often used to remove unwanted materials from PCP pores, thereby "activating" the material for characterisation studies.[33]

Initial EA analysis (Table 3.1) demonstrated a strong agreement between theoretical ($C_{20}H_8ClFeN_6O_4$) and experimental values of detected C, H and N atoms. However, the detected Cl content of the as-synthesised sample of **Fe(Cl)NDI-1** (3.17 %) was lower than the expected, causing a re-visitation of post-synthetic activation protocols to explore the inconsistency. Using the same as-synthesised material as analysed initially, an additional activation step was carried out using solvent exchange with acetone every 6−12 h, over a period of 7 days, followed by heating in a vacuum oven at 200 °C. The addition activation procedure led to a satisfactory Cl EA value, suggesting that Cl was consistent throughout the framework of **Fe(Cl)NDI-1** before the solvent exchange activation procedure, but was unable to be detected by the elemental analyser. To corroborate the findings of the EA analysis, XRF was carried out to further investigate the purity of as-synthesised **Fe(Cl)NDI-1**.

Table 3.1. EA data for unwashed and washed samples of **Fe(Cl)NDI-1**

	C / %	H / %	N / %	Cl / %
As-synthesised	49.73	2.86	17.04	3.17
Activated	49.75	2.40	17.25	6.95
Theoretical	49.26	1.65	17.25	7.27

Given the elemental composition of **Fe(Cl)NDI-1** ($C_{20}H_8ClFeN_6O_4$), only the elements Fe and Cl were expected to emit fluorescent X-rays with sufficient energy for detection. Theoretically, the atomic ratio of Fe:Cl in the material should be 1:1, reflecting their stoichiometric proportion within the sample. To achieve a uniform layer of **Fe(Cl)NDI-1** material that could be oriented parallel to the detector for reliable XRF results, a suspension of **Fe(Cl)NDI-1** was prepared in MeOH and spin-coated onto a glass slide. XRF measurements with spin-coated samples confirmed the atomic ratio of Fe:Cl (Table 3.2), demonstrating the purity of **Fe(Cl)NDI-1** samples in conjunction with EA results. The full output of the XRF measurements consisted of three separate measurements at different points of the spin-coated sample, and can be found in the Appendix, section 7.11, Figure 7.29.

Table 3.2. XRF data for **Fe(Cl)NDI-1**, demonstrating the difference between no sample preparation and spin-coating.

	Fe / atom%	Cl / atom%
Spin-coated	47	53
Fe(Cl)NDI-1 theory	50	50

The crystal structure data of **Fe(Cl)NDI-1** displayed a low guest accessible volume of 187.8 Å^3 (9.9%) that was observed as a result of its interpenetrated structure, suggesting that diffusion through **Fe(Cl)NDI-1** would be difficult for large molecules. In the context of serving as an energy storage device, porosity enables the diffusion of ions, allowing for efficient ion transport and enabling redox processes throughout a PCP framework. Without accessible pores, redox sites that require the diffusion of ions can only occur on the surface, limiting the redox functionality. Accordingly, porosity measurements were carried out on activated samples that had been soaked in solvent for seven days, then subject to heating in a vacuum oven at 200 °C to remove solvent molecules from pores within the framework of **Fe(Cl)NDI-1**. The porosity measurements (liquid nitrogen, see Figure 3.8 for the data and the Appendix, section 7.1 for details on the method used) revealed a BET surface area of 2.8 m^2 g^{-1} with an identical absorption/desorption curve, demonstrating that any pores within **Fe(Cl)NDI-1** are inaccessible through this technique. Due to the crystal structure and porosity data, we can conclude that the diffusion of atoms such as Li$^+$ or Na$^+$ to internal redox sites of **Fe(Cl)NDI-1** were unlikely to occur, due to inaccessibility *via* pore openings. Nevertheless, external redox sites offered the potential to coordinate charge-balancing ions, in the absence of internal redox sites.

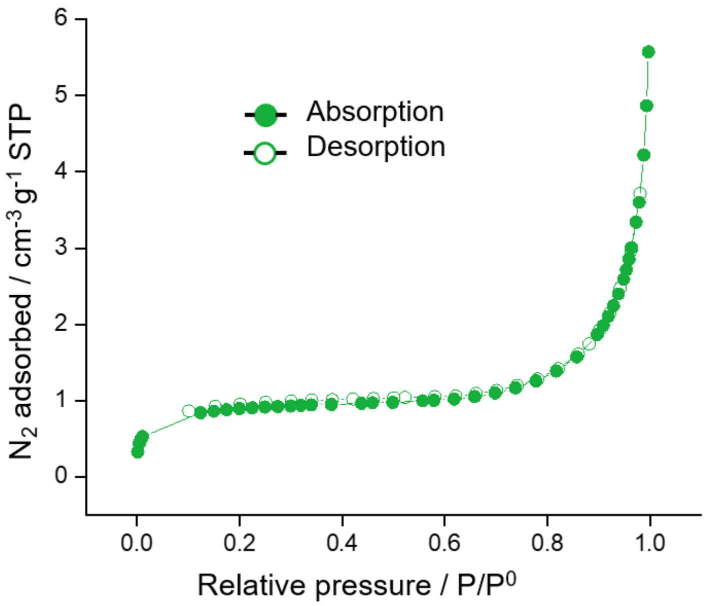

Figure 3.8. Porosity data for **Fe(Cl)NDI-1**. Almost identical absorption and desorption result in a BET surface area of 2.8 m^2 g^{-1}.

The phase purity of as-synthesised **Fe(Cl)NDI-1** was confirmed with PXRD, after a comparison was drawn between simulated and as-synthesised PXRD patterns. Successive analysis with EA and XRF techniques demonstrated the atomic purity of as-synthesised **Fe(Cl)NDI-1**. Finally, porosity measurements agreed with single crystal data, that **Fe(Cl)NDI-1** had very small pores, and was unlikely to hold solvent or impurities within its superstructure.

3.2.3 THERMAL AND CHEMICAL STABILITY OF Fe(Cl)NDI-1

The demonstrated stability of pyrazolate bonds in CPs has been shown to confer exceptional chemical and thermal stability to resulting frameworks.[19–22] Given that pyrazolate bonds serve as the backbone in the framework of **Fe(Cl)NDI-1**, it is reasonable to expect that **Fe(Cl)NDI-1** itself would exhibit similar attributes of thermal and chemical stability as reported by others.[19–22] Consequently, the potential inherent robustness of pyrazolate bonds in **Fe(Cl)NDI-1** would make it a promising candidate as a semiconductor in applications where such stability is favoured (i.e., conductive coatings, chemiresistors, sensing).

Accordingly, TGA was performed on **Fe(Cl)NDI-1** in air at a flow rate of 10 mL min^{-1} and a heating rate of 10 °C min^{-1}, revealing an initial decomposition temperature of 390 °C, beyond which the compound underwent continuous decomposition without any subsequent discernible events. Analysis of the residual mass% (Fe_2O_3, 18.8%) was in good agreement and within expected error of theoretical values (16.4%), after accounting for slight variations of mass% (~2%) at the beginning of the experiment. In addition, no mass loss was observed prior to the point of initial decomposition, confirming that no solvent molecules were present inside the framework of **Fe(Cl)NDI-1** at the time of analysis, corresponding with the crystal structure data that displayed the existence of small pores within the framework.

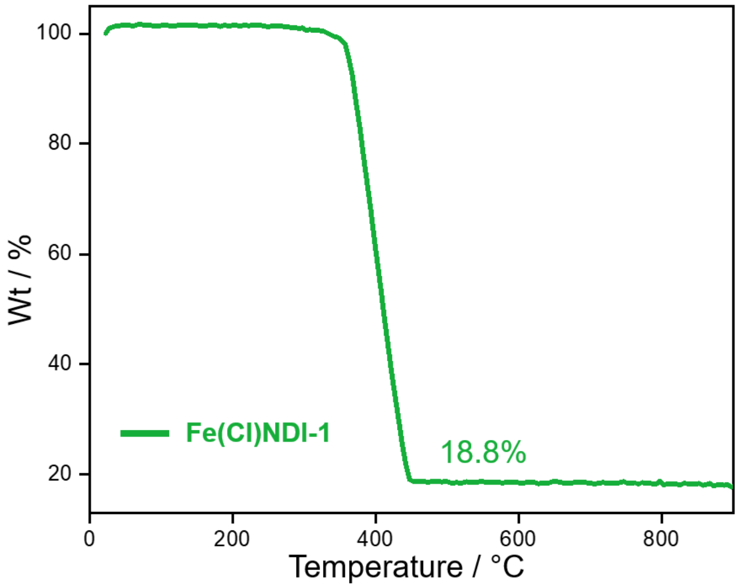

Figure 3.9. TGA data for **Fe(Cl)NDI-1** collected in air at a flow rate of 10 mL min^{-1} and a heating rate of 10 °C min^{-1}.

The high decomposition temperature exhibited by **Fe(Cl)NDI-1** (390 °C, air) ranked moderate-to-high in comparison to other M-pyrazolate materials (Table 3.3). In the case of frameworks with higher thermal stability **NiBTP** (430 °C, air) **ZnBTP** (510 °C, air)[19] both display M-pyrazolate bridged clusters with a high density of pyrazolate links, which could account for the higher thermal stability. On the other hand, lower thermal stability was observed in **Fe$_2$BDP$_3$** (280 °C, air) that featured a lower density of pyrazolate links (i.e., 1D chains). In comparison, **Fe(Cl)NDI-1** was interpenetrated, doubling the density of pyrazolate links in comparison to a single framework, and was likely the source of the moderate-to-high thermal stability. Overall, the effect of a pyrazolate backbone to promote increase thermal stability is underlined in the interpenetrated framework of **Fe(Cl)NDI-1**, and demonstrates its potential use as material for use in high temperature applications.

Table 3.3. A comparative analysis between several thermally stable PCPs that contain pyrazolate chains, and **Fe(Cl)NDI-1**.

	Decomposition point (°C)	Gas
Fe(Cl)NDI-1	390	Air
NiBTP[19]	430	Air
ZnBTP[19]	510	Air
Fe$_2$BDP$_3$[22]	280	Air

In addition to their effect on thermal stability, pyrazolate links have been proven to considerably enhance the chemical robustness of CP materials. Discussed previously, such pyrazolate materials have displayed extensive stability in addition to retention of porosity in heated acidic and basic aqueous media (Table 3.4). To evaluate the chemical stability of as-synthesised **Fe(Cl)NDI-1**, the material was suspended in acidic and basic aqueous media to uncover the material's chemical resistance for a period of 24 h whilst stirring at room temperature, after which PXRD patterns were obtained for the resulting materials to determine if any structural changes had occurred. In both 1 M HCl and 1 M NaOH solutions none of the peaks associated with the structure of **Fe(Cl)NDI-1** were able to be identified, leading to the conclusion that **Fe(Cl)NDI-1** decomposes in both 1 M aqueous solutions over a 24 h period. However, using formic acid, which has a higher pKa[34] (3.7) in comparison to the pKa of HCl[35] (1.8), the structural features of **Fe(Cl)NDI-1** as observed by PXRD remained largely intact. In addition to characterising the **Fe(Cl)NDI-1** peaks, new peaks were observed at 10.4, 11.9, 17.6 and 20.4 2θ confirming that a new crystalline material had formed, that were likely the results of decomposition. One possible path of decomposition could arise due to the lability of the Cl anion under both acidic and basic conditions. The potential dissociation of Cl anions from the framework of the Fe^{3+} metal centres could expose it to further attacks, ultimately leading to the breakdown of **Fe(Cl)NDI-1**. Based on the experimental results of the chemical stability tests, it is confirmed that **Fe(Cl)NDI-1** will exhibit lower chemical stability when exposed to both basic and acidic conditions after 24 hours. Therefore, any resulting devices such as sensors or batteries that could incorporate **Fe(Cl)NDI-1** and are regularly exposed to acidic or basic environments could see compromised performance, requiring care to be taken when selecting **Fe(Cl)NDI-1** for such tasks.

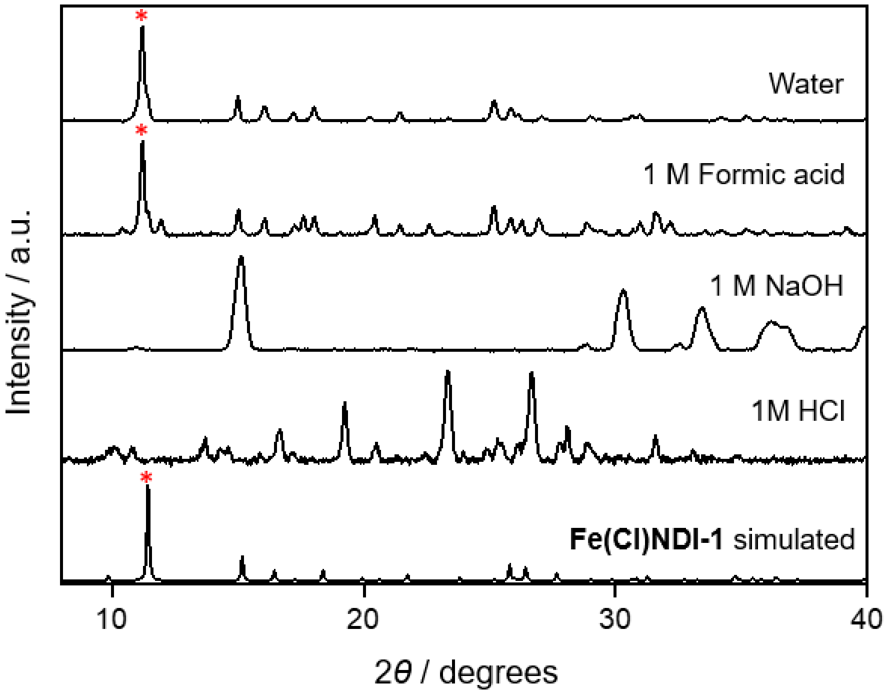

Figure 3.10. PXRD data for **Fe(Cl)NDI-1** after being subjected to stirring in aqueous acidic or basic media for 24 h. No decomposition is observed in water, some decomposition is observed in formic acid, total decomposition is observed in 1 M NaOH and 1 M HCl. The most intense peak of **Fe(Cl)NDI-1** has been highlighted with a red star for ease of identification.

Table 3.4. A comparative analysis between several chemically stable PCPs that contain pyrazolate chains, and **Fe(Cl)NDI-1**.

Material	Aqueous media used	Time	Temperature / °C	**Outcome**
Fe(Cl)NDI-1	1 M NaOH	1 day	25	Decomposed
Fe(Cl)NDI-1	1M HCl	1 day	25	Decomposed
Fe(Cl)NDI-1	1 M formic acid	1 day	25	Semi-decomposed
Fe(Cl)NDI-1	Water	14 day	25	Stable
NiBTP[19]	2 M NaOH	14 days	100	Stable
NiBTP[19]	2M HCl	14 days	100	Stable
$Zn_9O_2(OH)_2(L)_6$[21]	2 M NaOH	210 days	25	Stable
$Zn_9O_2(OH)_2(L)_6$[21]	2 M HCl	210 days	25	Stable

As previously observed, both the crystal structure and porosity data have indicated the presence of small pore sizes in **Fe(Cl)NDI-1**. However, it was crucial to investigate the electrochemical response of **Fe(Cl)NDI-1**, as the resulting properties would determine its viability for incorporation into an energy storage device, whether the redox processes occurred within or outside the framework. Redox processes had the potential to occur at either NDI **1** C=O sites (that were observed to undergo two reversible reductions in Chapter 2), or at the Fe metal centre. However, the insoluble nature of **Fe(Cl)NDI-1** necessitated the use of surface-confined cyclic voltammetry (SCCV) as the only viable option to determine the electrochemical response of **Fe(Cl)NDI-1**.

3.2.4 REDOX PROPERTIES AND BAND GAP OF Fe(Cl)NDI-1

In the context of CPs, SCCV has presented more challenges in comparison to its solution-state counterpart, requiring materials to be adhered to the surface of the working electrode before a corresponding voltammogram can be recorded. In order to determine an appropriate analytical method to determine the electrochemical response of **Fe(Cl)NDI-1**, several sample preparation methods were sought out. In the first instance, D'Alessandro and co-workers developed a SSCV method by forming a paste in each case with two insoluble PCPs, 1-Zn and 1-Cd, in minimal MeCN (10 mg mL^{-1}).[36] The working electrode (WE) was dipped into the MeCN/PCP paste, and was then analysed by submerging the WE into an electrolyte (1 mM [*n*-Bu_4N]PF_6 in MeCN) and performing scans at a rate of 100 mV s^{-1} and revealing the electrochemical responses of both materials. The method provided by D'Alessandro and co-workers was attempted for **Fe(Cl)NDI-1**, showing one sharp reductive peak at –1.35 V followed by two smaller oxidative peaks (–1.58 V, –1.18 V) with low intensities (Figure 3.11).

In addition to the lower observed intensities, the layer of **Fe(Cl)NDI-1** desorbed from the working electrode after the first cycle, causing successive measurements to be difficult to obtain. Therefore, alternative sample preparation methods to be explored.

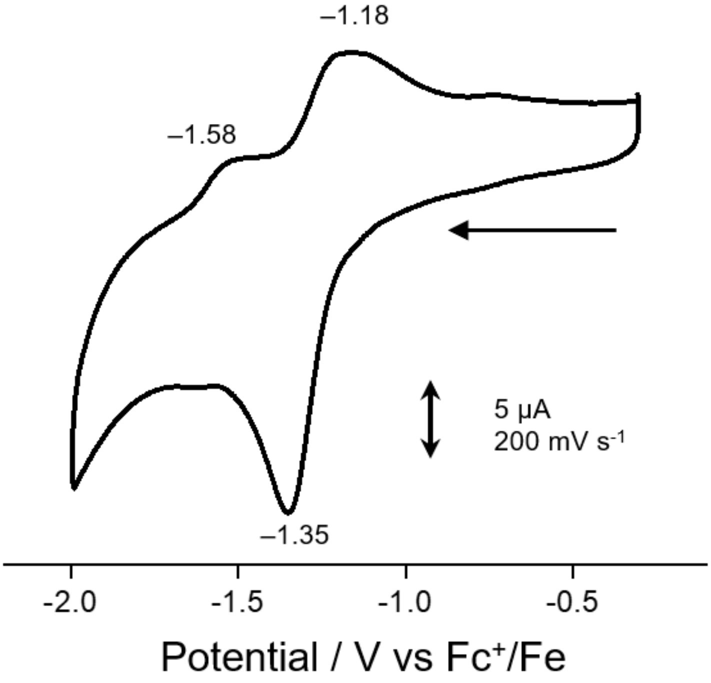

Figure 3.11. A cyclic voltammogram of **Fe(Cl)NDI-1** carried out by dipping the WE into a paste made from MeCN and **Fe(Cl)NDI-1**.

To obtain additional CV data and increase the adherence of the **Fe(Cl)NDI-1** thin films, an alternative sample preparation method developed by Dincă and co-workers for the previously discussed PCP **$Fe_2(BDT)_3$** was replicated.[31] Using a mixture of Nafion™ (5 wt%), carbon black (10 mg mL^{-1}) and **$Fe_2(BDT)_3$** (10 mg mL^{-1}) in MeCN, 2 x 5 μL of the suspension was drop-cast onto the surface of the WE and allowed to dry. The method provided by Dincă and co-workers was applied to **Fe(Cl)NDI-1**, producing a voltammogram with poorer peak resolution in comparison to the voltammogram obtained from the D'Alessandro method (Figure 3.12). The Dincă method using **Fe(Cl)NDI-1** was then repeated without carbon black (Figure 3.13), demonstrating similar peak resolution to what was observed in Figure 3.20. An additional experiment carried out without Nafion™ and carbon black was also trialled, demonstrating increased peak resolution (Figure 3.14).

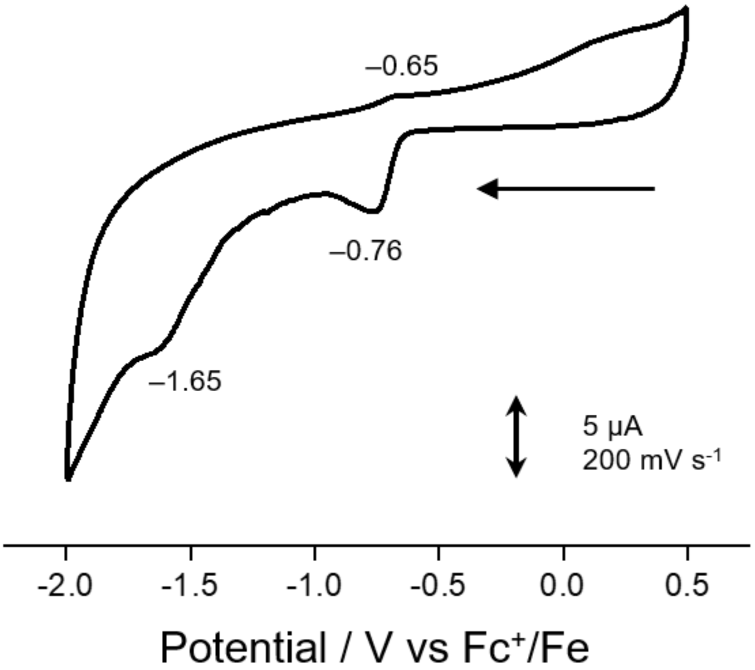

Figure 3.12. A cyclic voltammogram of **Fe(Cl)NDI-1** carried out by drop-casting the working electrode with a solution of MeCN containing carbon black, Nafion^{TM}, and **Fe(Cl)NDI-1**.

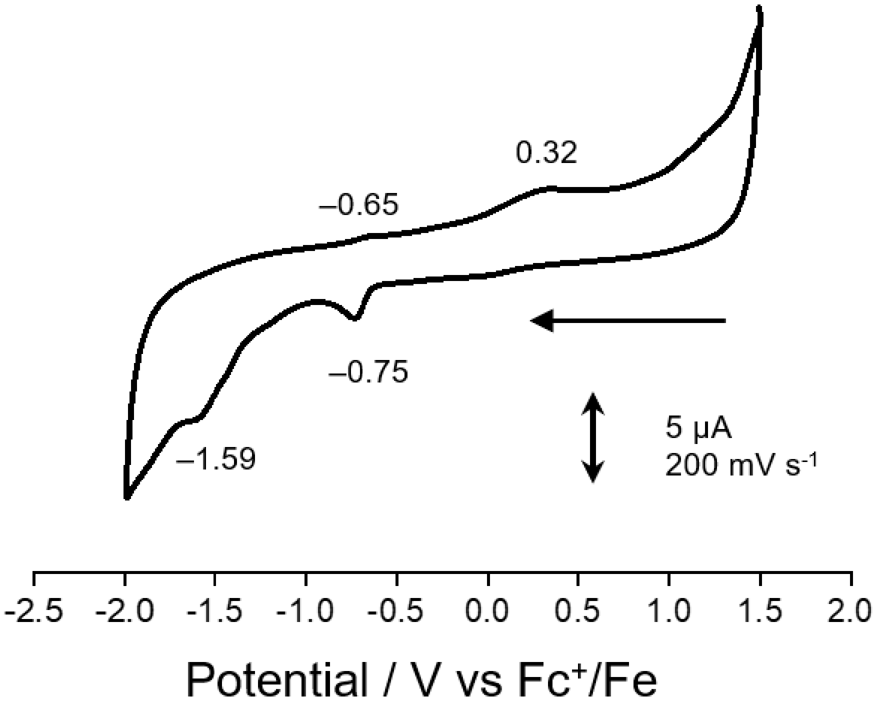

Figure 3.13. A cyclic voltammogram of **Fe(Cl)NDI-1** carried out by drop-casting the working electrode with a solution of MeCN containing, Nafion^{TM}, and **Fe(Cl)NDI-1**.

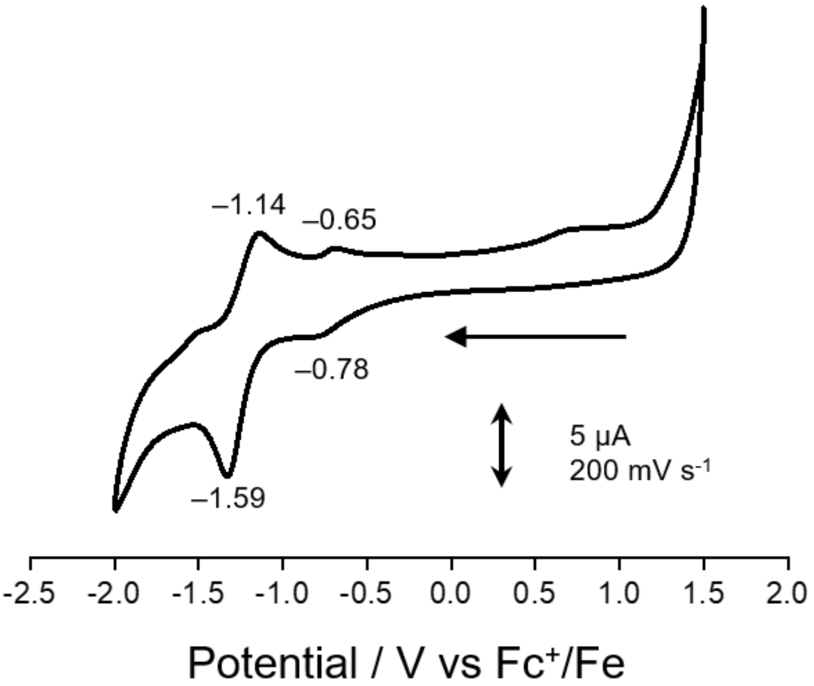

Figure 3.14. A cyclic voltammogram of **Fe(Cl)NDI-1** carried out by drop-casting the working electrode with a solution of MeCN containing, and **Fe(Cl)NDI-1**.

To further boost the resolution of peaks, the analyte solvent was changed to CH_2Cl_2, which evaporated more readily and allowed for faster, more dissociation-resistant films of **Fe(Cl)NDI-1**. Furthermore, the concentration of **Fe(Cl)NDI-1** was doubled from 10 mg mL^{-1} to 20 mg mL^{-1} to increase the amount of material on the WE. After drop-casting the analyte suspension (2×5 μL) on the WE, the resulting voltammograms showed two distinct reduction/oxidation peaks, indicating that two quasi-reversible one-electron redox processes occur (Figure 3.15). Comparative analysis between NDI **1** and **Fe(Cl)NDI-1** indicates similar matching between all oxidative and reduction peak potentials confirming that the electrochemical properties of NDI **1** are retained post-synthesis of **Fe(Cl)NDI-1**. Based on the confirmation of the redox properties of **Fe(Cl)NDI-1**, it can be inferred that redox processes could potentially take place on the surface of the CP superstructure due to the low porosity observed in the single crystal data.

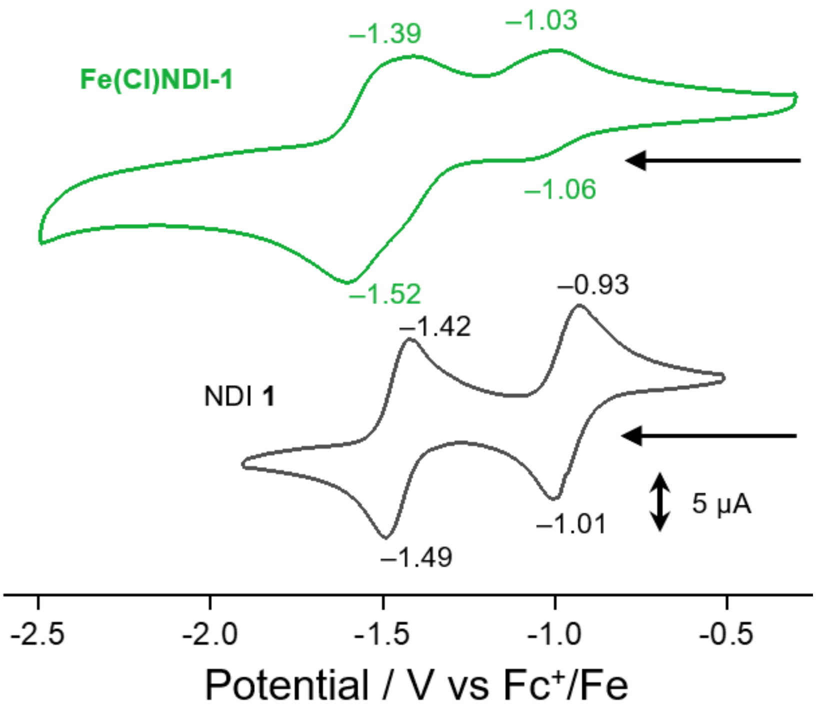

Figure 3.15. Cyclic voltammograms of NDI **1** (black) and **Fe(Cl)NDI-1** (green). The CV data for **Fe(Cl)NDI-1** was collected using SCCV by drop-casting a suspension of **Fe(Cl)NDI-1** in CH_2Cl_2 (20 mg mL^{-1}) onto the WE followed by submersion in a 1 mM solution of [*n*-Bu_4N]PF_6 in MeCN and analysis at 200 mV s^{-1}. The solution-state CV data for NDI **1** was collected in Chapter 2, where details can be found.

With the objective of reducing the Fe^{3+} centres of **Fe(Cl)NDI-1** to obtain a material with mixed-valency (Fe^{3+}/Fe^{2+}), various methods were explored, with the goal of enhancing the conductivity of **Fe(Cl)NDI-1** by several orders of magnitude. One procedure carried out by Yin and co-workers,[37] resulted in the generation of an air-stable reduced species Zr-PDI$^{\bullet-}$. Samples of pristine Zr-PDI were exposed to photoirradiation with blue light (455 nm) in the presence of gaseous Et_3N, that resulted in a significant colour change from red to black of both powders and thin films that were exposed. To explain this phenomenon, Yin and co-workers suggested that Et_3N became trapped within the cage-like pores within the framework of Zr-PDI, forming radical cations that stabilised the reduced species. In comparison with pristine Zr-PDI, the reduced species displayed a high photothermal conversion efficiency of 52.3%. In order to carry out the method employed by Yin and co-workers, **Fe(Cl)NDI-1** samples were mounted on a glass slide in the presence of gaseous Et_3N, and were exposed to a broad-spectrum blue light for 5, 10, 30, 60 min (see the Appendix, section 7.12, Figure 7.32). Post-irradiation, no change was observed to the characteristic red colour of **Fe(Cl)NDI-1**, despite exposure to progressively longer irradiation in comparison to the method set out by Yin and co-workers. The lack of colour change suggests that the reduction of Fe^{3+} centres was unsuccessful, likely due to the interpenetrated nature of **Fe(Cl)NDI-1** that prevented the coordination of the $Et_3N^{\bullet+}$ counterions. Upon discovering that Et_3N was unable to access Fe^{3+} metal centres of **Fe(Cl)NDI-1** and reduce them, methods were pursued to target alternative areas of **Fe(Cl)NDI-1**.

In the pursuit of identifying alternative areas on **Fe(Cl)NDI-1** to reduce and enhance its semiconductor properties, a study conducted by Wentz et al. was identified to have used tetrabutylammonium fluoride (TBAF) to reduce NDI ligands.[38] Notably, the synthesised Zn-NDI displayed large square-shaped pores, however, there was an absence of substantial π-orbital overlap between neighbouring NDI ligands, leading to restricted *through-space* charge transport within the material. Due to the limited availability of conductive pathways in Zn-NDI, the pristine material exhibited a pressed-pellet conductivity value of $<10^{-14}$ S cm^{-1}. After undergoing a chemical reduction in the presence of TBAF over the course of 24 h in DMF, a darkening of the Zn-NDI material was observed. Solid-state absorption measurements of the darker-coloured Zn-NDI revealed that new peaks (λ_{max} = 471, 607, 701, 784 nm) had formed that were indicative of NDI$^{\bullet-}$ radical anions, likely due to coordination with TBA$^+$ cations. Pressed pellet resistivity tests were carried out on the reduced material demonstrating a conductivity value between 2–6 x10^{-7} S cm^{-1}, showing an increase in conductivity of over 6 orders of magnitude in comparison to pristine material. The increase in conductivity can be explained by the switch between the two stable redox states of the Zn-NDI material, resulting in a new charge transport pathway that is formed when NDI orbitals are reduced in the presence of TBAF cations. In order to attempt the chemical reduction of **Fe(Cl)NDI-1**, the experimental procedure reported by Wentz et al. was replicated (see the Appendix, section 7.13). However, no visible colour change from the characteristic red colour of **Fe(Cl)NDI-1** was observed, despite several repeat attempts with increasing concentrations of TBAF. It was likely that the interpenetrated structure of **Fe(Cl)NDI-1** and resulting small pores prevented the coordination of stabilising cations inside the framework, preventing the internal structure of **Fe(Cl)NDI-1** from becoming a reduced species. Potentially, stabilising cations coordinated to available surface sites, yet there was no noticeable effect on the colour, leading to the conclusion that the employment of TBAF to reduce **Fe(Cl)NDI-1** was ineffective.

The attempts to reduce either Fe^{3+} metal centres or NDI units within **Fe(Cl)NDI-1** by generating mixed valency species *via* photoreduction with Et_3N, and chemical reduction of NDI ligands with TBAF, respectively, were unsuccessful. The interpenetrated framework of **Fe(Cl)NDI-1**, with its limited accessible spaces, presented challenges in achieving the coordination of counter anions. Despite the absence of a mixed valency or reduced ligand species, it was expected that **Fe(Cl)NDI-1** would exhibit above-average charge transport properties based on the *through-bond* and *through-space* pathways that were observable in the single crystal structural data. Therefore, a more fundamental study of the properties of **Fe(Cl)NDI-1** was undertaken, in order to estimate the semiconductor properties of the coordination framework.

$$F(R_\infty) = \frac{k}{s} = \frac{(1 - R_\infty)^2}{2R_\infty} \qquad (1)$$

To evaluate the charge transport properties of **Fe(Cl)NDI-1** as a single-valent species, the electronic characteristics of the material were initially assessed using diffuse reflectance spectroscopy measurements to determine its band gap. The reflectance data was transformed into the corresponding absorption spectra by applying the Kubelka−Munk (K−M) equation (Equation 1), where k is the absorption coefficient of the sample, s is the scattering coefficient, and R_∞ is the percentage of reflectance obtained in the diffuse reflectance data, where ∞ denotes a sufficient thickness to cover the supporting layer.[39] To then estimate the band gap energy, the Tauc method[40] was employed in which a straight line was fit to the region of steep linear increase of light absorbance and energy, denoting an estimate of the semiconducting properties of **Fe(Cl)NDI-1** (see Figure 3.16). The intersection point of the x-axis of the straight line provided an estimate of the band gap energy, which was revealed to be 1.91 eV. In comparison to other solid-state band gap measurements taken for other Fe-containing semiconducting PCP materials (i.e., **$Fe_2(BDT)_3$** =2.0 eV[31] and **$Fe_2(BDP)_3$** = 1.5 eV[22]), **Fe(Cl)NDI-1** is expected to display similar levels of semiconductive behaviour, which are discussed in the following section.

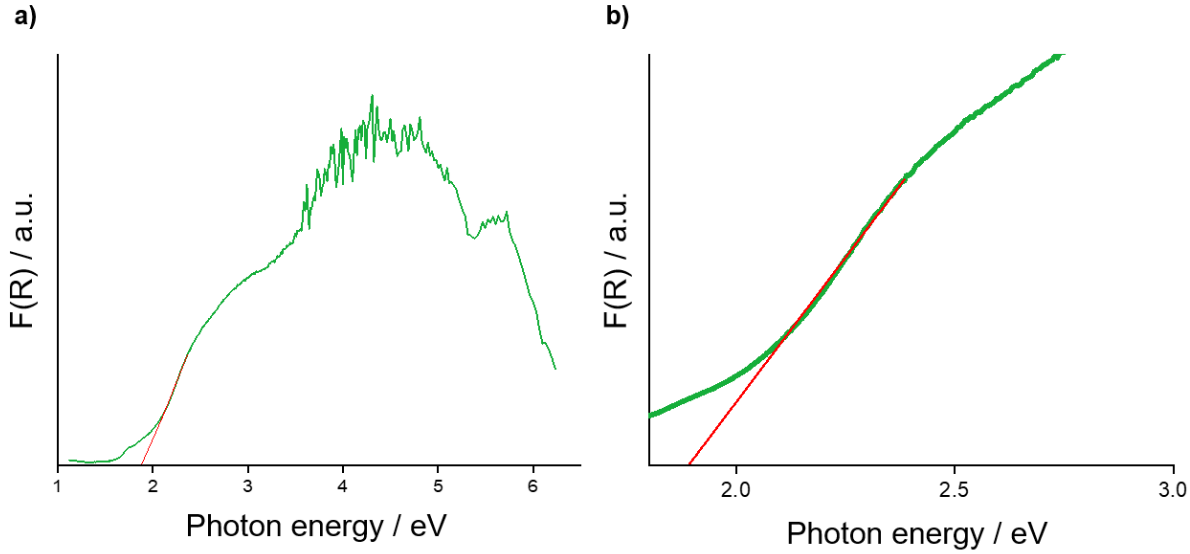

Figure 3.16. (a) The K−M transformed reflectance data **Fe(Cl)NDI-1**, (b) the onset of absorption fit with a straight line, indicating a band gap of 1.91 eV.

3.2.5 CONDUCTIVITY OF Fe(Cl)NDI-1

After determining the solid-state band gap of **Fe(Cl)NDI-1** to be in the same region as other semiconducting PCPs, conductivity analysis was pursued to quantify charge-transport properties. Employing the two-probe pellet press that was introduced in Chapter 2, resistivity measurements of **Fe(Cl)NDI-1** were taken, which after data processing, revealed a conductivity value of

2.84x10^{-5} S cm^{-1} (see Table 3.5 and 3.6). To ensure that the crystal structure of **Fe(Cl)NDI-1** was maintained throughout the resistivity process, PXRD measurements were taken at each stage of the sample preparation and resistivity process (Figure 3.19). Following the working hypothesis that the structure of **Fe(Cl)NDI-1** allowed for charge to flow *via* overlapped (Fe–N–N–)$_\infty$ orbitals (*through-bond*) and/or close spatially overlapped π-orbitals (*through-space*), previously conducted research was interrogated for materials with similar characteristics to **Fe(Cl)NDI-1** to draw appropriate comparisons (see Table 3.5 for details).

Reported on in Chapter 1, Yamashita and co-workers[41] coordinated NDI molecules end-substituted with pyridine to Cd metal centres, successfully achieving close (3.18 Å) co-facial overlap between NDI π-surfaces in their PCP **PCM-1** (Figure 3.17a). Despite twisting away from an eclipsed arrangement of NDI π-surfaces (60 °), a high conductivity was achieved *via* single crystal conductivity measurements (3.3x10^{-3} S cm^{-1}) that were attributed to the *through-space* charge transport pathway. In comparison to the conductivity of **Fe(Cl)NDI-1**, **PCM-1** displays a value that is two orders of magnitude higher, that is likely due to the combined effect of the shorter π–π distance between NDI surfaces, and the generally higher conductivity measurements obtained from single crystals. In another study, Kuang et al.,[42] synthesised a cage-like framework called **Cu^{I}NDI** that consisted of end-substituted NDI linkers that were connected and supported by Cu^{I} metal centres that was grown by diffusion of the NDI linkers into a solution of Cu(CH$_3$CN)$_4$PF$_6$ (Figure 3.17b). The resulting rod-like crystals displayed π–π distances of 3.44 Å between slip-stacked NDI units, a narrow band gap of 1.2 eV and a conductivity of 1.2x10^{-5} S cm^{-1}. Despite the single crystal measurement, which often show conductivity measurements several orders of magnitude higher than that of a pressed pellet measurement,[5] **Cu^{I}NDI** displayed relatively low conductivity, most likely due to the slip-stacked spatial arrangement of NDI aromatic surfaces.

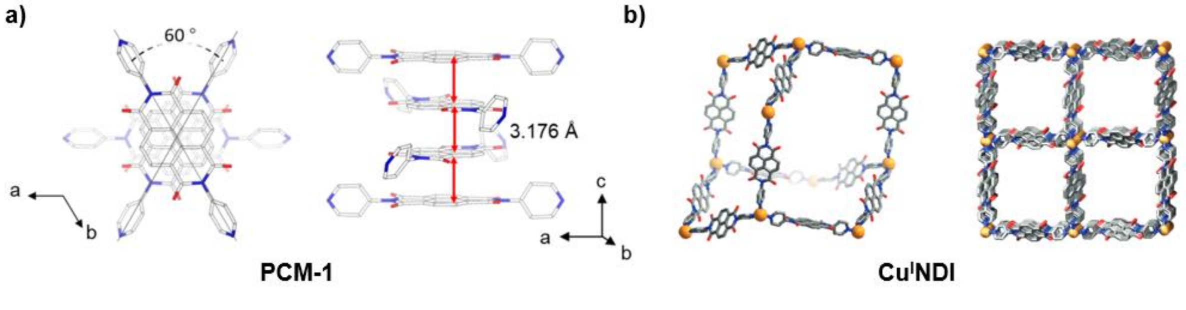

Figure 3.17. Structures of (a) **PCM-1**, copied from the work of Yamashita and co-workers[41] and (b) **Cu^{I}NDI**, copied from the work of Kuang et al.[42]

More recently, *through-space* charge transport was reported from a trio of M-pyNDI (M = Co, Zn, Ni) PCPs that utilised NDI **1** as a ligand and featured different π–π distances between NDI units.[43] The M-pyNDI materials display a topology very similar to that of **Fe(Cl)NDI-1** see Figure 3.14, allowing clear comparisons to be drawn between the two materials once conductivity analysis had been carried out. The smallest node size was observed in **Co-pyNDI**, resulting in the shortest π–π length (3.24 Å) between spatially overlapped π-surfaces, leading to the highest conductivity (8.79 x10^{-8} S cm^{-1}) among the three PCPs (see Table 3.5 for details). Despite **Co-pyNDI** displaying a shorter π–π distance (3.24 Å) in comparison to **Fe(Cl)NDI-1** (3.45 Å), the difference in recorded conductivity was three orders of magnitude in favour of **Fe(Cl)NDI-1**. Conventional wisdom dictates that the closer the π–π distance, the higher the value of the conductivity measurement when very similar topologies and π-orbital overlap between NDI π-surfaces are shown. However, despite **Co-pyNDI** having a shorter π–π distance, the conductivity of **Fe(Cl)NDI-1** was found to be superior. Therefore, another factor such as an additional charge transport pathway within **Fe(Cl)NDI-1** (i.e., *through-bond*, (Fe−N−N−)$_\infty$) could have influenced the superior conductivity value obtained for **Fe(Cl)NDI-1**. Furthermore, the specific details regarding the pressed pellet conductivity technique used to analyse **Co-pyNDI** were not released in the published texts, preventing a comparative analysis between techniques to be drawn. Nonetheless, based on the available evidence, it can conclude that there must exist another active charge transport pathway that contributes to the overall conductivity value obtained for **Fe(Cl)NDI-1**. The crystallographic evidence strongly suggests that the Fe−pyrazolate backbone, which forms the structural support in **Fe(Cl)NDI-1**, is the only candidate that can be attributed to the additional charge transport. However, further investigation and probing are necessary to precisely determine the extent and contribution of the Fe−pyrazolate backbone to the overall conductivity value exhibited by **Fe(Cl)NDI-1**.

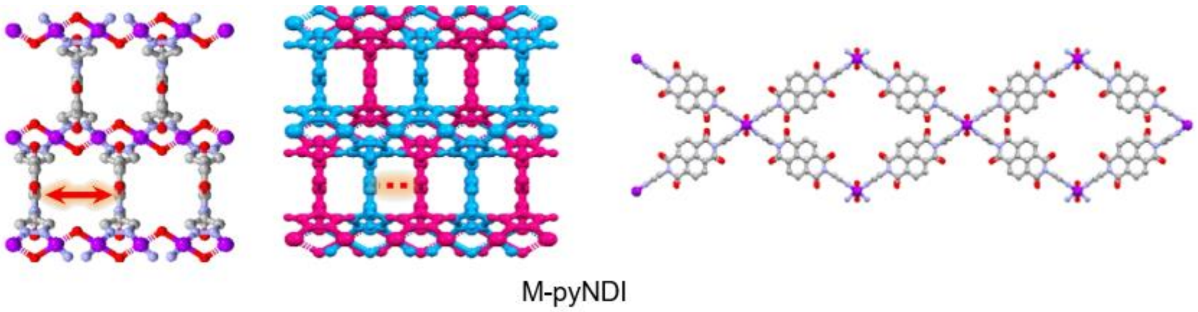

Figure 3.18. The isoreticular framework of the M-pyNDI (M = Co, Zn, Ni) PCPs, both images were copied from the work of Xue et al.[43]

Table 3.5. Important parameters and conductivity measurements of **Fe(Cl)NDI-1** and a range of PCPs with *through-space* conductive pathways.

	π–π distance (Å)	Measurement type	Conductivity (S cm^{-1})
Fe(Cl)NDI-1	3.45	Two-point probe pellet	2.84×10^{-5}
PCM-1	3.18	Two-point single crystal	3.3×10^{-3}
Cu^{I}NDI	3.44	Two-point single crystal	1.2×10^{-5}
Co-pyNDI	3.24	Two-point probe pellet	8.79×10^{-8}
Ni-pyNDI	3.37	Two-point probe pellet	6.03×10^{-8}
Zn-pyNDI	3.50	Two-point probe pellet	8.48×10^{-11}

To establish a meaningful comparison and gain a fundamental understanding of *through-bond* charge transport pathways in similar CPs incorporating NDI ligands and Fe–pyrazolate linkers, two examples of such materials were selected for comparison and contrast with **Fe(Cl)NDI-1** (see Table 3.6 for details). The PCP Fe(tri)$_2$ was discussed in Chapter 1,[32] exhibiting a framework with Fe^{2+} metal centres that were bridged by 1,2,3-triazole linkers to form a diamondoid-type structure. The pristine framework, Fe(tri)$_2$, displayed a low conductivity of $7\text{x}10^{-9}$ S cm^{-1}, but upon oxidation of the Fe^{2+} metal centres with thianthenium tetrafluoroborate, a mixed valency (Fe^{3+}/Fe^{2+}) species was obtained that displayed a conductivity that was 6 orders of magnitude higher (0.3 S cm^{-1}) than the pristine species. In comparison with **Fe(Cl)NDI-1** that displayed separation of 3.45 Å between Fe^{3+} metal centres, the Fe^{2+} metal centres of Fe(tri)$_2$ are separated by larger distances (5.89 Å), leading to the lower observed conductivities in the pristine material. Another conductive PCP displaying *through-bond* conductivity that was also featured in Chapter 1 was Fe$_2$(BDT)$_3$,[31] and displayed (Fe–N–N–)$_\infty$ charge transport pathways within its structure. The conductivity measurements of pristine Fe$_2$(BDT)$_3$ were carried out on single crystals, displaying a conductivity of $6\text{x}10^{-5}$ S cm^{-1}. Upon exposing Fe$_2$(BDT)$_3$ to air over a period of 12 days, some of the Fe^{2+} metal centres were oxidised to Fe^{3+}, resulting in a mixed valency species. Conductivity tests performed on the mixed valency species revealed a significantly enhanced value, that was five orders of magnitude higher (1.2 S cm^{-1}). In comparison to **Fe(Cl)NDI-1** that also displayed a (Fe–N–N–)$_\infty$ *through-bond* charge transport pathway and was analysed *via* a pressed pellet, the conductivity values for pristine Fe$_2$(BDT)$_3$ are very similar, despite the difference in conductivity measurement technique (i.e., single crystal).

Table 3.6. Parameters and conductivity measurements of **Fe(Cl)NDI-1** and a range of PCPs with *through-bond* conductive pathways.

	Oxidation state	Measurement type	Conductivity (S cm^{-1})
Fe(Cl)NDI-1	Fe^{3+}	Two-point probe pellet	2.84×10^{-5}
Fe(tri)$_2$	Fe^{2+}	Two-point probe pellet	7×10^{-9}
Fe(tri)$_2$(BF$_4$)$_x$	Fe^{2+}/Fe^{3+}	Two-point probe pellet	0.3
Fe$_2$(BDT)$_3$	Fe^{2+}	Two-point probe single crystal	6×10^{-5}
Fe$_2$(BDT)$_3$	Fe^{2+}/Fe^{3+}	Two-point probe single crystal	1.2

Considering the similarities of the two *through-bond* pathways observed in Fe$_2$(BDT)$_3$ and **Fe(Cl)NDI-1**, the former would be expected to possess a higher conductivity value due to the reduced disorder associated with single crystals (+ ~10^2–10^3 S cm^{-1})^5. However, the inverse is observed, after **Fe(Cl)NDI-1** was found to display a superior conductivity measurement in comparison to pristine Fe$_2$(BDT)$_3$ that closely matches the observed *through-bond* pathway in **Fe(Cl)NDI-1**. The observation that both Fe$_2$(BDT)$_3$ and Fe(tri)$_2$ systems are inferior semiconductors lead to the most likely explanation that there are two active charge transport pathways within **Fe(Cl)NDI-1**.

In summary, the conductive properties of both *through-bond* and *through-space* PCP materials have been compared to those of **Fe(Cl)NDI-1**. It was shown that **Fe(Cl)NDI-1** possesses two active charge transport pathways within its structure: (i) through-space *via* overlapped NDI π-surfaces and (ii) through-bond via mechanically bonded (Fe−N−N−)∞ pathways. However, neither pathway was deemed significant enough to fully account for the observed conductivity value. Nevertheless, a conclusive determination of the participation of each charge transport pathway was considered unattainable without the synthesis of additional materials or computational studies.

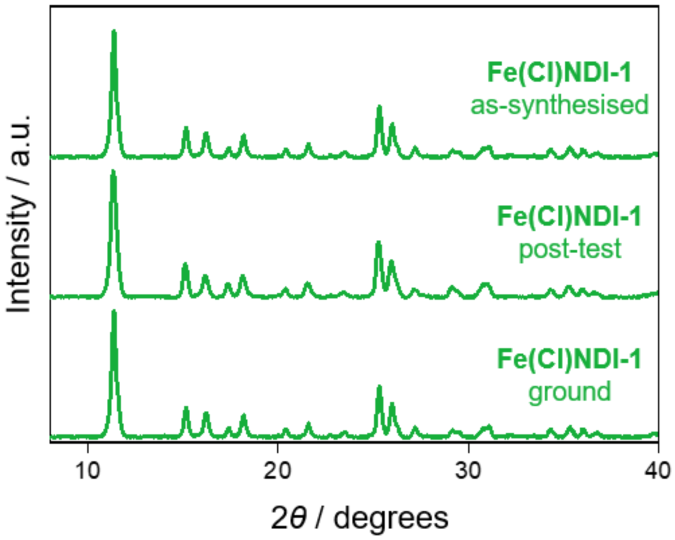

Figure 3.19. PXRD patterns demonstrating that the single crystal packing of **Fe(Cl)NDI-1** is maintained throughout the resistivity process.

3.2.6 COMPUTATIONAL STUDIES

Computational studies aimed to elucidate the location of the HOMO and LUMO in **Fe(Cl)NDI-1**, allowing conclusions to be drawn regarding the active charge transport pathway(s) in the system. The HOMO−LUMO calculations were carried out using the hybrid DFT within CP2K, using the density matrix method ADMM (full details can be found in experimental details, section 3.3). A fundamental understanding of the charge transport in the system is vital, allowing a deeper understanding the properties of **Fe(Cl)NDI-1**, facilitating the tailoring of future materials towards enhancing such charge transport pathways, ultimately increasing the semiconducting performance.

Based on the computational analysis, it was revealed that the frontier molecular orbitals within the **Fe(Cl)NDI-1** framework are spatially distributed across distinct regions (Figure 3.20). Specifically, the HOMO was identified to reside exclusively on the pyrazolate backbone and the bridging anion, suggesting the feasibility of hole transport through these orbitals. It is probable that the HOMO orbitals residing on the pyrazolate backbone and the bridging anion imply a *through-bond* pathway, facilitating hole transport. In contrast, the LUMO was located on the aromatic NDI units, exhibiting orbital overlap between each layer. The presence of the LUMO on and between the layers of overlapping NDI units strongly suggests the existence of a *through-space* pathway, enabling the transfer of electrons between electron-deficient orbitals. In addition to orbital depictions, a HOMO−LUMO band gap was obtained (2.46 eV), which when compared with the experimental band gap (1.91 eV) was in fair agreement compared to other conductive PCP materials.[44] Consequently, the frontier molecular orbital calculations display compelling evidence that the high conductivity observed in **Fe(Cl)NDI-**1 is the product of two charge transport pathways existing within one framework.

Further computational simulations were employed to model charge trapping phenomena within **Fe(Cl)NDI-1** to investigate the potential formation of polarons, that were carried out by generating a radial distortion around Fe sites, encouraging excess electrons to localise at Fe (full details can be found in experimental details, section 3.3). A polaron is a quasiparticle that arises due to an excess charge carrier that then becomes localised in a specific region and displaces surrounding ions.[45] The results of the polaron simulations reveal that, influenced by the presence of the Cl anion, polarons form, resulting in the trapping of electrons to generate Fe^{2+} metal centres. These polaron calculations offer a possible explanation for the higher conductivity values observed in **Fe(Cl)NDI-1**, as they suggest that the formation of Fe^{2+} metal centres contribute to the establishment of a mixed-valency framework (Fe^{2+}/Fe^{3+}).[46]

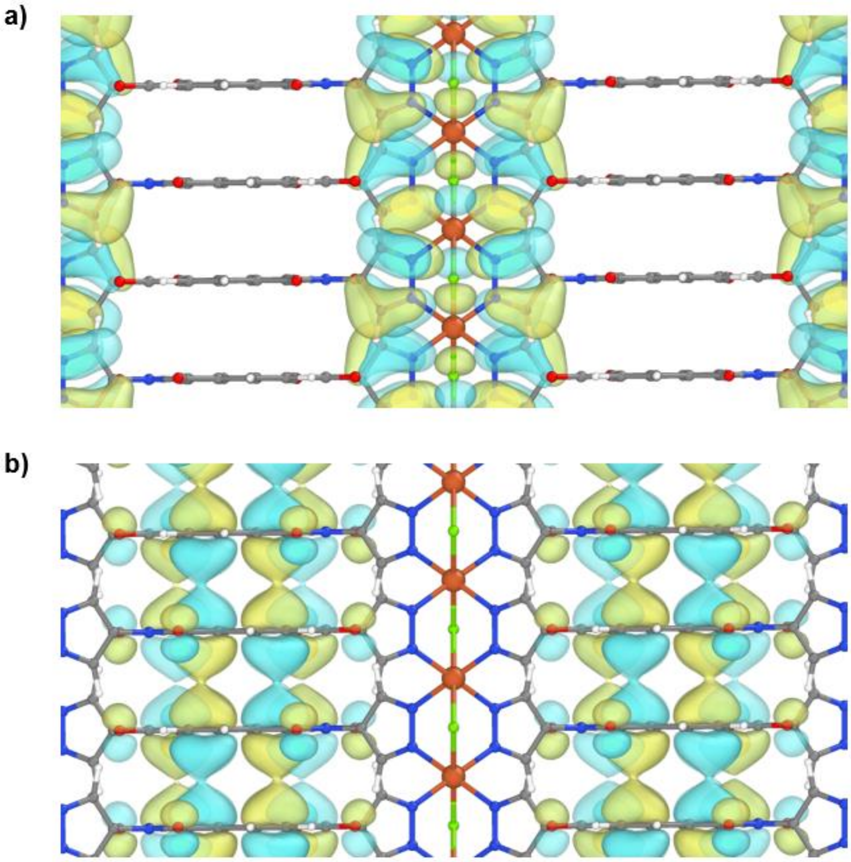

Figure 3.20. The calculated frontier molecular orbitals for **Fe(Cl)NDI-1**, a) the HOMO, which occurs on the pyrazolate backbone b) and the LUMO, which occurs on and in-between the NDI ligands. The atoms are represented by different colours: Red = Fe, blue = nitrogen, green = chlorine, grey = carbon, white = hydrogen.

The computational investigations conducted on **Fe(Cl)NDI-1** have yielded significant insights: (i) they have confirmed the presence of two charge transport pathways within the framework, (ii) provided a computational band gap consistent with experimental data, and (iii) demonstrated the potential formation of polarons influenced by the Cl anion. Consequently, these collective computational findings offer a comprehensive explanation for the observed high experimental conductivity measurements. Furthermore, the deeper understanding of **Fe(Cl)NDI-1** provided by computational calculations highlights the potential for further exploration into electroactive materials with similar supramolecular scaffolds and elements.

3.3 CONCLUSIONS

The objective of this study was to synthesise a conductive PCP with chemical and thermal stability, as well as high semiconductor properties, for use in energy storage applications. By combining NDI **1**, which contains open redox sites and low-lying LUMO orbitals, with readily available $FeCl_3$,

Fe(Cl)NDI-1 was generated. The framework featured connections between octahedrally coordinated Fe^{3+} metal centres and both Cl anions and NDI **1** pyrazole end groups, forming a pyrazolate backbone that supported the structure and potentially acted as a *through-bond* charge transport pathway. Another structural motif included electronically desirable spatial overlap with close π–π distances between NDI π-surfaces, resulting from the interpenetrated nature of the framework, potentially acting as a *through-space* charge transport pathway.

The material was confirmed to be pure and was found to have a low accessible surface area through experimental porosity measurements, limiting its suitability as an energy storage material. Additionally, **Fe(Cl)NDI-1** exhibited low stability in 1M HCl and 1M NaOH, although some resistance was observed in 1M formic acid. Diffuse reflectance data measurements of **Fe(Cl)NDI-1** then revealed an estimated band gap of 1.91 eV, suggesting that it would display similar semiconducting properties with other Fe–pyrazolate materials. Pressed pellet conductivity tests revealed a conductivity measurement of 2.84×10^{-5} S cm^{-1}, indicating the excellent charge transport properties of **Fe(Cl)NDI-1**.

Based on single crystal data, *through-space* and *through-bond* charge transport were both found to be possible within **Fe(Cl)NDI-1**. However, neither pathway alone explained the high conductivity measurement observed. Computational studies revealed the presence of two active charge transport pathways and a low band gap (2.46 eV) that agreed with experimental data, supporting the excellent charge transport properties observed experimentally. Furthermore, polaron simulations indicated the propensity for charge trapping that originated from the bridging Cl anion that resulted in the formation of Fe^{2+} metal centres, further substantiating the observed experimental conductivity measurement.

The coordination framework **Fe(Cl)NDI-1** exhibits remarkable semiconductive properties and redox activity through its NDI linkers. Although it possesses lower porosity, the outstanding conductive properties and redox capabilities make it a promising candidate for further exploration in energy storage applications. Future work will focus on expanding the family of Fe–pyrazolate materials by using **Fe(Cl)NDI-1** as a starting point to obtain additional isostructural materials with enhanced semiconductive properties to explore the potential properties of this material.

3.4 EXPERIMENTAL DETAILS

General details on materials and research methods as well as additional data for this Chapter can be found in the Appendix.

3.4.1 ELECTROCHEMICAL ANALYSIS

Surface-confined CV experiments were recorded at room temperature (25 ºC) using a layer of material that was adhered to the WE by (i) dipping into a paste (10 mg mL^{-1} in MeCN), (ii) drop-casting a mixture of Nafion™ (5% wt%), carbon black (10 mg mL^{-1}) and **Fe(Cl)NDI-1** (10 mg mL^{-1}) in MeCN, (iii) drop-casting a mixture of Nafion™ (10 mg mL^{-1}) and **Fe(Cl)NDI-1** (10 mg mL^{-1}) in MeCN, (iv) drop-casting a suspension of **Fe(Cl)NDI-1** (10 mg mL^{-1}) in MeCN, (v) drop-casting a suspension of **Fe(Cl)NDI-1** (20 mg mL^{-1}) in CH_2Cl_2. The drop-cast material was measured in Ar-purged electrolyte (0.1 M $TBAPF_6$ (recrystallised from hot EtOH)) in anhydrous acetonitrile using a Gamry Reference 3000 potentiostat/galvanostat/ZRA instrument interfaced to a PC. All surface-confined electrochemical experiments were performed using a glassy carbon working electrode (0.071 cm^2) that was polished routinely with 0.05-μm alumina–water slurry on a felt surface immediately before each use. The Pt wire counter electrode was flame-treated to remove any oxidised impurities from the electrode surface prior to each use. The Ag/AgCl (sat. KCl) reference electrode was stored in a 3 M KCl solution and rinsed with acetone followed by the analyte solvent to remove trace water prior to experiments. Voltammograms were referenced against the ferrocene/ferrocenium (Fc/Fc^+) redox couple as an external standard measured before and after sample measurements.

3.4.2 X-RAY ANALYSIS

Single crystal X-ray diffraction (SC-XRD) data were collected at Diamond Light Source using a Newport 4-circle diffractometer using a synchrotron radiation source and a Dectris Pilatus 300K detector.

3.4.3 MICROSCOPY

A FEI Helios dual beam scanning electron microscope at the GJ Russell microscopy facility, Durham University was used to obtain particle size and morphology of **Fe(Cl)NDI-1** (9.0 kV using an SE detector). To prepare samples for electron microscopy characterisation, the material was suspended in absolute EtOH and dispersed *via* sonication. A drop of the dispersion was then placed on to a silicon wafer and allowed to air dry. A Cressington scientific sputter coater equipped with an Au/Pd target and MTM-10 thickness monitor was then used to coat the sample with a thin conductive layer (10 nm), before SEM images were taken at the specified magnification.

3.4.3 COMPUTATIONAL ANALYSIS

All first-principles calculations were carried out using the implementation of hybrid DFT within CP2K.[47] We employ an implementation of the B3LYP hybrid DFT functional where long-range HF exchange integrals are truncated,[48,49] where a truncation radius of 6 Å is found to be well converged with regards to lattice parameters and band gaps.

The computational cost of hybrid calculations is reduced by the auxiliary density matrix method (ADMM)[50] in which exchange integrals are approximated through mapping onto smaller, more localised basis sets. We use double-ζ basis sets optimised from molecular calculations (MOLOPT)[51] and Goedecker–Teter–Hutter pseudopotentials available within CP2K.[52–54] Five multigrids were applied with a relative cutoff of 60 Ry and the finest grid having a cutoff of 600 Ry. As CP2K only samples the Γ-point, properties were converged with respect to supercell size as opposed to k-point sampling in reciprocal space. We use a $1 \times 2 \times 2$ supercell of the standardised primitive cell.

In order to look for polaron geometries, we make a radial distortion around Fe sites by pushing neighbouring ions away 0.2 Å, encouraging an excess electron added to the system to localise on a specified site. If the charge delocalises during geometry optimisation then the polaron is deemed to not be stable. A similar approach was has been taking in previous studies of polarons.[55,56]

3.4.4 SYNTHETIC DETAILS

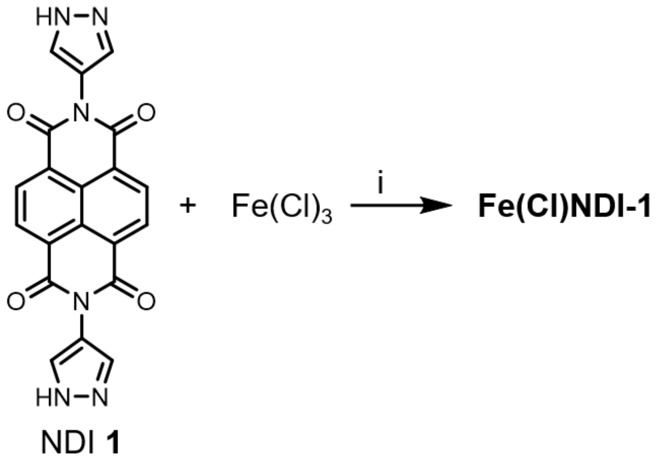

Figure 3.21. Reagents and conditions: (i) DMF, µW: 200 °C, 15 min, 81%.

[Fe(Cl)NDI-1]. A 35 mL microwave vial was equipped with a magnetic stirrer bar and charged with NDI **1** (200 mg, 0.5 mmol, 1.0 equiv.), $FeCl_3 \cdot 6H_2O$ (203.5 mg, 1.0 mmol, 2.0 equiv.) and anhydrous

DMF (12 mL). The mixture was subjected to dynamic microwave irradiation (200 °C, 300 W) under high stirring for 15 min. Upon cooling to rt, the reaction mixture was filtered and washed over the filter with DMSO until the washings appeared colourless, followed by absolute EtOH. The solids were then soaked in acetone for 1 week and then dried at 180 °C for 12 h in a vacuum oven (5 mbar) to yield activated **Fe(Cl)NDI-1** (199.1 mg, 0.41 mmol, 81%) as a red solid.

3.5 REFERENCES

(1) Furukawa, H.; Cordova, K. E.; O'Keeffe, M.; Yaghi, O. M. The Chemistry and Applications of Metal-Organic Frameworks. *Science* **2013**, *341*, 1230444. https://doi.org/10.1126/science.1230444.

(2) Li, J.-R.; Kuppler, R. J.; Zhou, H.-C. Selective Gas Adsorption and Separation in Metal–Organic Frameworks. *Chem. Soc. Rev.* **2009**, *38*, 1477. https://doi.org/10.1039/b802426j.

(3) Lee, J.; Farha, O. K.; Roberts, J.; Scheidt, K. A.; Nguyen, S. T.; Hupp, J. T. Metal–Organic Framework Materials as Catalysts. *Chem. Soc. Rev.* **2009**, *38*, 1450. https://doi.org/10.1039/b807080f.

(4) Murray, L. J.; Dincă, M.; Long, J. R. Hydrogen Storage in Metal–Organic Frameworks. *Chem. Soc. Rev.* **2009**, *38*, 1294. https://doi.org/10.1039/b802256a.

(5) Xie, L. S.; Skorupskii, G.; Dincă, M. Electrically Conductive Metal–Organic Frameworks. *Chem. Rev.* **2020**, *120*, 8536–8580. https://doi.org/10.1021/acs.chemrev.9b00766.

(6) Calbo, J.; Golomb, M. J.; Walsh, A. Redox-Active Metal–Organic Frameworks for Energy Conversion and Storage. *J. Mater. Chem. A* **2019**, *7*, 16571–16597. https://doi.org/10.1039/C9TA04680A.

(7) Nam, K. W.; Park, S. S.; dos Reis, R.; Dravid, V. P.; Kim, H.; Mirkin, C. A.; Stoddart, J. F. Conductive 2D Metal-Organic Framework for High-Performance Cathodes in Aqueous Rechargeable Zinc Batteries. *Nat. Commun.* **2019**, *10*, 4948. https://doi.org/10.1038/s41467-019-12857-4.

(8) Wada, K.; Sakaushi, K.; Sasaki, S.; Nishihara, H. Multielectron-Transfer-Based Rechargeable Energy Storage of Two-Dimensional Coordination Frameworks with Non-Innocent Ligands. *Angew. Chem. Int. Ed.* **2018**, *57*, 8886–8890. https://doi.org/10.1002/anie.201802521.

(9) Sheberla, D.; Bachman, J. C.; Elias, J. S.; Sun, C.-J.; Shao-Horn, Y.; Dincă, M. Conductive MOF Electrodes for Stable Supercapacitors with High Areal Capacitance. *Nat. Mater.* **2017**, *16*, 220–224. https://doi.org/10.1038/nmat4766.

(10) Feng, D.; Lei, T.; Lukatskaya, M. R.; Park, J.; Huang, Z.; Lee, M.; Shaw, L.; Chen, S.; Yakovenko, A. A.; Kulkarni, A.; Xiao, J.; Fredrickson, K.; Tok, J. B.; Zou, X.; Cui, Y.; Bao, Z. Robust and Conductive Two-Dimensional Metal−organic Frameworks with Exceptionally High Volumetric and Areal Capacitance. *Nat. Energy* **2018**, *3*, 30–36. https://doi.org/10.1038/s41560-017-0044-5.

(11) Xia, Z.; Jia, X.; Ge, X.; Ren, C.; Yang, Q.; Hu, J.; Chen, Z.; Han, J.; Xie, G.; Chen, S.; Gao, S. Tailoring Electronic Structure and Size of Ultrastable Metalated Metal–Organic Frameworks with Enhanced Electroconductivity for High-Performance Supercapacitors. *Angew. Chem. Int. Ed.* **2021**, *60*, 10228–10238. https://doi.org/10.1002/anie.202100123.

(12) Miner, E. M.; Fukushima, T.; Sheberla, D.; Sun, L.; Surendranath, Y.; Dincă, M. Electrochemical Oxygen Reduction Catalysed by Ni 3 (Hexaiminotriphenylene) 2. *Nat. Commun.* **2016**, *7*, 10942. https://doi.org/10.1038/ncomms10942.

(13) Panwar, N. L.; Kaushik, S. C.; Kothari, S. Role of Renewable Energy Sources in Environmental Protection: A Review. *Renew. Sust. Energ. Rev.* **2011**, *15*, 1513–1524. https://doi.org/10.1016/j.rser.2010.11.037.

(14) Dunn, B.; Kamath, H.; Tarascon, J.-M. Electrical Energy Storage for the Grid: A Battery of Choices. *Science* **2011**, *334*, 928–935. https://doi.org/10.1126/science.1212741.

(15) Liu, J.; Bao, Z.; Cui, Y.; Dufek, E. J.; Goodenough, J. B.; Khalifah, P.; Li, Q.; Liaw, B. Y.; Liu, P.; Manthiram, A.; Meng, Y. S.; Subramanian, V. R.; Toney, M. F.; Viswanathan, V. V.; Whittingham, M. S.; Xiao, J.; Xu, W.; Yang, J.; Yang, X.-Q.; Zhang, J.-G. Pathways for

Practical High-Energy Long-Cycling Lithium Metal Batteries. *Nat. Energy* **2019**, *4*, 180–186. https://doi.org/10.1038/s41560-019-0338-x.

(16) Larcher, D.; Tarascon, J.-M. Towards Greener and More Sustainable Batteries for Electrical Energy Storage. *Nat. Chem* **2015**, *7*, 19–29. https://doi.org/10.1038/nchem.2085.

(17) Zhao, R.; Liang, Z.; Zou, R.; Xu, Q. Metal-Organic Frameworks for Batteries. *Joule* **2018**, *2*, 2235–2259. https://doi.org/10.1016/j.joule.2018.09.019.

(18) Mehek, R.; Iqbal, N.; Noor, T.; Amjad, M. Z. B.; Ali, G.; Vignarooban, K.; Khan, M. A. Metal–Organic Framework Based Electrode Materials for Lithium-Ion Batteries: A Review. *RSC Adv.* **2021**, *11*, 29247–29266. https://doi.org/10.1039/D1RA05073G.

(19) Colombo, V.; Galli, S.; Choi, H. J.; Han, G. D.; Maspero, A.; Palmisano, G.; Masciocchi, N.; Long, J. R. High Thermal and Chemical Stability in Pyrazolate-Bridged Metal–Organic Frameworks with Exposed Metal Sites. *Chem. Sci.* **2011**, *2*, 1311–1319. https://doi.org/10.1039/C1SC00136A.

(20) Liu, X.-L.; Yin, Q.; Huang, G.; Liu, T.-F. Stable Pyrazolate-Based Metal-Organic Frameworks for Drug Delivery. *Inorg. Chem. Commun.* **2018**, *94*, 21–26. https://doi.org/10.1016/j.inoche.2018.06.001.

(21) Ma, F.-X.; Mi, F.-Q.; Sun, M.-J.; Huang, T.; Wang, Z.-A.; Zhang, T.; Cao, R. A Highly Stable Zn9-Pyrazolate Metal–Organic Framework with Metallosalen Ligands as a Carbon Dioxide Cycloaddition Catalyst. *Inorg. Chem. Front.* **2022**, *9*, 1812–1818. https://doi.org/10.1039/D1QI01555A.

(22) Herm, Z. R.; Wiers, B. M.; Mason, J. A.; Baten, J. M. van; Hudson, M. R.; Zajdel, P.; Brown, C. M.; Masciocchi, N.; Krishna, R.; Long, J. R. Separation of Hexane Isomers in a Metal-Organic Framework with Triangular Channels. *Science* **2013**, *340*, 960–964. https://doi.org/10.1126/science.1234071.

(23) Aubrey, M. L.; Wiers, B. M.; Andrews, S. C.; Sakurai, T.; Reyes-Lillo, S. E.; Hamed, S. M.; Yu, C.-J.; Darago, L. E.; Mason, J. A.; Baeg, J.-O.; Grandjean, F.; Long, G. J.; Seki, S.; Neaton, J. B.; Yang, P.; Long, J. R. Electron Delocalization and Charge Mobility as a Function of Reduction in a Metal–Organic Framework. *Nat. Mat.* **2018**, *17*, 625–632. https://doi.org/10.1038/s41563-018-0098-1.

(24) Schneebeli, S. T.; Frasconi, M.; Liu, Z.; Wu, Y.; Gardner, D. M.; Strutt, N. L.; Cheng, C.; Carmieli, R.; Wasielewski, M. R.; Stoddart, J. F. Electron Sharing and Anion–π Recognition in Molecular Triangular Prisms. *Angew. Chem. Int. Ed.* **2013**, *52*, 13100–13104. https://doi.org/10.1002/anie.201307984.

(25) Chen, D.; Avestro, A.-J.; Chen, Z.; Sun, J.; Wang, S.; Xiao, M.; Erno, Z.; Algaradah, M. M.; Nassar, M. S.; Amine, K.; Meng, Y.; Stoddart, J. F. A Rigid Naphthalenediimide Triangle for Organic Rechargeable Lithium-Ion Batteries. *Adv. Mat.* **2015**, *27*, 2907–2912. https://doi.org/10.1002/adma.201405416.

(26) Wu, Y.-L.; Horwitz, N. E.; Chen, K.-S.; Gomez-Gualdron, D. A.; Luu, N. S.; Ma, L.; Wang, T. C.; Hersam, M. C.; Hupp, J. T.; Farha, O. K.; Snurr, R. Q.; Wasielewski, M. R. G-Quadruplex Organic Frameworks. *Nat. Chem.* **2017**, *9*, 466–472. https://doi.org/10.1038/nchem.2689.

(27) Wang, G.; Chandrasekhar, N.; Biswal, B. P.; Becker, D.; Paasch, S.; Brunner, E.; Addicoat, M.; Yu, M.; Berger, R.; Feng, X. A Crystalline, 2D Polyarylimide Cathode for Ultrastable and Ultrafast Li Storage. *Adv. Mat.* **2019**, *31*, 1901478. https://doi.org/10.1002/adma.201901478.

(28) Sun, L.; Hendon, C. H.; Park, S. S.; Tulchinsky, Y.; Wan, R.; Wang, F.; Walsh, A.; Dincă, M. Is Iron Unique in Promoting Electrical Conductivity in MOFs? *Chem. Sci.* **2017**, *8*, 4450–4457. https://doi.org/10.1039/C7SC00647K.

(29) Debiagi, P.; Rocha, R. C.; Scholtissek, A.; Janicka, J.; Hasse, C. Iron as a Sustainable Chemical Carrier of Renewable Energy: Analysis of Opportunities and Challenges for Retrofitting Coal-

Fired Power Plants. *Renew. Sust. Energ. Rev.* **2022**, *165*, 112579. https://doi.org/10.1016/j.rser.2022.112579.

(30) Song, Z.; Zhou, H. Towards Sustainable and Versatile Energy Storage Devices: An Overview of Organic Electrode Materials. *Energy Environ. Sci.* **2013**, *6* (8), 2280–2301. https://doi.org/10.1039/C3EE40709H.

(31) Xie, L. S.; Sun, L.; Wan, R.; Park, S. S.; DeGayner, J. A.; Hendon, C. H.; Dincă, M. Tunable Mixed-Valence Doping toward Record Electrical Conductivity in a Three-Dimensional Metal–Organic Framework. *J. Am. Chem. Soc.* **2018**, *140*, 7411–7414. https://doi.org/10.1021/jacs.8b03604.

(32) Park, J. G.; Aubrey, M. L.; Oktawiec, J.; Chakarawet, K.; Darago, L. E.; Grandjean, F.; Long, G. J.; Long, J. R. Charge Delocalization and Bulk Electronic Conductivity in the Mixed-Valence Metal–Organic Framework Fe(1,2,3-Triazolate)$_2$ (BF$_4$)$_x$. *J. Am. Chem. Soc.* **2018**, *140*, 8526–8534. https://doi.org/10.1021/jacs.8b03696.

(33) Howarth, A. J.; Peters, A. W.; Vermeulen, N. A.; Wang, T. C.; Hupp, J. T.; Farha, O. K. Best Practices for the Synthesis, Activation, and Characterization of Metal–Organic Frameworks. *Chem. Mater.* **2017**, *29*, 26–39. https://doi.org/10.1021/acs.chemmater.6b02626.

(34) Jonathan. Clayden. *Organic Chemistry*, Second edition..; Oxford University Press: Oxford, 2012.

(35) Taft, R. W.; Bordwell, F. G. Structural and Solvent Effects Evaluated from Acidities Measured in Dimethyl Sulfoxide and in the Gas Phase. *Acc. Chem. Res.* **1988**, *21*, 463–469. https://doi.org/10.1021/ar00156a005.

(36) Ding, B.; Hua, C.; Kepert, C. J.; D'Alessandro, D. M. Influence of Structure–Activity Relationships on through-Space Intervalence Charge Transfer in Metal–Organic Frameworks with Cofacial Redox-Active Units. *Chem. Sci.* **2019**, *10*, 1392–1400. https://doi.org/10.1039/C8SC01128A.

(37) Lü, B.; Chen, Y.; Li, P.; Wang, B.; Müllen, K.; Yin, M. Stable Radical Anions Generated from a Porous Perylenediimide Metal-Organic Framework for Boosting near-Infrared Photothermal Conversion. *Nat. Commun.* **2019**, *10*, 767. https://doi.org/10.1038/s41467-019-08434-4.

(38) Wentz, H. C.; Skorupskii, G.; Bonfim, A. B.; Mancuso, J. L.; Hendon, C. H.; Oriel, E. H.; Sazama, G. T.; Campbell, M. G. Switchable Electrical Conductivity in a Three-Dimensional Metal–Organic Framework via Reversible Ligand n-Doping. *Chem. Sci.* **2020**, *11*, 1342–1346. https://doi.org/10.1039/C9SC06150A.

(39) Kubelka, P.; Munk, F. A Contribution to the Optics of Pigments. *Z. Technol. Phys.* **1931**, 12, 593−599.

(40) Tauc, J.; Grigorovici, R.; Vancu, A. Optical Properties and Electronic Structure of Amorphous Germanium. *Phys. Status Solidi (b)* **1966**, *15*, 627–637. https://doi.org/10.1002/pssb.19660150224.

(41) Qu, L.; Iguchi, H.; Takaishi, S.; Habib, F.; Leong, C. F.; D'Alessandro, D. M.; Yoshida, T.; Abe, H.; Nishibori, E.; Yamashita, M. Porous Molecular Conductor: Electrochemical Fabrication of Through-Space Conduction Pathways among Linear Coordination Polymers. *J. Am. Chem. Soc.* **2019**, *141*, 6802–6806. https://doi.org/10.1021/jacs.9b01717.

(42) Kuang, X.; Chen, S.; Meng, L.; Chen, J.; Wu, X.; Zhang, G.; Zhong, G.; Hu, T.; Li, Y.; Lu, C.-Z. Supramolecular Aggregation of a Redox-Active Copper-Naphthalenediimide Network with Intrinsic Electron Conduction. *Chem. Commun.* **2019**, *55*, 1643–1646. https://doi.org/10.1039/C8CC10269D.

(43) Xue, Z.; Zheng, J.-J.; Nishiyama, Y.; Yao, M.-S.; Aoyama, Y.; Fan, Z.; Wang, P.; Kajiwara, T.; Kubota, Y.; Horike, S.; Otake, K.; Kitagawa, S. Fine Pore-Structure Engineering by Ligand Conformational Control of Naphthalene Diimide-Based Semiconducting Porous Coordination

Polymers for Efficient Chemiresistive Gas Sensing. *Angew. Chem. Int. Ed.* **2023**, *62*. https://doi.org/10.1002/anie.202215234.

(44) Leong, C. F.; Wang, C.-H.; Ling, C. D.; D'Alessandro, D. M. A Spectroscopic and Electrochemical Investigation of a Tetrathiafulvalene Series of Metal–Organic Frameworks. *Polyhedron* **2018**, *154*, 334–342. https://doi.org/10.1016/j.poly.2018.07.023.

(45) Franchini, C.; Reticcioli, M.; Setvin, M.; Diebold, U. Polarons in Materials. *Nat. Rev. Mater.* **2021**, *6* (7), 560–586. https://doi.org/10.1038/s41578-021-00289-w.

(46) Pathak, A.; Shen, J.-W.; Usman, M.; Wei, L.-F.; Mendiratta, S.; Chang, Y.-S.; Sainbileg, B.; Ngue, C.-M.; Chen, R.-S.; Hayashi, M.; Luo, T.-T.; Chen, F.-R.; Chen, K.-H.; Tseng, T.-W.; Chen, L.-C.; Lu, K.-L. Integration of a (–Cu–S–)n Plane in a Metal–Organic Framework Affords High Electrical Conductivity. *Nat. Commun.* **2019**, *10*, 1721. https://doi.org/10.1038/s41467-019-09682-0.

(47) VandeVondele, J.; Krack, M.; Mohamed, F.; Parrinello, M.; Chassaing, T.; Hutter, J. Quickstep: Fast and Accurate Density Functional Calculations Using a Mixed Gaussian and Plane Waves Approach. *Comput. Phys. Communs.* **2005**, *167*, 103–128. https://doi.org/10.1016/j.cpc.2004.12.014.

(48) Guidon, M.; Hutter, J.; VandeVondele, J. Robust Periodic Hartree−Fock Exchange for Large-Scale Simulations Using Gaussian Basis Sets. *J. Chem. Theory Comput.* **2009**, *5*, 3010–3021. https://doi.org/10.1021/ct900494g.

(49) Spencer, J.; Alavi, A. Efficient Calculation of the Exact Exchange Energy in Periodic Systems Using a Truncated Coulomb Potential. *Phys. Rev. B* **2008**, *77*, 193110. https://doi.org/10.1103/PhysRevB.77.193110.

(50) Guidon, M.; Hutter, J.; VandeVondele, J. Auxiliary Density Matrix Methods for Hartree−Fock Exchange Calculations. *J. Chem. Theory Comput.* **2010**, *6*, 2348–2364. https://doi.org/10.1021/ct1002225.

(51) VandeVondele, J.; Hutter, J. Gaussian Basis Sets for Accurate Calculations on Molecular Systems in Gas and Condensed Phases. *J. Chem. Phys.* **2007**, *127*, 114105. https://doi.org/10.1063/1.2770708.

(52) Krack, M. Pseudopotentials for H to Kr Optimized for Gradient-Corrected Exchange-Correlation Functionals. *Theor. Chem. Acc.* **2005**, *114*, 145–152. https://doi.org/10.1007/s00214-005-0655-y.

(53) Goedecker, S.; Teter, M.; Hutter, J. Separable Dual-Space Gaussian Pseudopotentials. *Phys. Rev. B* **1996**, *54*, 1703–1710. https://doi.org/10.1103/PhysRevB.54.1703.

(54) Hartwigsen, C.; Goedecker, S.; Hutter, J. Relativistic Separable Dual-Space Gaussian Pseudopotentials from H to Rn. *Phys. Rev. B* **1998**, *58*, 3641–3662. https://doi.org/10.1103/PhysRevB.58.3641.

(55) Quirk, J. A.; Lazarov, V. K.; McKenna, K. P. Electronic Properties of 112 and 110 Twin Boundaries in Anatase TiO2. *Adv. Theory Simul.* **2019**, *2*, 1900157. https://doi.org/10.1002/adts.201900157.

(56) Elmaslmane, A. R.; Watkins, M. B.; McKenna, K. P. First-Principles Modeling of Polaron Formation in TiO2 Polymorphs. *J. Chem. Theory Comput.* **2018**, *14*, 3740–3751. https://doi.org/10.1021/acs.jctc.8b00199.

CHAPTER 4 |

ANION BRIDGE VARIATION OF ISOSTRUCTURAL FE(X)NDI-1 FRAMEWORKS

SYNOPSIS

This chapter describes the synthesis and study of novel Fe–pyrazolate PCPs **Fe(OH)NDI-1** and **Fe(Br)NDI-1** that are akin to **Fe(Cl)NDI-1**. The aim of the study is to replicate the Fe–pyrazolate backbone and high π–π overlap charge transport pathways found in **Fe(Cl)NDI-1** for semiconductor applications in the context of the novel Fe–pyrazolate materials. To effect structural modifications in **Fe(Cl)NDI-1** the design strategy focuses on the infrequently utilised approach of substituting bridging anion linkers. Through anion substitution, two distinct frameworks are synthesised that incorporate OH and Br anions in lieu of Cl. PXRD analysis reveals that as anion size increases, lattice size correspondingly expands **Fe(Br)NDI-1** > **Fe(Cl)NDI-1** > **Fe(OH)NDI-1**. Charge transport was then found to be intricately linked to the lattice size, demonstrating that a smaller lattice results is analogous to a higher conductivity (order of conductivity : **Fe(OH)NDI-1** > **Fe(Cl)NDI-1** > **Fe(Br)NDI-1**) due to closer distances between charge carriers. Complementary theoretical calculations substantiate the experimental conductivity results, affirming that charge transport in this series of Fe–pyrazolate PCPs is primarily governed by large-scale mechanisms such as band transport, superseding the anticipated formation of polarons, as predicted in Chapter 3 for **Fe(Cl)NDI-1**.

ACKNOWLEDGEMENTS

The following people are gratefully acknowledged for their contribution to this chapter. Dr. Jamie A. Gould for establishing the initial synthetic procedures. Dr Philip A. Hope for collecting the high-resolution electron microscopy images. Dr James Quirk for carrying out the theoretical calculations relating to frontier molecular orbitals polarons, and electron effective masses. Dr Stuart Cavill for providing access to a Keithley source meter to enable conductivity measurements.

4.1 INTRODUCTION

The most distinctive characteristics of PCPs are their well-ordered rigid structures that contain permanent porosity and are often stabilised by strong bonds between metal nodes, secondary building units, and organic linkers.[1] The permanent porosity in combination with unyielding frameworks give rise to high surface areas, enabling a wide range of applications that include catalysis,[2] separations,[3,4] and redox activity[5,6]. In the design of PCPs, the pre-selection of specific metal centres and organic linkers are employed to achieve a desired topology or functionality, resulting in a "net" that represents the connectivity of the PCP.[7] Isoreticular chemistry is a strategic design approach that aims to expand, replace, or modify the building blocks of a PCP while preserving the topology of the original net to obtain the most desirable properties.[8] Therefore, by using isoreticular design strategies, the porosity and rigid nature of PCPs can be modified while maintaining the original net to obtain the most desirable properties.[9]

Historically, isoreticular design, which was previously featured in Chapter 1, has been used to generate a wide range of frameworks with the same topological net.[10] Since the advent of conductive frameworks approximately 15 years ago, semiconductor capabilities have been explored in the context of isoreticular frameworks, utilising the various charge transport pathways (i.e., *through-space*, *through-bond*, *extended conjugation*).[11] In the context of conductive PCPs, focus has been directed towards changing the metal centre or to influence ligand spacing and the resulting conductivity of isoreticular materials.[12,13] For example, Park et al. exchanged metal centres (M = Mn, Co, Zn or Cd) in a range of isostructural PCPs with nickel-glyoximate ligands with a *through-bond* S···S charge transport pathway (Figure 4.1a).[12] The difference between the sizes of the respective metal centres ($Cd^{2+} > Mn^{2+} > Co^{2+} > Zn^{2+}$) coordinated to the nickel-glyoximate core had an inverse relationship with the S···S distance, ultimately affecting the *through-bond* charge transport pathway of overlapped $3p_z$ orbitals between adjacent sulfur atoms. Resultingly, charge transport followed the following trend Cd > Mn > Co > Zn, demonstrating how the size of one element in a framework can affect the conductivity. Another example demonstrated by Xie et al.[13] incorporated different metal centres (M = Mn, Zn, Cd) into a 2D framework that featured close interactions between tetrathiafulvalene tetrabenzoate (TTFTB) ligands that acted as a *through-space* charge transport pathway (Figure 4.1b). The size of the metal centres (Cd > Mn > Cd) modulated the interlayer spacing between linkers that provided the *through-space* pathway, causing conductivity to be reduced when a larger anion was present within the framework.

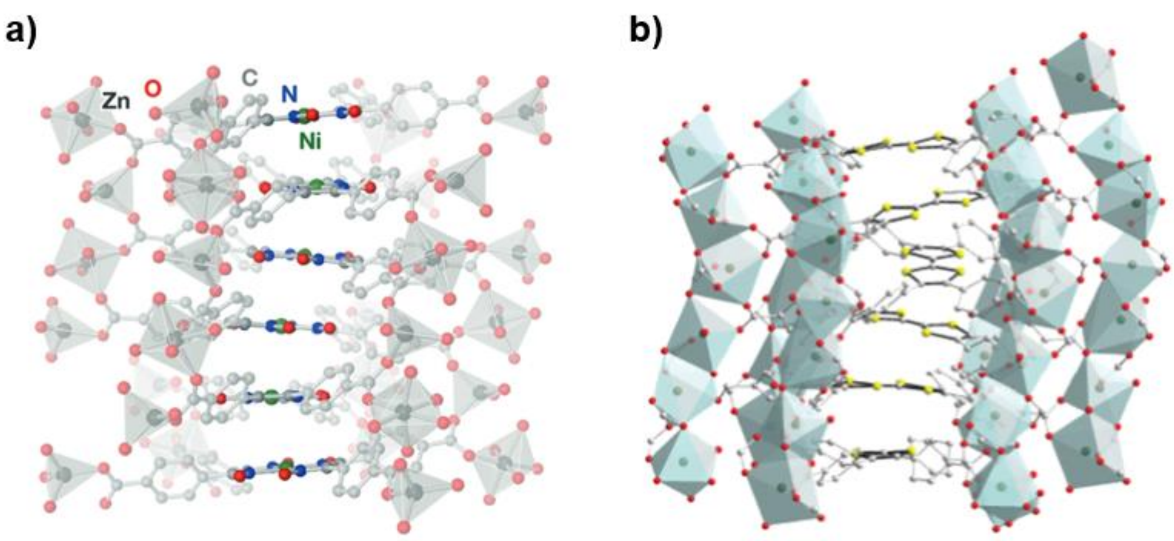

Figure 4.1. The structures of (a) the isostructural PCPs with nickel-glyoximate ligands, copied from the work of Park et al.[12] and (b) the isostructural 2D framework with TTFTB ligands, copied from the work of Xie et al.[13]

Changing the metal centre is an effective isoreticular strategy to influence topologies towards enhancing conductive pathways in PCPs. Another potential route to enhancing conductivity is exchanging inorganic linkers such as anions (i.e., F, Cl, Br). Currently, examples exist of post-synthetic inorganic linker exchange that have enhanced the properties of PCPs (e.g., stability, catalysis, sensing).[2,14–16] However, post-synthetic linker exchange often involves long procedures of up to 14 days,[14,16] when an alternative pre-synthetic isoreticular strategy could provide a more efficient route to isostructural materials with shorter distances between charge carriers that result in enhanced conductivity. Furthermore, no examples of inorganic linker exchange exist that have influenced the conductive properties of the resulting PCP, indicating a unique opportunity to capitalise on.

Herein, to explore synthesise novel isostructural materials and circumvent long reaction times observed in post-synthetic anion exchange strategies, this work will focus on pre-synthetically exchanging the inorganic ligand, Cl, within **Fe(Cl)NDI-1**. Having already demonstrated high conductivity *via* its two charge transport pathways (i.e., the *through-space* NDI **1** ligand overlap and the *through-bond* (Fe−N−N−)$_\infty$ backbone) in addition to high thermal stability and redox activity, **Fe(Cl)NDI-1** was an excellent material to expand build upon. Therefore, isoreticular synthesis to generate materials with the same net as **Fe(Cl)NDI-1** that incorporate different anions (i.e., F, Br) could result in altered spacing between charge carriers of either charge transport pathway, resulting in decreased or enhanced conductivity. Another potential outcome is the generation of frameworks that demonstrate increased porosity, while retaining the redox conductive properties observed in **Fe(Cl)NDI-1**. Consequently, the increased porosity may facilitate the diffusion of charge-balancing ions, potentially rendering the new materials to be more viable as active components in energy storage devices.

4.2 RESULTS AND DISCUSSION

4.2.1 SYNTHESIS OF PCPS WITH DIFFERENT BRIDGING ANIONS

The most accessible reticular strategy available to generate new frameworks with the same structural net as **Fe(Cl)NDI-1** was pre-synthetically exchanging the Cl bridging anion in **Fe(Cl)NDI-1** for alternatives. Performing an anion exchange offered several possibilities, such as expanding or contracting the framework net based on the anion size, thereby altering the *through-bond* and *through-space* charge transport pathways (i.e., π–π and Fe–N distances). Incorporation of large bridging anions could allow pores to form, creating spaces for the diffusion of ions and providing access to redox-active sites within the new structures. Additionally, the connectivity to bridging anions could influence the coordination atmosphere of ligands to the Fe metal centres, resulting in new materials with altered structural nets that have altered properties.

Therefore, in order to generate new coordination materials, several different starting materials were screened by using conditions that were optimised for **Fe(Cl)NDI-1**. Accordingly, NDI **1** was subject to microwave irradiation in the presence of five different metal salts (FeF_3, Fe(acetylacetonate)$_3$, $FeNO_3$, $FeSO_3$, $FeBr_3$) in separate reaction vessels (Figure 4.2). We hypothesised that smaller anions (F, O) would lead to more contracted, closely-packed frameworks in comparison to **Fe(Cl)NDI-1**, potentially decreasing the distance between NDI π-surfaces and reducing the distance between Fe–Fe metal centres. Such a decrease in distance could lead to an increase in orbital overlap in regard to both *through-bond* and *through-space* pathways. In contrast, larger anions (Br, NO_3, SO_3) were hypothesised to result in larger gaps due to the increase bulk of the coordinated anions, potentially causing pores to form within the framework, or generating PCP materials. The emergence of pores within new frameworks isostructural to **Fe(Cl)NDI-1** could lead to the accessibility of redox-active sites, leading to properties such as gas sensing[17] that have been observed in similar systems to **Fe(Cl)NDI-1**.

The synthetic reactions to combine NDI **1** with the five different salts were carried out using the protocols developed for **Fe(Cl)NDI-1** (see methods, section 4.5.2). Solid materials emerged from three of the reaction mixtures (Fe(acac)$_3$, FeF_2, $FeBr_2$), while the other reaction mixtures ($Fe(NO_3)_3$, $Fe(SO_3)_3$ produced no solid products. The new solids were named according to the available anion of the Fe salt used (i.e., Fe(acac)$_3$ = **Fe(OH)NDI-1**, FeF_2 = **Fe(F)NDI-1**, $FeBr_2$ = **Fe(Br)NDI-1**. The new solids were insoluble to all solvents, suggesting that they were PCP materials that were similar to **Fe(Cl)NDI-1**, allowing successive washes in DMSO and EtOH, before being dried in a vacuum oven at 180 °C. Conversely, the absence of any products from the reaction mixtures containing $Fe(NO_3)_3$ and $Fe(SO_3)_3$ can be attributed to the significantly large size of the ions, which may have hindered the formation of materials isostructural to **Fe(Cl)NDI-1**. Furthermore, the size, shape, or coordination points of NO_3 or

SO_3 could have prevented new materials that were structurally distinct from **Fe(Cl)NDI-1** to form as a result of unfulfilled coordination sites on the Fe metal centre.

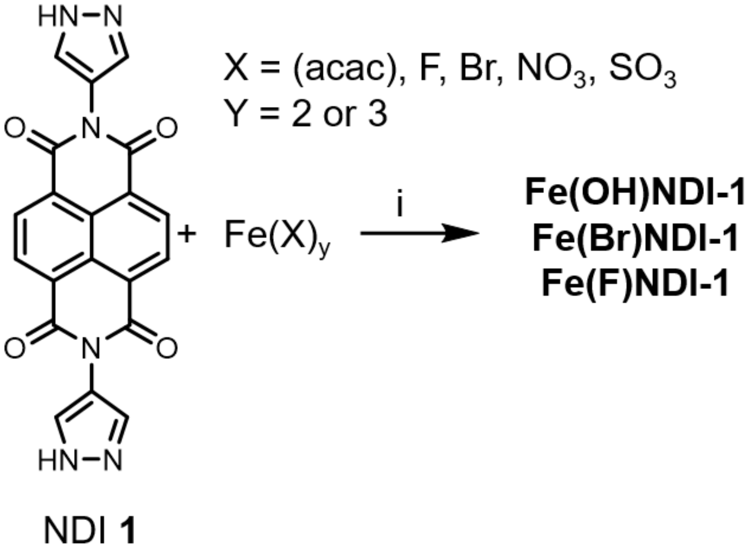

Figure 4.2. The synthetic protocol used to generate new frameworks similar to **Fe(Cl)NDI-1**. Reagents and conditions: (i) DMF, μW: 200 °C, 15 min.

4.2.2 POWDER X-RAY DIFFRACTION

PXRD is a common analytical technique that is used to analyse CPs, due to the majority of CPs having highly ordered crystalline frameworks that result in well-defined PXRD patterns. Shifting of PXRD peaks with the same lattice parameter towards higher or lower angles of 2θ has been observed in isostructural CPs when one component within the structure differs in size.[18,19] Isostructural materials have the same space group, resulting in PXRD peaks which have the same hkl coordinates. Therefore, when shifting is observed between peaks of the same hkl coordinate, that corresponds to a changed *d*-spacing value after the Bragg equation is solved for the corresponding peak 2θ value. For instance, Wan et al.[18] synthesised a range of isostructural PCPs containing different single and bimetal motifs (e.g., Ni, Ni-Zn, Ni-Fe) within each structure. The PXRD patterns of the PCP materials generated by Wan et al. shifted towards lower angles of 2θ when larger metal atoms with larger atomic radii were incorporated into the structure, indicating that an increase in lattice size had occurred. Another example comes from the work of Yuan et al.,[19] whom modified the linkers of their PCP to influence its chemical and physical properties. As Yuan et al. increased linker length in their PCPs, materials with higher porosity were generated that displayed peak shifting towards lower angles of 2θ in corresponding PXRD patterns. The shifted peaks indicated that the lattice size of the PCP materials with increased linker sizes had expanded, while remaining isostructural.

In addition to the PXRD peak shifting, additional PXRD peaks have been observed in powder patterns among isostructural CP materials.[3,20–22] For instance, in the development of zinc-based PCPs by Walton and co-workers,[20] slight variations in linker choices, such as the addition of an extra methyl group, led to additional reflections when PXRD patterns of the isostructural materials were compared. These differences manifested as slight shifts (0.1–0.5 2θ) in peak positions and the appearance of additional peaks while maintaining identical space groups. Similar observations of slight peak shifts or additional peaks have been reported in various other series of isostructural CP materials.[3,21,22]

Concerning the range of Fe–pyrazolate materials in this work, no single crystal structures of **Fe(OH)NDI-1**, **Fe(Br)NDI-1** and **Fe(F)NDI-1** were obtained. Therefore, given that a single crystal structure of **Fe(Cl)NDI-1** had already been resolved, PXRD proved to be an excellent method to: (i) determine the crystallinity of new materials and, (ii) to establish a comparison between the new materials and **Fe(Cl)NDI-1** in lieu of single crystal structures. In Figure 4.3, it's evident that **Fe(OH)NDI-1**, **Fe(Br)NDI-1** and **Fe(F)NDI-1** exhibit high-intensity patterns, indicating their crystalline nature and enabling a detailed examination and comparison with **Fe(Cl)NDI-1**.

Between the four PXRD patterns of the Fe–pyrazolate materials (see the appendix, section 8.1.9 for peak-picked powder patterns of **Fe(OH)NDI-1**, **Fe(Br)NDI-1** and **Fe(F)NDI-1**), seven common peaks were identified to match that had similar intensities and profiles. The *d*-spacing of each peak was calculated using the Bragg equation in conjunction using the 2θ value of each identified peak (Table 4.1). As seen in the single crystal data for **Fe(Cl)NDI-1** in Chapter 3, the array of stacked NDI units and the Fe–pyrazolate chain lie along the a-axis, which relates to the coordinate "h". Therefore, assuming that the set of four Fe–pyrazolate materials are isostructural and contain different bridging anions (i.e., Cl, OH, Br, F), *d*-spacings should rise when an anion with a larger radius is present and fall when a smaller anion is present. The *d*-spacing values show that all peaks apart from one matched to **Fe(Cl)NDI-1**, showing in that **Fe(OH)NDI-1** and **Fe(F)NDI-1** *d*-spacings are smaller and **Fe(Br)NDI-1** *d*-spacings are larger. The trend is broken by the second peak of Fe(Br)NDI-1, that shows a lower *d*-spacing in comparison to the same peak of **Fe(Cl)NDI-1**.

Table 4.1. *d*-spacing values of the seven annotated peaks found in Figure 4.2

	d-spacing (Å)						
Peak number	1	2	3	4	5	6	7
Cl	7.76	5.84	5.44	4.86	3.50	3.42	3.27
OH	7.70	5.81	5.33	4.80	3.42	3.34	3.20
Br	7.73	5.81	5.50	4.90	3.56	3.47	3.32
F	7.40	5.65	5.17	4.66	3.34	3.26	3.12
Mirror plane	(021)	(041)	(111)	(131)	(200)	(220)	(201)

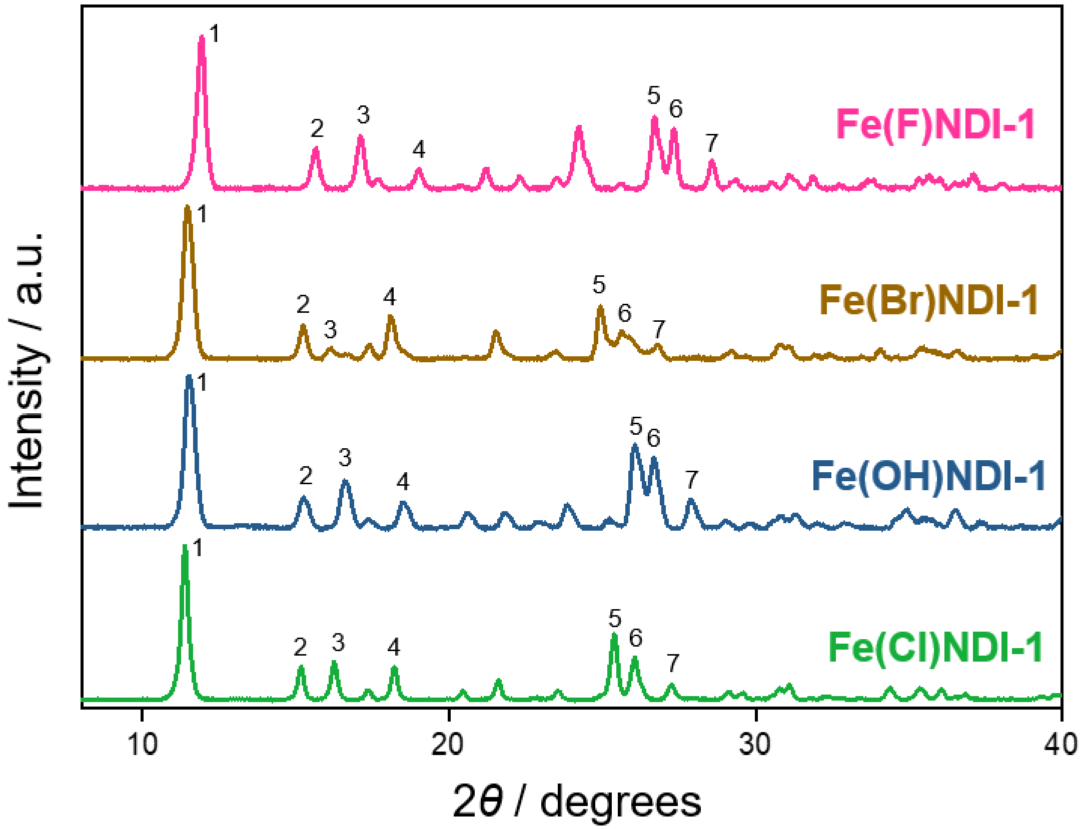

Figure 4.3. PXRD patterns of **Fe(Cl)NDI-1**, **Fe(OH)NDI-1**, **Fe(Br)NDI-1** and **Fe(F)NDI-1**. Matching isostructural peaks are annotated with numbers.

The results of the comparison between matching peaks do not confirm that each material is isostructural to one another. However, working under the assuming that they are isostructural, strong evidence from *d*-spacing values demonstrate that the lattice of each framework is bigger or smaller based on the size of the bridging anion in the framework. The indication that the lattice size differs between the frameworks is likely to have a significant impact on the charge transport properties of each PCP. For instance, a larger lattice size suggests that the distance between Fe atoms in the (Fe−N−N−)∞ chain and the distance between overlapped NDI units has increased, suggesting that the percolation of charge between overlapped frontier molecular orbitals will be reduced due to the increased distance. On the contrary, a smaller lattice suggests that the resulting frontier molecular orbitals will be positioned closer to one another, which can lead to an increase in semiconductor properties. The outlined structural differences have the potential to substantially influence the electronic and charge transport behaviour of the new material, in comparison to **Fe(Cl)NDI-1**. However, validation of the purity concerning each new framework with XRF and EA was essential to corroborate the PXRD findings.

4.2.3 ANALYSIS OF PURITY

Considering that each material was insoluble, paramagnetic, and of a polymeric nature, physical characterisation methods (EA, XRF) were performed in order to determine differences observed in the PXRD patterns, and to confirm the purity of each material. XRF was employed to identify and quantify the elements present in **Fe(OH)NDI-1**, **Fe(Br)NDI-1** and **Fe(F)NDI-1**. However, elements such as H, C, N, O and F were too small to be detected by XRF due to the low amount of fluorescent energy emitted by relaxing atoms of molecular weights lower than 23 (Na). Therefore, based on the limitations of XRF analysis, we anticipated being able to detect only Fe and Br, assuming that no impurities were present in the materials. The results (Table 4.2) show that all materials match well with the displayed theoretical values, suggesting that there are little to no Fe or Br contaminants within the materials (see the Appendix, section 7.11, Figures 7.30 and 7.31). However, due to the limitations of XRF, no information is available regarding possible contaminants with H, C, N, O and F elements, causing EA to be pursued.

Table 4.2. X-ray fluorescence results for **Fe(Cl)NDI-1**, **Fe(OH)NDI-1**, **Fe(Br)NDI-1**, **Fe(F)NDI-1**.

	Fe / %	Cl / %	Br / %
Fe(Cl)NDI-1 theory	50	50	-
Fe(Cl)NDI-1	47	53	-
Fe(Br)NDI-1 theory	50	-	50
Fe(Br)NDI-1	47.6	-	52.4

In order to reinforce the results obtained from XRF analyses and obtain information regarding elements with lower molecular weights (i.e., H, C, N, O and F), EA was carried out for **Fe(OH)NDI-1**, **Fe(Br)NDI-1** and **Fe(F)NDI-1**. Working under the presumption that each material was isostructural to **Fe(Cl)NDI-1** and contained a different bridging anion in place of Cl, the theoretical values were calculated accordingly. The returned EA shows that both **Fe(OH)NDI-1** ($C_{20}H_9FeN_6O_5$) and **Fe(Br)NDI-1** ($C_{20}H_8FeBrN_6O_4$) materials are within the expected theoretical values, and that there is little, if any, impurities within either material. However, the result displayed for **Fe(F)NDI-1** ($C_{20}H_8FeFN_6O_4$) show experimental values that are separated by >3% from the theoretical value of carbon, suggesting that there are significant impurities present within the material.

Table 4.3. Elemental analysis results for **Fe(OH)NDI-1**, **Fe(Br)NDI-1**, **Fe(F)NDI-1**. The compositional purity of all materials apart from **Fe(F)NDI-1** is confirmed.

	C / %	H / %	N / %	Cl / %	Br / %
Fe(Cl)NDI-1 theory	49.26	1.65	17.25	7.27	-
Fe(Cl)NDI-1	49.75	2.40	17.25	6.95	-
Fe(OH)NDI-1 theory	51.20	1.93	17.91	-	-
Fe(OH)NDI-1	51.48	2.81	17.60	-	-
Fe(Br)NDI-1 theory	45.15	1.52	15.80	-	15.02
Fe(Br)NDI-1	47.45	2.14	16.22	-	13.71
Fe(F)NDI-1 theory	50.98	1.71	17.84	-	-
Fe(F)NDI-1	47.58	1.90	15.19	-	-

4.2.4 PROPERTIES ANALYSIS

After PXRD, XRF and EA had been carried out for **Fe(OH)NDI-1**, **Fe(Br)NDI-1** and **Fe(F)NDI-1**, the data suggested that each material was isostructural to one another and possessed little impurities with exception to **Fe(F)NDI-1**. Therefore, we would expect each material to possess exceptional thermal resistance, due to the pyrazolate backbone that penetrated each material's superstructure. TGA would also reveal any substances escaping from pores within any of the materials, in addition to residual Fe_2O_3 values that would allow quantification of metal content.

After conducting thermal analysis, the data revealed that all materials exhibited excellent thermal resistances that had similar values to **Fe(Cl)NDI-1**, suggesting that each material contained the same pyrazolate backbone (Figure 4.4, Table 4.4). Analysis of the residual mass% revealed that **Fe(OH)NDI-1** (16.3% experimental, 17.0% theoretical) and **Fe(Br)NDI-1** (19.5% experimental, 15.0% theoretical) matched with theoretical values after accounting for the slight increase in mass (+2%) observed at the beginning of the analysis. However, values for **Fe(F)NDI-1** (24.0% experimental, 16.9% theoretical) were in large disparity, agreeing with EA data that impurities are present in as-synthesised **Fe(F)NDI-1** material. Specific to **Fe(OH)NDI-1**, a lower thermal resistance is observed in comparison to the other Fe–pyrazolate materials, suggesting that the bridging anion in each framework dictates the thermal stability, and was the first component to be lost during decomposition. **Fe(Cl)NDI-1** and **Fe(Br)NDI-1** share close decomposition points, suggesting that Fe binding to halides is stronger than that of oxygen.

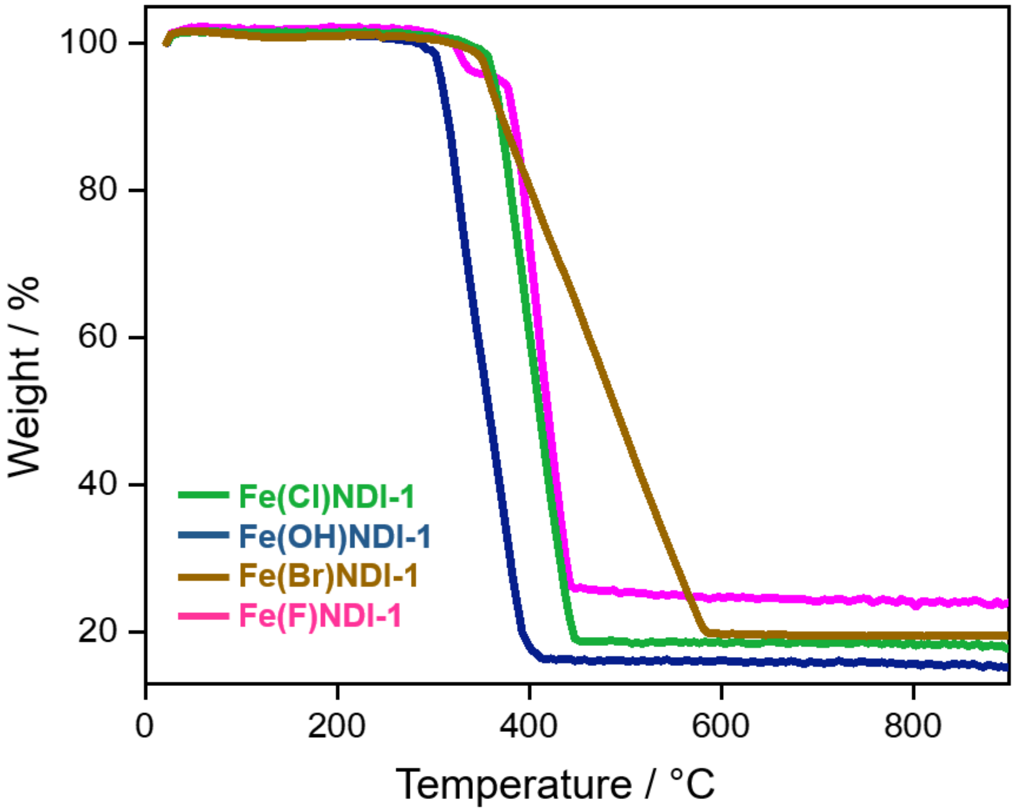

Figure 4.4. TGA data for **Fe(Cl)NDI-1**, **Fe(OH)NDI-1**, **Fe(Br)NDI-1** and **Fe(F)NDI-1** collected in air at a flow rate of 10 mL min^{-1} and a heating rate of 10 °C min^{-1}. Fe_2O_3 residue values can be found in Table 4.4

Table 4.4. TGA analysis of **Fe(OH)NDI-1**, **Fe(Br)NDI-1**, and **Fe(F)NDI-1**, using theoretical values that were calculated using Fe_2O_3 as the residual material.

	Theory / %	Experimental / %	Decomposition point (°C)
Fe(Cl)NDI-1	16.4	18.8	326
Fe(OH)NDI-1	17.0	16.2	280
Fe(Br)NDI-1	15.0	19.5	316
Fe(F)NDI-1	16.9	24.0	306

4.2.5 CYCLIC VOLTAMMETRY

The primary objective of this work is to create novel materials with enhanced properties in comparison to **Fe(Cl)NDI-1** (i.e., conductivity, porosity), that can serve as suitable candidates for integration as active components in energy storage devices. Hence, identifying the redox properties of the new Fe–pyrazolate materials was critical to ascertain suitability as battery component materials. Accordingly, **Fe(OH)NDI-1** and **Fe(Br)NDI-1** were analysed for their ability to accept electrons with the SCCV method developed to analyse **Fe(Cl)NDI-1**, in Chapter 3.

To generate voltammograms for **Fe(OH)NDI-1** and **Fe(Br)NDI-1**, an identical procedure was followed as used for **Fe(Cl)NDI-1** in Chapter 3, involving the drop-casting of a suspension of each material (20 mg mL^{-1}) onto the working electrode (WE), which was then submerged into a 1 mM solution of [*n*-Bu_4N]PF_6 in MeCN and analysed at 200 mV s^{-1}. The results depicted in Figure 4.5 show cyclic voltammograms of **Fe(OH)NDI-1** and **Fe(Br)NDI-1**, revealing two reductive peaks and two oxidative peaks. In the cases of both **Fe(OH)NDI-1** and **Fe(Br)NDI-1** first reductive peak is of low intensity and is attributed to the slow diffusion of ions through the solid material that was adhered on the WE.[23] A much more pronounced second reductive peak is observed for both compound **Fe(OH)NDI-1** and **Fe(Br)NDI-1**, mirroring the behaviour observed in **Fe(Cl)NDI-1**. Between the three frameworks, the points at which the second reduction take place are separated by 0.08 V, that is not considered significant due to the difficulty controlling the amount of material adhered to the surface of the WE. Oxidative peaks between the three frameworks are similar in shape and response, suggesting that the oxidation proceeds more readily than the reductive process.

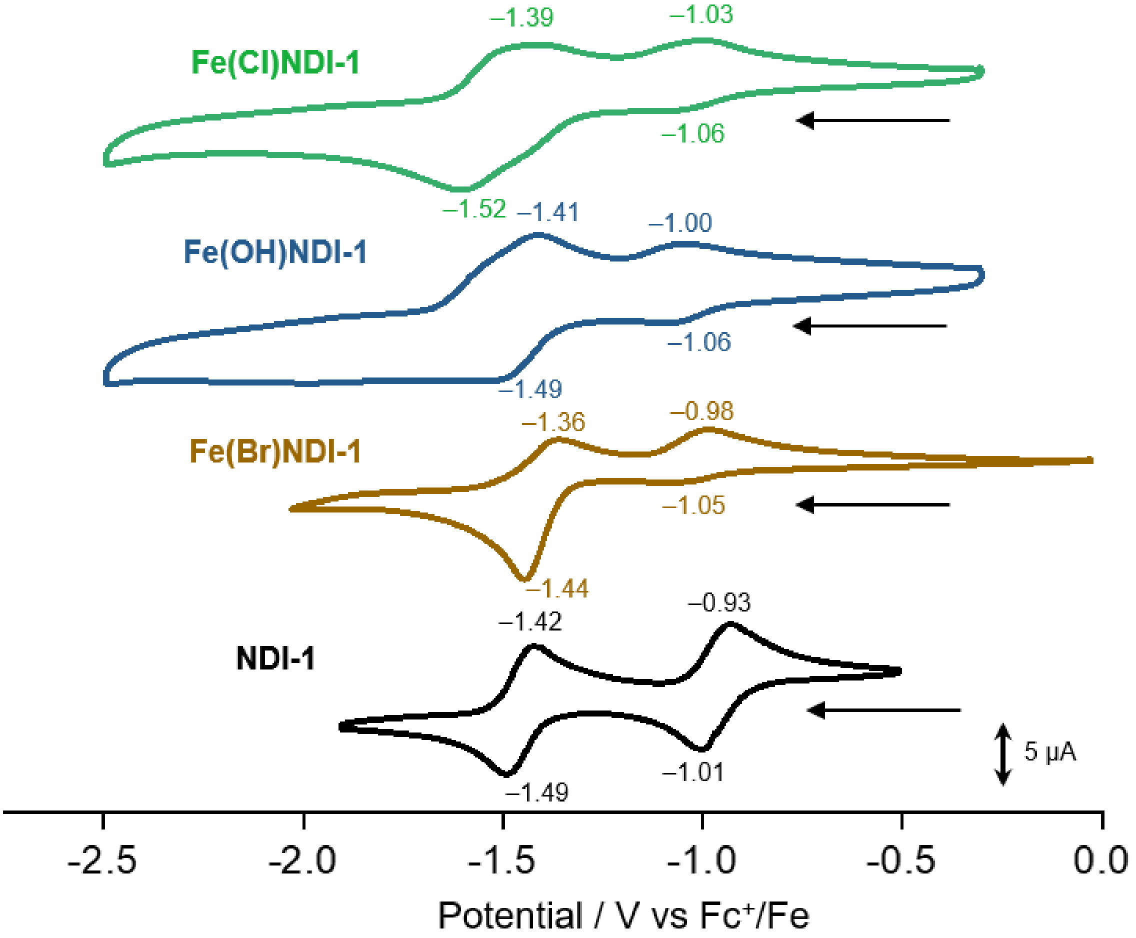

Figure 4.5. Cyclic voltammograms of **Fe(Cl)NDI-1**, **Fe(OH)NDI-1**, **Fe(Br)NDI-1** and NDI **1**. The CV data for **Fe(Cl)NDI-1**, **Fe(OH)NDI-1** and **Fe(Br)NDI-1** was collected using SCCV by drop-casting a suspension of the respective framework in DCM (20 mg mL^{-1}) onto the WE followed by submersion in a 1 mM solution of [*n*-Bu_4N]PF_6 in MeCN and analysis at 200 mV s^{-1}. The CV data for NDI **1** was collected in Chapter 2, in the solution state.

Hence, it can be deduced that the electrochemical response is consistent in the two new frameworks, **Fe(OH)NDI-1** and **Fe(Br)NDI-1**, both exhibiting near-analogous electrochemical behaviour to **Fe(Cl)NDI-1**. Furthermore, each of these frameworks displays electrochemical responses at similar positions to NDI **1**, substantiating the retention of the electrochemical characteristics of NDI **1** in all Fe–pyrazolate frameworks. Consequently, we can infer that, with the preserved electrochemical response of NDI **1**, both **Fe(OH)NDI-1** and **Fe(Br)NDI-1** possess the capacity to accommodate ions, making them suitable candidates for use in energy storage applications, provided that the porosity and conductivity of both are at appropriate levels.

4.2.6 POROSITY

In the context of an energy storage device, porosity plays a crucial role as it facilitates the diffusion of ions (e.g., Li^+, Na^+) to reach redox centres inside a PCP, enabling the transfer of charge between the cathode and anode in an electrochemical cell. In this study, only **Fe(OH)NDI-1** was subjected to porosity analysis due to limited availability of material for **Fe(Br)NDI-1**. Due to the absence of a crystal structure for **Fe(OH)NDI-1**, it was not possible to simulate the guest accessible volume within its structure, however, the smaller lattice as observed in PXRD measurements suggested it would display smaller pores than **Fe(Cl)NDI-1**. Porosity measurements were conducted for **Fe(OH)NDI-1** (Figure 4.6), revealing a BET surface area of 2.5 m^2 g^{-1}, suggesting that small pores existed in **Fe(OH)NDI-1** that are difficult to access through this technique, and is similar to the value obtained for **Fe(Cl)NDI-1** (2.8 m^2 g^{-1}).

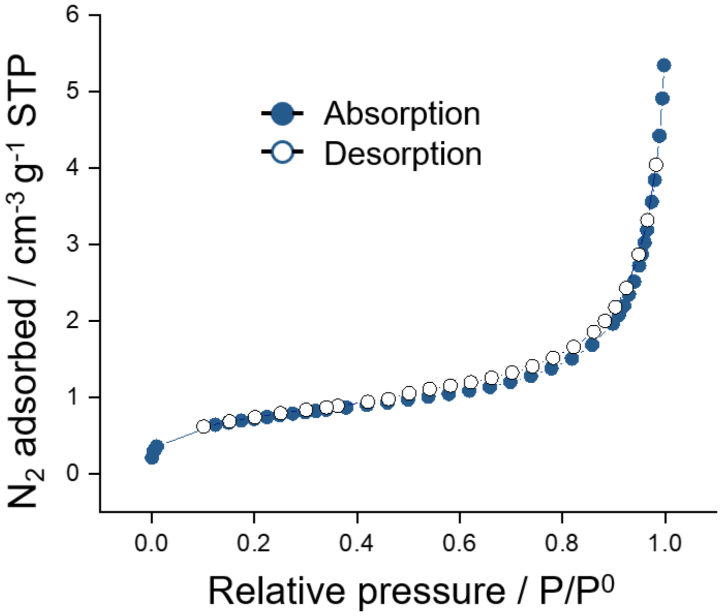

Figure 4.6. Porosity data for **Fe(OH)NDI-1**. Almost identical absorption and desorption curves denote small pores.

4.2.7 ESTIMATION OF BAND GAPS BY UV-VIS REFLECTANCE

To estimate the semiconductive properties of **Fe(OH)NDI-1** and **Fe(Br)NDI-1** and compare with **Fe(Cl)NDI-1**, UV-vis reflectance measurements were conducted to determine the estimated band gap of each material. The Kubelka-Munk (K–M) equation was employed to transform the absorption spectra, allowing for the estimation of the band gap using the Tauc method,[24] a method previously applied to **Fe(Cl)NDI-1** in Chapter 3. For both **Fe(OH)NDI-1** and **Fe(Br)NDI-1**, the band gap was estimated by identifying the intersection of the straight line with the x-axis (Figure 4.7), resulting in values of 2.19 eV and 2.05 eV, respectively (Table 4.5). In comparison to the band gap of **Fe(Cl)NDI-1**, both **Fe(OH)NDI-1** and **Fe(Br)NDI-1** exhibited similar values, suggesting that their optical semiconductor properties should be similar.

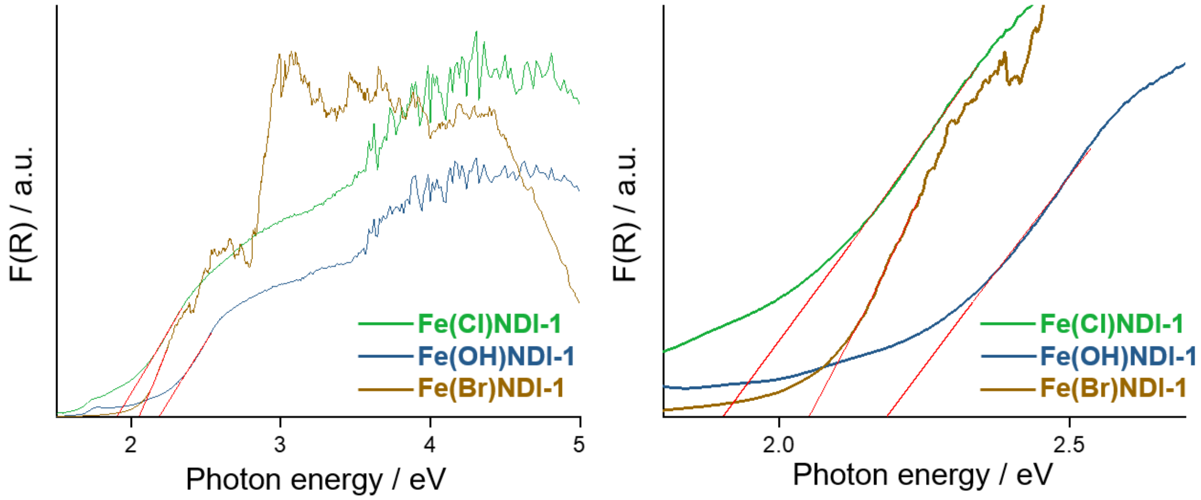

Figure 4.7. (a) K–M transformed UV-vis reflectance data for **Fe(Cl)NDI-1**, **Fe(OH)NDI-1**, and **Fe(Br)NDI-1**. A straight line has been fit to the first steep linear increase of light absorbance and energy, (b) a close-up of the straight line.

Table 4.5. The estimated experimental band gaps that were determined with K-M transformed UV-vis reflectance data.

	Experimental band gap / eV
Fe(Cl)NDI-1	1.91
Fe(OH)NDI-1	2.19
Fe(Br)NDI-1	2.05

4.2.8 CONDUCTIVITY

Conductivity measurements were carried out in order to assess the performance of **Fe(OH)NDI-1** and **Fe(Br)NDI-1** and draw a comparison to **Fe(Cl)NDI-1** allowing determination of the best semiconductor between the three materials. PXRD and supporting purity analysis has shown that each material was isostructural to one another and displayed two charge transport pathways (i.e., *through-space via* overlapped NDI orbitals and *through-bond via* the $(\text{Fe}-\text{N}-\text{N}-)_\infty$ backbone). The lattice of each isostructural framework was found to contract or expand based upon the bridging anion in each framework **Fe(OH)NDI-1**> **Fe(Cl)NDI-1** > **Fe(Br)NDI-1**, affecting the distance between charge carriers in both charge transport pathways. Therefore, it was expected that conductivity would follow the trend observed in lattice sizes, where smaller distances between charge carriers would translate to more orbital overlap and higher conductivity, suggesting that **Fe(OH)NDI-1** would display the highest conductivity, and **Fe(Br)NDI-1** the lowest.

The pressed pellet measurements of **Fe(OH)NDI-1** and **Fe(Br)NDI-1** were conducted using the method established for determining the conductivity of NDIs **1–4**, as described in Chapter 2 (see general experimental methods, section 7.1). The results indicated that **Fe(OH)NDI-1** displayed a conductivity of 2.21×10^{-4} S cm^{-1}, while **Fe(Br)NDI-1** exhibited a lower conductivity of 2.44×10^{-7} S cm^{-1} (Table 4.6). Raw I–V curves used to calculate the conductivity of each framework can be found in the Appendix, section 7.9, Figures 7.21 and 7.22. To ensure that each material retained their crystal structure throughout the sample preparation and experimental conductivity procedure, PXRD analysis was performed at every stage (Figure 4.8 and 4.9)

Table 4.6. Conductivity results for **Fe(Cl)NDI-1**, **Fe(OH)NDI-1** and **Fe(Br)NDI-1**. A clear trend is observed, that shows that the order of conductivity follows **Fe(OH)NDI-1** > **Fe(Cl)NDI-1** > **Fe(Br)NDI-1**, which was linked to anion sizes influencing lattice sizes.

	Anion	Atomic radii (empirical)[25]	Conductivity / S cm^{-1}
Fe(Cl)NDI-1	Cl	100	2.84×10^{-5}
Fe(OH)NDI-1	OH	60	2.21×10^{-4}
Fe(Br)NDI-1	Br	115	2.44×10^{-7}

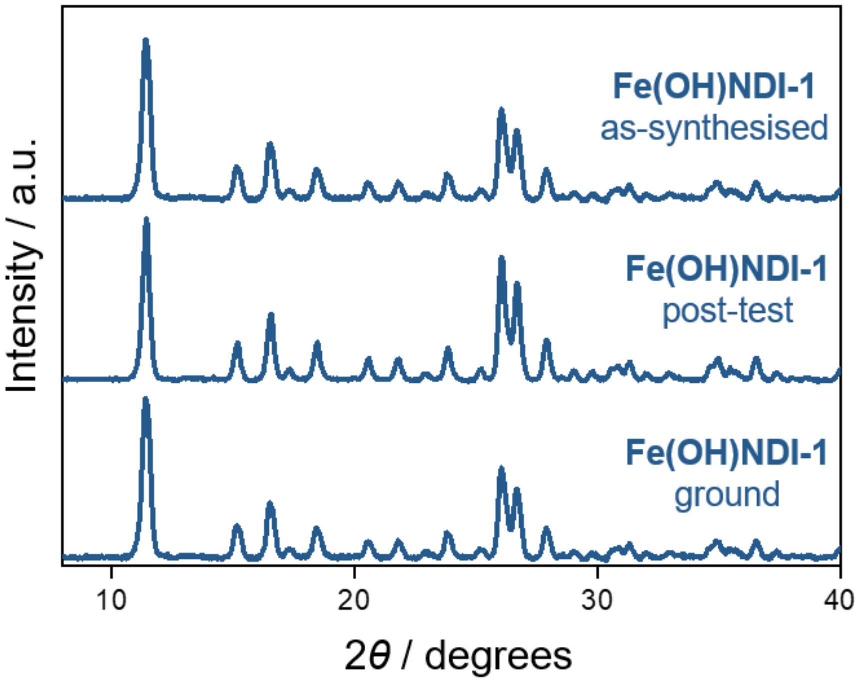

Figure 4.8. PXRD patterns demonstrating that the single crystal packing of **Fe(OH)NDI-1** is maintained throughout the resistivity process.

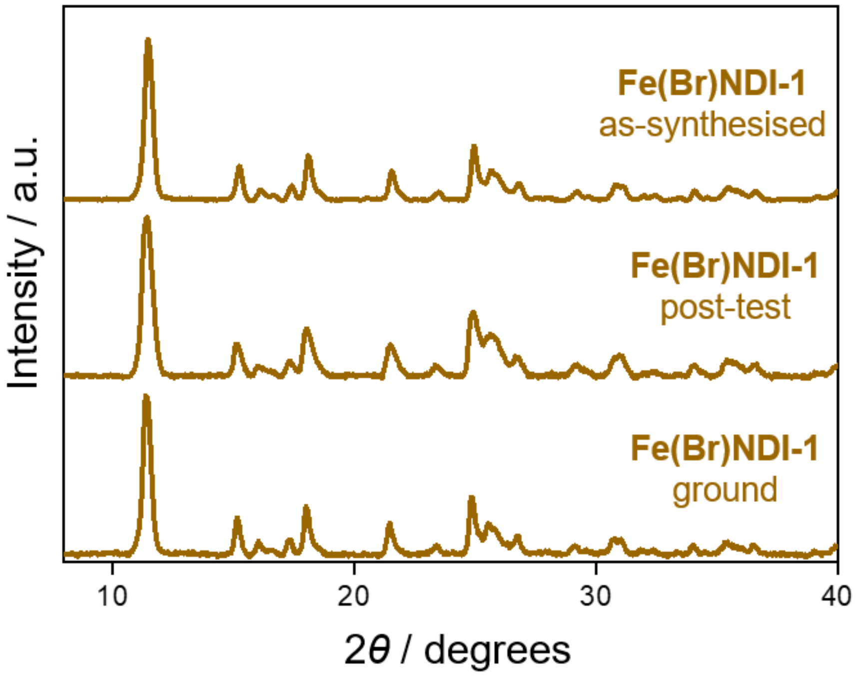

Figure 4.9. PXRD patterns demonstrating that the single crystal packing of **Fe(Br)NDI-1** is maintained throughout the resistivity process.

The results of the conductivity analysis conclusively show that the incorporation of a larger or smaller bridging anion affects the charge transport pathways in each isostructural material towards the order of conductivity **Fe(OH)NDI-1** > **Fe(Cl)NDI-1** > **Fe(Br)NDI-1**, validating the PXRD findings. The tests insinuate that **Fe(OH)NDI-1** would be the most proficient semiconductor, and the most promising candidate as active material in an energy storage. However, the conductivity results do not suggest the contribution of each charge transport pathway to the observed conductivity results, prompting theoretical calculations to be carried out.

4.2.9 THEORETICAL STUDIES

To delve deeper into the charge transport pathways of **Fe(OH)NDI-1** and **Fe(Br)NDI-1**, computational calculations were executed to pinpoint the locations of the frontier molecular orbitals and to determine the computational band gaps. Structures of **Fe(OH)NDI-1** and **Fe(Br)NDI-1** were adapted from the single crystal structure of **Fe(Cl)NDI-1**, and were optimised to take into account the larger or smaller bridging anion present (see the experimental details, section 4.5.1 for details). As a result of the optimised structures, different distances (Table 4.7) were observed between charge carriers within each of the established charge transport pathways (i.e., the pyrazolate backbone ((Fe–N–N–)∞) and the overlapped NDI layers), see Figure 4.10.

With reference to the calculations carried out for **Fe(Cl)NDI-1**, which established the HOMO on the pyrazolate backbone and the LUMO on the overlapped NDI layers, it was anticipated that **Fe(OH)NDI-1** and **Fe(Br)NDI-1**, being isostructural, would exist in similar positions. It was observed that the location of the frontier molecular orbitals in **Fe(OH)NDI-1** and **Fe(Br)NDI-1** were in the same areas in comparison to **Fe(Cl)NDI-1**, but rested on slightly different positions suggesting that there were subtle differences between each framework that led to different orbital arrangements.

In regards to the LUMO depictions located on and in-between NDI layers for each framework, orbital overlap is observed to lessen in the following order **Fe(OH)NDI-1** > **Fe(Cl)NDI-1** > **Fe(Br)NDI-1**, suggesting that charge transport between the LUMO orbitals would follow the same trend. Conversely, HOMO depictions are almost identical between **Fe(Cl)NDI-1** and **Fe(Br)NDI-1**, but when **Fe(OH)NDI-1** is viewed, they are located on slightly different areas of the Fe–pyrazolate backbone, due to the change from a halogen (Cl, Br) to a chalcogen (O). The fact that there is no overlap between HOMO orbitals suggests the order of conductivity originates from overlap between LUMO orbitals (i.e., the *through-space* pathway), rather than the overlap between constituents of the Fe–pyrazolate backbone (i.e., the *through-bond* pathway).

Resulting from the frontier molecular orbital calculations, HOMO-LUMO band gaps were generated for **Fe(OH)NDI-1** and **Fe(Br)NDI-1**, which were 2.22 eV and 2.39 eV respectively. The computational band gaps were of similar levels to those found experimentally by solid-state UV-vis measurements and were deemed in good agreement with each other.

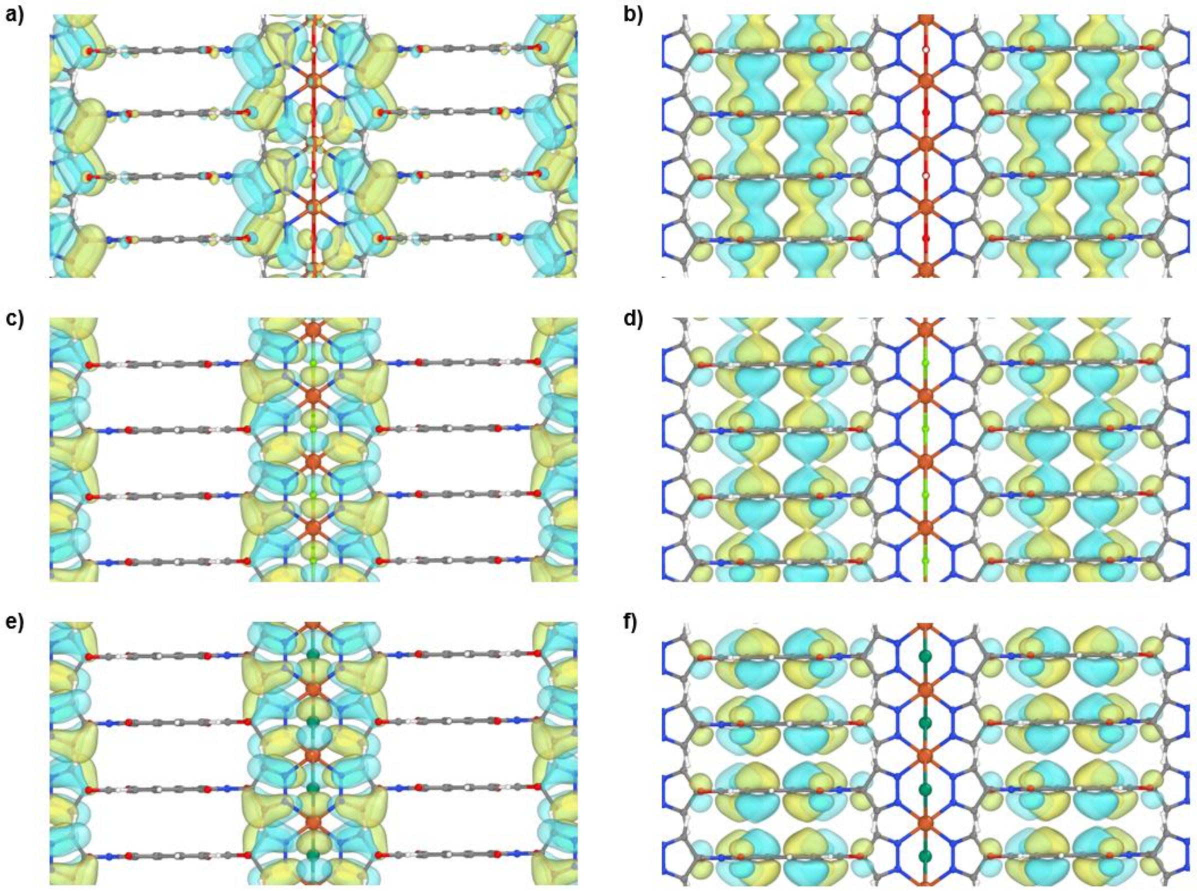

Figure 4.10. Calculated frontier molecular orbitals of a) HOMO and b) LUMO of **Fe(OH)NDI-1**, c) HOMO and d) LUMO of **Fe(Cl)NDI-1**, e) HOMO and f) LUMO of **Fe(Br)NDI-1**.

Further computational simulations were conducted to model scenarios of charge trapping within the frameworks of **Fe(OH)NDI-1** and **Fe(Br)NDI-1**, aiming to determine if polarons are generated within their structures. The simulations revealed that no polarons form in either of the two new frameworks, in contrast to the observation in **Fe(Cl)NDI-1**, where polarons were identified. If polarons were to manifest as predicted, leading to a mixed valency state (Fe^{2+}/Fe^{3+}), it would be expected that **Fe(Cl)NDI-1** would demonstrate a higher experimental conductivity measurement. Consequently, given that **Fe(OH)NDI-1** exhibits the highest experimental conductivity, but is shown to not form polarons *via* calculations, heavily suggests that polarons do not form within any of the Fe–pyrazolate frameworks presented in this study.

As an alternative to polaron formation dominating the conductivity, it was assumed that conductivity was driven by large-scale processes, such as delocalisation *via* bands. Calculations were then carried out to ascertain the electron effective mass (EEM), considering all directions except those corresponding to the interactions of the LUMO orbital (i.e., the *through-space* pathway). The resulting EEM values (Table 4.7) qualitatively align with the observations in the experimental conductivity measurements, further supporting the conclusion that polarons do not form in any of the range of Fe–pyrazolate PCPs.

Table 4.7. Band gaps and π–π distances generated computationally, with experimental conductivity measurements for **Fe(Cl)NDI-1**, **Fe(OH)NDI-1**, **Fe(Br)NDI-1**.

	Computational band gap / eV	Calculated π–π distance / Å	Electron effective mass	Conductivity / S cm^{-1}
Fe(Cl)NDI-1	2.46	3.47	2.04	2.84×10^{-5}
Fe(OH)NDI-1	2.22	3.34	1.59	2.21×10^{-4}
Fe(Br)NDI-1	2.39	3.56	2.15	2.44×10^{-7}

4.3 POST-SYNTHETIC VARIATION OF THE METAL CENTRE

To investigate the *through-bond* pathway, specifically the (Fe−N−N−)$_\infty$ backbone in **Fe(Cl)NDI-1**, our objective was to synthesise isostructural materials mirroring the topology of **Fe(Cl)NDI-1** while featuring diverse metal centres. Through the synthesis and examination of such isostructural variants, we sought to ascertain two critical aspects, (i) whether Fe emerges as the most conductive metal in this context, and (ii) to delineate the extent of Fe's contribution to the overall framework conductivity. Prior research has demonstrated that Fe–pyrazolate CPs exhibit enhanced conductivity due to their *through-bond* coordination pathway when compared to isostructural counterparts featuring alternative metal centres.[26] However, it is imperative to substantiate this claim by generating our own set of materials for empirical verification.

In order to generate isostructural materials with a different metal centre, multiple cobalt salts were screened ($CoCl_2$, $CoBr_2$, $Co(acac)_2$, $CoF_2{\cdot}4H_2O$) by reacting the appropriate metal chloride salt with NDI **1**, using conditions optimised for **Fe(Cl)NDI-1** in Chapter 3 (Figure 4.11 and more synthetic details in the synthetic methods, section 4.5.2). Reactions between $CoCl_2$, $Co(acac)_3$, and $CoBr_2$ and NDI **1** led to a solid product that appeared to be insoluble in all solvents, indicating that a CP had been synthesised in each case. The new materials were appropriately named **Co(Cl)NDI-1**, **Co(OH)NDI-1** and **Co(Br)NDI-1** after the metal salt that was used in their synthesis. Each new material was analysed by PXRD and compared with the Fe–pyrazolate PCP that contained the same anion (e.g., **Fe(Cl)NDI-1** with **Co(Cl)NDI-1**).

A comparison drawn between the PXRD patterns of **Co(Cl)NDI-1** and **Fe(Cl)NDI-1**, demonstrated a near-perfect match which confirms the two materials are isostructural (Figure 4.12). Slight shifting towards higher angles of 2θ is observed with respect to **Co(Cl)NDI-1** indicating it has a smaller *d*-spacings in comparison to **Fe(Cl)NDI-1**, suggesting that the distances between charge carriers are be lessened in **Co(Cl)NDI-1**. The smaller lattice of **Co(Cl)NDI-1** can be ascribed to the smaller atomic radii of the Co metal centre in comparison to Fe.

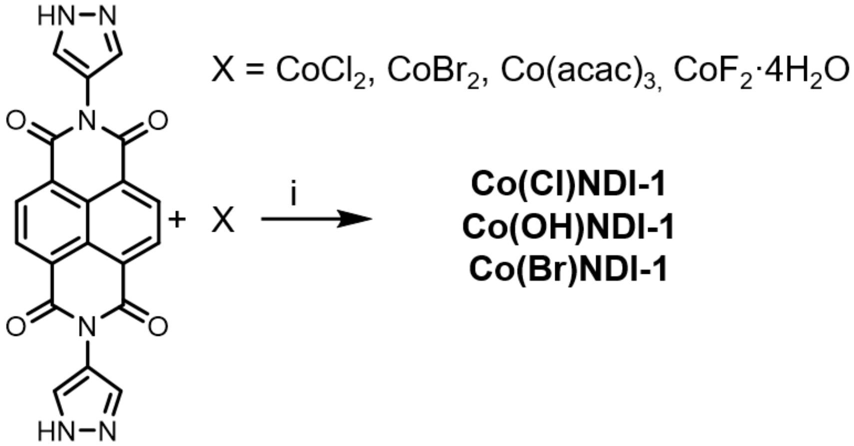

Figure 4.11. Synthesis of **Co(Cl)NDI-1**, **Co(OH)NDI-1**, **Co(Br)NDI-1**. Reagents and conditions: (i) DMF, μW: 200 °C, 15 min.

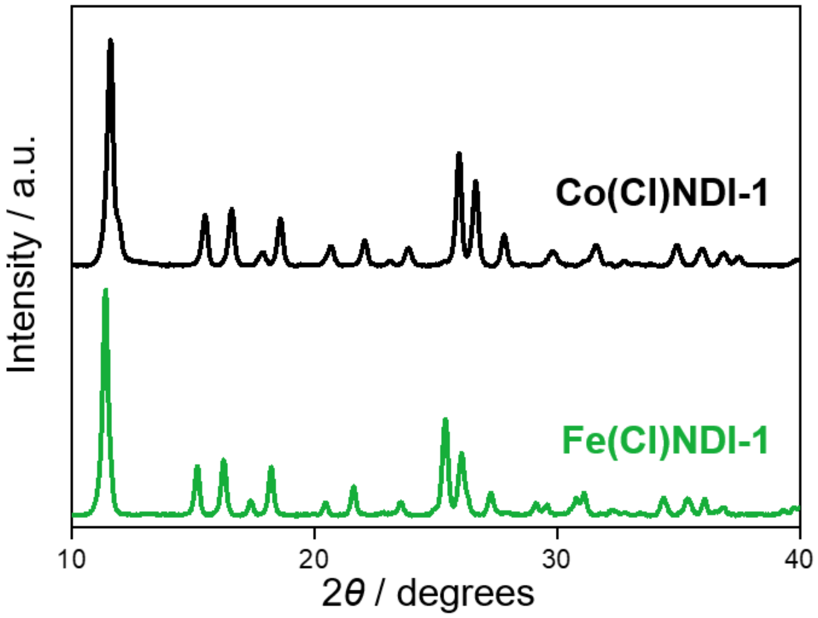

Figure 4.12. PXRD patterns of **Fe(Cl)NDI-1** and **Co(Cl)NDI-1**.

Comparative powder patterns between **Fe(OH)NDI-1** and **Co(OH)NDI-1** in addition to powder patterns of **Fe(Br)NDI-1** and **Co(Br)NDI-1** both show extra peaks in the patterns of both Co materials, indicating that there are additional crystalline materials present within both samples (Figure 4.13 and 4.14). In addition, both **Co(OH)NDI-1** and **Co(Br)NDI-1** demonstrated relatively weak diffraction patterns in comparison to **Fe(OH)NDI-1** and **Fe(Br)NDI-1** respectively, demonstrating the low crystallinity of both newly synthesised samples. Synthetic protocols that successfully formed **Fe(Cl)NDI-1** were also replicated for **Co(F)NDI-1** using CoF_2 in place of $FeCl_3$. However, no solid was obtained from the reaction mixture.

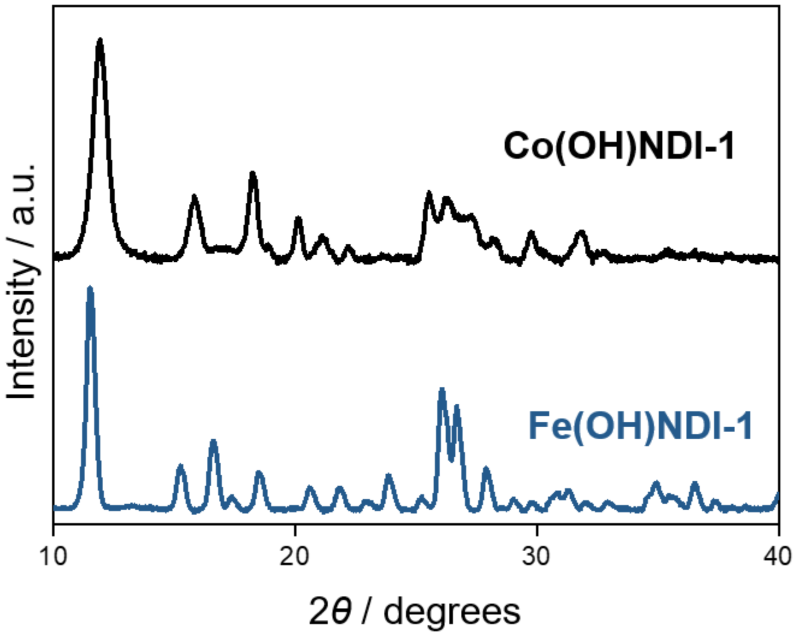

Figure 4.13. PXRD patterns of **Fe(OH)NDI-1** and **Co(OH)NDI-1**.

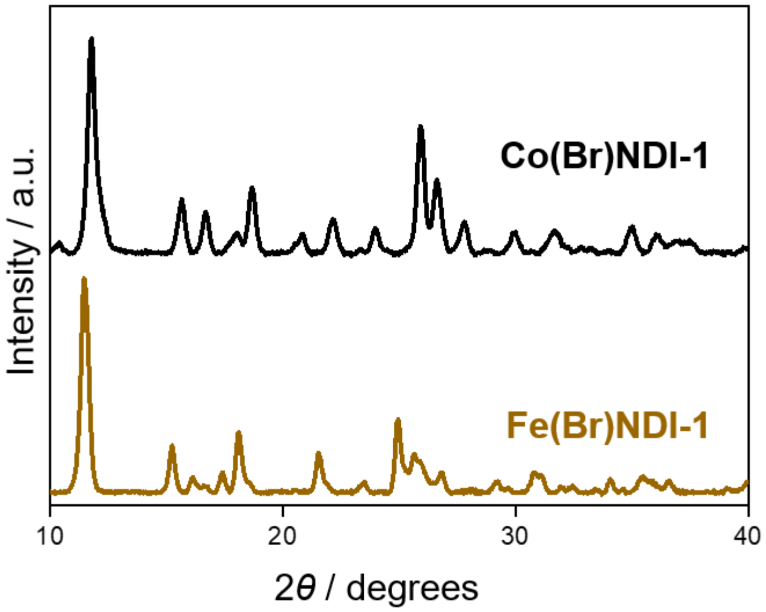

Figure 4.14. PXRD patterns of **Fe(Br)NDI-1** and **Co(Br)NDI-1**.

To facilitate purification and activation for purity analysis via EA and XRF, the Co-pyrazolate materials were immersed in DMSO for a duration of 7 days. However, after only 24 hours of soaking, it was observed that all three soaking solvents exhibited discoloration, indicating each of the frameworks were decomposing. As a comparative measure, the metal salts utilised in the synthesis of each framework were dissolved in a fresh batch of DMSO. The resulting colours of the dissolved metal salts corresponded to those observed in the soaked frameworks, leading us to the conclusion that both the metals and anions were being released from each framework. Consequently, effective washing and purification of the frameworks proved unattainable, necessitating the discontinuation of this line of synthetic approach.

4.4 CONCLUSIONS

The primary objective of this study was to synthesise a series of novel conductive PCPs that were isostructural to **Fe(Cl)NDI-1**, containing different bridging anions. The goal was achieved through an isoreticular strategy that pre-synthetically modified bridging ligands (OH, F, Br in place of Cl), a process aimed at influencing the spacing between charge carriers of the *through-bond* and *through-space* pathways observed in **Fe(Cl)NDI-1**. Two new isostructural frameworks, denoted as **Fe(OH)NDI-1** and **Fe(Br)NDI-1**, were successfully synthesised and confirmed to be of high purity. Framework **Fe(OH)NDI-1** contained an OH group as the bridging anion, while framework **Fe(Br)NDI-1** featured a Br group in the same position. PXRD analysis of the new frameworks revealed that *d*-spacing values of similar peaks in each PXRD pattern corresponded to larger or smaller lattice sizes based upon the size of the bridging anion. Therefore the PXRD analysis suggested that in comparison to **Fe(Cl)NDI-1**, **Fe(OH)NDI-1** had smaller distances between charge carriers in both *through-bond* and *through-space* charge transport pathways, while distances in **Fe(Br)NDI-1** were larger. Furthermore, **Fe(OH)NDI-1** was evaluated for its porosity, leading to the conclusion that it, similar to **Fe(Cl)NDI-1**, had limited porosity, which could potentially impede the diffusion of charge balancing ions such as Li^+.

Following the successful synthesis of the three isostructural frameworks, attempts were made to exchange metal centres within each of the synthesised structures. Unfortunately, endeavours to exchange metals were impeded by the observed instability of the materials in the washing solvents, ultimately necessitating the cessation of this particular line of synthesis.

To probe the conductive properties of **Fe(OH)NDI-1** and **Fe(Br)NDI-1** and draw comparisons with **Fe(Cl)NDI-1**, pressed pellet measurements were conducted. The conductivity results revealed a clear distinction in charge transport properties, with a conductivity trend of **Fe(OH)NDI-1** > **Fe(Cl)NDI-1** > **Fe(Br)NDI-1**, that was in line with what was observed in the PXRD analysis. Theoretical calculations supported the observation of lattice changes in **Fe(OH)NDI-1** and **Fe(Br)NDI-1** through PXRD, demonstrating alterations in the distances between charge carriers. Furthermore, band gap calculations placed HOMO orbitals on the pyrazolate backbone, and LUMO orbitals between the π-overlapped NDI units, demonstrating that there were two active charge transport pathways within each framework. Calculated band gaps were consistent with other semiconducting materials. Polaron calculations demonstrated that, in conjunction with experimental conductivity results, polarons were unlikely to form in the Fe–pyrazolate frameworks. EEM calculations then demonstrated a qualitative match with experimental conductivity results, confirming that charge travelled *via* a large-scale process such as bands.

The successful synthesis of this series of Fe–pyrazolate PCPs, featuring two charge transport pathways in one framework, represents to our knowledge the first time that anion bridges have been substituted with an isoreticular strategy that resulted in a change in the conductivity of the material. These results hold the potential for use of this pre-synthetic anion-swapping strategy towards designing new conductive PCPs in the future based upon the Fe–pyrazolate backbone and overlap of NDI linkers. In particular, with regards to **Fe(Cl)NDI-1** and **Fe(OH)NDI-1**, additional empirical studies would be highly valuable in ascertaining the feasibility of Li+ ion access to redox-active sites within the constrained pores, thereby establishing their potential utility in energy storage applications.

4.5 EXPERIMENTAL DETAILS

General details on materials and research methods as well as additional data for this Chapter can be found in the Appendix.

4.5.1 COMPUTATIONAL ANALYSIS

All first-principles calculations were carried out using the implementation of hybrid DFT within CP2K.[27] We employ an implementation of the B3LYP hybrid DFT functional where long-range HF exchange integrals are truncated,[28,29] where a truncation radius of 6 Å is found to be well converged with regards to lattice parameters and band gaps.

The computational cost of hybrid calculations is reduced by the auxiliary density matrix method (ADMM)[30] in which exchange integrals are approximated through mapping onto smaller, more localised basis sets. We use double-ζ basis sets optimised from molecular calculations (MOLOPT)[31] and Goedecker–Teter–Hutter pseudopotentials available within CP2K.[32–34] Five multigrids were applied with a relative cutoff of 60 Ry and the finest grid having a cutoff of 600 Ry. As CP2K only samples the

Γ-point, properties were converged with respect to supercell size as opposed to *k*-point sampling in reciprocal space. We use a 1 × 2 × 2 supercell of the standardized primitive cell.

In order to look for polaron geometries, we make a radial distortion around Fe sites by pushing neighbouring ions away 0.2 Å, encouraging an excess electron added to the system to localise on a specified site. If the charge delocalises during geometry optimisation then the polaron is deemed to not be stable. A similar approach was has been taking in previous studies of polarons.[35,36]

Band structures and effective masses are calculated using the implementation of DFT+U in VASP.[37] The PBE functional[38] is employed with a value of U = 4.0 eV on the d-orbitals of Fe. Band structure plots and special k-point paths for the standardised primitive cell are generated using the Sumo package.[39] Effective masses are calculated in the direction corresponding to transport between layers of the ligands.

4.5.2 SYNTHETIC METHODS

GENERAL PROCEDURE FOR 2D COORDINATION POLYMERS

A microwave vial was equipped with a magnetic stirrer bar and charged with NDI **1** (1.0 equiv.), metal salt (2.0 equiv.) and anhydrous DMF (4 or 12 mL). The mixture was subjected to dynamic microwave irradiation (200 °C, 300 W) under high stirring for 15 min. Upon cooling to rt, the reaction mixture was filtered and washed over the filter with DMSO until the washings appeared colourless, followed by absolute EtOH. The solids were then soaked in acetone that was frequently exchanged for 1 week and then dried at 180 °C for 12 h in a vacuum oven (5 mbar) to yield the appropriate activated 2D coordination polymer.

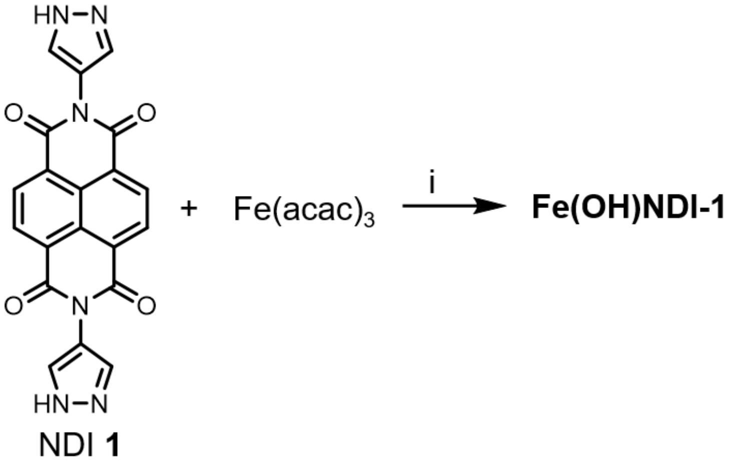

Figure 4.15. Synthesis of **Fe(OH)NDI-1**. Reagents and conditions: (i) DMF, μW: 200 °C, 15 min, 86%.

[Fe(OH)NDI-1]. Applying the ***General Procedure*** for 2D coordination polymer synthesis described above, **Fe(OH)NDI-1** (201.3 mg, 0.43 mmol, 86 %) was prepared from NDI **1** (200 mg, 0.5 mmol, 1.0 equiv.) and Fe(acac)$_3$ (203.5 mg, 1.0 mmol, 2.0 equiv.) as a brown powder. **Elemental analysis:** Anal. calc for formula: $C_{20}H_9FeN_6O_5$ C, 51.20; H, 1.93; Fe, 11.90; N, 17.91; O, 17.05. Anal. found: C, 51.20; H, 2.81; N, 17.60, (0 % C, +0.88 % H, –031 % N).

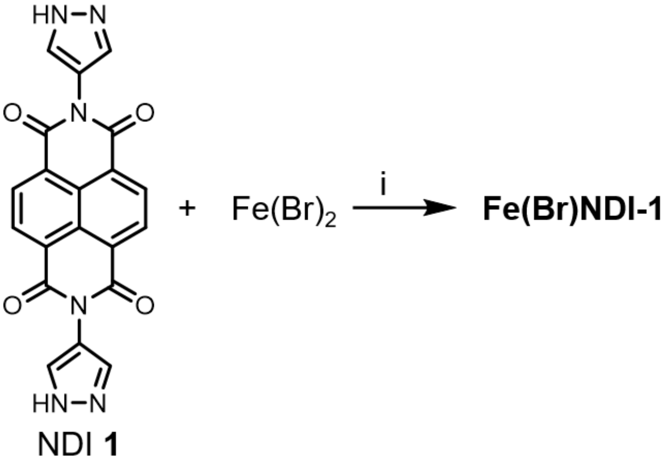

Figure 4.16. Synthesis of **Fe(Br)NDI-1**. Reagents and conditions: (i) DMF, µW: 200 °C, 15 min, 76%.

[Fe(Br)NDI-1]. Applying the ***General Procedure*** for 2D coordination polymer synthesis described above, Fe(Br)NDI-1 (202.5 mg, 0.38 mmol, 76 %) was prepared from NDI 1 (200 mg, 0.5 mmol, 1.0 equiv.) and $FeBr_2$ (215.65 mg, 1.0 mmol, 2.0 equiv.) as a dark red powder. Elemental analysis: Anal. calc for formula: $C_{20}H_8BrFeN_6O_4$ C, 45.15; H, 1.52; Br, 15.02; Fe, 10.50; N, 15.80; O, 12.03. Anal. found: C, 47.45; H, 2.14; N, 16.22; Br, 6.95 (+2.30 % C, +0.63 % H, +0.42 % N,).

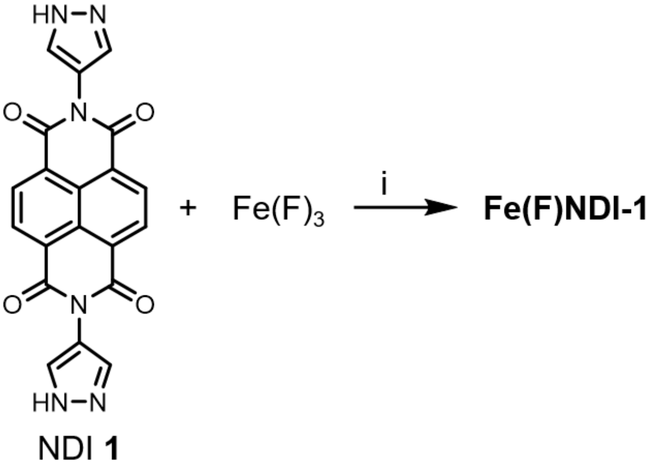

Figure 4.17. Synthesis of **Fe(F)NDI-1**. Reagents and conditions: (i) DMF, µW: 200 °C, 15 min, 84%.

[Fe(F)NDI-1]. Applying the ***General Procedure*** for 2D coordination polymer synthesis described above, **Fe(F)NDI-1** (199.3 mg, 0.42 mmol, 84 %) was prepared from NDI **1** (200 mg, 0.5 mmol, 1.0 equiv.) and FeF_3 (113 mg, 1.0 mmol, 2.0 equiv.) as a red powder. **Elemental analysis:** Anal. calc for formula: $C_{20}H_8FFeN_6O_4$ C, 50.98; H, 1.71; F, 4.03; Fe, 11.85; N, 17.84; O, 13.58. Anal. found: C, 47.58; H, 1.90; N, 15.19, (–3.40 % C, +0.19 % H, –2.65 % N).

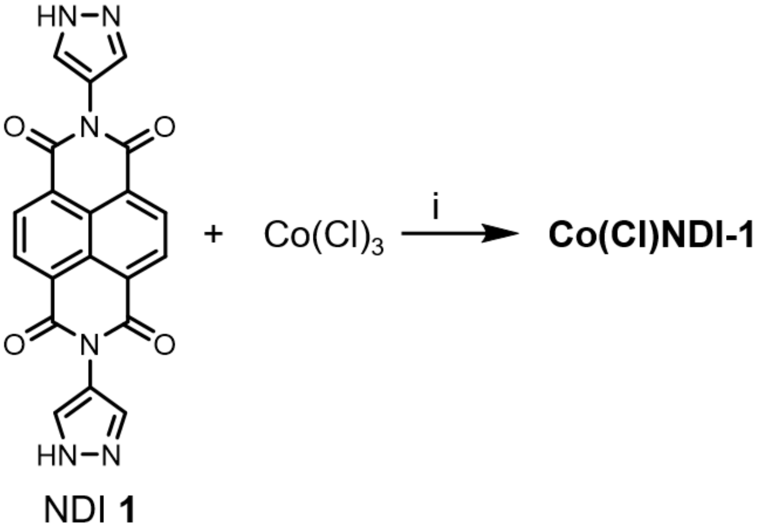

Figure 4.18. Synthesis of **Co(Cl)NDI-1**. Reagents and conditions: (i) DMF, μW: 200 °C, 15 min, 78%.

[Co(Cl)NDI-1]. Applying the ***General Procedure*** for 2D coordination polymer synthesis described above, **Co(Cl)NDI-1** (189.2 mg, 0.39 mmol, 78 %) was prepared from NDI **1** (200 mg, 0.5 mmol, 1.0 equiv.) and $CoCl_2$ (130 mg, 1.0 mmol, 2.0 equiv.) as a light brown powder.

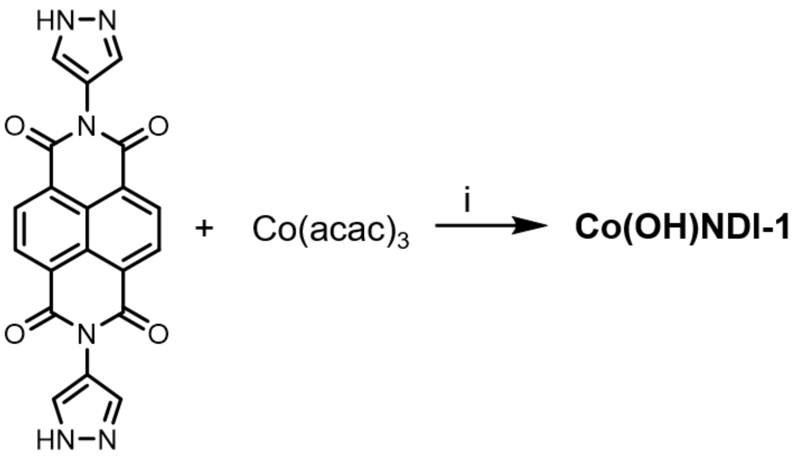

NDI **1**

Figure 4.19. Synthesis of **Co(OH)NDI-1**. Reagents and conditions: (i) DMF, μW: 200 °C, 15 min, 78%.

[Co(OH)NDI-1]. Applying the ***General Procedure*** for 2D coordination polymer synthesis described above, **Co(OH)NDI-1** (185 mg, 0.39 mmol, 78 %) was prepared from NDI **1** (200 mg, 0.5 mmol, 1.0 equiv.) and Fe(acac)$_3$ (356.26 mg, 1.0 mmol, 2.0 equiv.) as a dark brown powder.

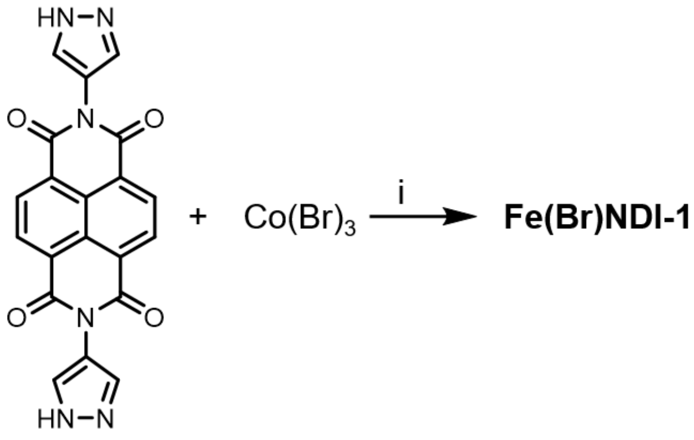

NDI **1**

Figure 4.20. Synthesis of **Co(Br)NDI-1**. Reagents and conditions: (i) DMF, μW: 200 °C, 15 min, 70%.

[Co(Br)NDI-1]. Applying the ***General Procedure*** for 2D coordination polymer synthesis described above, **Co(Br)NDI-1** (189.3 mg, 0.35 mmol, 70 %) was prepared from NDI **1** (200 mg, 0.5 mmol, 1.0 equiv.) and Co(Br)$_3$ (218.74 mg, 1.0 mmol, 2.0 equiv.) as a brown powder.

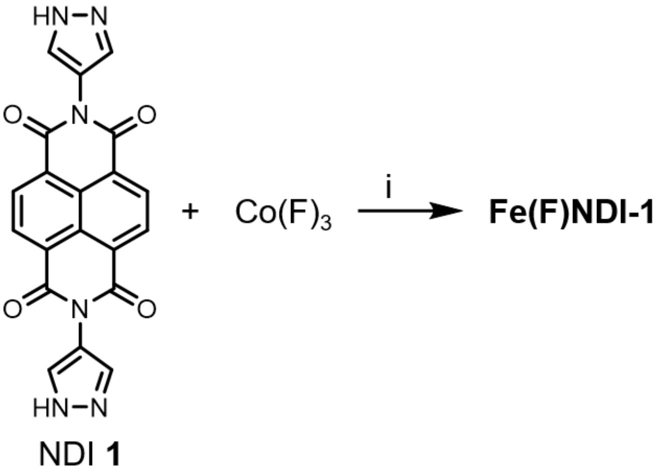

Figure 4.21. Synthesis of **Co(F)NDI-1**. Reagents and conditions: (i) DMF, µW: 200 °C, 15 min.

[Co(F)NDI-1] attempted preparation. Applying the ***General Procedure*** for 2D coordination polymer synthesis described above, **Co(F)NDI-1** was attempted to be prepared from NDI **1** (200 mg, 0.5 mmol, 1.0 equiv.) and $FeF_2{\cdot}4H_2O$ (356.26 mg, 1.0 mmol, 2.0 equiv.).

4.6 REFERENCES

(1) Furukawa, H.; Cordova, K. E.; O'Keeffe, M.; Yaghi, O. M. The Chemistry and Applications of Metal-Organic Frameworks. *Science* **2013**, *341*, 1230444. https://doi.org/10.1126/science.1230444.

(2) Wang, Y.; Huang, N.-Y.; Shen, J.-Q.; Liao, P.-Q.; Chen, X.-M.; Zhang, J.-P. Hydroxide Ligands Cooperate with Catalytic Centers in Metal–Organic Frameworks for Efficient Photocatalytic CO2 Reduction. *J. Am. Chem. Soc.* **2018**, *140*, 38–41. https://doi.org/10.1021/jacs.7b10107.

(3) Das, M. C.; Guo, Q.; He, Y.; Kim, J.; Zhao, C.-G.; Hong, K.; Xiang, S.; Zhang, Z.; Thomas, K. M.; Krishna, R.; Chen, B. Interplay of Metalloligand and Organic Ligand to Tune Micropores within Isostructural Mixed-Metal Organic Frameworks (M′MOFs) for Their Highly Selective Separation of Chiral and Achiral Small Molecules. *J. Am. Chem. Soc.* **2012**, *134*, 8703–8710. https://doi.org/10.1021/ja302380x.

(4) Herm, Z. R.; Wiers, B. M.; Mason, J. A.; Baten, J. M. van; Hudson, M. R.; Zajdel, P.; Brown, C. M.; Masciocchi, N.; Krishna, R.; Long, J. R. Separation of Hexane Isomers in a Metal-Organic Framework with Triangular Channels. *Science* **2013**, *340*, 960–964. https://doi.org/10.1126/science.1234071.

(5) Calbo, J.; Golomb, M. J.; Walsh, A. Redox-Active Metal–Organic Frameworks for Energy Conversion and Storage. *J. Mater. Chem. A* **2019**, *7*, 16571–16597. https://doi.org/10.1039/C9TA04680A.

(6) Li, J.; Kumar, A.; Johnson, B. A.; Ott, S. Experimental Manifestation of Redox-Conductivity in Metal-Organic Frameworks and Its Implication for Semiconductor/Insulator Switching. *Nat. Commun.* **2023**, *14*, 1–10. https://doi.org/10.1038/s41467-023-40110-6.

(7) Britt, D.; Tranchemontagne, D.; Yaghi, O. M. Metal-Organic Frameworks with High Capacity and Selectivity for Harmful Gases. *Proc. Natl. Acad. Sci. U.S.A.* **2008**, *105*, 11623–11627. https://doi.org/10.1073/pnas.0804900105.

(8) Mai, Z.; Liu, D. Synthesis and Applications of Isoreticular Metal–Organic Frameworks IRMOFs-n (n = 1, 3, 6, 8). *Cryst. Growth Des.* **2019**, *19*, 7439–7462. https://doi.org/10.1021/acs.cgd.9b00879.

(9) Yaghi, O. M.; Kalmutzki, M. J.; Diercks, C. S. *Introduction to Reticular Chemistry: Metal-Organic Frameworks and Covalent Organic Frameworks*; John Wiley & Sons, 2019.

(10) Dutta, A.; Pan, Y.; Liu, J.-Q.; Kumar, A. Multicomponent Isoreticular Metal-Organic Frameworks: Principles, Current Status and Challenges. *Coord. Chem. Rev.* **2021**, *445*, 214074. https://doi.org/10.1016/j.ccr.2021.214074.

(11) Xie, L. S.; Skorupskii, G.; Dincă, M. Electrically Conductive Metal–Organic Frameworks. *Chem. Rev.* **2020**, *120*, 8536–8580. https://doi.org/10.1021/acs.chemrev.9b00766.

(12) Park, S. S.; Hontz, E. R.; Sun, L.; Hendon, C. H.; Walsh, A.; Van Voorhis, T.; Dincă, M. Cation-Dependent Intrinsic Electrical Conductivity in Isostructural Tetrathiafulvalene-Based Microporous Metal–Organic Frameworks. *J. Am. Chem. Soc.* **2015**, *137*, 1774–1777. https://doi.org/10.1021/ja512437u.

(13) Xie, L. S.; Park, S. S.; Chmielewski, M. J.; Liu, H.; Kharod, R. A.; Yang, L.; Campbell, M. G.; Dincă, M. Isoreticular Linker Substitution in Conductive Metal–Organic Frameworks with Through-Space Transport Pathways. *Angew. Chem. Int. Ed.* **2020**, *59*, 19623–19626. https://doi.org/10.1002/anie.202004697.

(14) Rieth, A. J.; Wright, A. M.; Skorupskii, G.; Mancuso, J. L.; Hendon, C. H.; Dincă, M. Record-Setting Sorbents for Reversible Water Uptake by Systematic Anion Exchanges in Metal–Organic Frameworks. *J. Am. Chem. Soc.* **2019**, *141*, 13858–13866. https://doi.org/10.1021/jacs.9b06246.

(15) Lv, H.; Ma, C.; Zhu, Z.; Li, Q.-H.; Chen, S.; Wang, F.; Li, S. A Light-Sensitive Metal-Organic Framework Composite Encapsulated by Ion Exchange for Photocatalytic Organic Reaction. *J. Solid. State. Chem.* **2023**, *322*, 123948. https://doi.org/10.1016/j.jssc.2023.123948.

(16) Rosen, A. S.; Notestein, J. M.; Snurr, R. Q. High-Valent Metal–Oxo Species at the Nodes of Metal–Triazolate Frameworks: The Effects of Ligand Exchange and Two-State Reactivity for C−H Bond Activation. *Angew. Chem.* **2020**, *132*, 19662–19670. https://doi.org/10.1002/ange.202004458.

(17) Xue, Z.; Zheng, J.-J.; Nishiyama, Y.; Yao, M.-S.; Aoyama, Y.; Fan, Z.; Wang, P.; Kajiwara, T.; Kubota, Y.; Horike, S.; Otake, K.; Kitagawa, S. Fine Pore-Structure Engineering by Ligand Conformational Control of Naphthalene Diimide-Based Semiconducting Porous Coordination Polymers for Efficient Chemiresistive Gas Sensing. *Angew. Chem. Int. Ed.* **2023**, *62*. https://doi.org/10.1002/anie.202215234.

(18) Wan, J.; Li, J.; Xiao, Z.; Tang, D.; Wang, B.; Xiao, Y.; Xu, W. Transition Bimetal Based MOF Nanosheets for Robust Aqueous Zn Battery. *Front. Mater.* **2020**, *7*. https://doi.org/10.3389/fmats.2020.00194.

(19) Yuan, S.; Huang, L.; Huang, Z.; Sun, D.; Qin, J.-S.; Feng, L.; Li, J.; Zou, X.; Cagin, T.; Zhou, H.-C. Continuous Variation of Lattice Dimensions and Pore Sizes in Metal–Organic Frameworks. *J. Am. Chem. Soc.* **2020**, *142*, 4732–4738. https://doi.org/10.1021/jacs.9b13072.

(20) Jasuja, H.; Burtch, N. C.; Huang, Y.; Cai, Y.; Walton, K. S. Kinetic Water Stability of an Isostructural Family of Zinc-Based Pillared Metal–Organic Frameworks. *Langmuir* **2013**, *29*, 633–642. https://doi.org/10.1021/la304204k.

(21) Zhou, C.-C.; Yan, H.; Liu, H.-T.; Li, R.-Y.; Lu, J.; Wang, S.-N.; Li, Y.-W. Proton Conductivity Studies on Five Isostructural MOFs with Different Acidity Induced by Metal Cations. *New J. Chem.* **2020**, *44*, 17821–17830. https://doi.org/10.1039/D0NJ04179C.

(22) Wang, H.-N.; Sun, H.-X.; Fu, Y.-M.; Meng, X.; Zou, Y.-H.; He, Y.-O.; Yang, R.-G. Varied Proton Conductivity and Photoreduction CO 2 Performance of Isostructural Heterometallic Cluster Based Metal–Organic Frameworks. *Inorg. Chem. Front.* **2021**, *8*, 4062–4071. https://doi.org/10.1039/D1QI00742D.

(23) Leong, C. F.; Chan, B.; Faust, T. B.; Turner, P.; D’Alessandro, D. M. Electronic, Optical, and Computational Studies of a Redox-Active Napthalenediimide-Based Coordination Polymer. *Inorg. Chem.* **2013**, *52*, 14246–14252. https://doi.org/10.1021/ic402173z.

(24) Tauc, J.; Grigorovici, R.; Vancu, A. Optical Properties and Electronic Structure of Amorphous Germanium. *Phys. Status Solidi (b)* **1966**, *15*, 627–637. https://doi.org/10.1002/pssb.19660150224.

(25) Slater, J. C. Atomic Radii in Crystals. *J. Chem. Phys.* **2004**, *41*, 3199–3204. https://doi.org/10.1063/1.1725697.

(26) Sun, L.; Hendon, C. H.; Park, S. S.; Tulchinsky, Y.; Wan, R.; Wang, F.; Walsh, A.; Dincă, M. Is Iron Unique in Promoting Electrical Conductivity in MOFs? *Chem. Sci.* **2017**, *8*, 4450–4457. https://doi.org/10.1039/C7SC00647K.

(27) VandeVondele, J.; Krack, M.; Mohamed, F.; Parrinello, M.; Chassaing, T.; Hutter, J. Quickstep: Fast and Accurate Density Functional Calculations Using a Mixed Gaussian and Plane Waves Approach. *Comput. Phys. Commun.* **2005**, *167*, 103–128. https://doi.org/10.1016/j.cpc.2004.12.014.

(28) Guidon, M.; Hutter, J.; VandeVondele, J. Robust Periodic Hartree−Fock Exchange for Large-Scale Simulations Using Gaussian Basis Sets. *J. Chem. Theory Comput.* **2009**, *5*, 3010–3021. https://doi.org/10.1021/ct900494g.

(29) Spencer, J.; Alavi, A. Efficient Calculation of the Exact Exchange Energy in Periodic Systems Using a Truncated Coulomb Potential. *Phys. Rev. B* **2008**, *77*, 193110. https://doi.org/10.1103/PhysRevB.77.193110.

(30) Guidon, M.; Hutter, J.; VandeVondele, J. Auxiliary Density Matrix Methods for Hartree−Fock Exchange Calculations. *J. Chem. Theory Comput.* **2010**, *6*, 2348–2364. https://doi.org/10.1021/ct1002225.

(31) VandeVondele, J.; Hutter, J. Gaussian Basis Sets for Accurate Calculations on Molecular Systems in Gas and Condensed Phases. *J. Chem. Phys.* **2007**, *127*, 114105. https://doi.org/10.1063/1.2770708.

(32) Krack, M. Pseudopotentials for H to Kr Optimized for Gradient-Corrected Exchange-Correlation Functionals. *Theor. Chem. Acc.* **2005**, *114*, 145–152. https://doi.org/10.1007/s00214-005-0655-y.

(33) Goedecker, S.; Teter, M.; Hutter, J. Separable Dual-Space Gaussian Pseudopotentials. *Phys. Rev. B* **1996**, *54*, 1703–1710. https://doi.org/10.1103/PhysRevB.54.1703.

(34) Hartwigsen, C.; Goedecker, S.; Hutter, J. Relativistic Separable Dual-Space Gaussian Pseudopotentials from H to Rn. *Phys. Rev. B* **1998**, *58*, 3641–3662. https://doi.org/10.1103/PhysRevB.58.3641.

(35) Quirk, J. A.; Lazarov, V. K.; McKenna, K. P. Electronic Properties of 112 and 110 Twin Boundaries in Anatase TiO2. *Adv. Theory Simul.* **2019**, *2*, 1900157. https://doi.org/10.1002/adts.201900157.

(36) Elmaslmane, A. R.; Watkins, M. B.; McKenna, K. P. First-Principles Modeling of Polaron Formation in TiO2 Polymorphs. *J. Chem. Theory Comput.* **2018**, *14*, 3740–3751. https://doi.org/10.1021/acs.jctc.8b00199.

(37) Kresse, G.; Furthmüller, J. Efficient Iterative Schemes for *Ab Initio* Total-Energy Calculations Using a Plane-Wave Basis Set. *Phys. Rev. B* **1996**, *54*, 11169–11186. https://doi.org/10.1103/PhysRevB.54.11169.

(38) Perdew, J. P.; Burke, K.; Ernzerhof, M. Generalized Gradient Approximation Made Simple. *Phys. Rev. Lett.* **1996**, *77*, 3865–3868. https://doi.org/10.1103/PhysRevLett.77.3865.

(39) Ganose, A. M.; Jackson, A. J.; Scanlon, D. O. Sumo: Command-Line Tools for Plotting and Analysis of Periodic *ab Initio* Calculations. *J. open source softw.* **2018**, *3*, 717. https://doi.org/10.21105/joss.00717.

CHAPTER 5 |

FORMATE-BRIDGED COORDINATION POLYMERS WITH HIGHLY CONDUCTIVE *THROUGH-SPACE* CHARGE TRANSPORT PATHWAYS

SYNOPSIS

This Chapter is dedicated to the exploration of alternative linkers to contrast with the anion bridges (Cl, OH, Br) within the series of Fe–pyrazolate PCPs discussed in Chapters 3 and 4. The goal is to produce conductive frameworks that preserve the Fe–pyrazolate backbone and NDI π-orbital overlap observed in **Fe(Cl)NDI-1**, while accessing a new topological framework and explore its conductive properties. By employing synthetic methodologies from Chapter 3, a novel non-porous framework featuring formate bridges between Fe metal centres and close proximity between NDI units was synthesised. The framework demonstrated redox activity and remarkable thermal stability in the absence of a pyrazolate backbone. Conductivity tests on pressed pellet samples using a two-probe setup revealed a high conductivity reading of 3.27×10^{-4} S cm^{-1}. To elucidate the dominant charge transport pathway, two additional isostructural frameworks were synthesised containing Co (**CoCPNDI-1**) and Mn (**MnCPNDI-1**) metal centres. A comparative analysis between the three isostructural framework suggested that charge transport primarily occurs *through-space*, assumedly *via* the π-orbitals of the NDI molecules. This study underscores the profound impact of altering a single component in a framework and suggests that the combined approach of linker replacement and isostructural design holds significant promise for the development of the next generation of energy storage materials.

ACKNOWLEDGEMENTS

The following people are gratefully acknowledged for their contribution to this chapter: Dr Adrian C. Whitwood for collecting crystallographic data and solving the X-ray crystal structure of **FeCPNDI-1**, **CoCPNDI-1** and **MnCPNDI-1**. Crystal Yu for the extensive work to determine the best synthetic conditions for **FeCPNDI-1**. Dr Stuart Cavill for providing access to a Keithly source meter to enable conductivity measurements.

5.1 INTRODUCTION

Coordination polymers (CPs) constitute systematically organised and rigid frameworks characterised by repeating units.[1] The ability to pre-synthetically modify CP constituent units offers an almost limitless range of possibilities for the field of CPs, allowing for tailored adjustments of properties.[2] One experimental design strategy that was pursued in Chapter 4, is known as isoreticular design, and revolves around creating isostructural materials with topologically identical frameworks.[3] The resulting materials yielded from isostructural design often display varying pore sizes or additional functional groups, taking advantage of a single advantageous topological net.[4] However, isostructural materials are constrained by a single isoreticular net, imposing limitations on property tuning. Therefore, to broaden the spectrum of accessible properties, the substitution of specific repeating units within a CP can give rise to novel topological nets, leading to the emergence of desirable properties and enabling a comparative analysis with the previous net.

To target specific linkers and alter the topology of a CP framework, several critical factors must be taken into account for successful modification. Firstly, the new linker should offer multiple coordination sites that are compatible with the existing metal centre. A study conducted by Sun et al.[5] explored the use of four distinct bidentate linkers with different metal centres, leading to the emergence of four distinct topological families (Figure 5.1a). The results indicated that Fe was the optimal metal to enhance *through-bond* conductive pathways in porous coordination polymers (PCPs) across these families. However, Sun et al. report that over half of the frameworks were missing among the four topological families, suggesting incompatibilities between certain metals and linkers. Secondly, the coordination modes (e.g., syn-syn, syn-anti) of the new linker should be different from the outgoing linker. For instance, Duan and colleagues developed a series of 3d–4f CPs with 1D and 3D dimensionality.[6] The six frameworks exhibited different topological nets (of which two can be viewed in Figure 5.1b, c), influenced by the multiple available coordination modes of the formate and gly bridging ligands, that ultimately dictated the resulting framework topology. Notably, three of the frameworks displayed magnetocaloric effects, indicating potential for further development of similarly-connected materials.

In the context of the Fe–pyrazolate frameworks discussed in Chapters 3 and 4, this study aims to target the replacement of the corresponding anion linkers (i.e., OH, Cl, Br). The objective is to access different geometries distinct from the isostructural network of the Fe–pyrazolate PCPs, while retaining the conductive Fe metal centre, the redox-active NDI **1** ligands, and the chemically and thermally stable Fe–pyrazolate backbone. By altering the π-2 bridging ligand, the geometry around the metal centre has the potential to change, thereby affecting the orbital overlap of the NDI **1** ligands, possibly enhancing conductive *through-space* pathways. Furthermore, porosity could be induced, providing access to the redox centres of the NDI **1** ligand, which were previously inaccessible in the range of Fe–pyrazolate

PCPs in chapters 3 and 4. Ultimately, the objective of this work is to create a new framework capable of serving as an active material in an energy storage device.

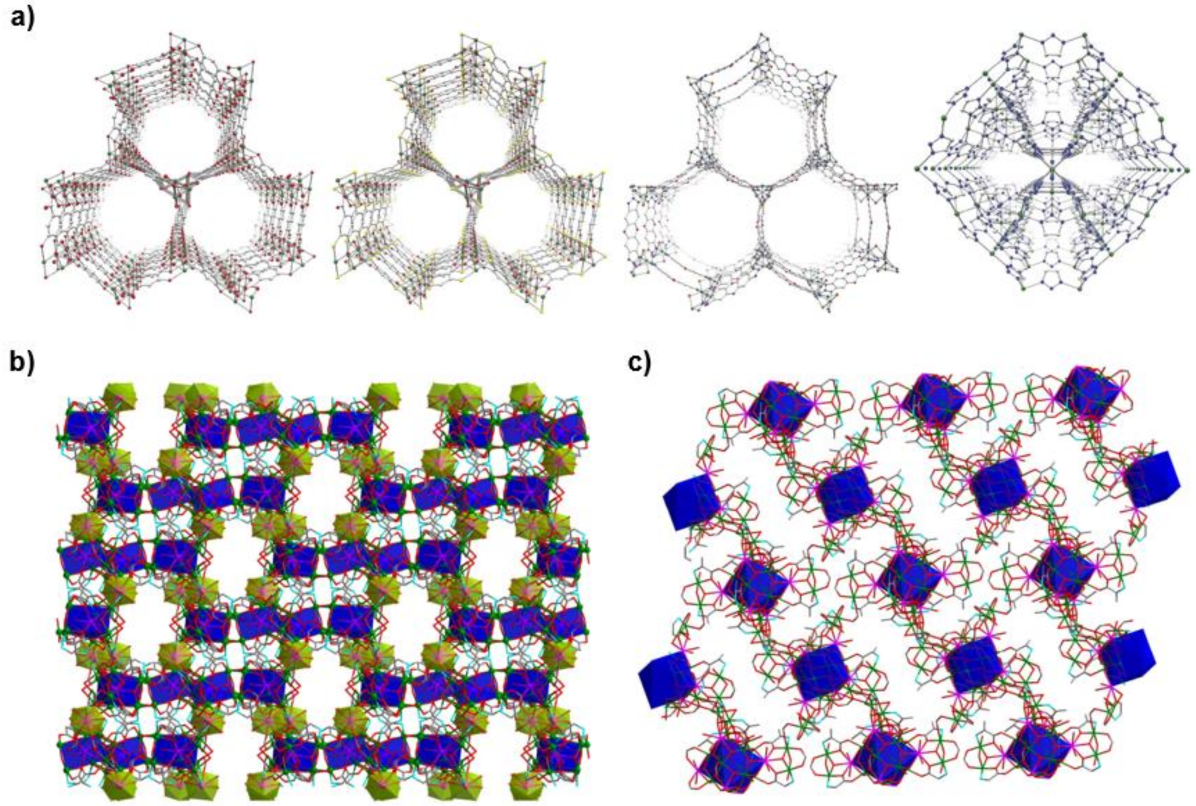

Figure 5.1. Structures of (a) The four families of PCPs, copied from the work of Sun et al.[5] (b) Gd–Cu CP with alternating syn-syn and syn-anti formate bridge orientations(c) Gd–Cu CP with syn-syn and syn-syn/anti bridge orientations, both images copied from the work of Duan and Colleagues.[6]

5.2 RESULTS AND DISCUSSION

5.2.1 SYNTHESIS OF FECPNDI-1

To strategically modulate the coordination environment surrounding the central Fe metal, a more intricate linker than those employed in the Fe–pyrazolate structures (Cl, OH, Br) was chosen – specifically, formate. The introduction of a formate bridge had the potential to vastly expand the potential growth directions of a framework as a consequence of the manifold coordination modes exhibited by formate. A potential outcome of a novel framework net would be, for example, alternative *through-space* packing interactions between NDI **1** ligands or additional porosity. The novel packing configurations would offer an alternative perspective to the arrangements observed in the Fe–pyrazolate frameworks discussed in chapters 3 and 4, facilitating comparisons between the two materials towards in relation to semiconductivity.

To successfully integrate formate bridges into a framework containing Fe metal centres and NDI **1** units, synthetic procedures proved effective to generate **FeCPNDI-1**. The procedure involved subjecting FeCl·6H_2O and NDI **1** to microwave irradiation in DMF, in the presence of 100 equivalents of formic acid , resulting in a brown solid, which was isolated *via* filtration and subsequent washing on the filter with DMSO and EtOH. The experimental procedure was refined in order to achieve full consumption of the NDI **1** starting material, while using the lowest possible temperature and amount of formic acid (see the appendix, Section 8.1.15, Figure 8.36 and Figure 8.37), resulting with the procedure to produce as-synthesised **FeCPNDI-1** as outlined in methods, Section 5.5.1, Figure 5.9. The brown solid exhibited a noticeable difference in appearance from **Fe(Cl)NDI-1** (which is a red solid), causing PXRD analysis to be carried out. Upon comparison of the two patterns (Figure 5.2), it became clear that the new material, subsequently named **FeCPNDI-1**, possessed a unit cell that was significantly different from that of **Fe(Cl)NDI-1**, causing us to believe that a new CP had been synthesised (Figure 5.2).

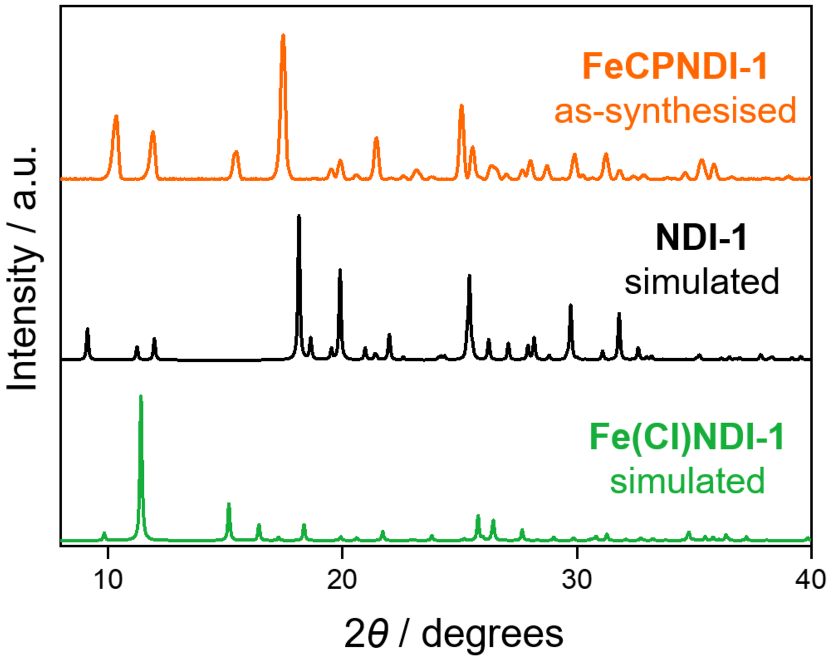

Figure 5.2. PXRD patterns of as-synthesised **FeCPNDI-1** (orange) compared to those of NDI **1** (black) and **Fe(Cl)NDI-1** simulated from single crystal X-ray data.

As a result of the new PXRD pattern, experiments aimed at obtaining single crystals of **FeCPNDI-1** were attempted over the course of 7 days at a lower temperature of 140 °C to enable slow growth (see synthetic details, Section 5.5.1, Figure 5.12 for full details). The newly discovered framework (see the Appendix, section 7.17, Table 7.3 for full crystallographic details) was identified as a CP featuring Fe^{3+} metal centres, NDI **1** linkers, and formate bridges (Figure 5.3a). The Fe^{3+} metal centres displayed octahedral coordination around its periphery, connecting to two NDI **1** linkers (Fe−N = 2.18 Å) and four formate bridges SBUs (Fe−O = 2.12 Å c-axis, 2.13 Å b axis). Each Fe metal centre displayed a formal oxidation state of Fe^{3+}, donating two electrons to formate oxygen atoms, and one to an NDI **1** pyrazole end group nitrogen atom. Between Fe metal centres that were connected *via* formate bridges, an angle of 108° (Figure 5.3b) was observed. Furthermore, hydrogen bonding interactions (Figure 5.3c) are observed between pyrazole end groups of NDI **1** and formate oxygens (O···H = 2.08 Å). The formate bridge itself represented a potential *through-bond* charge transport pathway, enabling charge transport between Fe metal centres *via* the formate bridge. Another potential charge transport pathway, that emerged as a result of the continuous framework, was identified at closest π–π distance (3.24 Å) between unevenly overlapped NDI **1** π-surfaces (Figure 5.3d). The resulting π-orbital overlap could result in electron delocalisation between LUMO orbitals located on the NDI **1** molecules, forming a *through-space* pathway.

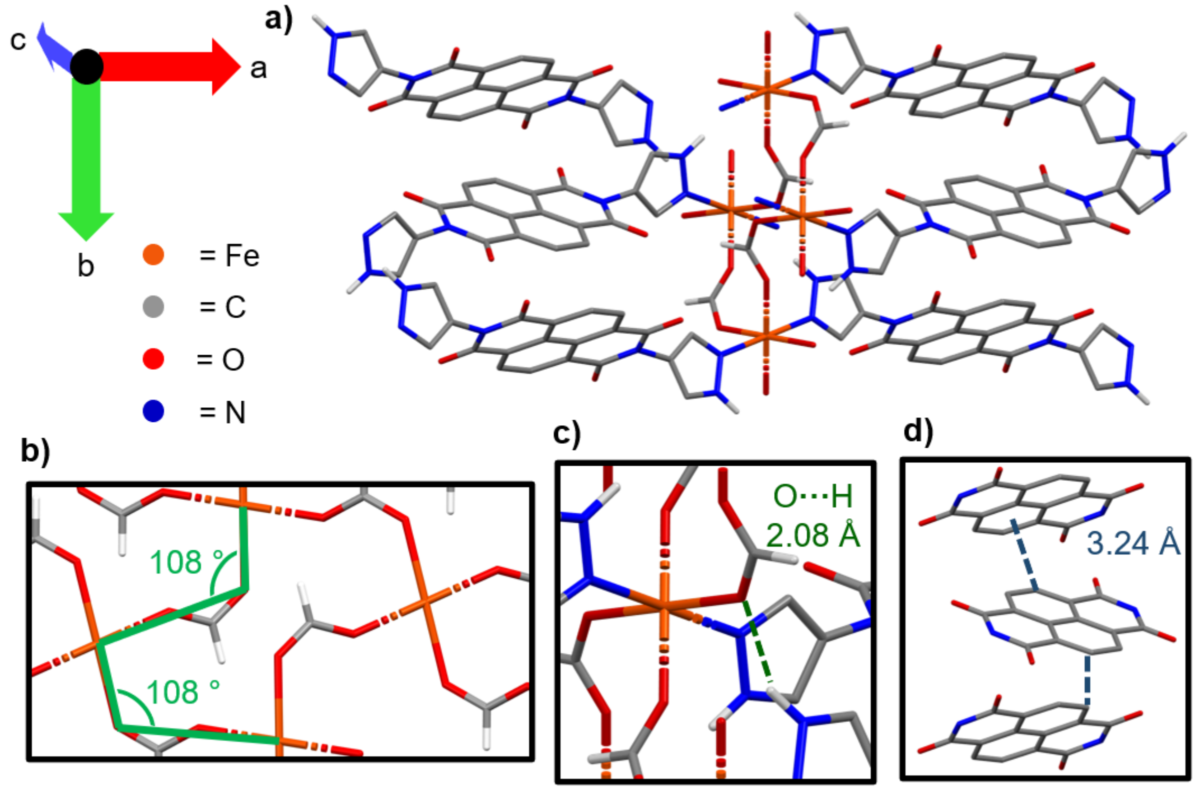

Figure 5.3. Single crystal packing of **FeCPNDI-1**, showing a) the close-packed structure of **FeCPNDI-1**, b) formate bridging ligands resulting in angles of 108 ° between Fe metal centres, c) hydrogen bonding between NDI **1** ligands and the formate bridge, d) the π-stacking between overlapped NDI **1** ligands.

The structural distinction between **FeCPNDI-1** and **Fe(Cl)NDI-1** is starkly different. The incorporation of the formate bridge fundamentally reshapes the coordination framework, introducing a coordination mode that yields a 108° angle between Fe metal centres. The bonding configuration leads to the absence of the Fe–pyrazolate backbone that is observed in **Fe(Cl)NDI-1**, potentially resulting in reduced thermal stability. Furthermore, the structure lacks porosity as a result of the formate bridge orientation, rendering interpenetration to not be present. Consequently, the stacking of NDI **1** linkers no longer occurs uniformly with close distances (3.45 Å) and extensive overlap. Instead, an uneven stacking pattern is observed, with the closest distances between NDI **1** units at the nearest point measuring 3.24 Å. Potentially, the closer NDI–NDI distance could signify an amplification of the *through-space* charge transport pathway, leading to an increased conductivity measurement. To comprehensively investigate the properties of **FeCPNDI-1**, it is imperative to ensure the material is analytically pure, thereby precluding any interference from impurities in the subsequent properties analysis techniques.

5.2.2 PURITY ANALYSIS OF FeCPNDI-1

Given that **FeCPNDI-1** exhibited insolubility in all solvents and was a CP, only elemental analysis (EA), X-ray fluorescence (XRF), and PXRD could be employed to ascertain its compositional purity. Potential impurities might arise from unreacted by-products of either starting material ($FeCl·6H_2O$ or NDI **1**). An initial comparison between the as-synthesised PXRD pattern and a pattern simulated from the single crystal data of **FeCPNDI-1** revealed a very close match in peak positions, affirming the phase purity of the material and ruling out the presence of foreign crystalline substances (Figure 5.4). In order to confirm the compositional purity of **FeCPNDI-1**, further investigation was conducted through EA and XRF analyses.

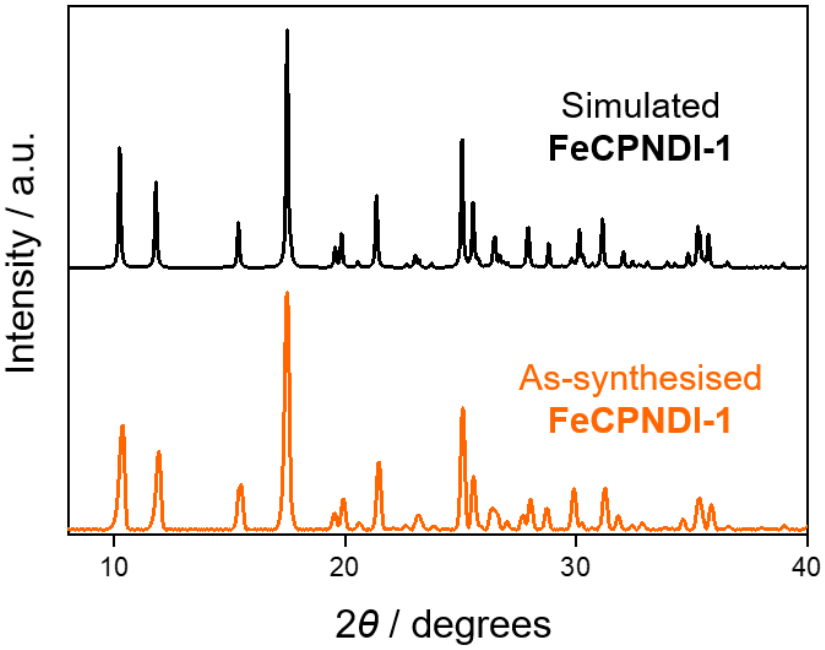

Figure 5.4. PXRD patterns of as-synthesised **FeCPNDI-1** and **FeCPNDI-1** simulated from the single crystal data. Both patterns show exact matching between peaks, demonstrating the phase purity of the as-synthesised material.

Consequently, EA conducted for **FeCPNDI-1** ($C_{22}H_{12}FeN_6O_8$) and demonstrated remarkably close agreement between the anticipated and experimental values (Table 5.1). The coherence between the values is attributed to the non-porous nature of **FeCPNDI-1**, which lacks channels for small molecules to become entrapped.

Table 5.1 Elemental analysis results for as-synthesised **FeCPNDI-1**.

	C / %	H / %	N / %	Remainder / %
Theoretical	48.2	2.3	15.3	34.1
Experimental	48.6	2.2	15.4	33.8

To further ascertain the purity of **FeCPNDI-1**, XRF analysis was conducted, which is sensitive to the emission of fluorescent X-rays by atoms with an atomic number greater than 11 (Na). In the case of **FeCPNDI-1** ($C_{22}H_{12}FeN_6O_8$), only Fe atoms emitted X-rays with sufficient energy to be detectable. Consequently, any impurities originating from $FeCl_3 \cdot 6H_2O$ during the synthetic process would be identified. The XRF results unequivocally confirmed that Fe was the only detectable element, thereby affirming the absence of chlorine atoms (Table 5.2). With the completion of the purity analysis involving PXRD, EA, and XRF, **FeCPNDI-1** was considered ready for an examination of its thermal, chemical, and electroactive properties, with the aim of evaluating its redox-active properties and potential charge transport pathways.

Table 5.2. XRF results for **FeCPNDI-1**.

	Fe / %	Cl / %
Theoretical	100	0
Expected	100	0

5.2.3 PROPERTIES ANALYSIS OF FECPNDI-1

The application of TGA aimed to evaluate of the thermal stability of **FeCPNDI-1** after the material has been confirmed as pure. Furthermore, TGA would enable a comparative analysis across the series of Fe–pyrazolate frameworks developed in Chapters 3 and 4, shedding light on the impact of the absence of a Fe–pyrazolate backbone. Given the established thermal strength of pyrazolate materials[7–10] and the findings in Chapters 3 and 4, it was expected that compound **FeCPNDI-1** would exhibit an earlier decomposition point in comparison to **Fe(Cl)NDI-1**.

The TGA was carried out under a flow of N_2 (10 mL min^{-1}) unveiling that **FeCPNDI-1** undergoes two distinct decomposition events, culminating in a breakdown of the framework. The initial decomposition, commencing at approximately 285 °C, can be attributed to the loss of both formate bridges. The subsequent decomposition event occurring around 525°C, lacks a specific component attribution within **FeCPNDI-1**, suggesting it corresponds to the complete disintegration of the framework. The TGA result implies that the bonds between Fe metal centres and pyrazole end groups (Fe–N) observed in **Fe(Cl)NDI-1** demonstrate greater thermal stability compared to those between Fe metal centres and formate oxygen atoms (Fe–O) observed in **FeCPNDI-1**.

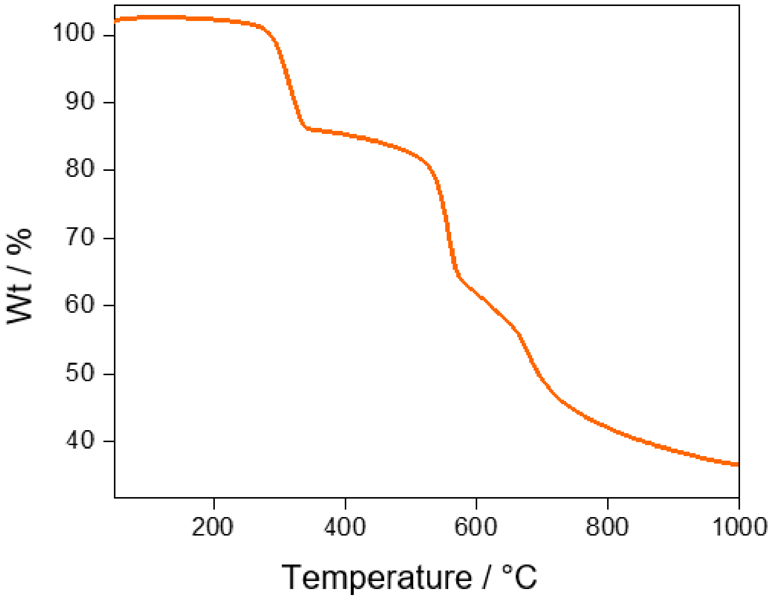

Figure 5.5. TGA of **FeCPNDI-1**, carried out under a 10 mL s^{-1} flow of N_2.

To evaluate the electrochemical behavior of **FeCPNDI-1** and ascertain whether the redox properties of NDI **1** were retained upon its incorporation into the framework, SCCV experiments were conducted. Devices such as batteries and supercapacitors rely on molecules that facilitate the uptake and diffusion of ions, ensuring efficient energy release. Although **FeCPNDI-1** may not support the ion diffusion necessary for energy storage mechanisms, it still holds potential as a conductive material that arises from the *through-space* and *through-bond* pathways provided by co-facially oriented NDI π-surfaces and extended Fe–formate chains, respectively.

The surface-confined loading of **FeCPNDI-1** was replicated from a prior method developed for **Fe(Cl)NDI-1** in Chapter 3. A suspension of **FeCPNDI-1** (10 mg mL^{-1} in CH_2Cl_2) was drop-cast (2 x 20 µL) onto a glassy carbon electrode and allowed to air-dry. The resulting thin layer of **FeCPNDI-1** was then immersed into an electrolyte solution (0.1 M $TBAPF_6$ in MeCN) with counter and reference electrodes already in place, and subsequently subjected to appropriate positive and negative potentials. The electrochemical response of **FeCPNDI-1** was recorded, as shown in Figure 5.6, revealing two distinct reduction/oxidation peaks, indicating two pseudo-reversible one-electron processes. A close match is observed between the reduction potentials of **FeCPNDI-1** and NDI **1**, confirming that the redox properties of NDI **1** were retained upon incorporation into the framework of **FeCPNDI-1**. However, in comparison to solution-state data obtained for NDI **1**, the first reduction of **FeCPNDI-1** is broadened which is attributed to the poor diffusion of counter anions through the densely packed solid material, leading to redox processes localising at the surface of **FeCPNDI-1** crystallites.[11] In order to determine that the first redox process observed in **FeCPNDI-1** was the result of slow reaction kinetics, several CV experiments at different scan rates would have to be carried out.[11] The peak potentials of the first reduction and the second oxidation could then be plot against the square root of the scan rate, and if the relationship is linear, the process is governed by slow reaction kinetics.[11] However, multiple scans of the same sample were not carried out due to the propensity for the thin layer of **FeCPNDI-1** to desorb from the surface of the WE.

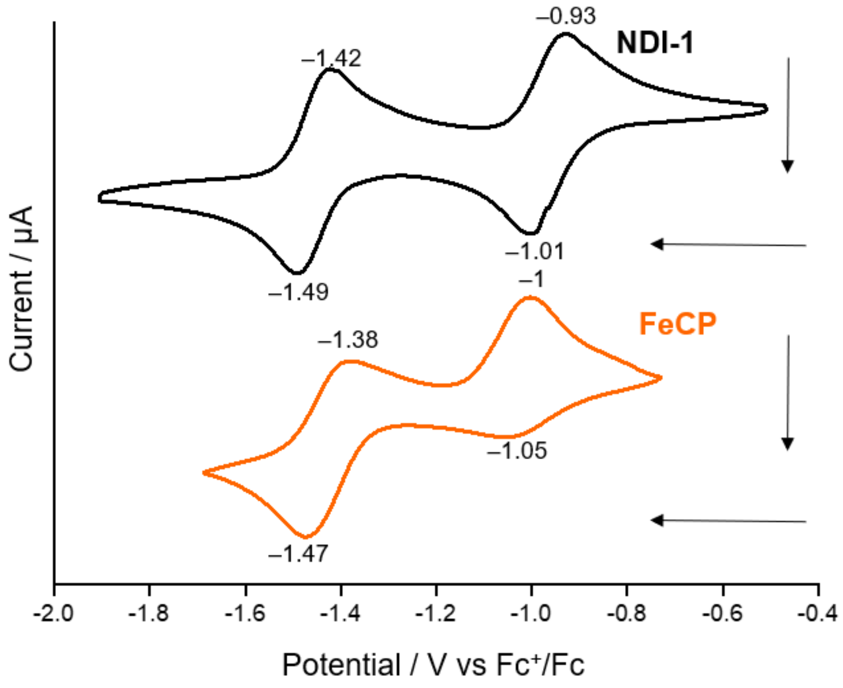

Figure 5.6. cyclic voltammograms of **FeCPNDI-1** and NDI **1**. The CV data for FeCPNDI-1 was collected using SCCV by drop-casting a suspension of the framework in DCM (20 mg mL^{-1}) onto the WE followed by submersion in a 1 mM solution of [*n*-Bu_4N]PF_6 in MeCN and analysis at 200 mV s^{-1}. The CV data for NDI **1** was collected in Chapter 2, in the solution state. Both voltammograms were normalised to one another with respect to current.

After the redox properties of **FeCPNDI-1** were determined, the focus shifted towards determining the semiconductor activity of the potential charge transport pathways observed in the structure of **FeCPNDI-1**. Based upon the single crystal data, the formate bridge between Fe metal centres or the unevenly overlapped NDI **1** π-surfaces could both provide a charge transport pathway, prompting conductivity measurements.

Resistivity analysis of pressed pellets of **FeCPNDI-1** were conducted using the methodology initially developed in Chapter 2. Impressively, **FeCPNDI-1** exhibited a conductivity of 3.28×10^{-4} S cm^{-1}, see the Appendix, Section 7.9, Figure 7.22 for the I–V curve data. The conductivity measurement could not be attributed to either charge transport pathway, as there was no comparative material that displayed similar packing of NDI π-surfaces or Fe–formate bridges. To ensure that the packing arrangement observed in the single crystal data of **FeCPNDI-1** was maintained throughout the resistivity process, PXRD patterns were collected at each stage. The PXRD patterns confirmed the phase purity of the frameworks throughout the resistivity procedure (Figure 5.7). Nonetheless, the conductivity measurement of **FeCPNDI-1** does not conclusively determine which charge transport pathway is active within its framework, requiring synthesis of additional materials to allow for a comparative analysis to be drawn.

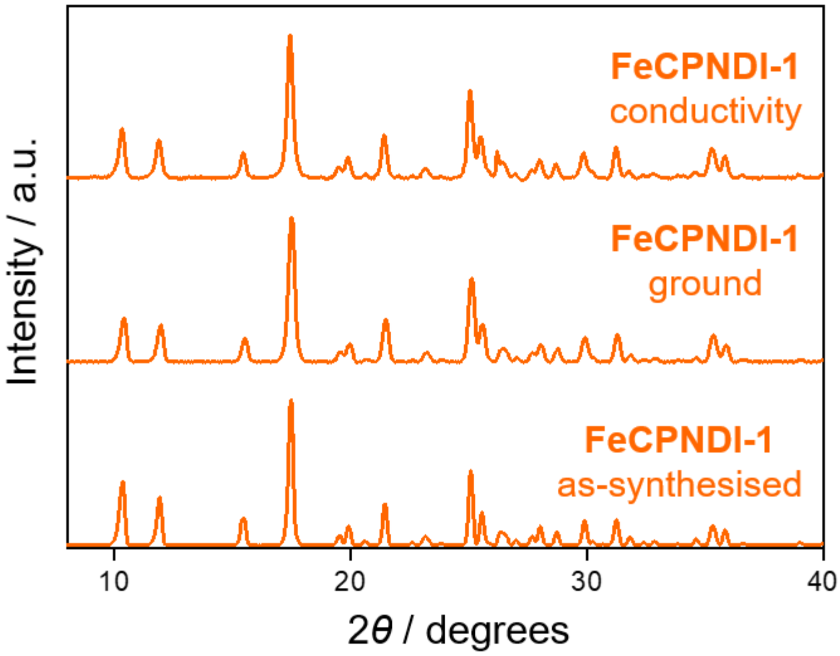

Figure 5.7. PXRD patterns of **FeCPNDI-1** material as-synthesised, post-grinding, and post-conductivity tests.

5.3 SYNTHESIS AND ANALYSIS OF CoCPNDI-1 AND MnCPNDI-1

It was suspected that charge transport occurred in **FeCPNDI-1** *via* partially overlapped NDI **1** π-surfaces (3.24 Å at the closest point) that acted as a *through-space* pathway or *via* the formate backbone that acted as a *through-bond* pathway. In order to investigate the origin of the high conductivity observed in **FeCPNDI-1**, an isostructural design strategy was enacted, in order to deactivate the potential *through-bond* pathway. If the origin of the high charge transport in **FeCPNDI-1** was able to be elucidated, future experiments could aim to replicate either the Fe–formate bridge or the unevenly overlapped NDI units in a new coordination framework in order to obtain high semiconducting properties.

In order to deactivate the Fe–formate *through-bond* pathway, the objective was to synthesise several other coordination frameworks isostructural to **FeCPNDI-1** with different metal centres, which would influence the overlap of orbitals between chemically bonded formate bridges and Fe metal centres. Previous literature indicates isostructural frameworks containing Fe metal centres exhibited superior charge transport in comparison to other metal centres, therefore we would expect that other metal centres would demonstrate lesser conductivity values.[5] The reaction protocols used for **FeCPNDI-1** were replicated with the exception of using alternative metal salt sources in place of $FeCl_3 \cdot 6H_2O$ in an effort to create new isostructural frameworks. By employing $CoCl_2$ and $MnCl_2 \cdot 4H_2O$ instead of $FeCl_3 \cdot 6H_2O$, two new brown solids, designated as **CoCPNDI-1** and **MnCPNDI-1**, respectively, were obtained (see experimental details, Section 5.5.1, Figure 5.13 and Figure 5.14). Both as-synthesised **CoCPNDI-1** and **MnCPNDI-1** were subjected to PXRD analysis, confirming the formation of two new materials with an isostructural arrangement to **FeCPNDI-1** (Figure 5.8, 5.9 and 5.10).

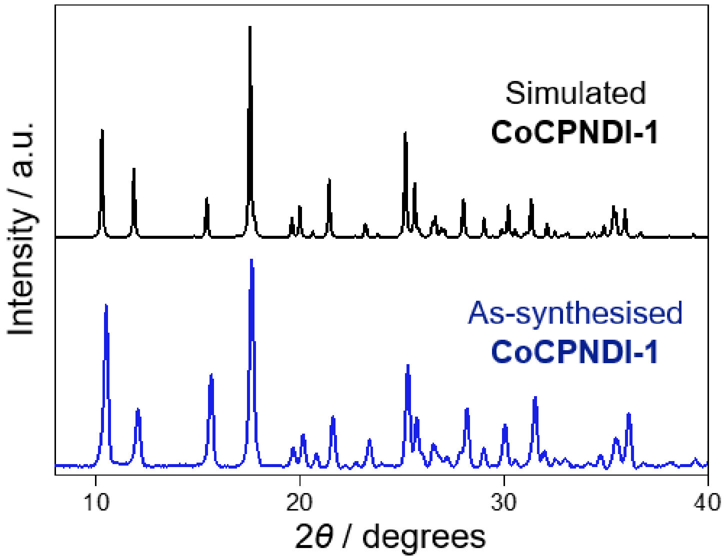

Figure 5.8. PXRD patterns of as-synthesised **CoCPNDI-1** and **CoCPNDI-1** simulated from the single crystal data. Both patterns show exact matching between peaks, demonstrating the phase purity of the as-synthesised material.

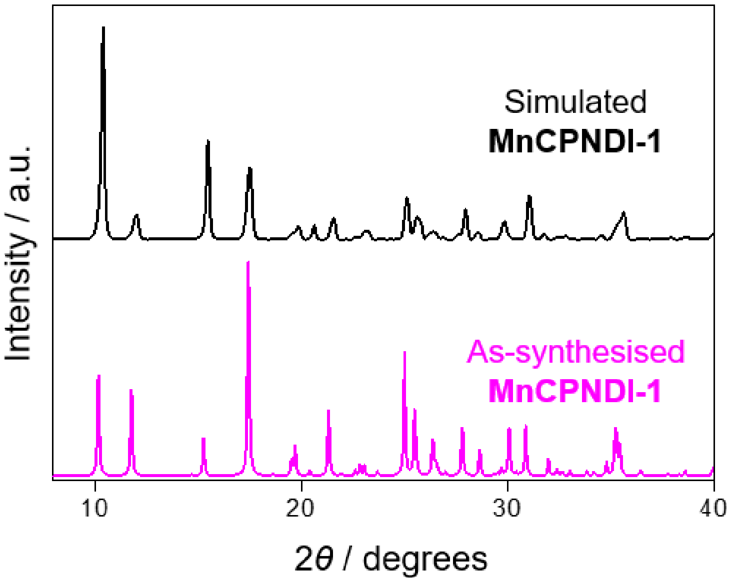

Figure 5.9. PXRD patterns of as-synthesised **MnCPNDI-1** and **MnCPNDI-1** simulated from the single crystal data. Both patterns show exact matching between peaks, demonstrating the phase purity of the as-synthesised material.

The growth of single crystals for both **CoCPNDI-1** and **MnCPNDI-1** was imperative to validate the PXRD data and affirm that both materials shared an isostructural nature with **FeCPNDI-1**. Hence, solvothermal synthetic conditions identical to those used for generating single crystals of **FeCPNDI-1** (see experimental details, Section 5.5.1, Figure 5.16 and Figure 5.17) were carried out over a period of seven days. The solvothermal process yielded single crystals for both **CoCPNDI-1** and **MnCPNDI-1**, providing structural information for both CP frameworks (see the Appendix, section 7.17, Table 7.3 for full crystallographic details). Simulated patterns of **CoCPNDI-1** and **MnCPNDI-1** closely matched the powder patterns of the as-synthesised materials, confirming that both as-synthesised samples adopted the single crystal packing (Figure 5.8 and 5.9). However, before proceeding with any properties analysis, compositional purity assessments using EA and XRF were carried out on the as-synthesised samples of **CoCPNDI-1** and **MnCPNDI-1**.

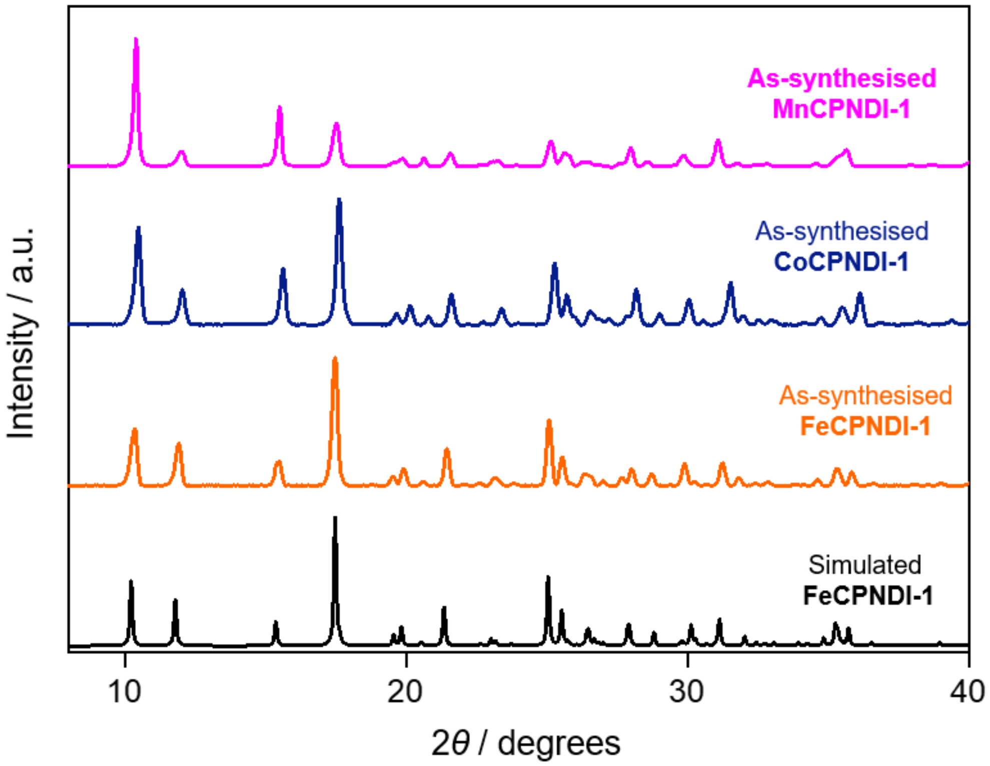

Figure 5.10. PXRD patterns of **FeCPNDI-1**, **CoCPNDI-1** and **MnCPNDI-1**, with simulated **FeCPNDI-1** data for further comparison. The data shows that all materials are isostructural.

Following the successful growth of single crystals and the confirmation the isostructural nature of **CoCPNDI-1** and **MnCPNDI-1**, EA was conducted on the corresponding as-synthesised samples to assess compositional purity. Similar to the results obtained for **FeCPNDI-1**, we observed a very close match between the theoretical and experimental EA results for both **CoCPNDI-1** **(**$C_{22}H_{12}CoN_6O_8$) and **MnCPNDI-1** ($C_{22}H_{12}MnN_6O_8$), providing further confirmation of their purity (see Table 5.3 and 5.4). Further compositional purity assessments were conducted on the as-synthesised samples of **CoCPNDI-1** and **MnCPNDI-1** using XRF, aiming to detect the coordinating metal centre (Co or Mn, respectively) and identify any potential Cl impurities originating from the metal salt starting material. As detailed in Table 5.5 and Table 5.6, the XRF analysis exclusively detected the respective metal centres of **CoCPNDI-1** and **MnCPNDI-1**, affirming the suitability of both as-synthesised samples for subsequent properties analysis.

Table 5.3. Elemental analysis results for **CoCPNDI-1** that demonstrate close matching with theoretical values.

	C / %	H / %	N / %	Remainder / %
Theoretical	48.1	2.2	15.1	34.6
Expected	48.3	2.2	15.4	34.2

Table 5.4. Elemental analysis results for **MnCPNDI-1** that demonstrate close matching with theoretical values.

MnCPNDI-1	C / %	H / %	N / %	Remainder / %
Theoretical	48.3	2.0	15.2	34.5
Expected	48.6	2.2	15.5	33.7

Table 5.5. Results of XRF analysis using an as-synthesised sample of **CoCPNDI-1**.

	Co / %	Cl / %
Theoretical	100	0
Expected	100	0

Table 5.6. Results of XRF analysis using an as-synthesised sample of **MnCPNDI-1**.

	Mn / %	Cl / %
Theoretical	100	0
Expected	100	0

The compositional purity of **CoCPNDI-1** and **MnCPNDI-1** having been confirmed, the next step was to conduct TGA to assess whether the change in metal, in comparison to **FeCPNDI-1**, resulted in changed thermal stability. The TGA results (Figure 5.11 and Table 5.3) revealed almost identical thermal stability between **CoCPNDI-1** (292 °C) and **FeCPNDI-1** (285 °C). However, while **MnCPNDI-1** exhibited an identical decomposition profile to the other two frameworks, it was distinguished by displaying a first decomposition point of 317 °C, which was over 20 °C higher than that of **FeCPNDI-1** and **CoCPNDI-1**. The first mass loss for all frameworks indicates the decoupling of formate linkers from the framework, while the second mass loss represents the complete breakdown of the framework. Considering the isostructural nature of the three frameworks, the difference in the first decomposition point was rationalised by attributing it to stronger chemical bonds between Mn metal centres and oxygen atoms located on the formate linker. However, little evidence of continuous frameworks that include foramte bridges have been reported in the literature, requiring further study to be carried out to determine the source of this increased thermal stability of **MnCPNDI-1**.

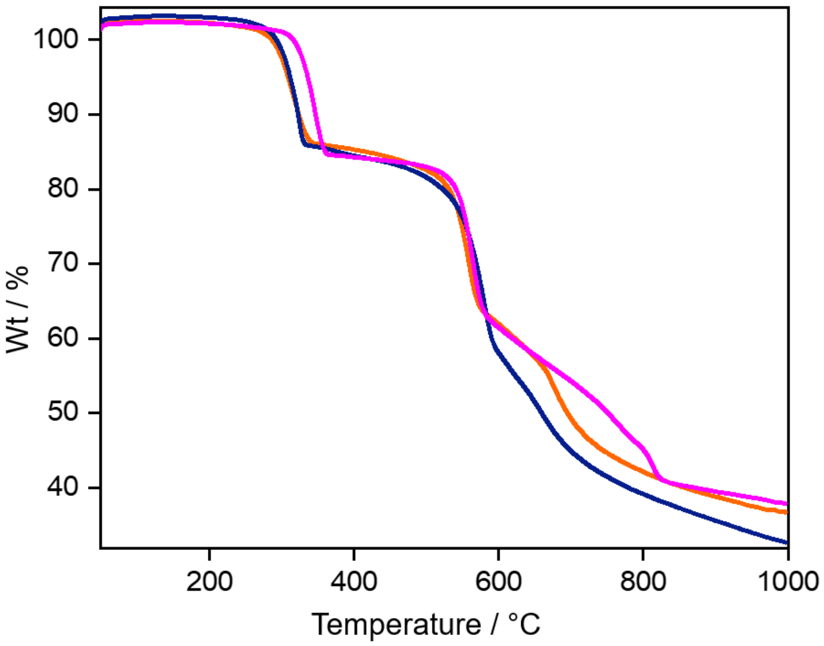

Figure 5.11. The thermal traces of **FeCPNDI-1**, **CoCPNDI-1**, **MnCPNDI-1**, demonstrating close to identical first and second thermal decomposition pathways.

Table 5.7. TGA details for **FeCPNDI-1**, **CoCPNDI-1**, **MnCPNDI-1**.

	Decomposition point / °C	$T2^{onset}$ / °C
FeCPNDI-1	285	525
CoCPNDI-1	292	541
MnCPNDI-1	317	538

The primary objective behind synthesising the new frameworks, **CoCPNDI-1** and **MnCPNDI-1**, was to evaluate the charge transport pathways in **FeCPNDI-1**. By altering the metal centre, the aim was to potentially deactivate any *through-bond* charge transport pathways between the Fe metal centres and the formate linkers. In previous work by Sun et al., conductivity was observed to be unique to frameworks containing Fe metal centres in range of isostructural frameworks with different metal centres.[5] Therefore, the hypothesis was that in frameworks **CoCPNDI-1** and **MnCPNDI-1**, by containing Co and Mn metals respectively, the conductivity would be lowered, indicating a potential deactivation of the *through-bond* charge transport pathway. The conductivity analysis would allow for the determination of the contribution of each potential charge transport pathway, shedding light on the origin of the high conductivity observed in **FeCPNDI-1**.

The resistivity measurements of the two isostructural frameworks **CoCPNDI-1** and **MnCPNDI-1** were conducted using the two-point probe pellet press method developed in Chapter 2. The resistivity tests yielded results (see table 5.8) showing that both **CoCPNDI-1** (1.86×10^{-4} S cm^{-1}) and **MnCPNDI-1**

(1.15×10^{-4} S cm^{-1}) exhibited conductivity readings that closely matched **FeCPNDI-1**, with only negligible differences between them. The I–V curve data is available in the Appendix, Section 7.9, Figures 7.22, 7.23, 7.24. In other conductive *through-bond* CP materials, a change in the metal centre often led to observable differences in recorded conductivities, likely due to orbital overlap between chemically bonded atoms.[5] The nearly identical conductivity readings observed among the trio of isostructural frameworks strongly suggest that any *through-bond* pathways existing in these materials contribute very little to the observed conductivity readings.

Table 5.8. Conductivity values for **FeCPNDI-1**, **CoCPNDI-1** and **MnCPNDI-1**, demonstrating very close matching between values that are indicative of *through-space* charge transport.

	Conductivity / S cm^{-1}
FeCPNDI-1	3.27×10^{-4}
CoCPNDI-1	1.86×10^{-4}
MnCPNDI-1	1.15×10^{-4}

Hence, the notable conductivity observed in these three isostructural frameworks is attributed primarily to the close overlap (3.24 Å) between the π-orbitals of the NDI **1** units in each framework. It is theorised that the close proximity of NDI **1** units enables electrons to move between LUMO orbitals, establishing a *through-space* charge transport pathway. However, the absence of additional comparative frameworks, and the appropriate computational studies to determine the location of the frontier molecular orbitals suggests that additional work needs to be carried out in order to understand this series of isostructural framework.

5.4 CONCLUSIONS

This study aimed to diversify the family of pyrazolate frameworks elucidated in Chapters 3 and 4. The objective was to replace existing bridging anions (Cl, OH, Br) with formate ligands, which, due to their versatile coordination modes, were anticipated to yield a CP with a different topological net. The synthetic protocols employed resulted in the emergence of a new non-porous framework, denoted as **FeCPNDI-1**, featuring a distinct topological arrangement compared to **Fe(Cl)NDI-1**, that was featured in Chapter 3. Single crystal data revealed the formate bridge's introduction engendered new potential charge transport pathways, either through Fe metal centres linked by the formate bridge or *via* unevenly-overlapped NDI **1** linkers. Despite the absence of the pyrazolate backbone, **FeCPNDI-1** exhibited noteworthy thermal stability (285 °C) and a high conductivity measurement of 3.27×10^{-4} S cm^{-1}. Nevertheless, the precise mechanism of charge transport in **FeCPNDI-1** remained unclear, prompting the adoption of an isoreticular strategy to synthesise frameworks with the same topological net as **FeCPNDI-1** by varying metal centre identities, to investigate the two potential charge transport pathways.

Two novel frameworks, denoted as **CoCPNDI-1** and **MnCPNDI-1**, were synthesised, with Co and Mn metal centres, respectively, replacing Fe. Both frameworks were confirmed to be isostructural to **FeCPNDI-1** and were then verified for purity through PXRD, EA, and XRF analyses. Notably, **MnCPNDI-1** exhibited the highest thermal stability, attributed to enhanced bonding between the Mn metal centre and the O atoms of formate linkers. Furthermore, the conductivities of **CoCPNDI-1** (1.86×10^{-4} S cm^{-1}) and **MnCPNDI-1** (1.15×10^{-4} S cm^{-1}) closely matched the value observed for **FeCPNDI-1**. The consistent conductivity across the three frameworks strongly suggests that the formate-bridged Fe metal centres do not function as a significant *through-bond* charge transport pathway. The similar conductivity measurements indicate that the primary charge transport pathway is *through-space*, facilitated by unevenly-overlapped NDI **1** units.

These findings illuminate how substituting a ligand with greater bonding modes can profoundly influence the topological net of the resulting framework. The electronic properties of the formate-bridged frameworks, although distinct from the Fe–pyrazolate frameworks, are notably impressive despite the absence of the pyrazolate backbone. The high conductivity in both sets of CPs in chapters 3, 4 and 5 suggest that through linker replacement, coupled with an isostructural design strategy, frameworks with similar properties are likely to be generated. Therefore, this work holds significant promise in the quest for the next generation of energy storage materials.

5.5 EXPERIMENTAL DETAILS

General details on materials and research methods as well as additional data for this Chapter can be found in the Appendix.

5.5.1 X-RAY ANALYSIS

Diffraction data were collected at 110 K on an Oxford Diffraction SuperNova diffractometer with Mo-Ka radiation (l = 0.071073 nm) or Cu-Ka radiation (l = 0.15418 nm) using a Cannon EOS CCD camera. The crystal was cooled with liquid nitrogen to 110 K using an Oxford Instruments Cryojet. Diffractometer control, data collection, initial unit cell determination, frame integration and unitcell refinement was carried out with 'CrysAlisPro'.[12] Face-indexed absorption corrections were applied using spherical harmonics, implemented in SCALE3 ABSPACK scaling algorithm.[13] OLEX2[14] was used for overall structure solution, refinement and preparation of computer graphics and publication data. Within OLEX2, the structures were solved with the Superflip Structure solution program using 'charge flipping'[15] or with the ShelXS/ShelXT structure solution programs using Direct Methods.[16] Refinement by full-matrix least-squares used the SHELXL-97 algorithm within OLEX2. All non-hydrogen atoms were refined anisotropically and hydrogen atoms were placed S2 using a 'riding model' and included in the refinement at calculated positions.

5.5.2 SYNTHETIC METHODS

GENERAL PROCEDURE FOR COORDINATION POLYMERS

A 35 mL microwave vial was equipped with a magnetic stirrer bar and charged with NDI **1** (0.67 equiv.), metal salt (1 equiv.), formic acid (100 equiv.) and DMF (12 mL). The mixture was subjected to dynamic microwave irradiation (160 °C, 300 W) under high stirring for 15 min. Upon cooling to rt, the reaction mixture was filtered and washed over the filter with DMSO until the washings appeared colourless, followed by absolute EtOH. The solids were dried at 180 °C for 12 h in a vacuum oven (5 mbar) to yield the appropriate 2D non-porous coordination polymer.

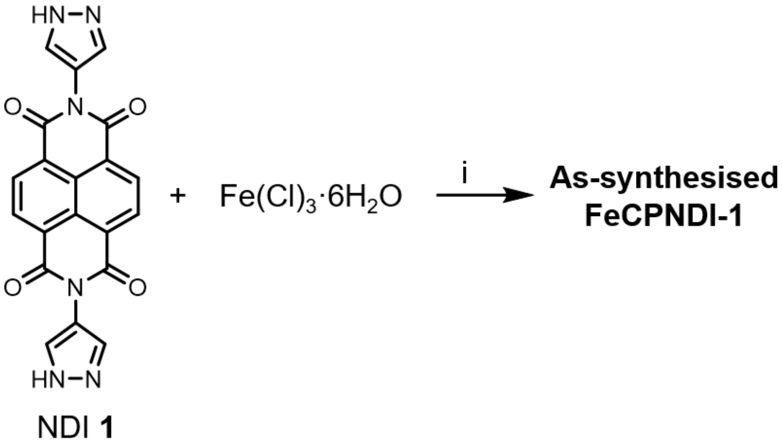

Figure 5.12. As-synthesised preparation of **FeCPNDI-1**. Reagents and conditions: (i) Formic acid, DMF, µW: 160 °C, 15 min, 91%.

[FeCPNDI-1]. Applying the ***General Procedure*** described above, **FeCPNDI-1** (248.5 mg, 0.46 mmol, 91%) was prepared from NDI **1** (200 mg, 0.5 mmol, 0.67 equiv.), $FeCl_3 \cdot 6H_2O$ (200 mg, 0.74 mmol, 1 equiv.) and formic acid (2.61 mL, 74 mmol, 100 equiv.) as a dark brown powder. **Elemental analysis:** Anal. calc for formula: $C_{22}H_{12}FeN_6O_8$ C, 48.6; H, 2.2; N, 15.4, Anal. found: C, 48.2; H, 2.3; N, 15.3, (–0.4% C, +0.1% H, –0.1% N).

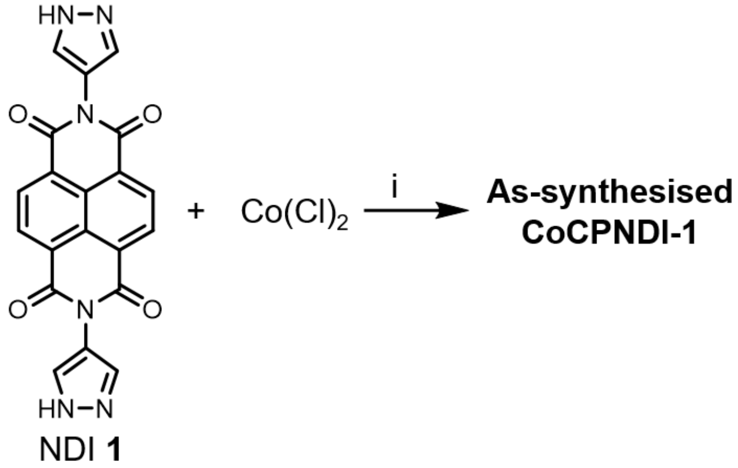

Figure 5.13. As-synthesised preparation of **CoCPNDI-1**. Reagents and conditions: (i) Formic acid, DMF, µW: 160 °C, 15 min, 91.3%.

[CoCPNDI-1]. Applying the ***General Procedure*** described above, **CoCPNDI-1** (249.9 mg, 0.46 mmol, 91.3%) was prepared from NDI **1** (200 mg, 0.5 mmol, 0.67 equiv.), $CoCl_2$ (96 mg, 0.74 mmol, 1 equiv.) and formic acid (2.61 mL, 74 mmol, 100 equiv.) as a dark brown powder. **Elemental analysis:** Anal. calc for formula: $C_{22}H_{12}CoN_6O_8$ C, 48.3; H, 2.2; N, 15.4, Anal. found: C, 48.1; H, 2.2; N, 15.1, (–0.2% C, 0% H, –0.3% N).

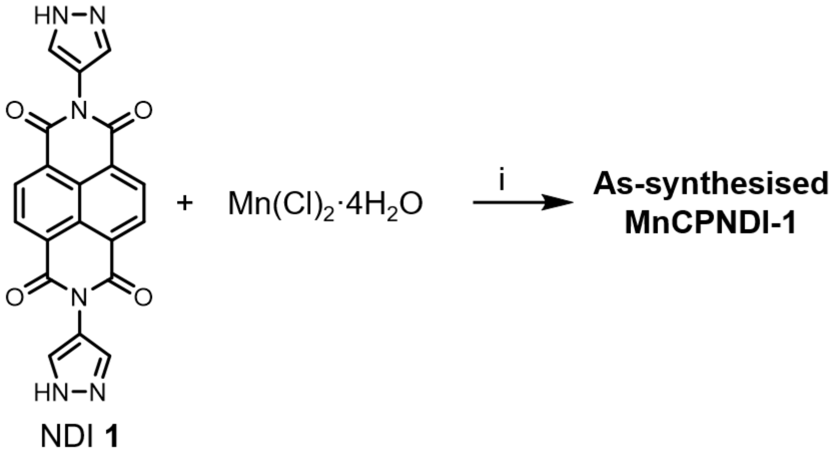

Figure 5.14. As-synthesised preparation of **MnCPNDI-1**. Reagents and conditions: (i) Formic acid, DMF, µW: 160 °C, 15 min, 92.4%.

[MnCPNDI-1]. Applying the ***General Procedure*** described above, **MnCPNDI-1** (250.9 mg, 0.46 mmol, 92.4%) was prepared from NDI **1** (200 mg, 0.5 mmol, 0.67 equiv.), $MnCl_2{\cdot}4H_2O$ (197.9 mg, 0.74 mmol, 1 equiv.) and formic acid (2.61 mL, 74 mmol, 100 equiv.) as a dark brown powder. **Elemental analysis:** Anal. calc for formula: $C_{22}H_{12}MnN_6O_8$ C, 48.6; H, 2.2; N, 15.5, Anal. found: C, 48.3; H, 2.0; N, 15.2, (–0.3% C, –0.2% H, –0.3% N).

GENERAL PROCEDURE FOR GROWING SINGLE CRYSTALS

A 10 mL screw-cap scintillation vial was charged with NDI **1** (1 equiv.), metal salt (3 equiv.), formic acid (30 equiv.) and DMF (2 mL), and then sealed tightly. The mixture was first sonicated then heated for 7 days at 140 °C. Upon cooling to rt, the reaction mixture was filtered and washed over the filter with DMSO until the washings appeared colourless, followed by absolute EtOH. The resulting mix of insoluble crystalline and amorphous material was submitted for SC-XRD immediately after vacuum filtration.

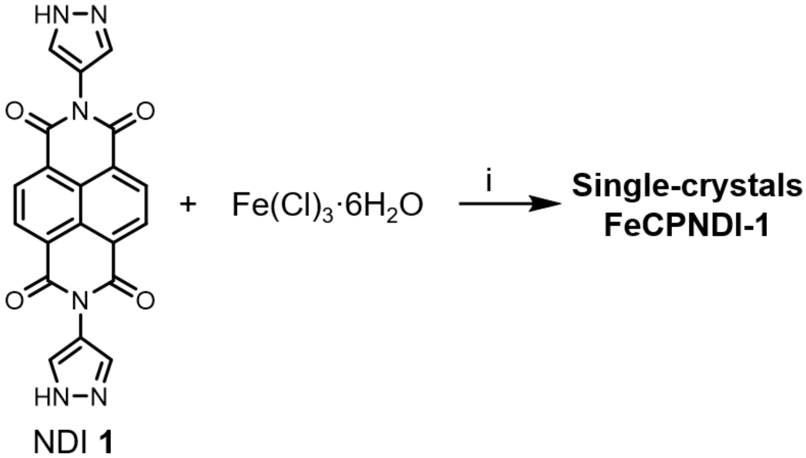

Figure 5.15. Single crystal preparation of **FeCPNDI-1**. Reagents and conditions: (i) Formic acid, DMF, 140 °C, 7 days.

[FeCPNDI-1] Single crystals. Applying the ***Single Crystal General Procedure*** described above, single crystals of **FeCPNDI-1** were prepared from NDI **1** (51.8 mg, 0.13 mmol, 1 equiv.), $FeCl_3 \cdot 6H_2O$ (86.5 mg, 0.32 mmol, 3 equiv.) and formic acid (132 µL, 3.25 mmol, 30 equiv.), yielding a mix of black coloured crystals and a black-coloured tar-like material.

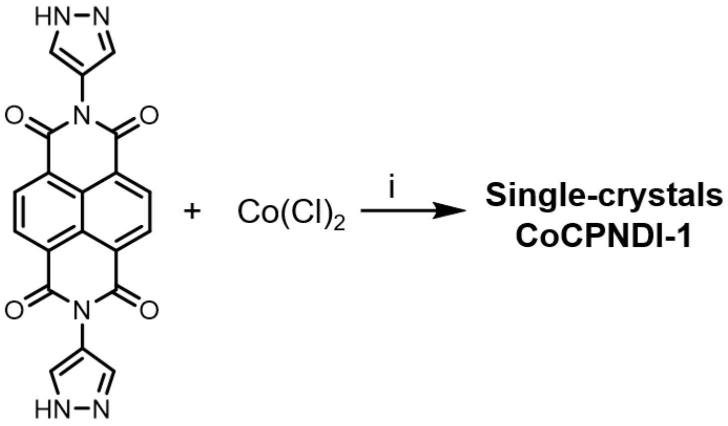

NDI **1**

Figure 5.16. Single crystal preparation of **CoCPNDI-1**. Reagents and conditions: (i) Formic acid, DMF, 140 °C, 7 days.

[CoCPNDI-1] Single crystals. Applying the ***Single Crystal General Procedure*** described above, single crystals of **CoCPNDI-1** were prepared from NDI **1** (51.8 mg, 0.13 mmol, 1 equiv.), $CoCl_2$ (41.5 mg, 0.32 mmol, 3 equiv.) and formic acid (132 µL, 3.25 mmol, 30 equiv.), yielding a mix of black coloured crystals and a black-coloured tar-like material.

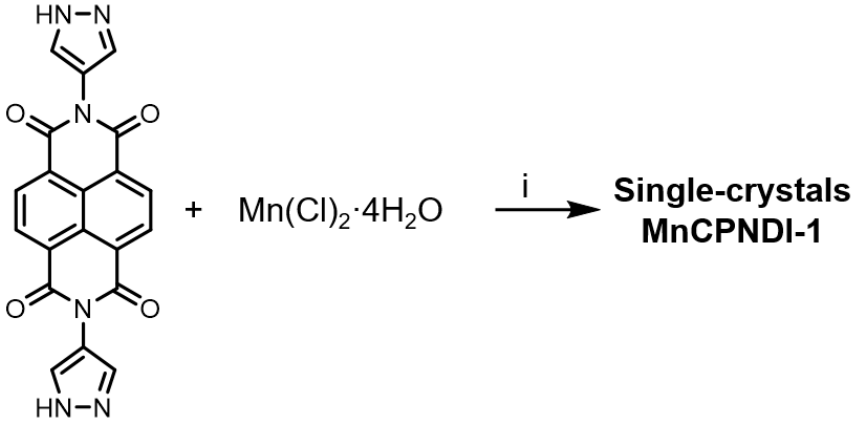

NDI **1**

Figure 5.17. Single crystal preparation of **MnCPNDI-1**. Reagents and conditions: (i) Formic acid, DMF, 140 °C, 7 days.

[MnCPNDI-1] Single crystals. Applying the ***Single Crystal General Procedure*** described above, single crystals of **MnCPNDI-1** were prepared from NDI **1** (51.8 mg, 0.13 mmol, 1 equiv.), $MnCl_2{\cdot}4H_2O$ (63.3 mg, 0.32 mmol, 3 equiv.) and formic acid (132 µL, 3.25 mmol, 30 equiv.), yielding a mix of black coloured crystals and a black-coloured tar-like material.

5.6 REFERENCES

(1) Yaghi, O. M.; O'Keeffe, M.; Ockwig, N. W.; Chae, H. K.; Eddaoudi, M.; Kim, J. Reticular Synthesis and the Design of New Materials. *Nature* **2003**, *423* (6941), 705–714. https://doi.org/10.1038/nature01650.

(2) Stock, N.; Biswas, S. Synthesis of Metal-Organic Frameworks (MOFs): Routes to Various MOF Topologies, Morphologies, and Composites. *Chem. Rev.* **2012**, *112* (2), 933–969. https://doi.org/10.1021/cr200304e.

(3) Guillerm, V.; Kim, D.; Eubank, J. F.; Luebke, R.; Liu, X.; Adil, K.; Lah, M. S.; Eddaoudi, M. A Supermolecular Building Approach for the Design and Construction of Metal–Organic Frameworks. *Chem. Soc. Rev.* **2014**, *43* (16), 6141–6172. https://doi.org/10.1039/C4CS00135D.

(4) Yang, S.; Lin, X.; Lewis, W.; Suyetin, M.; Bichoutskaia, E.; Parker, J. E.; Tang, C. C.; Allan, D. R.; Rizkallah, P. J.; Hubberstey, P.; Champness, N. R.; Mark Thomas, K.; Blake, A. J.; Schröder, M. A Partially Interpenetrated Metal–Organic Framework for Selective Hysteretic Sorption of Carbon Dioxide. *Nature Mater* **2012**, *11* (8), 710–716. https://doi.org/10.1038/nmat3343.

(5) Sun, L.; Hendon, C. H.; Park, S. S.; Tulchinsky, Y.; Wan, R.; Wang, F.; Walsh, A.; Dincă, M. Is Iron Unique in Promoting Electrical Conductivity in MOFs? *Chem. Sci.* **2017**, *8* (6), 4450–4457. https://doi.org/10.1039/C7SC00647K.

(6) Li, Z.-Y.; Wang, Y.-X.; Zhu, J.; Liu, S.-Q.; Xin, G.; Zhang, J.-J.; Huang, H.-Q.; Duan, C.-Y. Three Series of 3d–4f Heterometallic Polymers Based on [LnCu6] or [Ln6Cu24] Clusters and Formate Bridges: Displaying Significant Magnetocaloric Effect. *Crystal Growth & Design* **2013**, *13* (8), 3429–3437. https://doi.org/10.1021/cg400333d.

(7) Colombo, V.; Galli, S.; Choi, H. J.; Han, G. D.; Maspero, A.; Palmisano, G.; Masciocchi, N.; Long, J. R. High Thermal and Chemical Stability in Pyrazolate-Bridged Metal–Organic Frameworks with Exposed Metal Sites. *Chem. Sci.* **2011**, *2* (7), 1311–1319. https://doi.org/10.1039/C1SC00136A.

(8) Liu, X.-L.; Yin, Q.; Huang, G.; Liu, T.-F. Stable Pyrazolate-Based Metal-Organic Frameworks for Drug Delivery. *Inorganic Chemistry Communications* **2018**, *94*, 21–26. https://doi.org/10.1016/j.inoche.2018.06.001.

(9) Ma, F.-X.; Mi, F.-Q.; Sun, M.-J.; Huang, T.; Wang, Z.-A.; Zhang, T.; Cao, R. A Highly Stable Zn9-Pyrazolate Metal–Organic Framework with Metallosalen Ligands as a Carbon Dioxide Cycloaddition Catalyst. *Inorg. Chem. Front.* **2022**, *9* (8), 1812–1818. https://doi.org/10.1039/D1QI01555A.

(10) Herm, Z. R.; Wiers, B. M.; Mason, J. A.; Baten, J. M. van; Hudson, M. R.; Zajdel, P.; Brown, C. M.; Masciocchi, N.; Krishna, R.; Long, J. R. Separation of Hexane Isomers in a Metal-Organic Framework with Triangular Channels. *Science* **2013**, *340* (6135), 960–964. https://doi.org/10.1126/science.1234071.

(11) Leong, C. F.; Chan, B.; Faust, T. B.; Turner, P.; D'Alessandro, D. M. Electronic, Optical, and Computational Studies of a Redox-Active Napthalenediimide-Based Coordination Polymer. *Inorg. Chem.* **2013**, *52* (24), 14246–14252. https://doi.org/10.1021/ic402173z.

(12) CrysAlisPro, Oxford Diffraction Ltd. Version 1.171.34.40.

(13) *Empirical Absorption Correction Using Spherical Harmonics, Implemented in SCALE3 ABSPACK Scaling Algorithm within CrysAlisPro Software, Oxford Diffraction Ltd. Version 1.171.34.40.*

(14) Dolomanov, O. V.; Bourhis, L. J.; Gildea, R. J.; Howard, J. A. K.; Puschmann, H. OLEX2: A Complete Structure Solution, Refinement and Analysis Program. *Journal of Applied Crystallography* **2009**, *42* (2), 339–341. https://doi.org/10.1107/S0021889808042726.

(15) Sheldrick, G. M. A Short History of SHELX. *Acta Cryst A* **2008**, *64* (1), 112–122. https://doi.org/10.1107/S0108767307043930.

(16) *Sheldrick, G.M.; SHELXS-97, Crystal Structure Solution. Gottingen, Germany: University of Gottingen. 1997.*

CHAPTER 6 |

SUMMARY AND OUTLOOK

This thesis provides a comprehensive exploration of strategies for modulating *through-space* and *through-bond* charge transport pathways within self-assembled organic frameworks and coordination frameworks, aiming for enhanced conductivity. This research was initiated in October 2019 and concluded in October 2023.

In Chapter 1, a foundational understanding of charge transport in solid-state materials is established. *Through-space* charge transport among discrete aromatic molecules is scrutinised, emphasising the challenge of aligning π-orbitals towards achieving electronically desirable orientations. Effective strategies of hydrogen bonding and metal coordination are identified for controlling interactions between aromatic molecules, leading to conductive *through-space* charge transport pathways. Chapter 1 also delves into *through-space* charge transport in coordination polymers (CPs), highlighting effective metal-linker combinations that result in good orbital overlap and high *through-bond* charge transport. Notably, mixed valency CPs featuring Fe^{2+}/Fe^{3+} metal centres are identified for their notable charge transport properties within a *through-bond* charge transport pathway.

Chapter 2 focused on the synthesis and assembly of a series of naphthalene diimide (NDI) molecules. These molecules are end-substituted with four distinct pyrazole end groups, differentiated by additional methyl groups or regiochemical variations. The aim was to investigate the impact of hydrogen bonding between the different pyrazole end groups. Solution-state studies reveal typical absorption and emission responses for all four synthesised molecules, along with two reversible reductions observed through cyclic voltammetry. In the solid state, these molecules self-assemble into supramolecular structures, displaying varying degrees of electronically desirable overlap between NDI π-orbitals. Experimental conductivity and computational studies reveal that the molecule with the highest π-orbital overlap, in conjunction with good π–π distances in the solid state, outperforms the other synthesised molecules. The work in Chapter 1 highlights that the most electronically desirable *through-space* charge transport is achieved *via* a twisted orientation of co-facial π-surfaces, as opposed to the parallel arrangement observed in an alternative end-substituted NDI displayed in this Chapter.

Chapter 3 was dedicated to the design and synthesis of a CP characterised by notable thermal and chemical robustness. The CP was engineered with the potential to facilitate both *through-bond* and *through-space* charge transport pathways, positioning it for application as an active material in an energy storage device. One of the NDI molecules developed in Chapter 2 was selected as an organic linker due to its low-lying LUMO orbitals, redox availability, and two potential coordination points for metals. Upon synthetic combination of an iron chloride salt and the NDI molecule, a 2D interpenetrated framework was unveiled that showcased a Fe–pyrazolate backbone, high π-orbital overlap between NDI linkers, and chloride bridges between Fe metal centres. Experimental conductivity tests and computational calculations confirm the framework's high conductivity and suggest the presence of two charge transport pathways, *through-space* and *through-bond,* within one framework.

Chapter 4 explored an isoreticular design strategy in order to exploit the topological net of the framework developed in Chapter 3. Two new materials were synthesised with different Fe–anion salts which were confirmed by powder X-ray diffraction (PXRD) to retain the same isostructural net as observed in the CP developed in Chapter 3. Further analysis of the PXRD results indicates that the lattice of the new frameworks has either decreased or increased, depending on the size of the incorporated anion, thus impacting distances between charge carriers. Conductivity measurements revealed that the framework containing the largest anion exhibited the poorest conductivity, while the framework with the larger anion displayed the highest conductivity. Computational work demonstrated that orbital overlap is maximised in the framework displaying the smallest lattice, and calculations to determine the effective electron mass align with experimental conductivity results, confirming that the framework with the smaller anion proved to be the best semiconducting material. Hence, in Chapter 4, the isostructural design strategy led to the development of isostructural materials that modulated *through-space* and *through-bond* charge transport pathways towards becoming more electronically desirable.

Chapter 5 endeavoured to replicate the attractive Fe–pyrazolate backbone and impressive π-orbital overlap between NDI observed in Chapters 3 and 4. The chapter explored the use of an alternative inorganic linker with different bonding modes compared to the anions observed in Chapters 3 and 4, aiming to assess the effect on charge transport pathways. By combining the NDI ligand used in Chapters 3 and 4 with Fe and a formate bridge, a new framework with entirely different characteristics emerged. The new framework featured a Fe–formate bridge, and uneven overlap NDI ligands, both potentially serving as charge transport pathways. In order to broaden the range of frameworks, an isoreticular strategy is employed to generate isostructural materials with Mn and Co metal centres. Conductivity analysis of the three materials yielded very similar high values, on par with what was observed in Chapter 4 for the highest conducting material, suggesting that the charge transport in this set of isostructural materials occurs almost entirely *through-space*.

This work in this Thesis effectively demonstrated how the assembly of solid-state materials directly influenced charge transport in a range of organic and mixed organic-inorganic materials. Through meticulous examination, critical aspects such as the position of hydrogen bonding groups, orientation of aromatic groups, and the size of components within a framework were detailed. From the experimental and computational studies of each self-assembled structure, each aspect was shown to contribute to a respective charge transport pathway. Although not attempted in this work, it is anticipated that all featured materials in the thesis will be evaluated as active materials in energy storage devices, given the impressive charge transport and redox properties observed in each material.

CHAPTER 7 |

APPENDIX

7.1 GENERAL EXPERIMENTAL DETAILS

Materials. Unless otherwise stated, all reagents and solvents were purchased from commercial suppliers and used without further purification unless stated otherwise. Anhydrous solvents were obtained from a neutral alumina Solvent Purification System under nitrogen and stored normally over activated (>250 °C at 0.01 mbar overnight) 3 Å molecular sieves under a dry Ar atmosphere. Solvents and solutions required for air-sensitive manipulations and samples were degassed thoroughly using a minimum of three freeze–pump–thaw cycles and stored under an Ar atmosphere. Microwave-assisted reactions were carried out in heavy-walled microwave vials sealed with crimp-style septum caps using a CEM Discover S microwave reactor.

Product confirmation. Analytical thin-layer chromatography (TLC) was performed on aluminum-backed silica gel 60 plates pre-loaded with F254 indicator (Sigma Aldrich) and visualised under UV light irradiation (254 and 365 nm). Nuclear magnetic resonance (NMR) spectra were recorded at 298 K on a JEOL 400-ECS spectrometer with a working frequency of 400 and 101 MHz for ^{1}H and ^{13}C nuclei, respectively. The operating temperature of the NMR spectrometer was measured with the aid of a MeOH internal calibrant. ^{13}C NMR experiments were proton decoupled. Chemical shifts (δ) are reported in parts per million (ppm) relative to the signals corresponding to the residual non-deuterated solvents ($CDCl_3$: δ_H = 7.26 ppm, δ_C = 77.23 ppm; CD_3SOCD_3: δ_H = 2.50 ppm, δ_C = 39.57 ppm). Deuterated solvents were routinely stored in a dry box over activated silica gel desiccant and used as received. Coupling constants (J) are reported in Hertz (Hz) and ^{1}H multiplicities are reported in accordance with the following convention: s = singlet, d = doublet, t = triplet, q = quadruplet, p = pentet, m = multiplet. NMR spectra were processed using MestReNova software, Version 14. Low- and high-resolution mass spectra (HR-MS) were measured on a Bruker compact^{TM} quadrupole time-of-flight (qTOF) mass spectrometer equipped with either an electrospray ionisation (ESI) or atmospheric-pressure chemical ionisation (APCI) source in positive (*ve*+) and/or negative (*ve*–) modes. Elemental analyses were carried out on an Exeter Analytical CE-440 elemental analyzer (horizontal furnace, static combustion) that was calibrated against an acetanilide standard as well as by use of *S*-benzyl thiuronium chloride as an internal standard.

Thermal analysis. Thermogravimetric analyses were carried out on a PL Thermal Sciences STA 625 under nitrogen flow of 10 mg mL^{-1} on 10 mg sample masses.

Electrochemical analysis. Solution-state CV experiments were recorded at room temperature (25 ºC) on Ar-purged samples (1 mM containing 0.1 M $TBAPF_6$ electrolyte (recrystallised from hot EtOH)) in anhydrous DMF using a Gamry Reference 3000 potentiostat/galvanostat/ZRA instrument interfaced to a PC. All solution-state electrochemical experiments were performed using a glassy carbon working electrode (0.071 cm^2) that was polished routinely with 0.05-µm alumina–water slurry on a felt surface immediately before each use. The Pt wire counter electrode was flame-treated to remove any oxidised impurities from the electrode surface prior to each use. The Ag/AgCl (sat. KCl) reference electrode was stored in a 3 M KCl solution and rinsed with acetone followed by the analyte solvent to remove trace water prior to experiments. Voltammograms were referenced against the ferrocene/ferrocenium (Fc/Fc^+) redox couple as an external standard measured before and after sample measurements.

Surface-confined CV experiments were recorded at room temperature (25 ºC) using a layer of material that was adhered to the WE by drop-casting a suspension of a material (20 mg mL^{-1}) in CH_2Cl_2. The drop-cast material was measured in Ar-purged electrolyte (0.1 M $TBAPF_6$ (recrystallised from hot EtOH)) in anhydrous acetonitrile using a Gamry Reference 3000 potentiostat/galvanostat/ZRA instrument interfaced to a PC. All surface-confined electrochemical experiments were performed using a glassy carbon working electrode (0.071 cm^2) that was polished routinely with 0.05-µm alumina–water slurry on a felt surface immediately before each use. The Pt wire counter electrode was flame-treated to remove any oxidised impurities from the electrode surface prior to each use. The Ag/AgCl (sat. KCl) reference electrode was stored in a 3 M KCl solution and rinsed with acetone followed by the analyte solvent to remove trace water prior to experiments. Voltammograms were referenced against the ferrocene/ferrocenium (Fc/Fc^+) redox couple as an external standard measured before and after sample measurements.

Optical analysis. Absorption spectra (200–1100 nm) were recorded on a Shimadzu UV-2401PC or UV-1800 spectrophotometer equipped with W/D2 lamps on samples in N_2-purged solvents. Fluorescence spectroscopy was carried out on a Shimadzu RF-5301PC spectrofluorophotometer equipped with a 150 W Xe lamp against machine-specific calibration curves and on samples in N_2-purged solvents. Solid-state UV-Vis absorption spectra (200–1100 nm) were recorded using either an Ocean Optics spectrometer or a Cary 5000 photospectrometer, using an integrating sphere attachment.

X-ray analysis. The images of the crystal structures obtained were processed using the program Mercury. Powder X-ray diffraction (PXRD) data was collected on a Bruker Advance D8 diffractometer using Nickel-filtered Cu-Kα radiation ($\lambda = 1.5418$ Å) in reflection mode. PXRD samples were prepared by suspending the sample in MeOH and transferring to the 25 mm sample plate, yielding a thin layer of sample. Alternatively, PXRD diffraction data was collected on a Panalytical Aeris diffractometer, using a Cu radiation ($\lambda = 1.5418$ Å) source. Samples were mounted on sample plates without further manipulations. All simulated PXRD were generated from the solvent-free SCXRD structures using Mercury (v 2022.3) with a step of 0.1º. X-ray fluorescence (XRF) spectroscopy was performed on a Horiba XGT-7200 X-ray fluorescence spectrometer, using a Rh radiation source and tube voltages of 50kV. Samples were prepared by spin-coating onto a glass slide, and then placed on the internal stage, which was then put under partial vacuum before analysis was carried out.

Hirshfeld analysis. Hirshfeld analysis and energy framework calculations were performed using CrystalExplorer17.5 software employing the TONTO utility for DFT calculations carried out at the B3LYP/6-31g(d,p) level of theory.[1] A scale has been included in all figures containing a Hirshfeld surface, wherein a fully red surface has a value of +1 a.u., and indicates that there are intermolecular contacts that are closer than the sum of the van der Walls radii (i.e., close contacts). A blue surface refers to the opposite, that intermolecular contacts are further away than the sum of the van der Walls radii (i.e., no contacts). A white surface refers to the intermolecular contacts in that area being equal to the sum of the van der Waals radii (i.e., medium contacts). For energy framework calculations, a molecular shell with a 3.8 Å radius was generated around a central molecule, and the interaction energies (electrostatic, dispersion and total) between the molecular pairs were calculated. The scale factors for benchmarked energies used for the construction of energy models were taken from Mackenzie et al.[2] The lattice energy was calculated as the halved sum of the interaction energies between the given molecule and all the surrounding molecules within 25 Å radius.[2]

Conductivity analysis. Conductivity measurements were carried out using a "home-built" two-point probe pellet press device operated at room temperature and in air. The home-built device consisted of an upper and lower stainless-steel rods that were supported by an internal pressure sensor that was housed inside a stainless-steel casing. Before the measurement was taken, samples were prepared by grinding with a pestle and mortar in MeOH for 1 minute to ensure a uniform distribution of crystallite sizes, and was then dried and re-activated in the oven at 200 °C for 12 h. Once activated, the ground sample was carefully deposited inside a glass sample tube which was positioned onto the lower steel rod, followed by screwing of the upper casing that held the upper rod to generate 80 kg of pressure between the rods. The press was re-tightened several times until the pressure reading stabilised at 80 kg. The conductivity press was then connected to a sourcemeter (Keithley model 2450) and connected *via* test leads with crocodile-clip heads to the two stainless steel rods. To the resulting pellet, current–voltage (I–V) curves were obtained from –1 V to +1 V to obtain linear plots from which a conductivity could be calculated. Two repeat tests on new pellets were carried out to ensure reliability. Pellets were measured by a micrometer (Moore & Wright 966B, 4'–5') and then extracted and measured by PXRD, confirming that each material retained its original single crystal packing. The thickness of the pellets ranged from 500 μm–1100 μm depending on the amount of sample added (2–4 mg).

Porosity analysis. Porosity was measured using a Micromeritics Tristar II Plus. Nitrogen adsorption/desorption isotherms were measured in liquid nitrogen. Before analysis samples were degassed at 200 ºC for 16 h. The BET model was used to calculate surface area.

7.2 NUCLEAR MAGNETIC RESONANCE

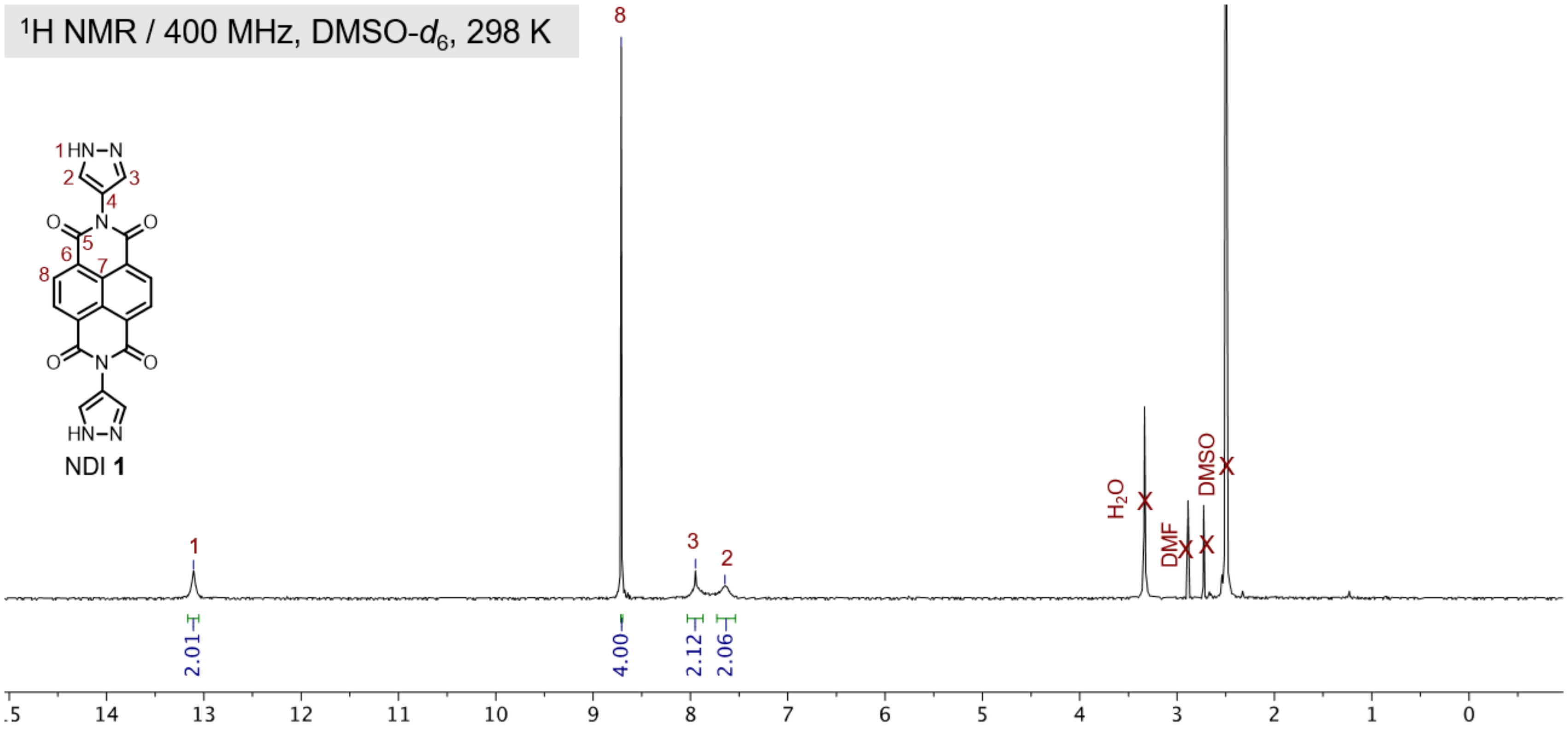

Figure 7.1. ^{1}HNMR spectrum (400 MHz, DMSO-d_6, 298 K) of NDI **1**.

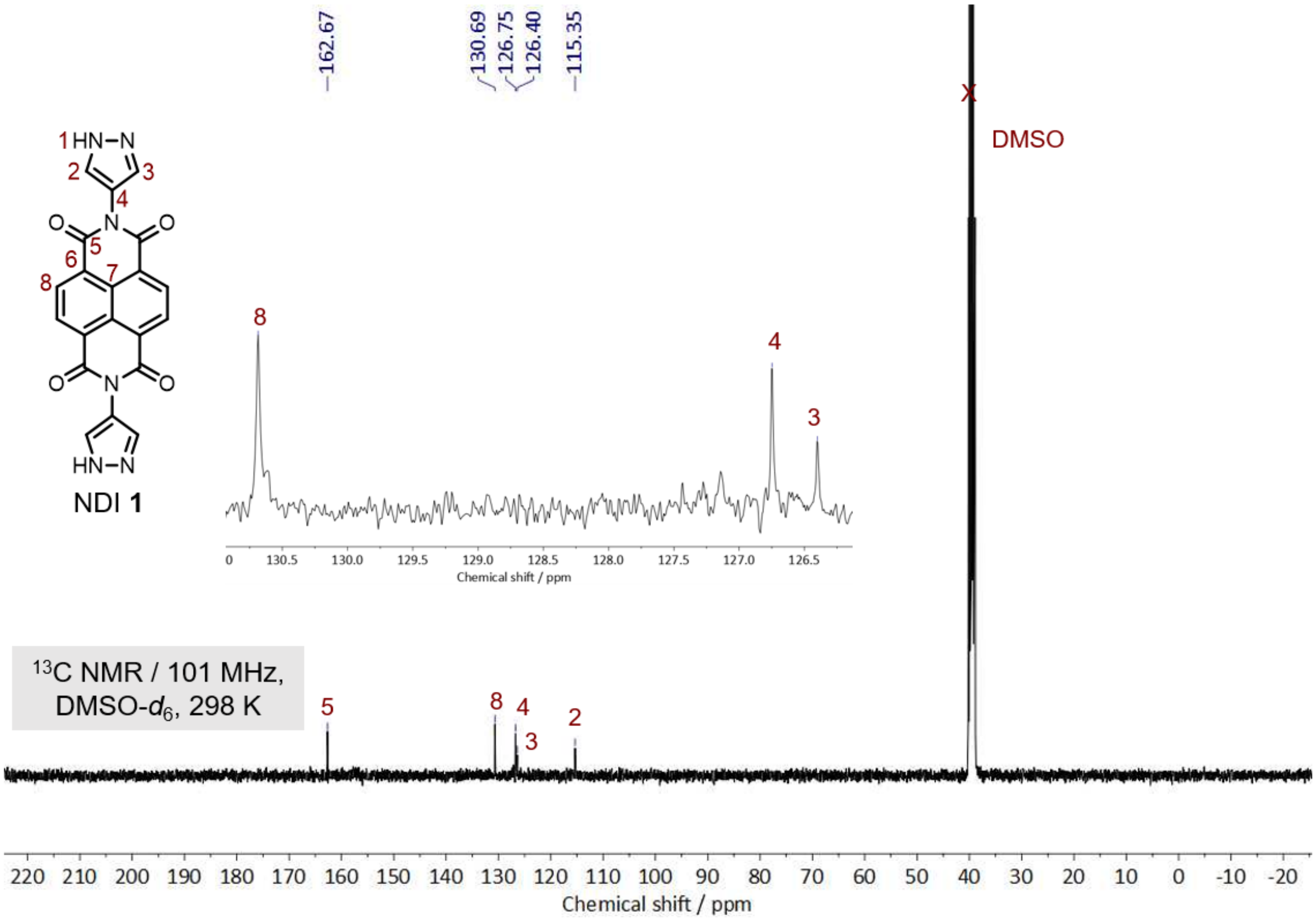

Figure 7.2. ^{13}C NMR spectrum (101 MHz, DMSO-d_6, 298 K) of NDI **1**.

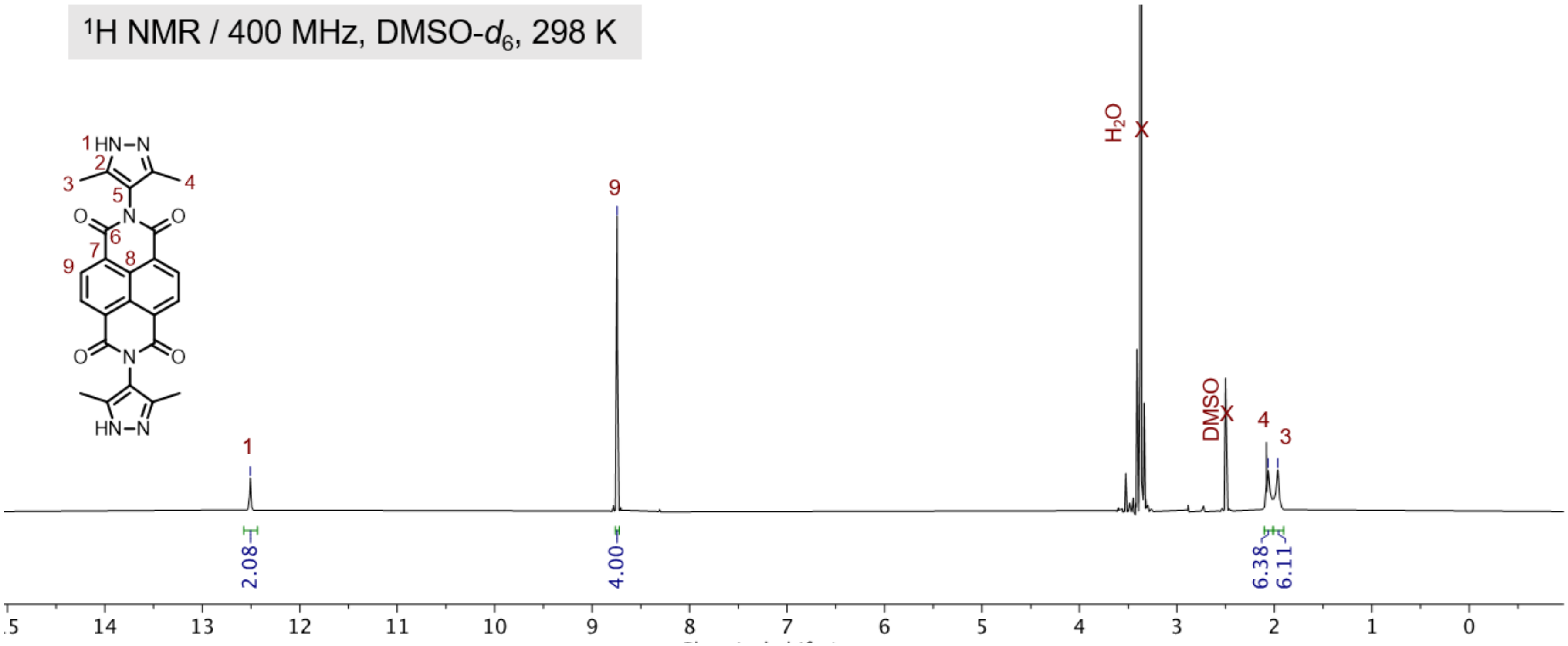

Figure 7.3. ^{1}HNMR spectrum (400 MHz, DMSO-d_6, 298 K) of NDI **2**.

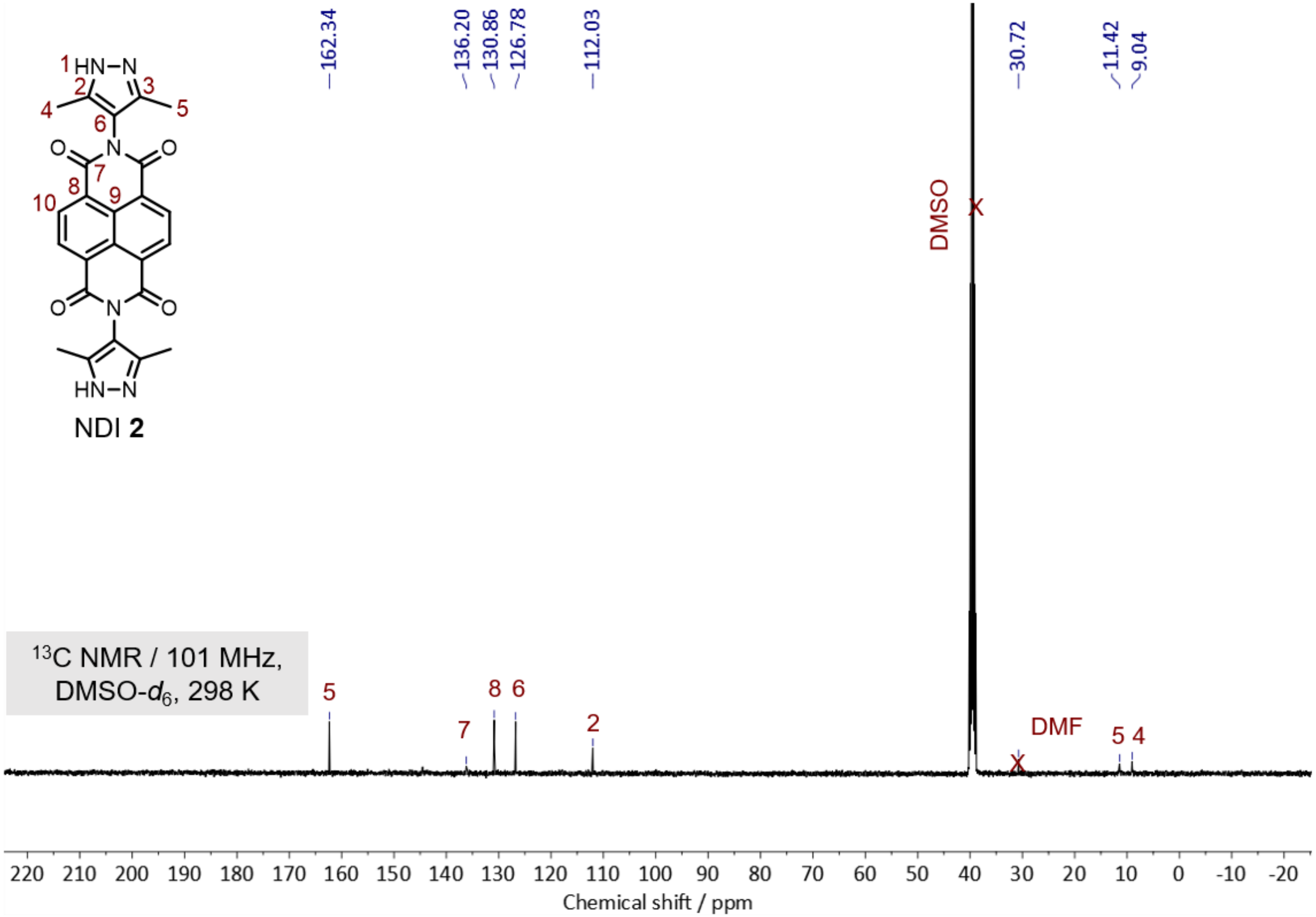

Figure 7.4. ^{13}C NMR spectrum (101 MHz, DMSO-d_6, 298 K) of NDI **2**.

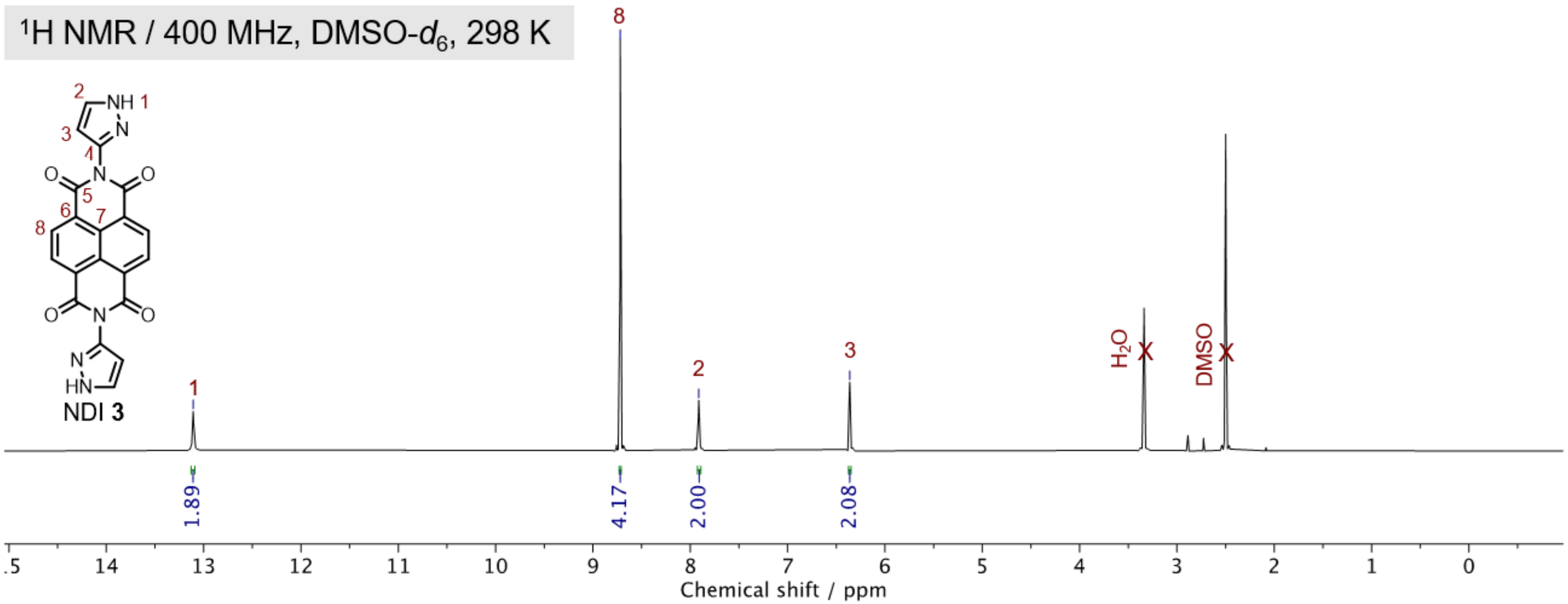

Figure 7.5. ^{1}HNMR spectrum (400 MHz, DMSO-d_6, 298 K) of NDI **3**.

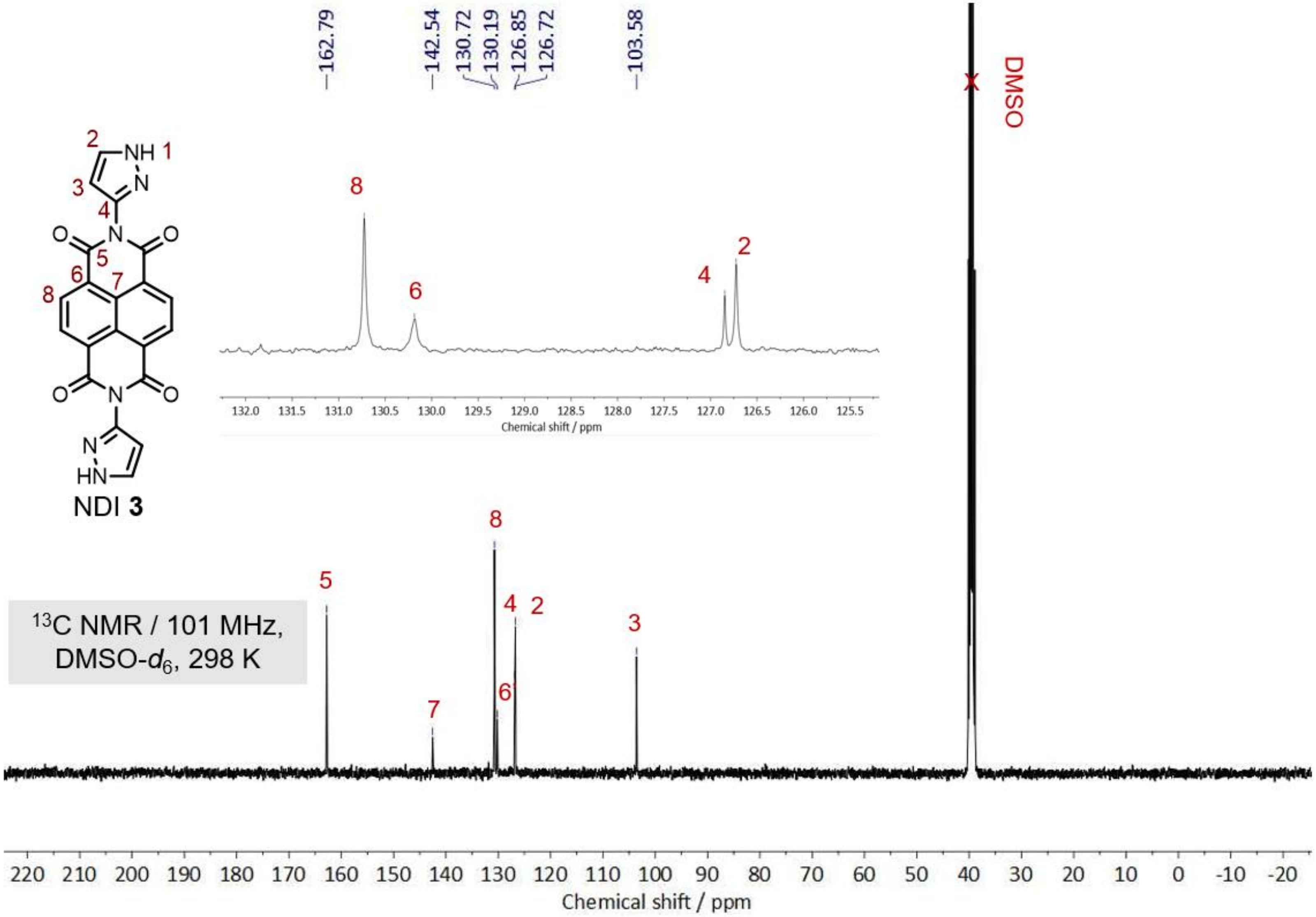

Figure 7.6. ^{13}C NMR spectrum (101 MHz, DMSO-d_6, 298 K) of NDI **3**.

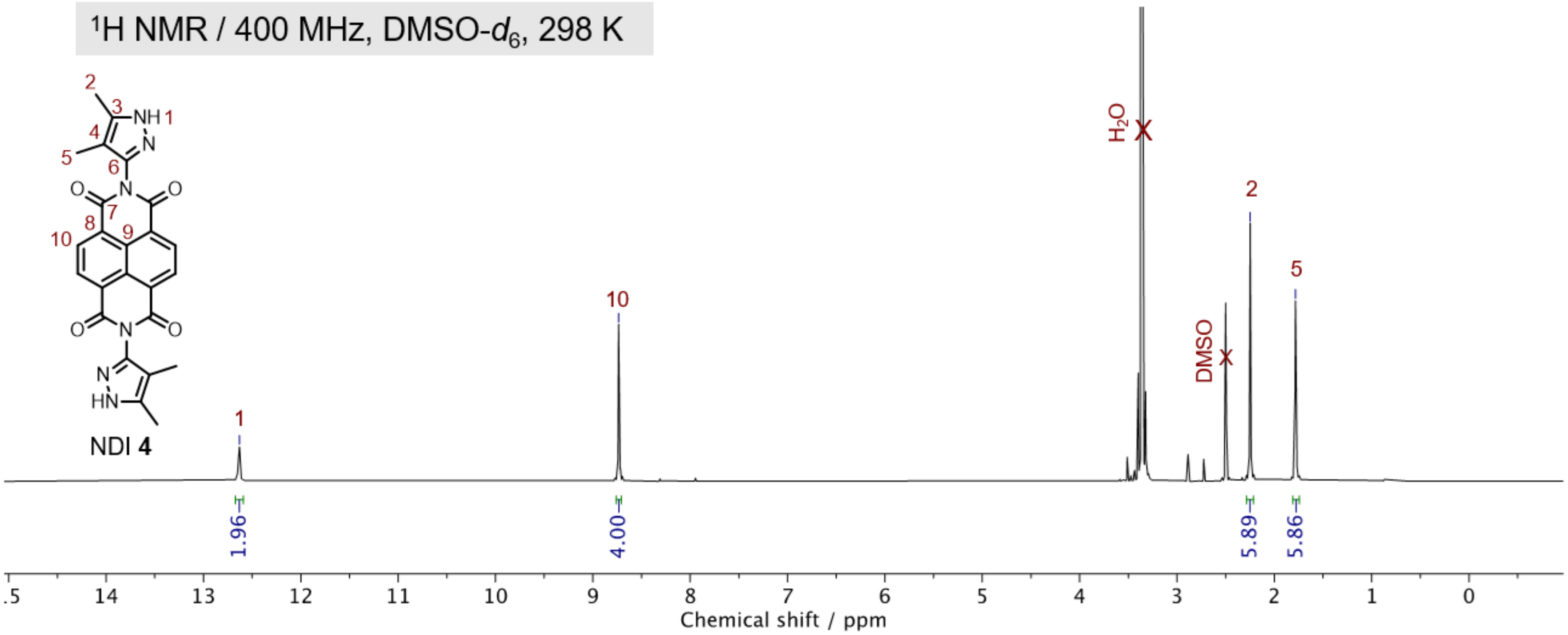

Figure 7.7. ^{1}HNMR spectrum (400 MHz, DMSO-d_6, 298 K) of NDI **4**.

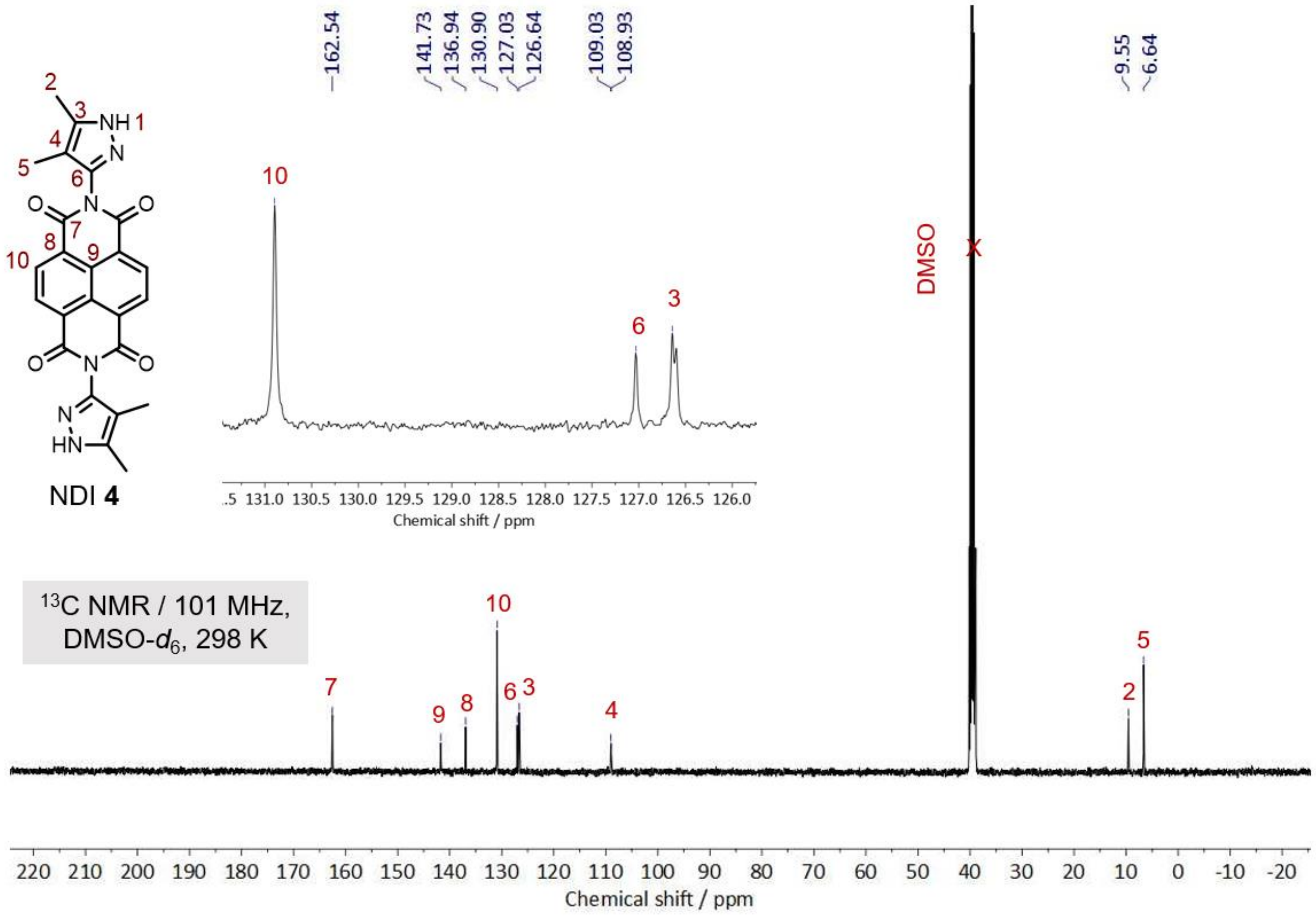

Figure 7.8. ^{13}C NMR spectrum (101 MHz, DMSO-d_6, 298 K) of NDI **4.**

7.3 MASS SPECTROMETRY

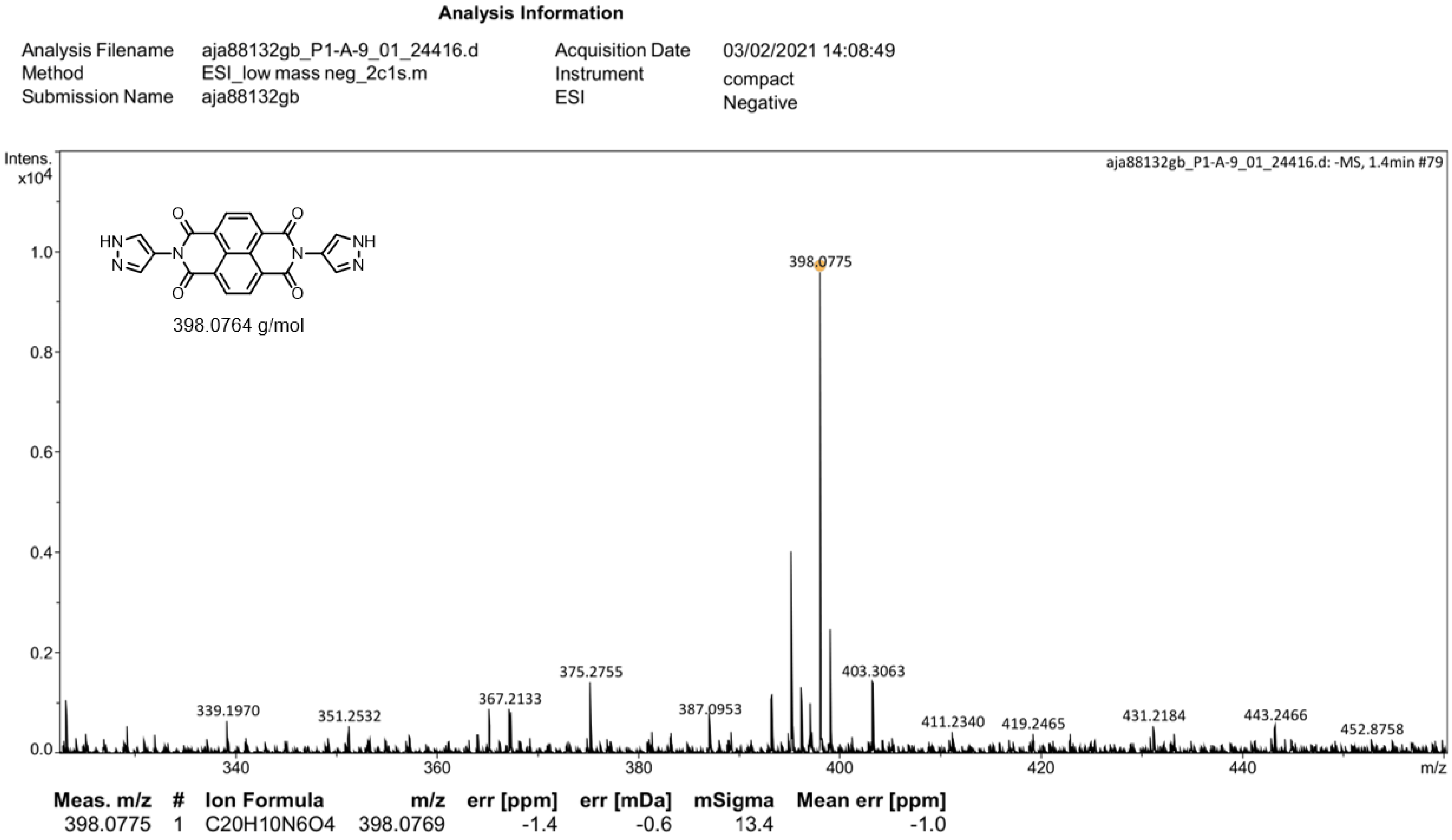

Analysis Information

Analysis Filename	aja88132gb_P1-A-9_01_24416.d	Acquisition Date	03/02/2021 14:08:49
Method	ESI_low mass neg_2c1s.m	Instrument	compact
Submission Name	aja88132gb	ESI	Negative

Meas. m/z	#	Ion Formula	m/z	err [ppm]	err [mDa]	mSigma	Mean err [ppm]
398.0775	1	$C_{20}H_{10}N_6O_4$	398.0769	-1.4	-0.6	13.4	-1.0

Figure 7.9. Mass spectrum (ESI, Negative mode, $CHCl_3$) of NDI **1**.

Analysis Information

Analysis Filename	aja85807gb_P1-C-9_01_21812.d	Acquisition Date	20/10/2020 16:23:29
Method	ESI_low mass neg_2c1s.m	Instrument	compact
Submission Name	aja85807gb	ESI	Negative

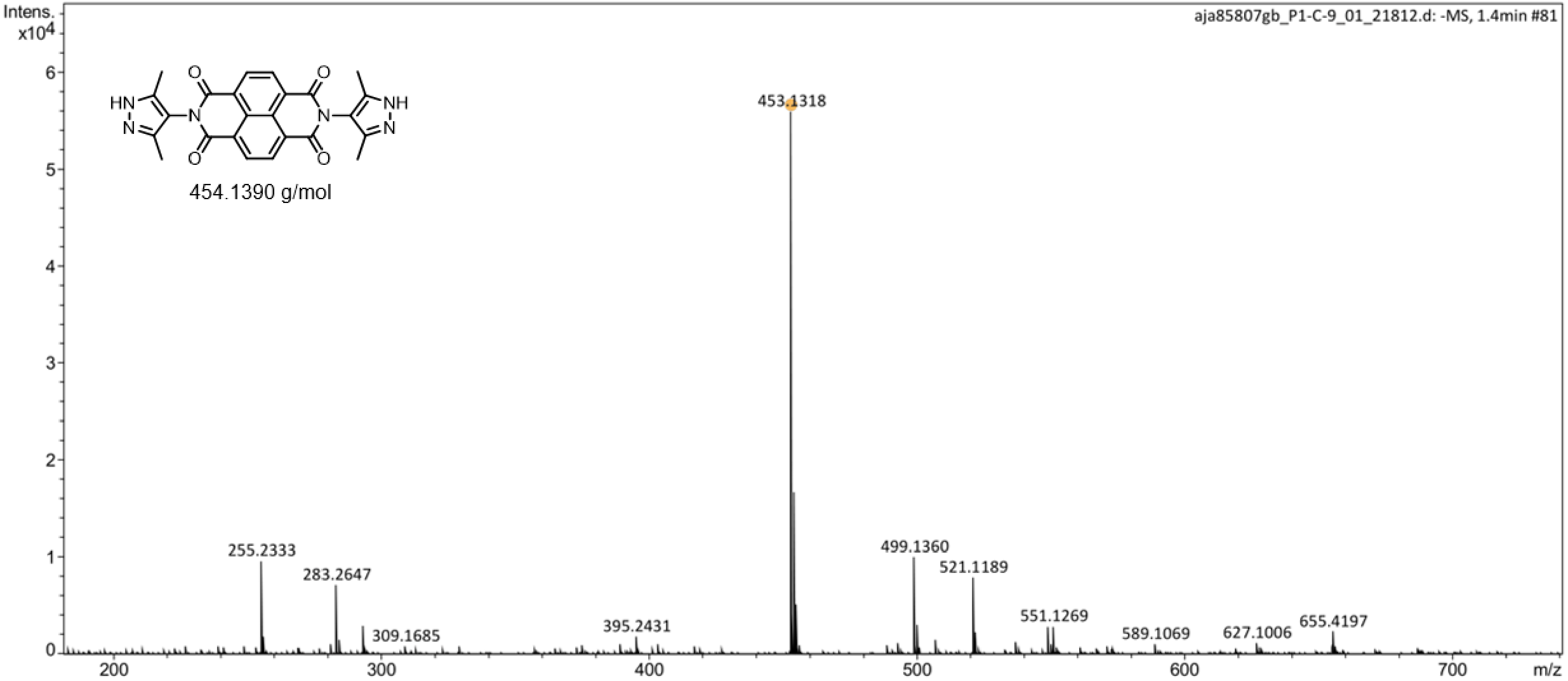

Meas. m/z	#	Ion Formula	m/z	err [ppm]	err [mDa]	mSigma	Mean err [ppm]
453.1318	1	C24H17N6O4	453.1317	-0.3	-0.1	27.4	-3.7

Figure 7.10. Mass spectrum (ESI, Negative mode, $CHCl_3$) of NDI **2**.

Analysis Information

Analysis Filename	aja88133gb_P1-B-1_01_24417.d	Acquisition Date	03/02/2021 14:11:47
Method	ESI_low mass neg_2c1s.m	Instrument	compact
Submission Name	aja88133gb	ESI	Negative

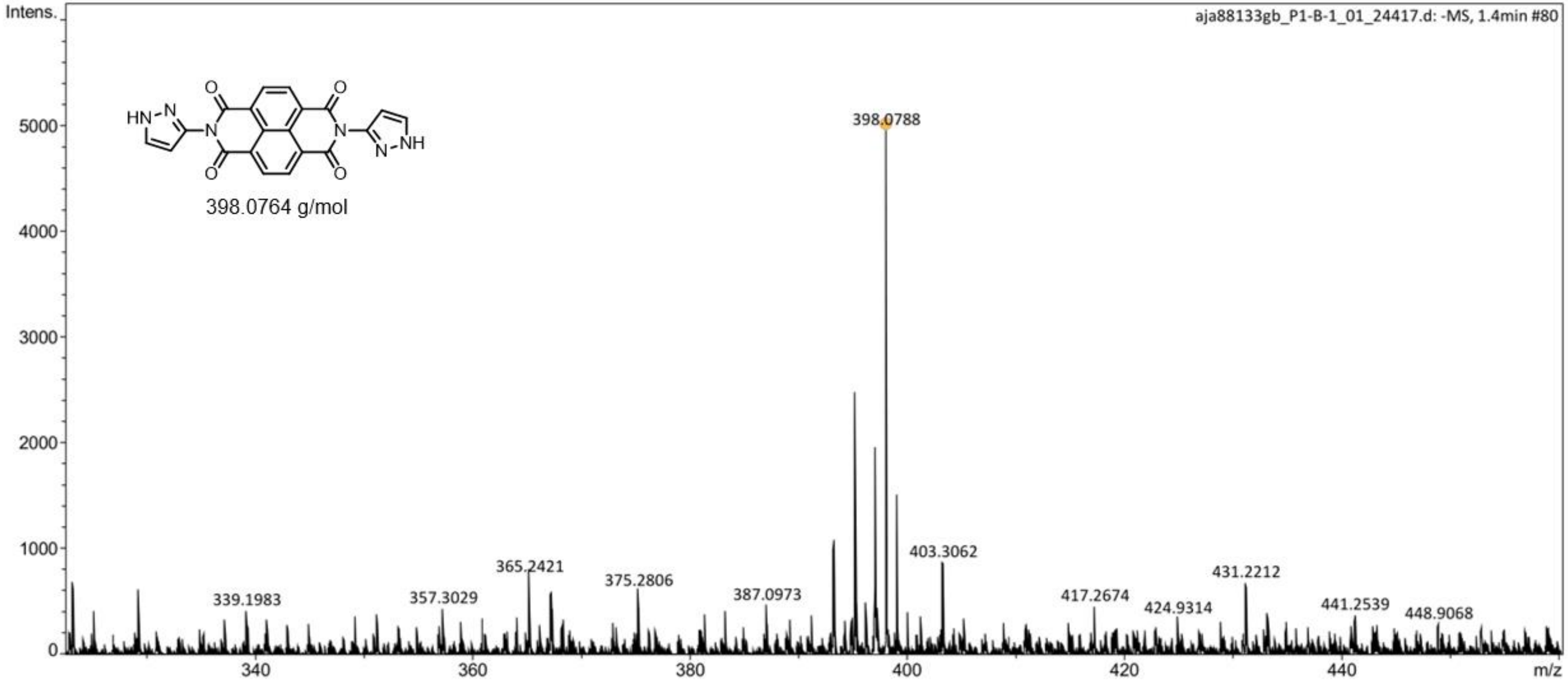

Meas. m/z	#	Ion Formula	m/z	err [ppm]	err [mDa]	mSigma	Mean err [ppm]
398.0788	1	$C_{20}H_{10}N_6O_4$	398.0769	-4.7	-1.9	45.4	-1.4

Figure 7.11. Mass spectrum (ESI, Negative mode, $CHCl_3$) of NDI **3**.

Analysis Information

Analysis Filename	aja88134gb_P1-B-2_01_24418.d	Acquisition Date	03/02/2021 14:14:47
Method	ESI_low mass neg_2c1s.m	Instrument	compact
Submission Name	aja88134gb	ESI	Negative

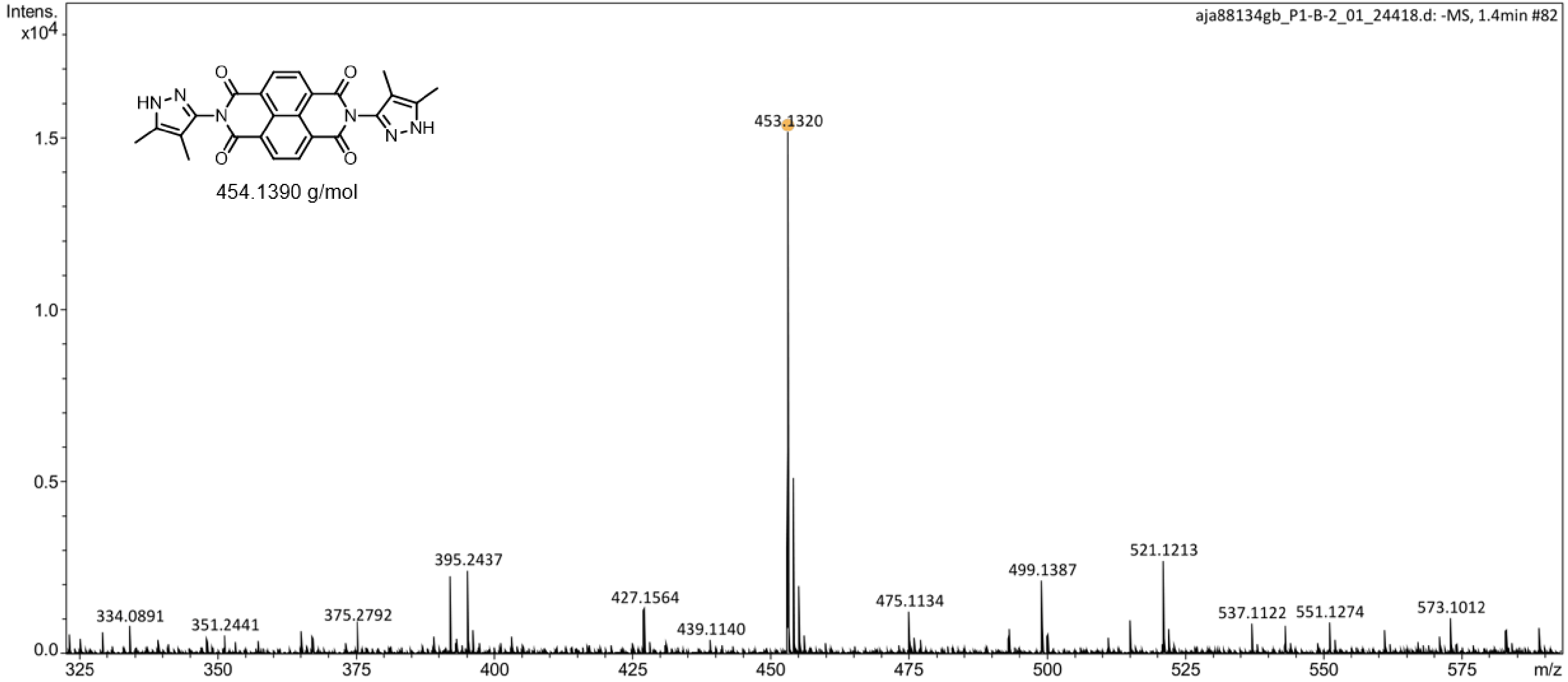

Meas. m/z	#	Ion Formula	m/z	err [ppm]	err [mDa]	mSigma	Mean err [ppm]
453.1320	1	C24H17N6O4	453.1317	-0.8	-0.4	40.8	-2.2

Figure 7.12. Mass spectrum (ESI, Negative mode, $CHCl_3$) of NDI **4**

7.4 MOLAR ABSORPTION COEFFICIENTS

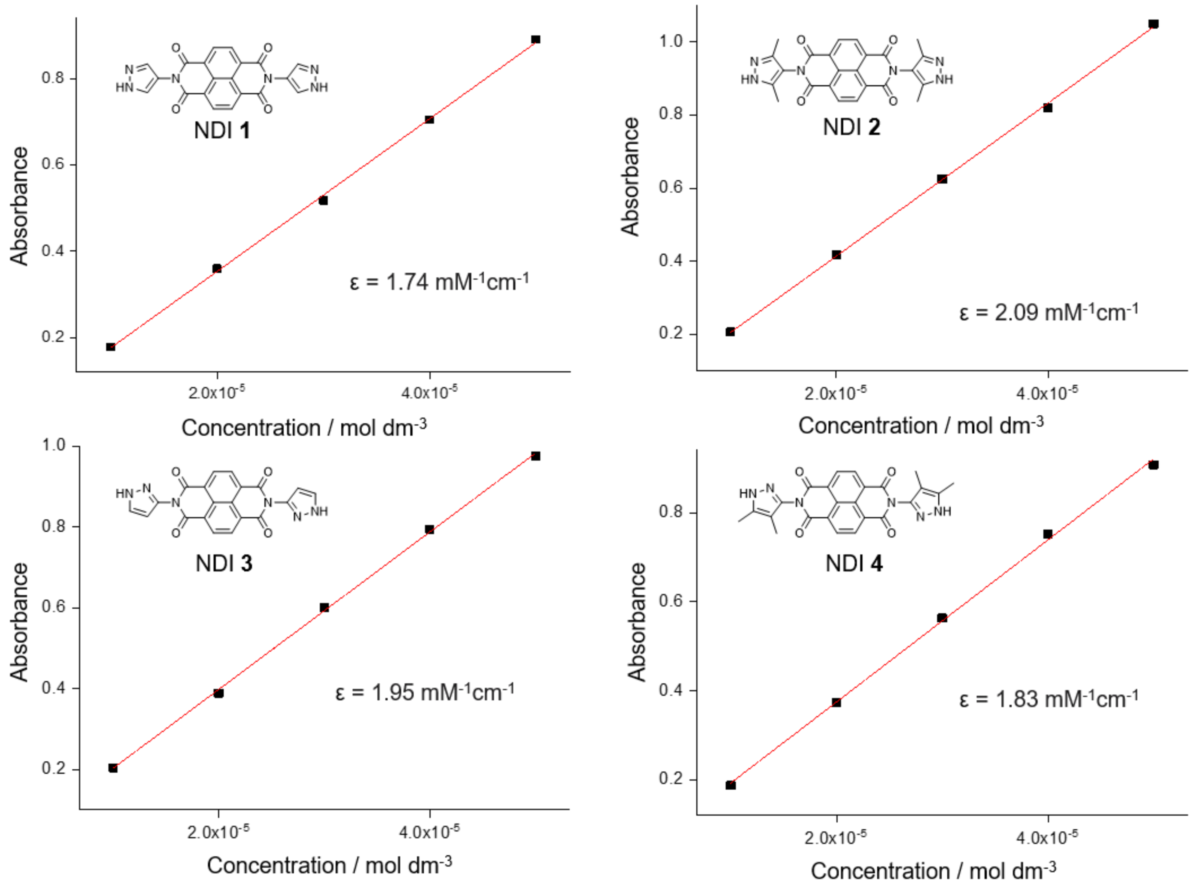

Figure 7.13. Straight lines that were used to calculate the molar absorption coefficient for NDIs **1**–**4**. All analysis was performed at 379 nm.

7.5 CRYSTALLOGRAPHIC DATA OF 1–4

Table 7.1. Crystallographic information for NDIs **1**–**4**.

Compound	**1**	**2**	**3**	**4**
CCDC reference no.				
Empirical formula	$C_{20}H_{10}N_6O_4$	$C_{24}H_{18}N_6O_4$	$C_{20}H_{10}N_6O_4$	$C_{24}H_{18}N_6O_4$
Formula weight	398.34	454.44	398.34	454.44
Crystal size / mm^3	0.18 × 0.05 × 0.03		0.155 × 0.037 × 0.012	0.16 × 0.116 × 0.092
Temperature / K	120.0	173(2)	120.0	110.05(10)
Crystal system	monoclinic	monoclinic	monoclinic	monoclinic
Space group	$P\ 2_1/n$	$P\ 2_1/c$	$I\ 2/a$	$P\ 2_1/n$
a / Å	10.8944(8)	9.6269(19)	6.9411(10)	7.4937(3)
b / Å	5.0224(4)	9.0035(18)	9.1199(10)	13.4366(4)
c / Å	15.1139(11)	12.682(3)	25.691(4)	10.0702(4)
α / °	90	90	90	90
β / °	102.448(5)	103.16(3)	92.713(13)	102.645(4)
γ / °	90	90	90	90
Volume / Å^3	807.53(11)	1070.3(4)	1624.4(4)	989.373
Z	2	2	4	2
ρ_{calc} / g cm^{-3}	1.638		1.629	1.525
μ / mm^{-1}	1.005		0.999	0.894
F(000)	408.0		816.0	472.0
2θ range for data collection / °	914 to 143.966		6.89 to 134.66	11.156 to 134.074
Reflections collected	10561	6818	4498	3401
Independent refl. (R_{int}, R_{sigma})	1546 (0.1098, 0.0835)	1804	1383 (0.1365, 0.3415)	1753 (0.0190, 0.0268)
Data/restraints/parameters	1546/0/157		1383/0/157	1753/0/191
Goodness-of-fit on F^2	1.015		0.814	1.050
Final R indexes [$I \geq 2\sigma(I)$]	$R_1 = 0.0560$, $wR_2 = 0.1221$	$R_1 = 0.0595$, $wR_2 = 0.1650$	$R_1 = 0.0571$, $wR_2 = 0.0764$	$R_1 = 0.0380$, $wR_2 = 0.0961$
Final R indexes [all data]	$R_1 = 0.0989$, $wR_2 = 0.1417$	$R_1 = 0.0631$, $wR_2 = 0.1674$	$R_1 = 0.1857$, $wR_2 = 0.0953$	$R_1 = 0.0464$, $wR_2 = 0.1025$
Largest diff. peak/hole / e Å^{-3}	0.27/–0.23		0.26/–0.25	0.25/–0.19

7.6 HIRSHFELD SURFACES FINGERPRINT PLOTS

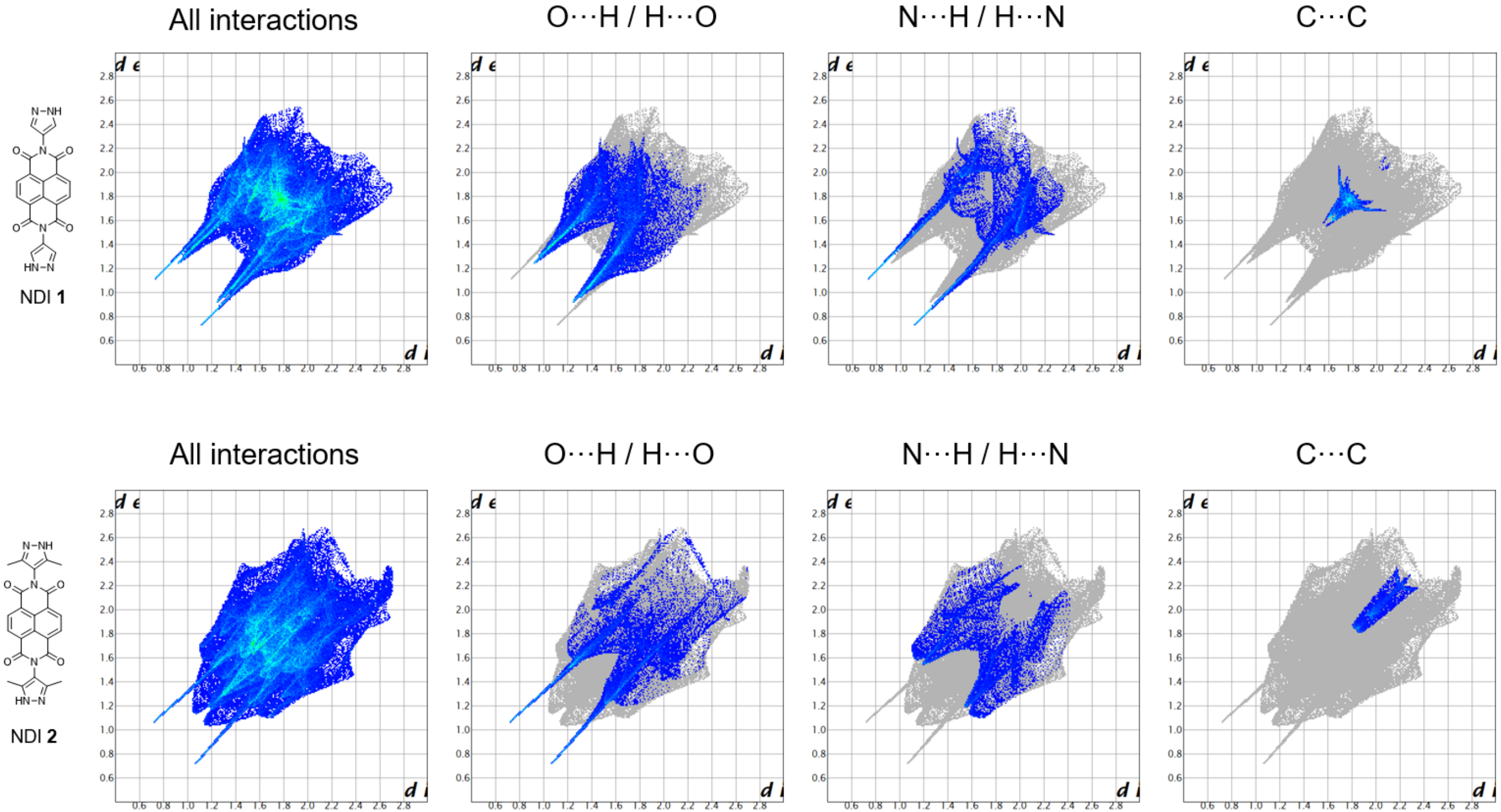

Figure 7.14. Fingerprint regions of NDIs **1** and **2**.

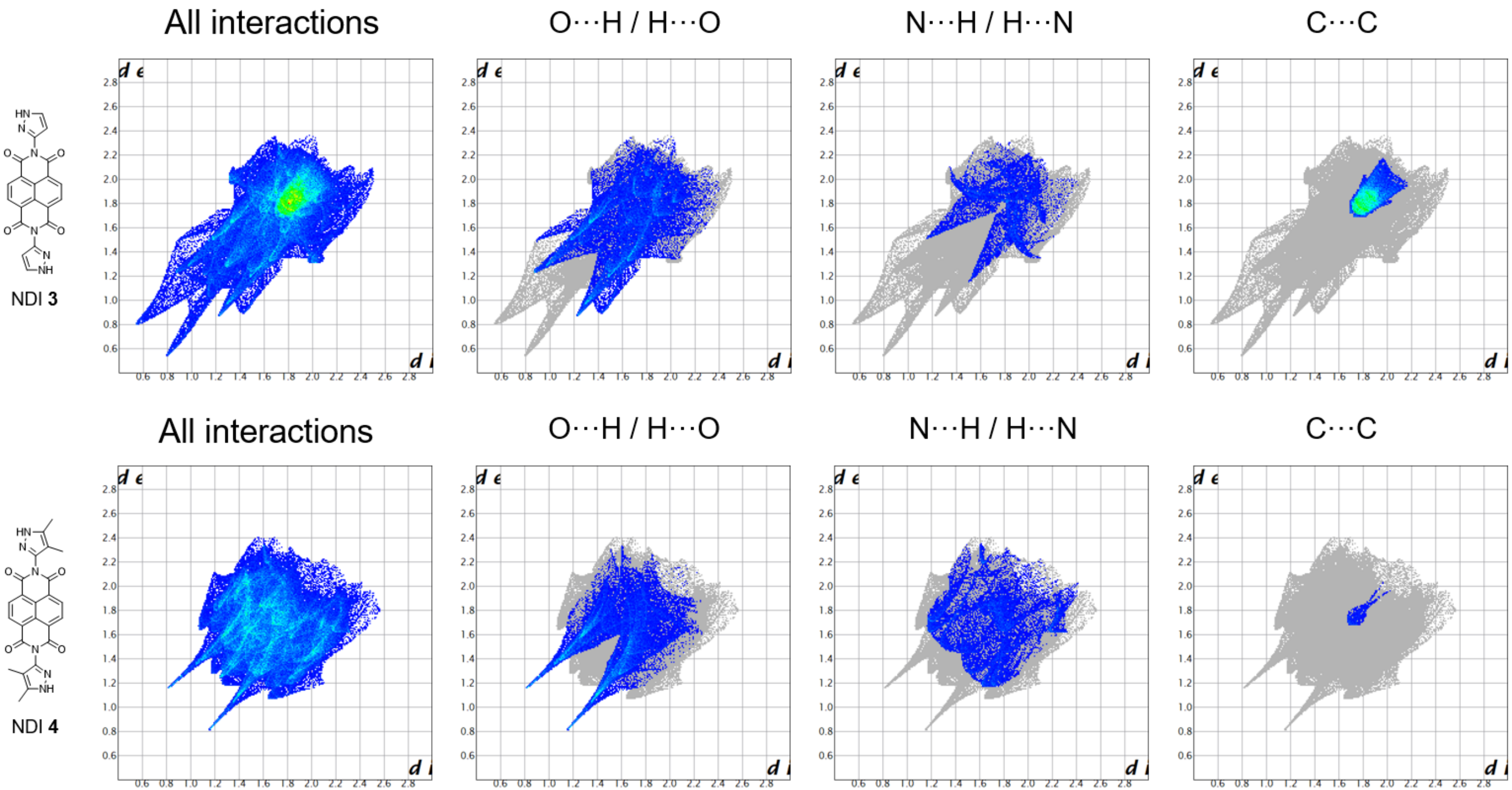

Figure 7.15. Fingerprint regions of NDIs **3** and **4**.

7.7 THE CONDUCTIVITY PRESS SCHEMATIC

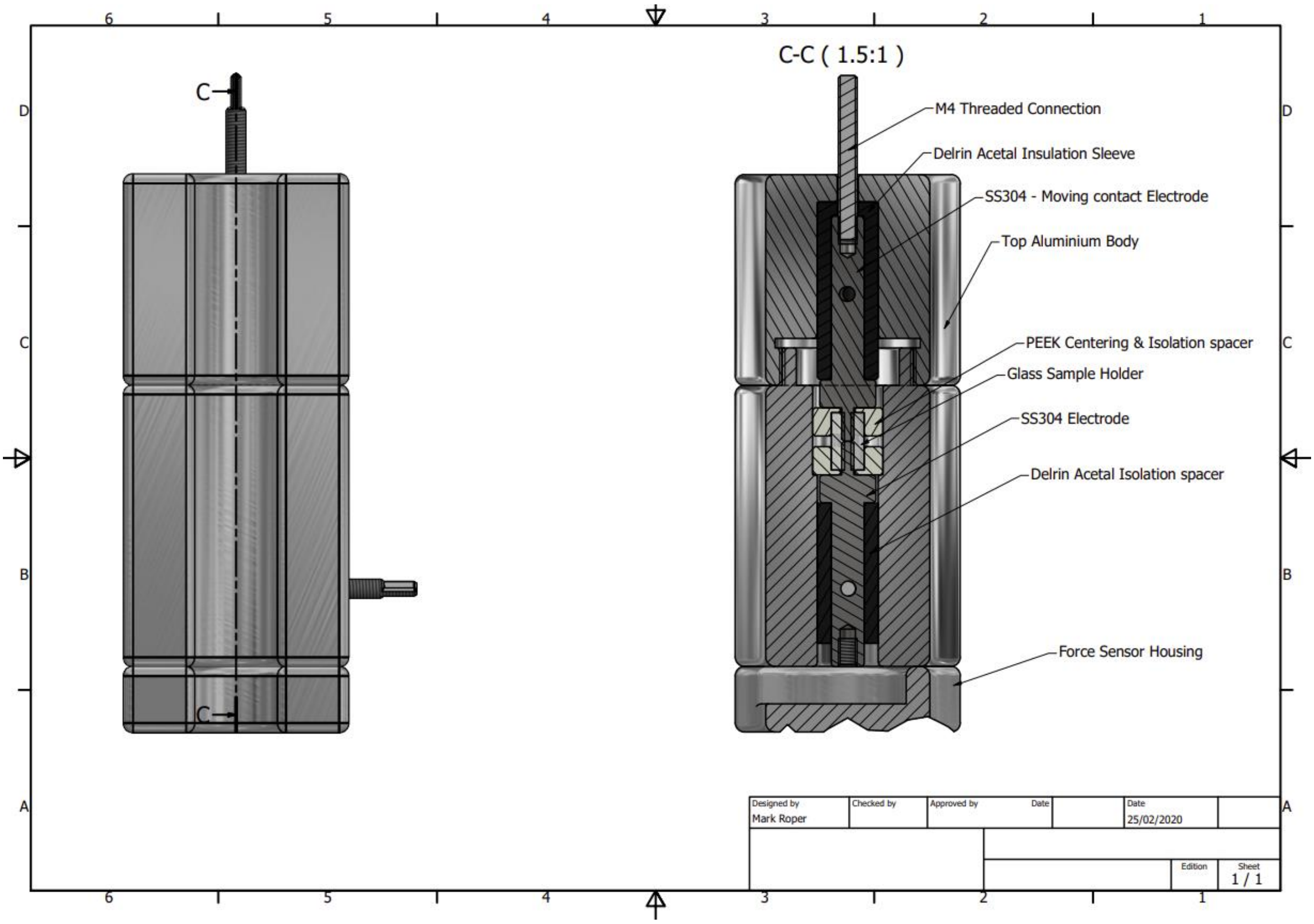

Designed by	Checked by	Approved by	Date	Date
Mark Roper				25/02/2020

Figure 7.16. Complete assembly overview of the conductivity press.

7.8 TYPICAL CONDUCTIVITY PRESS SETUP

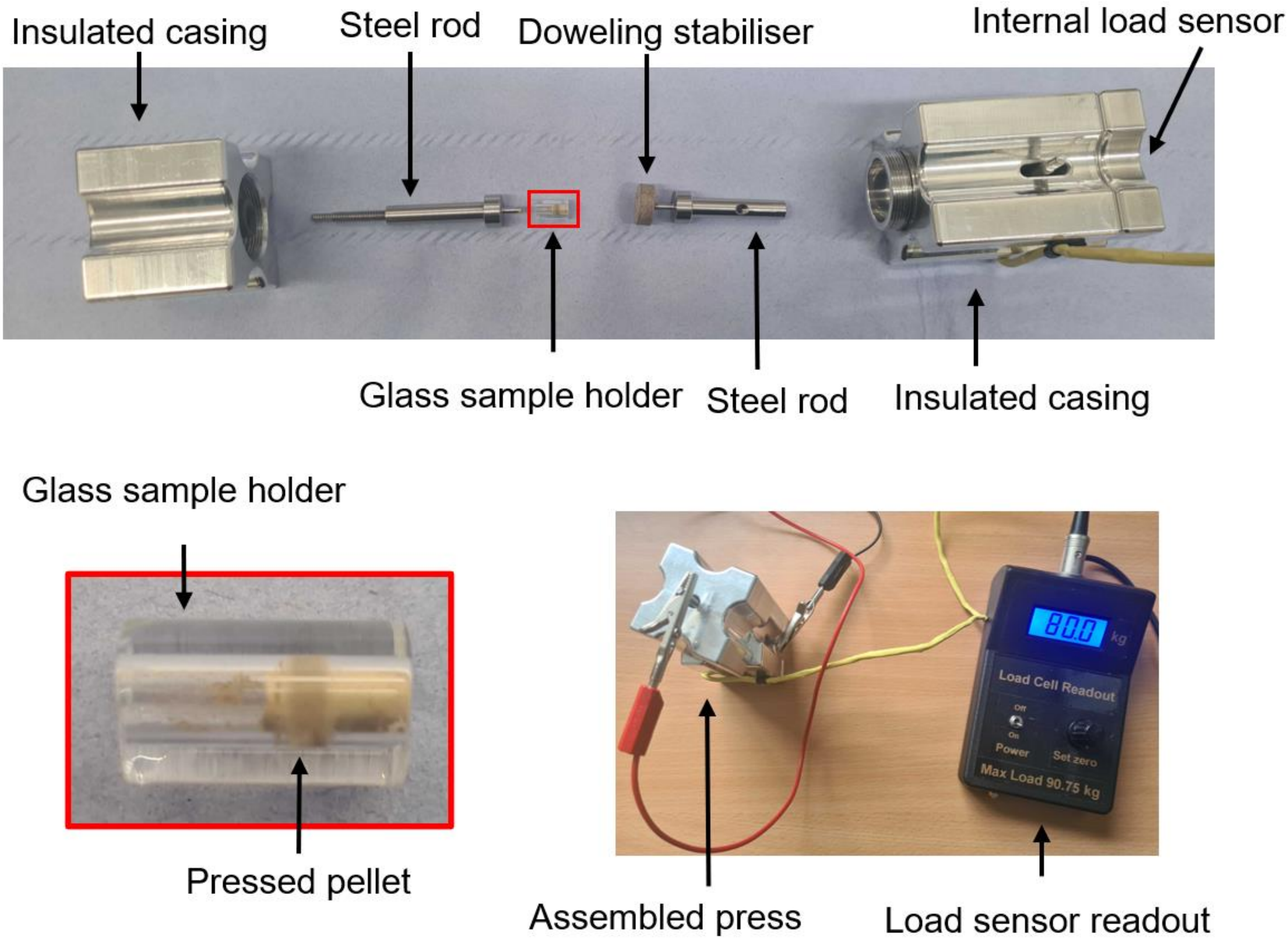

Figure 7.17. The typical experimental setup for two-probe pellet press measurements, with annotations.

7.9 I–V CURVES

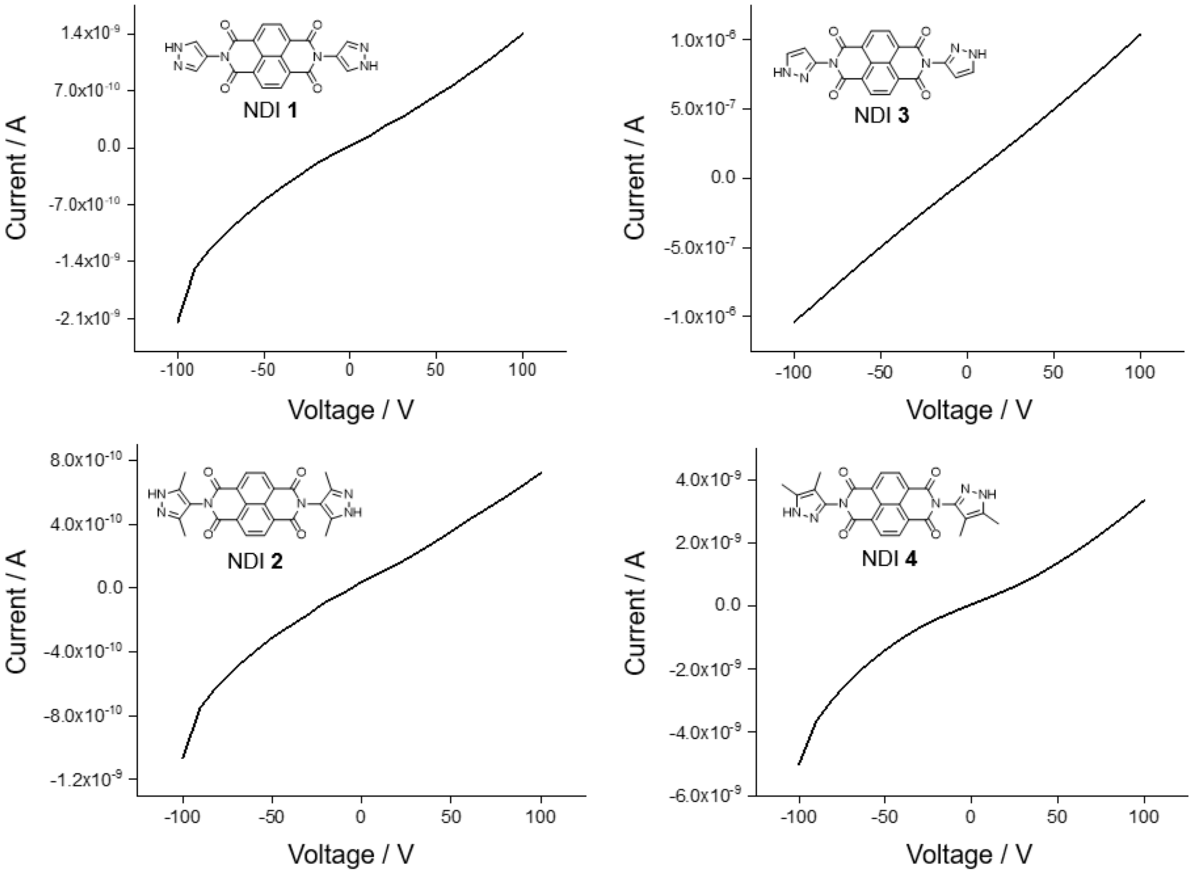

Figure 7.18. I-V curves for NDIs **1**–**4**.

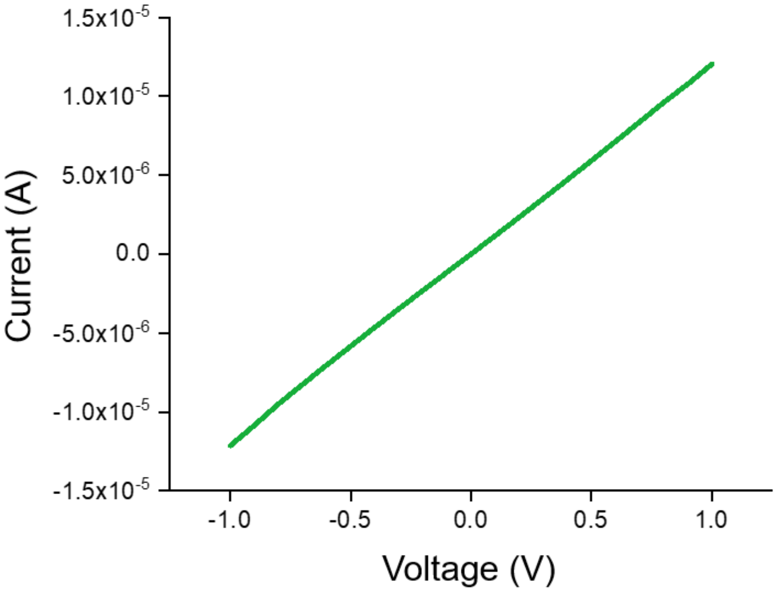

Figure 7.19. I–V curve for a pressed pellet sample of **Fe(Cl)NDI-1**.

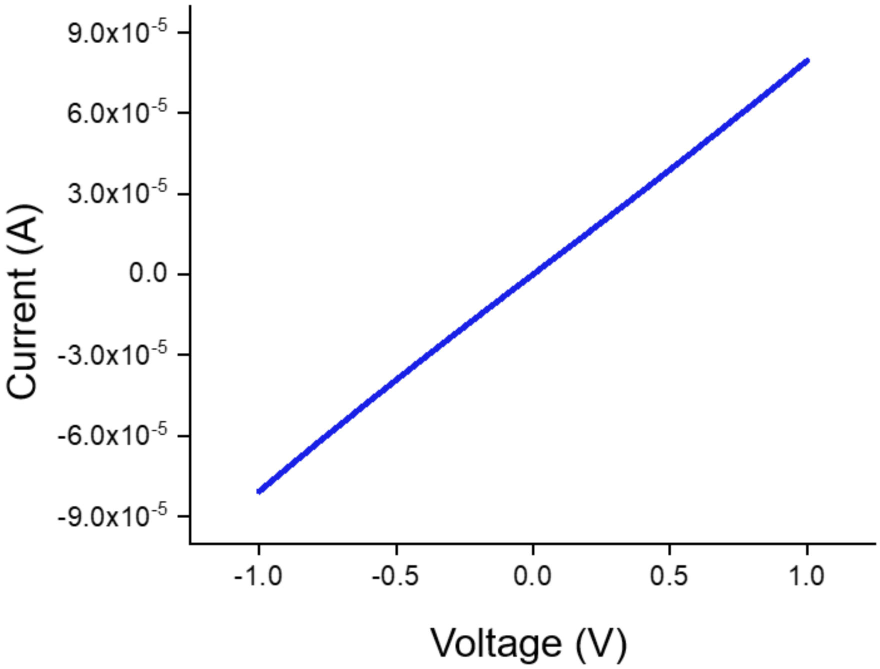

Figure 7.20. I–V curve for a pressed pellet sample of **Fe(OH)NDI-1**.

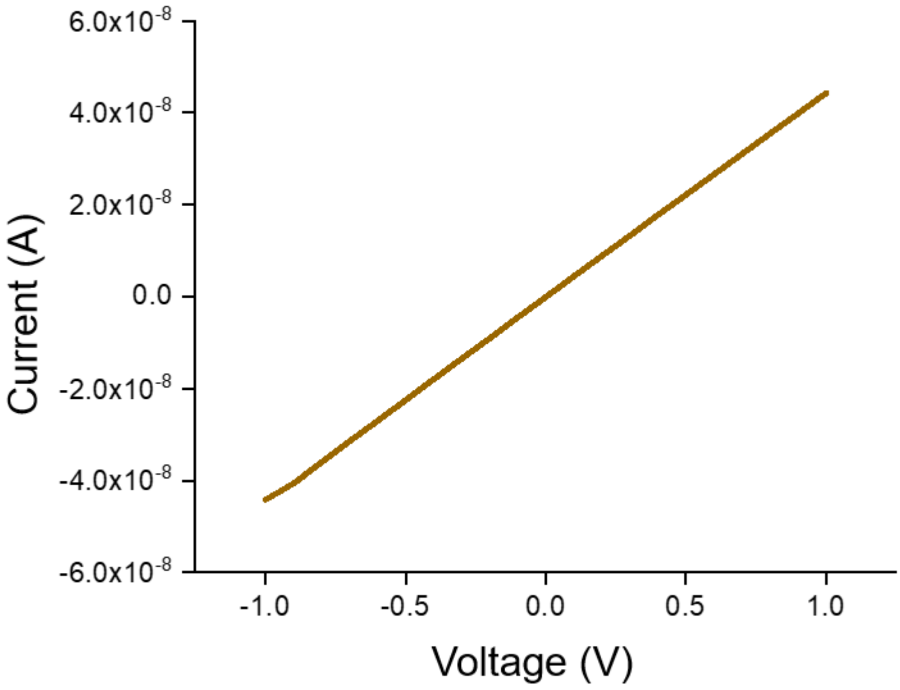

Figure 7.21. I–V curve for a pressed pellet sample of **Fe(Br)NDI-1**.

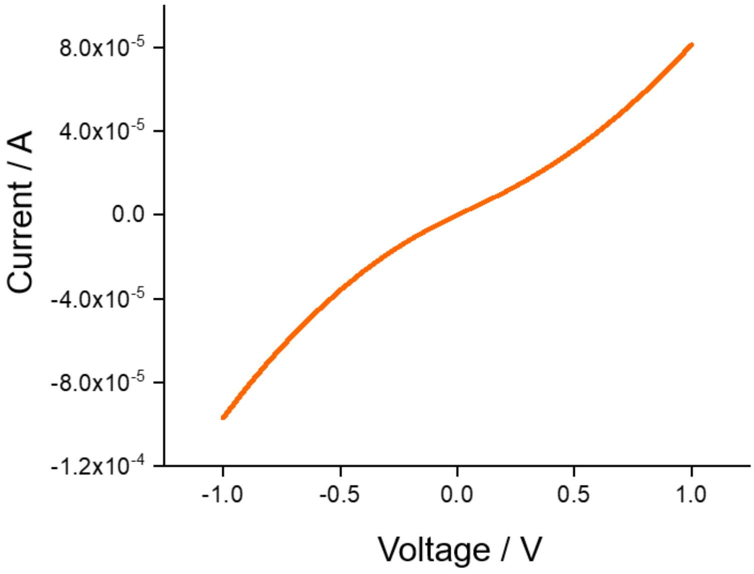

Figure 7.22. I–V curve for a pressed pellet sample of **FeCPNDI-1**.

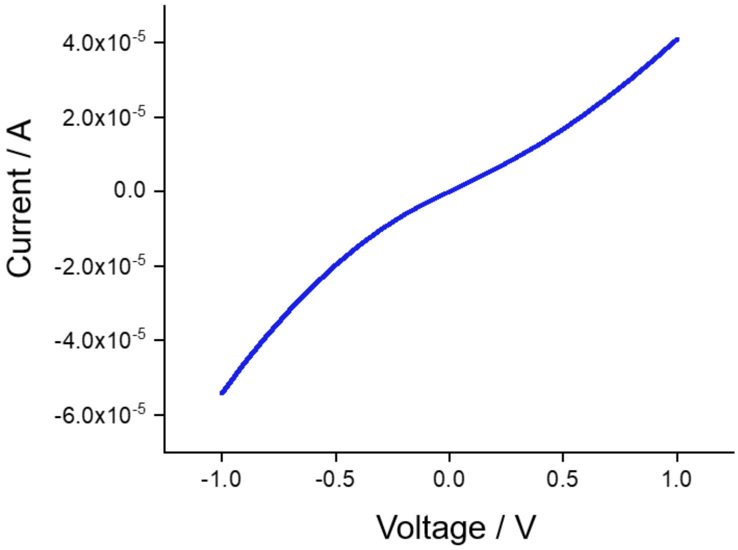

Figure 7.23. I–V curve for a pressed pellet sample of **CoCPNDI-1**.

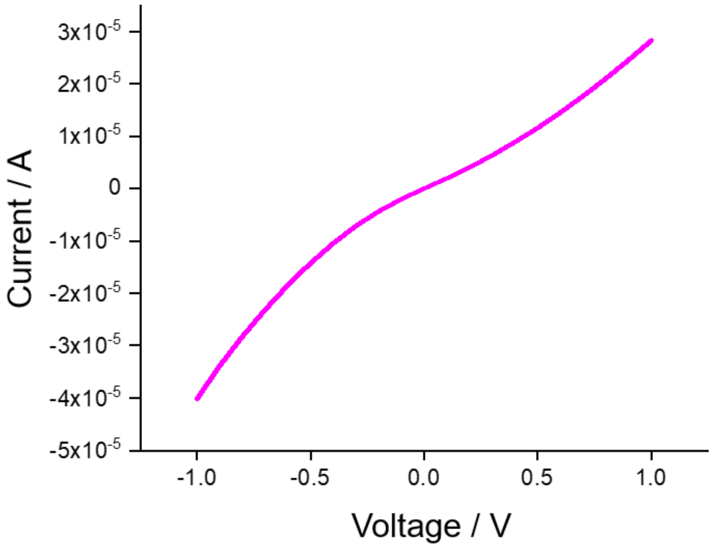

Figure 7.24. I–V curve for a pressed pellet sample of **MnCPNDI-1**.

The I–V curves of **FeCPNDI-1**, **CoCPNDI-1**, **MnCPNDI-1** were observed to show a slight non-linear character. The non-linear character is likely to relate to poor contacts between either the probes and the material, or the material with adjacent crystallites.[3] The conductivity of each material was extracted from the "linear operating range", i.e., the narrow range just above and below 0 A that corresponded to a straight line. The emergence of the straight line allows for the calculation of the conductivity of the material as displayed in the main text, Table 5.4.

7.10 PXRD DATA

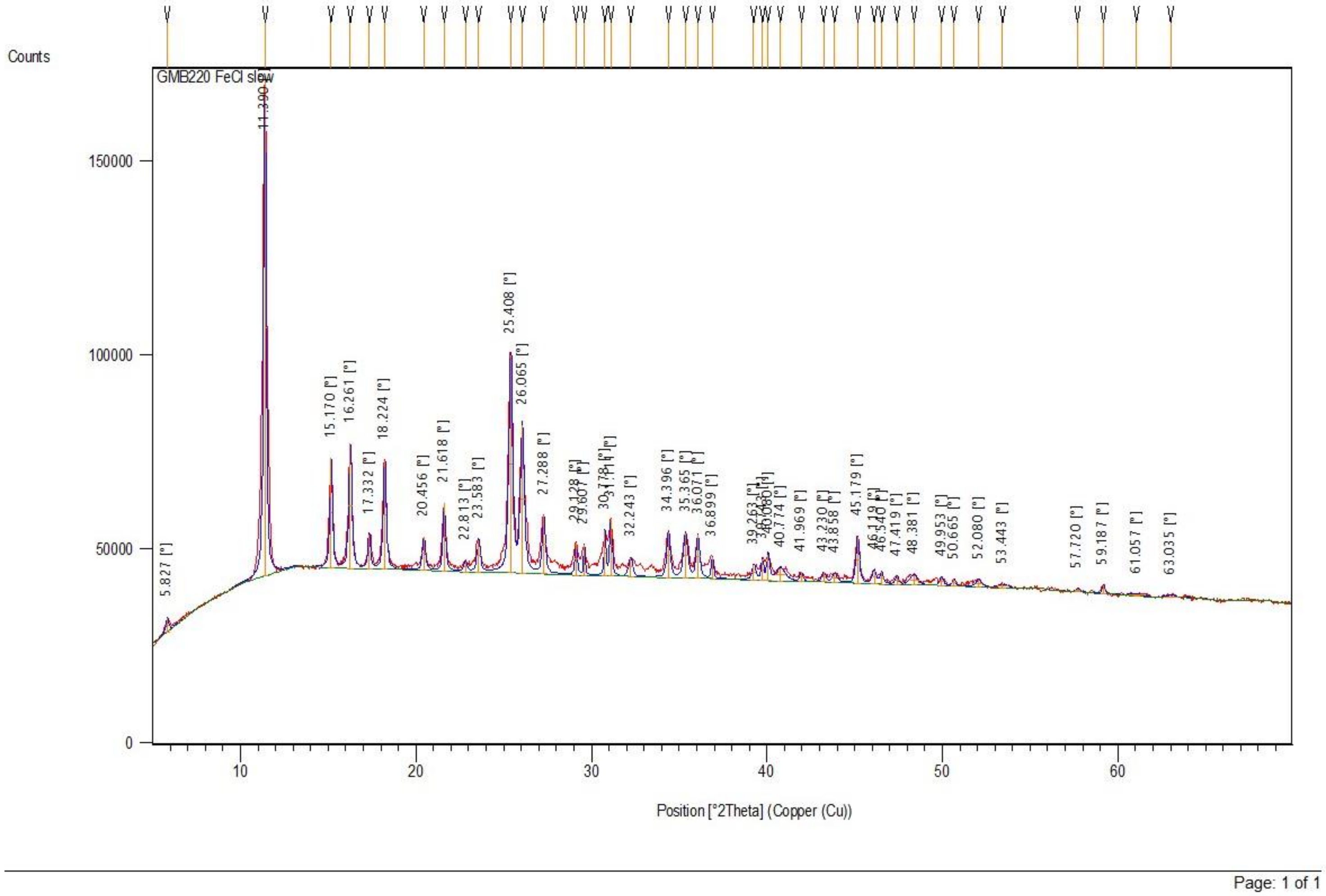

Figure 7.25. The peak-picked PXRD pattern of **Fe(Cl)NDI-1**. The red line is the original pattern, the blue line is the background-removed pattern.

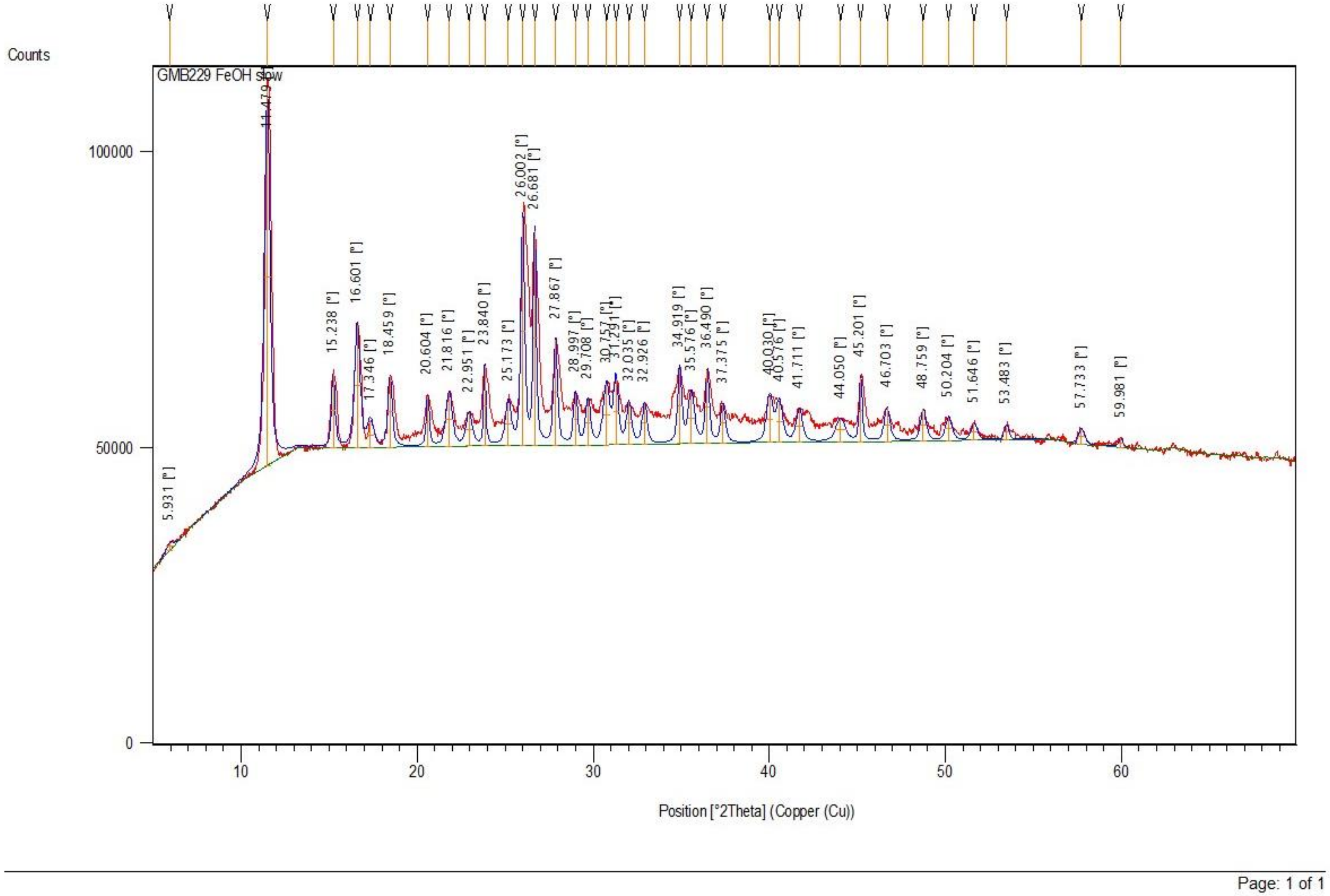

Figure 7.26. Peak-picked PXRD pattern of **Fe(OH)NDI-1**. The red line is the original pattern, the blue line is the background-removed pattern.

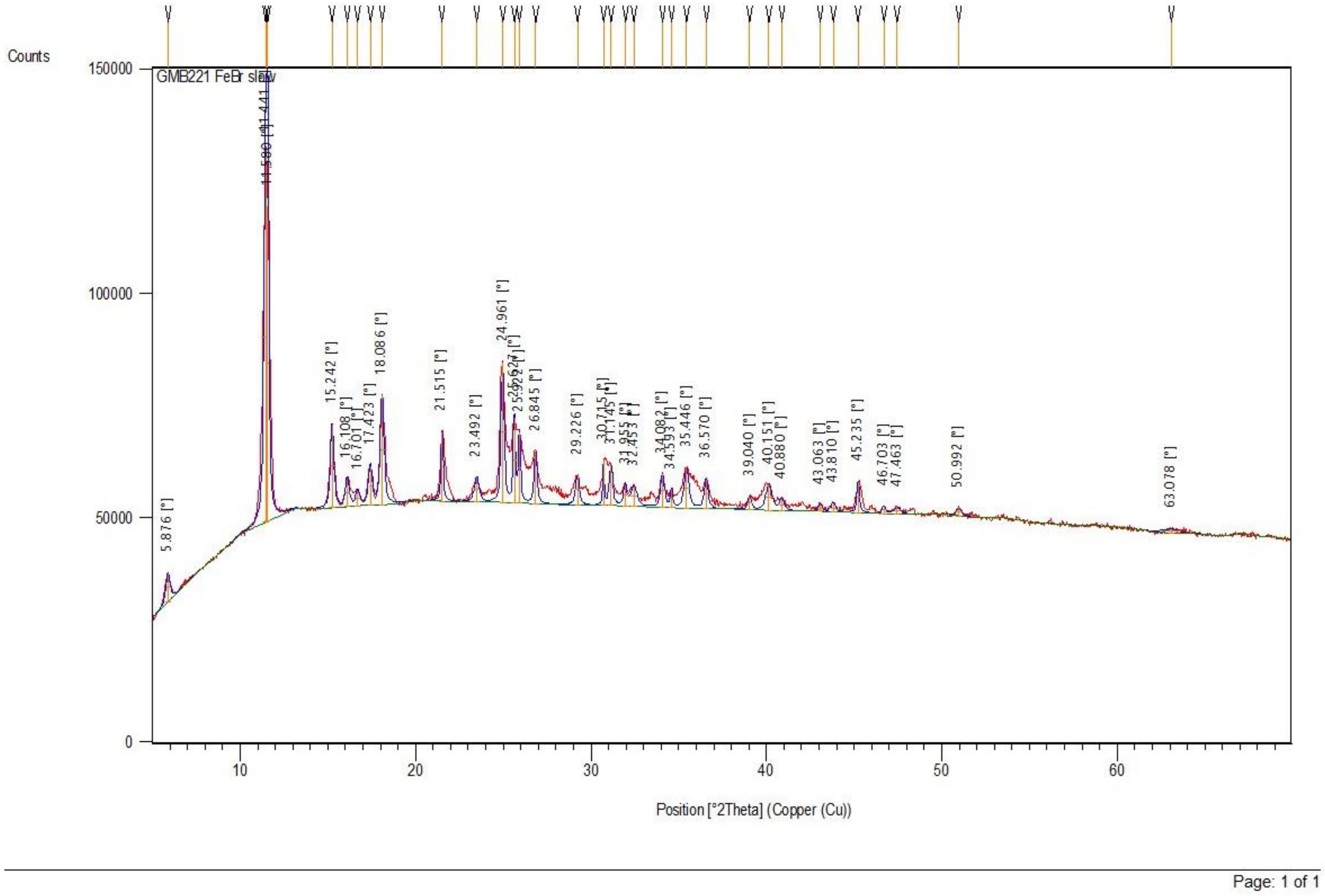

Figure 7.27. Peak-picked PXRD pattern of **Fe(Br)NDI-1**. The red line is the original pattern, the blue line is the background-removed pattern.

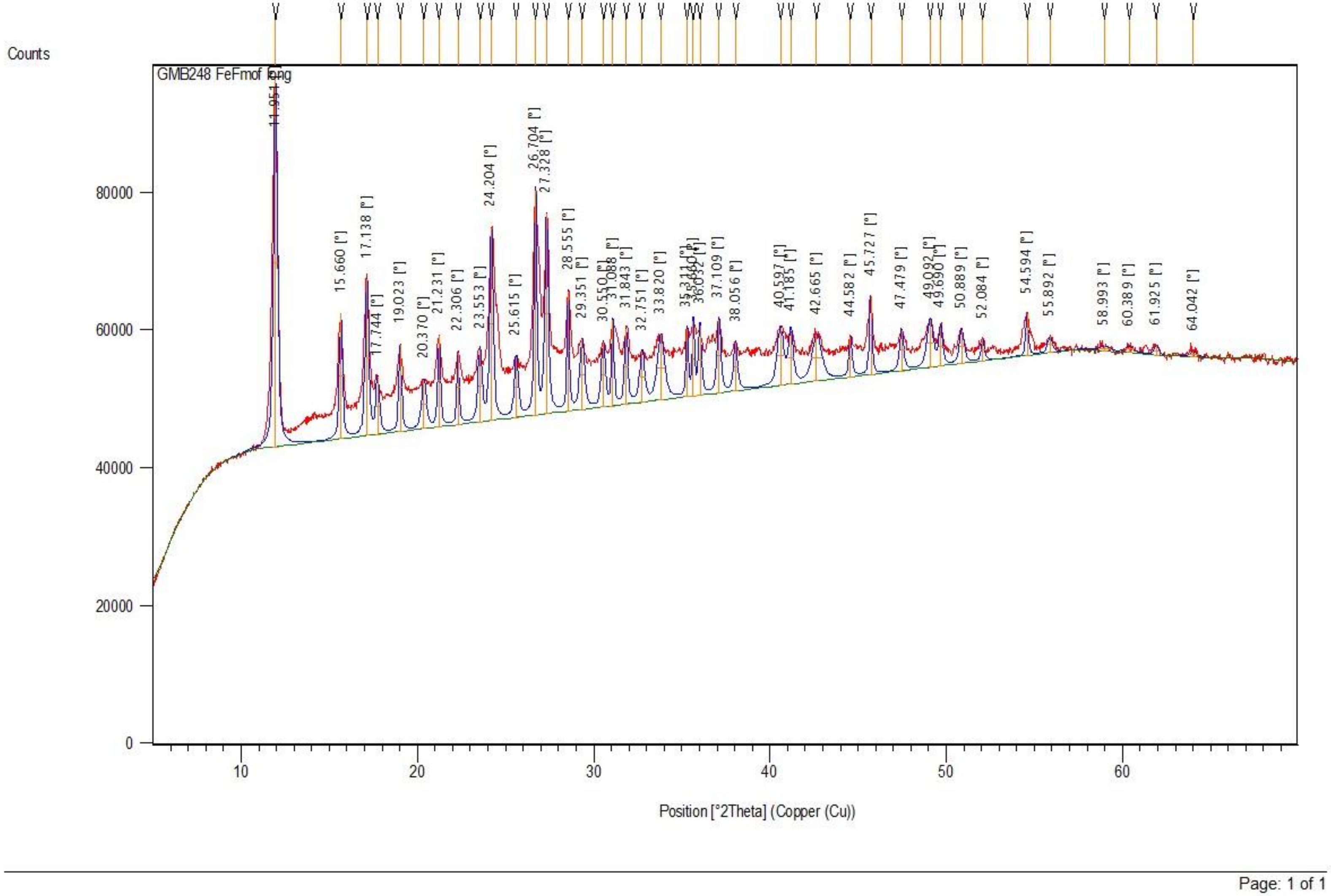

Figure 7.28. Peak-picked PXRD pattern of **Fe(F)NDI-1**. The background has not been removed from powder pattern for clarity.

7.11 XRF ANALYSIS

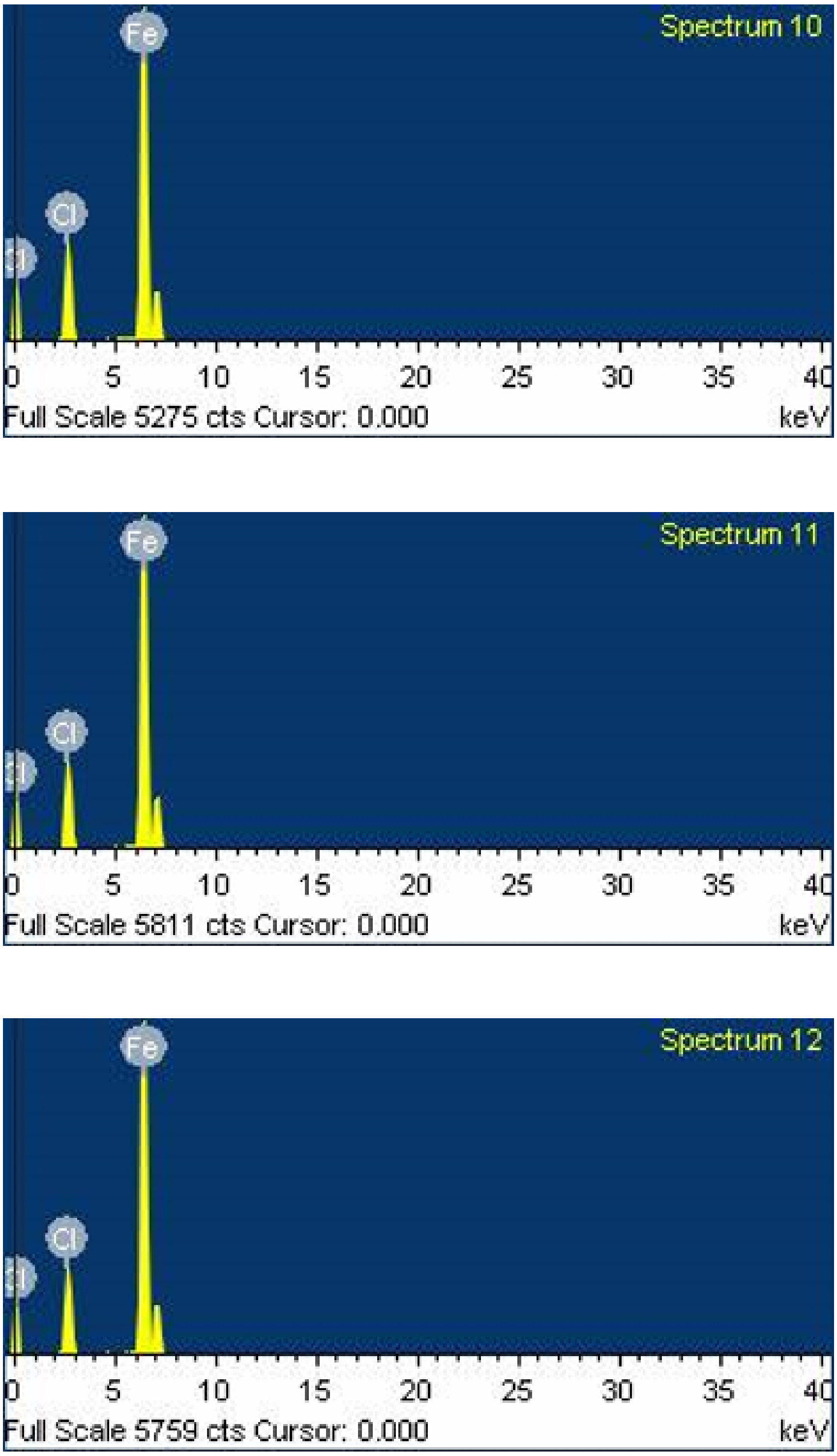

Figure 7.29. X-ray fluorescence spectra of **Fe(Cl)NDI-1**.

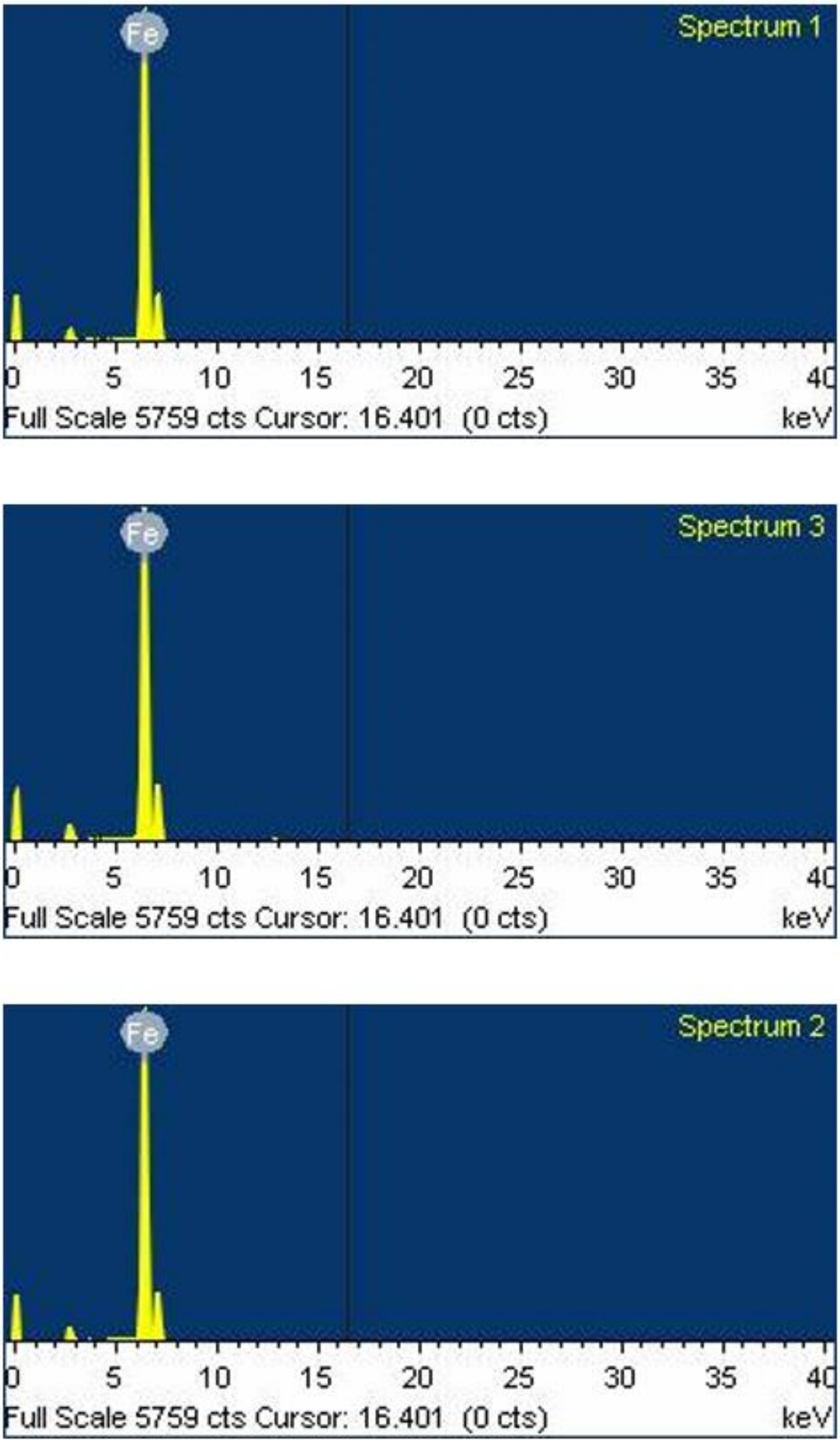

Figure 7.30. X-ray fluorescence spectra of **Fe(OH)NDI-1**.

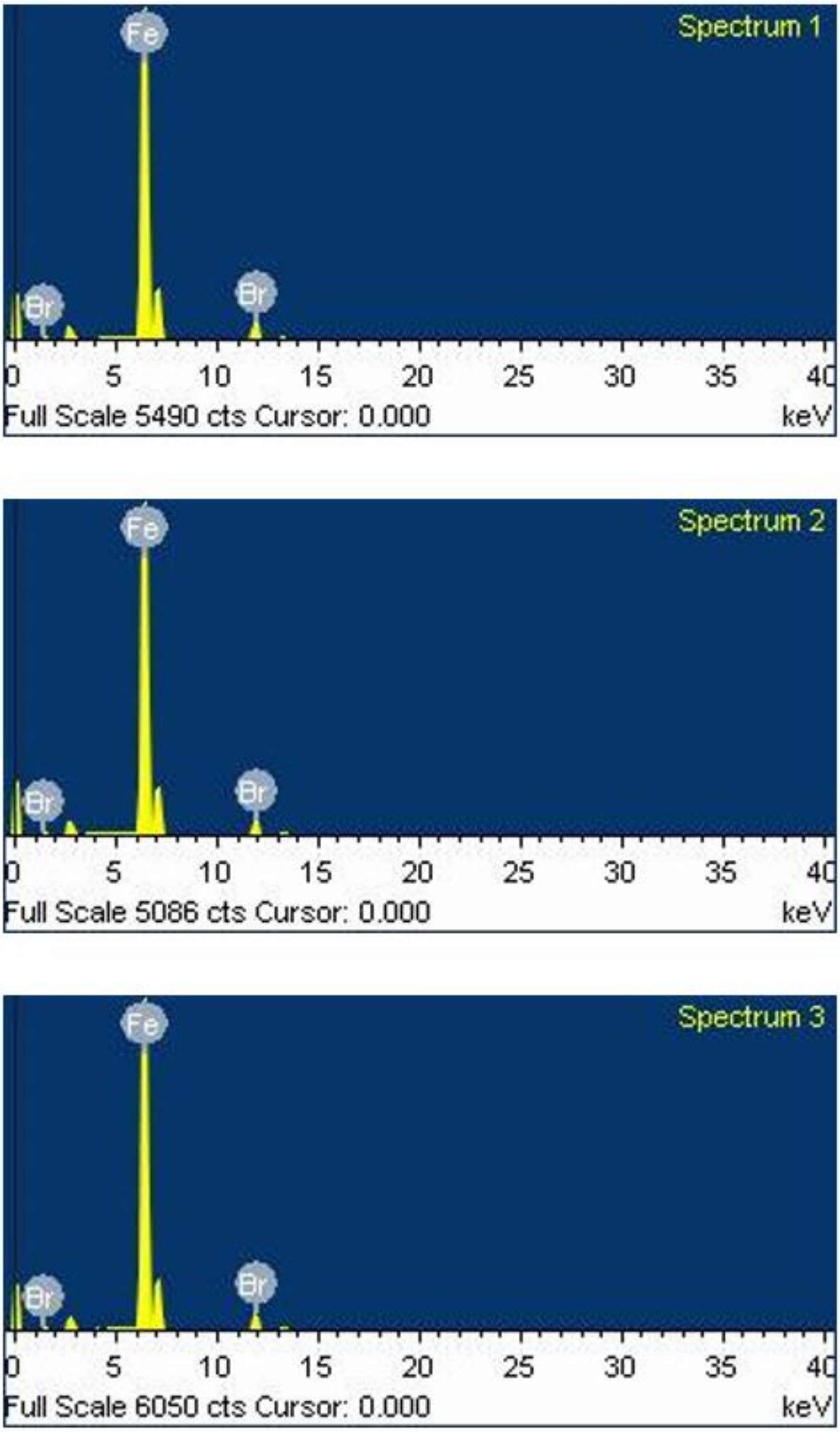

Figure 7.31. X-ray fluorescence spectra of **Fe(Br)NDI-1**.

7.12 PHOTOREDUCTION EXPERIMENTS

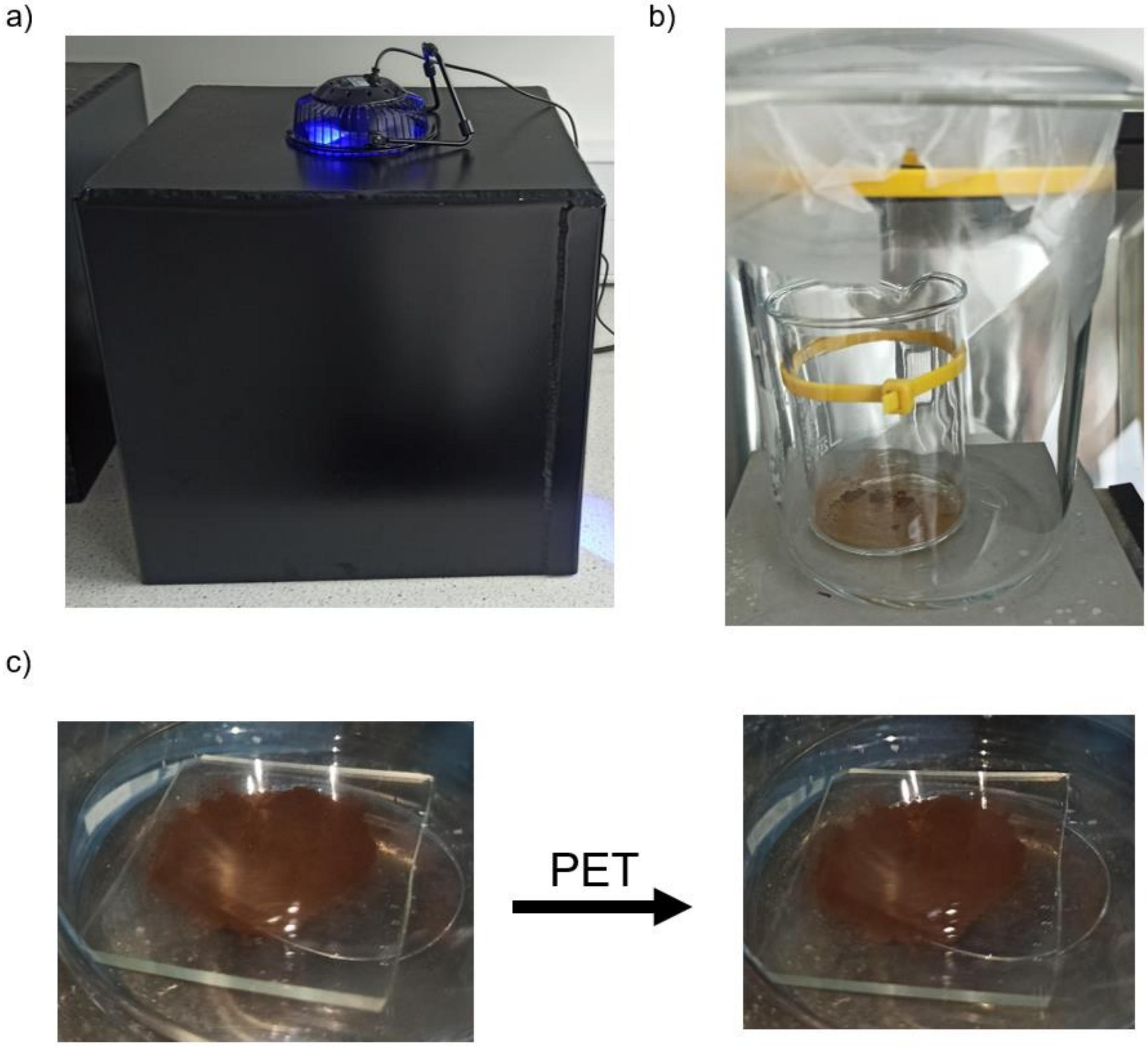

Figure 7.32. The experimental setup for photoreductions (a) The active photoreduction setup with broad spectrum (200-1000 nm) light source, (b) the experimental setup, including 250 mL beaker containing Et_3N that was covered with parafilm and a watch glass which also contained a 50 mL beaker containing **Fe(Cl)NDI-1** sample with glass slide, (c) indication of no colour change after the experiment had been completed. PET = Photo-induced electron transfer.

Fe(Cl)NDI-1 (50 mg) was deposited on a pre-cut glass slide, inside a 50 mL breaker. The 50 mL breaker was then placed inside a 250 mL breaker, that contained Et_3N (20 mL). Parafilm was spread over the lip of the 250 mL breaker followed by a watch glass after 5 min to ensure dispersion of Et_3N into the beaker. The experimental set up was then placed inside a photo-reactor and was left for 5, 10, 30 and 60 min.

7.13 CHEMICAL REDUCTION

To a two-neck 100 mL flame-dried RBF equipped with a stir bar, **Fe(Cl)NDI-1** (25 mg) was added over a positive flow of N_2. Dry, degassed DMF was then added, followed by a dry degassed solution 1M TBAF in TFH (200 µL). The resulting suspension was stirred for 24 h at rt, and was then isolated after washing in dry, degassed Et_2O.

7.14 TABLE OF CRYSTALLOGRAPHIC DATA FOR FE(CL)NDI-1

Table 7.2 Crystallographic data for **Fe(Cl)NDI-1**.

Compound name	**Fe(Cl)NDI-1**
Empirical formula	$C_{20}H_8ClFeN_6O_4$
Formula weight	487.61
Space group	C m m a
a (Å)	6.9046(5)
b (Å)	30.758(2)
c (Å)	8.9712(10)
α (°)	90
β (°)	90
γ (°)	90
Cell volume (Å^3)	1905.23
Z	4
R-Factor (%)	9.62
Temperature (K)	283–303 (room temperature)
D_x (g cm^{-3})	1.700
Radiation source	Synchrotron

7.15 SEM IMAGES

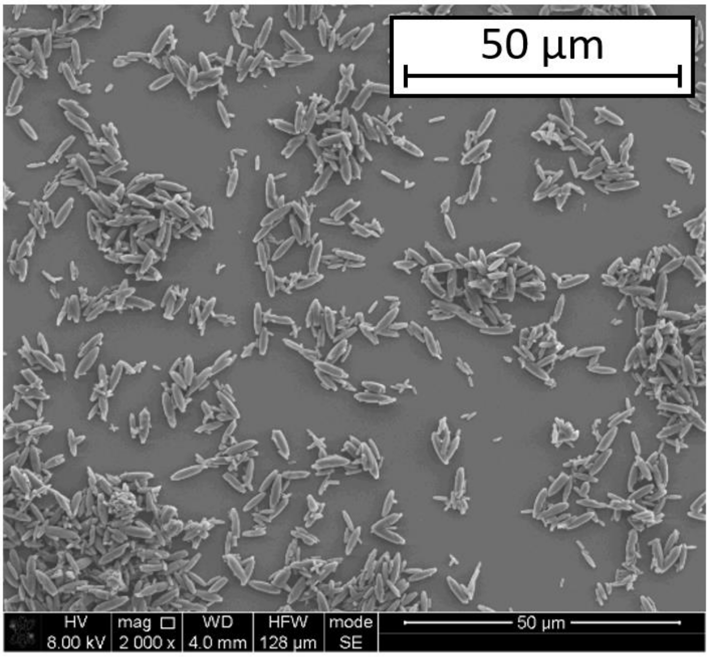

Figure 7.33. SEM image **Fe(Cl)NDI-1** at ×200 magnification.

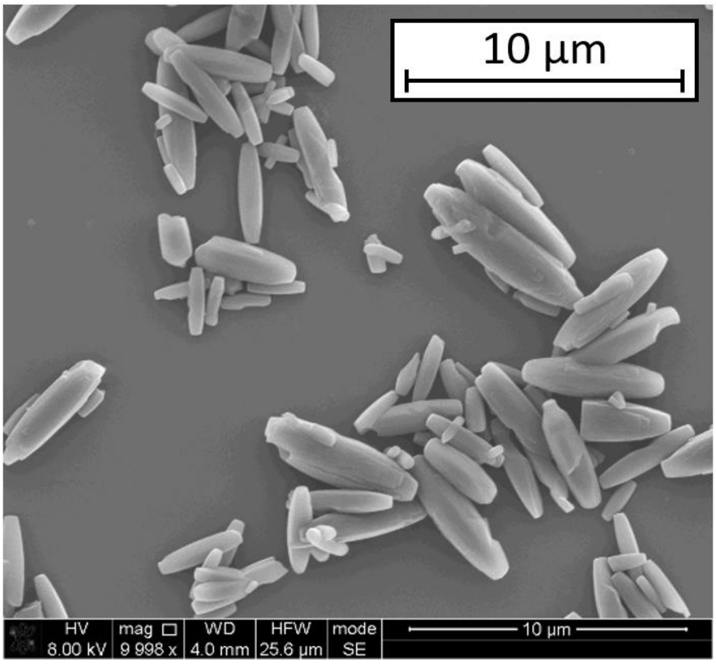

Figure 7.34. SEM image **Fe(Cl)NDI-1** at ×9998 magnification.

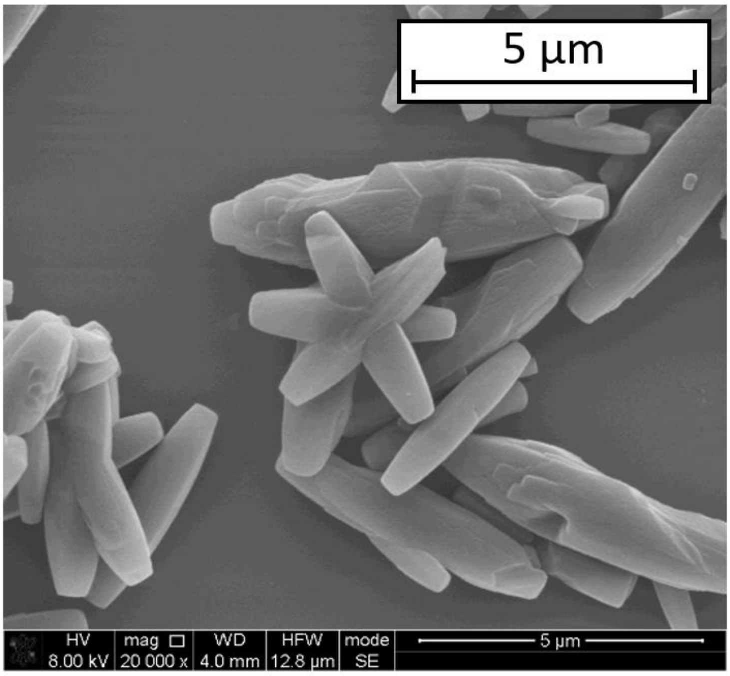

Figure 7.35. SEM image **Fe(Cl)NDI-1** at ×20000 magnification.

7.16 TUNING OF TEMPERATURE AND FORMIC ACID IN THE SYNTHESIS OF FeCPNDI-1

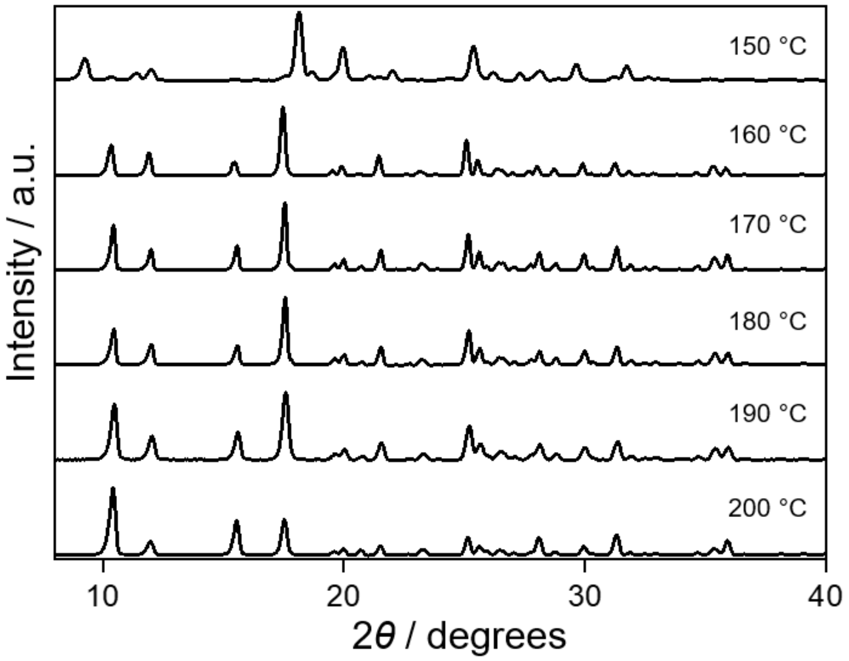

Figure 7.36. Synthetic experiments were carried out using increasingly lower temperature, by 10 °C in each instance. Starting material is observed to remain in the reaction mixture at 150 °C.

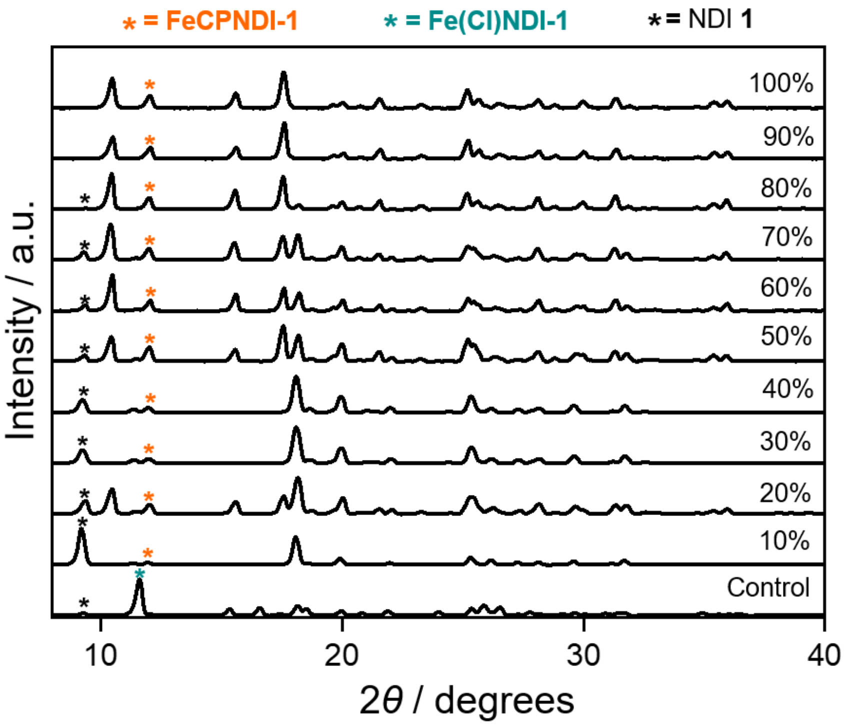

Figure 7.37. All experiments were carried out at 160 °C for 15 min using varying amounts of formic acid in the microwave without post-synthetic washing on the filter with DMSO and EtOH to reveal any starting materials left post-reaction.

To determine the optimal formic acid concentration for generating phase-pure **FeCPNDI-1**, a series of synthetic procedures were conducted with decreasing concentrations, each reduced by 10% from an original concentration of 100 equivalent of formic acid. The screening experiment reveals that unless a concentration of <90% formic acid is employed under the conditions illustrated in Figure 16, unreacted NDI **1** starting material persists in the reaction mixture. Thus, based on this screening study, it is established that to ensure the formation of **FeCPNDI-1**, 100% of the original formic acid concentration should be used to generate the as-synthesised material.

7.17 CRYSTALLOGRAPHIC INFORMATION FOR FECPNDI-1, COCPNDI-1, MNCPNDI-1

Table 7.3. Crystallographic information for **FeCPNDI-1**, **CoCPNDI-1**, **MnCPNDI-1**.

Compound	**FeCPNDI-1**	**CoCPNDI-1**	**MnCPNDI-1**
CCDC reference no.	-	-	-
Empirical formula	$C_{22}H_{12}FeN_6O_8$	$C_{22}H_{12}CoN_6O_8$	$C_{22}H_{12}MnN_6O_8$
Formula weight	544.22	547.00	543.31
Crystal size / mm^3	-	-	-
Temperature / K	110	109.95	110
Crystal system	monoclinic	monoclinic	monoclinic
Space group	$P\,2_1/c$	$P\,2_1/c$	I 2/a
a / Å	17.2846(10)	17.2370(8)	17.3772(6)
b / Å	8.3177(4)	8.2887(3)	8.3182(2)
c / Å	6.8303(3)	6.8748(3)	6.8584(3)
α / °	90	90	90
β / °	91.181(5)	91.624(4)	90.722(3)
γ / °	90	90	90
Volume / Å^3	981.771	968.956	991.283
Z	2	2	2
Z'	0.5	0.5	0.5
ρ_{calc} / g cm^{-3}	1.841	1.876	1.820
R-Factor (%)	3.84	4.07	3

7.18 REFERENCES

(1) Spackman, M. A.; Jayatilaka, D. Hirshfeld Surface Analysis. *CrystEngComm* **2009**, *11* (1), 19–32. https://doi.org/10.1039/B818330A.

(2) Mackenzie, C. F.; Spackman, P. R.; Jayatilaka, D.; Spackman, M. A. CrystalExplorer Model Energies and Energy Frameworks: Extension to Metal Coordination Compounds, Organic Salts, Solvates and Open-Shell Systems. *IUCrJ* **2017**, *4* (5), 575–587. https://doi.org/10.1107/S205225251700848X.

(3) Nafari, A.; Angenete, J.; Svensson, K.; Sanz-Velasco, A.; Olin, H. Combining Scanning Probe Microscopy and Transmission Electron Microscopy. In *Scanning Probe Microscopy in Nanoscience and Nanotechnology 2*; Bhushan, B., Ed.; NanoScience and Technology; Springer: Berlin, Heidelberg, 2011; pp 59–99. https://doi.org/10.1007/978-3-642-10497-8_3.